Dye sensitized solar cell: Optimizing materials, methods and optoelectronic effects

Thesis Submitted to AcSIR For the Award of

the Degree of

DOCTOR OF PHILOSOPHY

In Chemical Sciences

By

Shruti Agarkar

Registration No.: 10CC12A26019

Under the guidance of

Dr. Satishchandra B Ogale

CSIR-National Chemical Laboratory, Pune, India

सीएसआयआर–राष्ट्रीय रासायनिक प्रयोगशाला
(वैज्ञानिक तथा औद्योगिक अनुसंधान परिषद)
डॉ. होमी भाभा मार्ग, पुणे – 411 008. भारत
CSIR-NATIONAL CHEMICAL LABORATORY
(Council of Scientific & Industrial Research)
Dr. Homi Bhabha Road, Pune - 411008. India

CERTIFICATE

This is to certify that the work presented in the thesis entitled **"Dye Sensitized Solar Cell: Optimizing materials, methods and optoelectronic effects"** by **Shruti Agarkar**, submitted for the degree Doctor of Philosophy in Chemical Sciences was carried out under my supervision at the Physical and Materials Chemistry Division, National Chemical Laboratory, Pune, 411008, India. All the materials from other sources have been duly acknowledged in the thesis.

Dr. Satishchandra B. Ogale

(Research Guide)

Date: 10/7/2014

Place: NCL– PUNE

Communication Channels
NCL Level DID : 2590
NCL Board No. : +91-20-25902000
EPABX : +91-20-25893300
: +91-20-25893400
FAX
Director's Office : +91-20-25902601
COA's Office : +91-20-25902660
COS&P's Office : +91-20-25902664
WEBSITE
www.ncl-india.org

DECLARATION

I hereby declare that the thesis entitled "**Dye sensitized solar cell: Optimizing materials, methods and optoelectronic effects**" submitted for the degree Doctor of Philosophy in Chemical Sciences to the Academy of Scientific & Innovative Research (AcSIR), has been carried out by me at the Physical and Materials Chemistry Division of National Chemical Laboratory, Pune under the guidance of Dr. Satishchandra B. Ogale. Such material as has been obtained by other sources has been duly acknowledged in this thesis. The work is original and has not been submitted in part or full by me for any other degree or diploma to other University.

Sagarkar

Date: 10th July 2014

Shruti Agarkar

(Research Student)

National Chemical Laboratory,

Pune - 411008

Dedicated to my Family

Family is like branches on a tree, we all grow in different directions but our roots remain as one!!

Acknowledgements

There are so many people, whose support, encouragement and inspiration are very much necessary to accomplish any major achievements in life, especially, if it involves the elements of fulfilling one's cherish dreams. For me, this thesis is such an important destiny and I am indeed indebted to lot of people for their wishes and blessings for completing this journey. I take this opportunity to acknowledge and extend my sincere gratitude towards all these people who have been involved, directly or indirectly, to make the research work described in this thesis possible.

First, I would like to thank Dr. Satishchandra Ogale, my Ph.D. supervisor, for giving me an opportunity to pursue my Ph.D. research with him. It has been a great privilege to work under his able guidance and his dynamic laboratory environment for the past five years. I greatly appreciate the insights he provided in various studies pursued in my work. His innovative thinking and highly spirited attitude have inspired me to conduct and complete my doctoral research quite efficiently. He has not only grafted my scientific skills and knowledge but also moulded me into a better human being. His guidance always challenged me intellectually and provided a perfect ambience that I needed to grow as a materials chemist. I am really grateful to him for his critical comments and tremendous efforts in preparing this dissertation. I thank him for their endless support filled with patience and enthusiasm during my whole tenure of Ph.D.

I sincerely thank various funding agencies namely, the Council of Scientific and Industrial Research (CSIR), the Department of Science and Technology (DST), the Department of Information Technology (DIT), and last but not the least, the Govt. of India for the research fellowship and travel grants.

I express my sincere thanks to Dr. S. Sivaram, former Director of CSIR-NCL, Dr.Sourav Pal, Director, CSIR-NCL and Dr. Anil Kumar, HOD, Physical and Materials Chemistry Division, for providing the infrastructure and facilities for performing my research at CSIR-NCL and for their whole-hearted help and constant support from the very first days in National Chemical Laboratory. Also I would like to thank Dr.(Mrs.) Jyoti P. Jog, Dr. Sreekumar, Dr. P.A. Joy, Dr. Krishnamoorty, Dr. C.S Gopinath and Dr.(Mrs.) Swati Joshi for their timely advice and help. I also appreciate Dr. K. R. Patil and Mr. R. S. Gholap for their help in materials characterization.

A special thanks to all collaborators, especially Dr. B. B. Kale, CMET, Pune , Dr.S. N. Kale, DIAT, Pune, Dr Sujatha Devi , CGCRI, Kolkata and Dr Deepa Khushlani, TIFR Mumbai . I also admire and appreciate the help of Dr. C. G. Suresh, Mr.Naveen Pavithran, Mr. Deepak Jori, Mrs. Puranik, Mrs. Kolhe and Mr. Punekar, throughout this journey.

I would like to thank my senior colleagues Dr. Hrushikesh Joshi, Dr. Sneha Kulkarni, Dr. Kashinath Bogle, Dr. Rajesh Hyam, Dr. Sarfraj Mujawar, Dr. Anup Kale, Dr. Tushar Jagdale, Dr. Abhimanu Rana, Dr. Vivek Dhas, Dr. Subas Muduli and Dr. Prasad Yadav for their mentoring and care during my initial research days. A very special thanks to all my current lab-mates Dr. Debanjan Guin, Dr. Vivek Antad, Dr. Sarika Kelkar, Dr. Arif Sheikh, Dr. Parvez Shaikh, Dr. Meenakshi, Datta Kumar, Meenal, Mandakini, Reshma, Lily, Mukta, Onkar, Vishal, Anil, Satish, Abhik, Rohan, Umesh, Wahid, Yogesh, Deepti, Rounak, Pradeep, Pooja, Dhanya, Shraddha, Satyawan, Aniruddh, Aparna, Ketaki, Rupali, Nilima, Dr. Sambhaji, Harish Sir, Ashish Sir, Upendra, Praverthana, Sumit, Kush, Tanya, Divya, Aparna, Sumit and Ishita for all their support and for creating an interesting laboratory atmosphere.

Finally I specially acknowledge my husband Ketan for his understanding, support, love and care and for being there with me at all times. I would like to take this opportunity to thank my family Baba, Aai, Kaka, Kaku (my in-laws), Tanmay and last but not the least aaji for allowing me to pursue my ambition. I would like to take this opportunity to thank my sister Richa, my brother in law Nikhil, Vivek Mama and my dear newphew Arjun for their love and constant affection.

I would like to thank all my teachers from primary school till my master's degree for imbibing good values and knowledge in me.

Last but by no means least I thank Lord Ganpati for making my life so special.

Shruti Agarkar…….

List of Abbreviations

AFM	Atomic Force Microscopy
AM	Air Mass
B-H plot	Benesei-Hildbrand plot
CB	Conduction Band
CIS	$CuInSe_2$
CIGS	$Cu(In,Ga)Se_2$
CPP	Current Perpendicular to Plane
CT	Charge Transfer
CV	Cyclic Voltammetry
DOS	Density of States
DRS	Diffuse Reflectance Spectroscopy
DSSC	Dye Sensitized Solar Cell
EIS	Electrochemical Impedance Spectroscopy
F-D curve	Force-Distance curve
FESEM	Field Emission Scanning Electron Microscope
FF	Fill Factor
FTIR	Fourier Transform Infra-red
FTO	Fluorine doped Tin oxide
FWHM	Full Width at Half Maximum
HOMO	Highest Occupied Molecular Orbital
HRTEM	High Resolution Transmission Electron Microscope
HDA	Hexadecylamine

IPCE	Incident photon-to-current conversion efficiency
ITO	Indium doped Tin Oxide
J_{SC}	Short circuit current density
LH	Light Harvesting
LHE (λ)	Light harvesting efficiency at wavelength λ
LUMO	Lowest Unoccupied Molecular Orbital
NBs	Nanobeads
NFs	Nanoflowers
NMR	Nuclear Magnetic Resonance
NPs	Nanoparticles
PL	Photo-luminescence
P_{max}	Maximum power
PET	Poly Ethylene Terphthalate
SAED	Selected Area Electron Diffraction
STM	Scanning Tunnelling Microscope
TIP	Titanium tetra isopropoxide
TEM	Transmission Electron Microscope
tBA	tertiary Butyl Alcohol
UV-VIS-NIR	Ultraviolet-Visible-Near
XRD	X-ray Diffraction
VB	Valence Band
V_{OC}	Open circuit potential
TCO	Transparent Conducting Oxide

Contents

Abstract

Solar energy has the potential to fulfill an important part of the sustainable energy demand of future generations. Developing affordable and highly efficient photovoltaic technologies has always been a cherished goal of materials scientists and device community. Exploring non-silicon alternatives based on the novel scientific opportunities afforded by the emergence of nanotechnology (the so-called third generation cells) has gained significant momentum in this respect during the past two decades. With respect to the present status of PV technologies, improvements in three areas have to be made: costs, applicability and sustainability. Semiconductor-grade silicon wafers still being relatively expensive, great efforts have been put into the development of potentially cheaper thin-film solar cells. Dye Sensitized Solar Cells developed by O'Regan and Grátzel have attracted lot of interest and is considered as a promising future technology, owing to its inherent cost reduction potential, which is based on the use of inexpensive components, its relatively simple production technology and its wide applicability. The significant collective efforts by the scientific community over the past 20 years have not only pushed the efficiencies higher but have brought out several new ways of making robust and durable DSSC cells fairly affordably with good efficiencies. This thesis work is based on DSSCs and is organized in seven chapters including introduction.

Chapter 1 explains the current challenge faced by the world in terms of energy availability, excessive usage of fossil fuels leading to their exhaustion followed by their negative influence on health and environment. The shortage of fossil fuels has directed the world to search for alternative clean and green energy sources. Nuclear energy is one such alternative, but to meet the current energy requirements we need to build a new 1 GW (giga watt)-electric nuclear fission plant everyday for the next 50 years somewhere on this planet. This is close to impossible. We

therefore discuss use of renewable energy sources like hydroelectric resource, from tides & ocean currents to geothermal integrated over all of the land area. Globally extractable wind power and solar energy striking the earth are perhaps the best alternatives for conventional energy resources. We emphasize the use solar energy which is available in plenty as the best resource to meet the current energy needs partially but in a clean way. Later in the chapter we explain various energy harvesting approaches, energy conservation devices which include solar cells, both traditional Silicon Vs GenNext solar cells, and discuss in details about the advantages and disadvantages of both types of solar cells. Later in the chapter we point out the novelty, design and strengths of Dye Sensitized Solar Cells (DSSCs) which includes use of nanomaterials engineering, optimizing device architecture etc. Current status of research which includes literature survey, followed by DSSC applications and later the technology position of DSSC, are discussed in details. The maximum theoretically predicted efficiency of DSSCs, the areas of scientific goals necessary to enhance DSSC performance and other criteria for technological execution of DSSCs are examined in detail. Lastly, the motivation of the present work, work plan, and the layout of the thesis are presented in this first chapter.

Chapter 2 deals with basic synthesis and characterization techniques involved in DSSC research derived from the materials and device design aspects involved. Also the basic scientific issues, identification of key device parameters needed for device performance optimization are discussed in detail. Towards the end, DSSC measurement procedures, choices of materials systems, and the basis for the same are also analyzed in details.

Chapter 3 discusses making of small area DSSC device. DSSC fabrication protocol including making of the slurry used for photoanode construction, photo-anode fabrication, dye loading, electrolyte preparation and making of counter electrode are explained in detail. Here the best

efficiency achieved in the lab using the above mentioned materials is demonstrated. Use of different morphologies in DSSC photoanodes is also highlighted. Later in the chapter scaling up issues for large area solar cells and their different device architectures are also illustrated.

Chapter 4 gives insights into some important characterization techniques used to improve the device performance. In particular the impedance measurement is discussed in several details with examples. Impedance is used as a key tool for the characterization of the opto-electronic properties of DSSCs and thereby deciphering the specific role of different components of the device architecture. This is brought out via various case studies. Also the cyclic voltammetry and Tafel polarization plot used to determine the performance DSSC counter electrode are explained in details.

Chapter 5 deals with the development of a natural dye, namely Isobutrin, belonging to the chalcogenide class, extracted from special class of flowers identified as the flame of forest, as a sensitizer in DSSCs. The first half of this chapter deals with the extraction of this dye from the flowers followed by its detailed characterization. The second half of the chapter includes use of this dye as sensitizer in DSSCs followed by its DSSC characterization: I-V, IPCE, lifetime, stability data etc. The important highlight of this chapter is the formation of Ti-isobutrin chelate leading to a strong dye to TiO_2 charge transfer in the visible region. The Ti-Isobutrin chelate formation is studied using Benesi-Hildebrand plot.

Chapter 6 elaborates our efforts towards the development of low cost, low temperature processed DSSCs on flexible substrates. In this chapter a detailed procedure for making binder free TiO_2 paste which cures at room temperature is explained. The first half of the chapter deals with optimizing the ratio of solvent and TiO_2 followed by detailed characterization of the paste

and the photoanodes made from it involving FESEM, confocal microscope images , FTIR etc. Solar cell device characterizations such as I-V, IPCE, impedance, dye loading etc. are described in the second half of the chapter. The highlight of this chapter is that this TiO_2 paste can be coated on any substrate (FTO, ITO-PET, Stainless steel etc) by using a simple hand held brush to give an impressive efficiency of 3% on FTO substrate (It is a room temperature solar paint!!).

The thesis is concluded with **Chapter 7** describing summary, conclusions and directions for future work.

An Appendix is included as the last part which includes preliminary results of some of the interesting ongoing unpublished work.

Chapter 1

Introduction

This chapter gives an overview of the current international renewable and clean energy challenge, highlighting the adverse effects of the currently used polluting fuels on environment and health. The importance of the abundantly available solar energy Vs other renewable energy sources is discussed in detail. The different ways of harnessing and utilizing solar energy are also explained in brief. Towards the end, progress in solar photovoltaics (PV) is described which includes all the three generations of solar cells (starting from mono crystalline silicon solar cells to Dye sensitized solar cells up to the recently developed Perovskite solar cells). The current state of the art of these PV technologies is discussed. Finally, the presentation of the outline of current thesis concludes this introductory chapter.

1.1. Need for Renewable Energy. Human activities are closely dependent on the use of several forms and sources of energy to perform work. The energy content of an energy source is the available energy per unit of weight or volume, and the challenge is to effectively extract and use this energy without significant losses in conversion, transportation or utilization. Thus, the more the energy consumed, greater is the amount of work accomplished. By implication the economic development is thus directly correlated with greater levels of energy consumption. The developed nations have been consuming energy at a very high rate for several decades and the developing countries such as China and India have begun to use more and more energy for nation building developments. Clearly the problem of pollution is going to be serious unless clean and green technologies are advanced in the near future and our dependence on conventional polluting fuels in dramatically reduced.

Figure 1. Rapid development needs rapid energy consumption

At the beginning of the 21st century, the use of fossil fuels notably petroleum, were dominant. Out of the world's total power production, 86.4% is derived from fossil fuels. These fossil fuels are formed by decomposition of dead organisms which are buried deep under the earth's crust due to exposure to heat and pressure. Fossil fuels contain high carbon and hydrogen containing compounds like coal, petroleum and natural gas. Volatile compounds containing low carbon-hydrogen ratio like methane gas are also found along with petroleum in and around fossil fuel reserves. It is estimated that the primary sources of energy consist of petroleum 36.0%, coal 27.4%, and natural gas 23.0%, amounting to an 86.4% share for fossil fuels in the primary energy consumption in the world.[1]

Unfortunately each stage in the processing of fossil fuels like extraction, transport, processing, and combustion carry significant and multiple hazards for health and the environment.[2] Amongst the serious consequences of these hazards are extreme weather related events having a bearing upon climate change.[3] Many of the environmental problems we face today result from our over dependence on fossil fuels. These impacts include global warming, air quality deterioration, oil spills, and acid rain. Among the gases emitted while burning of fossil fuels, one of the most significant is carbon dioxide, a gas that traps heat in the earth's atmosphere. Over the last 150 years, burning fossil fuels has resulted in more than a 25 percent increase in the amount of carbon dioxide in our atmosphere.[4] Fossil fuels are also responsible for increased levels of atmospheric methane and nitrous oxide, although they are not the major source of these gases. Due to the increased amount of carbon dioxide in air the global average surface temperature has increased by 0.5-1.1 degrees Fahrenheit (0.3-0.6 degrees Celsius).[2] Scientists worldwide have

concluded that the observed increase in global average temperature over the last century is not of natural origin and that there is a visible human influence on global climate conditions.

Climate scientists also predict that if carbon dioxide levels continue to increase, the planet will become warmer in the next century.[2] The projected temperature increase will most likely result in a variety of adverse impacts. In coastal areas, rising of the sea-level due to the warming of the oceans and the melting of glaciers may lead to flooding of wetlands, river deltas and even populated areas. Altered weather patterns may result in more extreme weather events and agricultural zones could suffer an increase in the number of droughts.[3]

Several important pollutants are produced by fossil fuel combustion: carbon monoxide, nitrogen oxides, sulfur oxides, and hydrocarbons. In addition, suspended particulates contribute to air pollution, and the nitrogen oxides and hydrocarbons can combine in the atmosphere to form tropospheric ozone, the major constituent of smog.[2] Various health hazards are related to the pollutants.

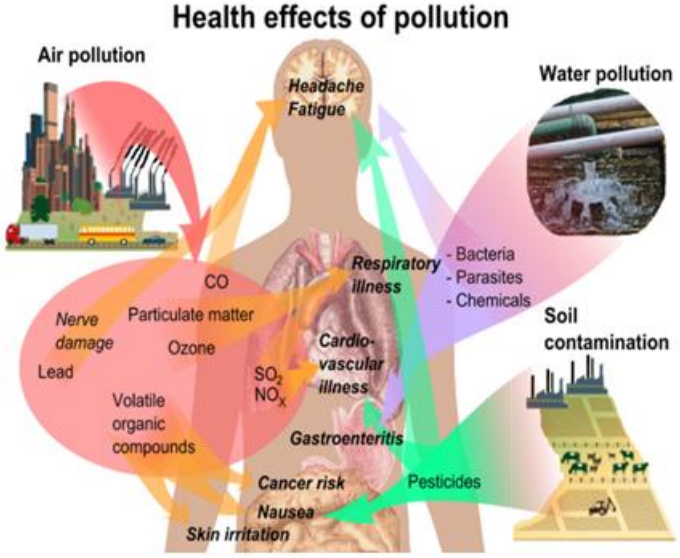

Figure 2. Health hazards of pollution caused by incomplete combustion of fossil fuels

(http://www.immukare.com/)

Carbon monoxide is a gas formed as a by-product during the incomplete combustion of all fossil fuels. Exposure to carbon monoxide can cause headaches and place additional stress on people with heart disease. Cars and trucks are the primary source of carbon monoxide emissions.

Two oxides of nitrogen namely nitrogen dioxide and nitric oxide are formed in combustion. Nitrogen oxides appear as yellowish-brown clouds over many city skylines. They can irritate lungs, cause bronchitis and pneumonia, and decrease resistance to respiratory infections. They also lead to the formation of smog. Sulfur oxides are produced by the oxidization of the available sulfur in a fuel. Utilities that use coal to generate electricity produce two-thirds of the nation's sulfur dioxide emissions. Nitrogen oxides and sulfur oxides are important constituents of acid rain. These gases combine with water vapor in clouds to form sulfuric and nitric acids, which become part of rain and snow. As the acids accumulate, lakes and rivers become too acidic for plant and animal life. Acid rain also affects crops and buildings.[4]

Figure 3. Hazards of use of fossil fuels

The white haze that can be seen over many cities is tropospheric ozone, or smog. This gas is not emitted directly into the air; rather, it is formed when ozone precursors, mainly non-methane hydrocarbons and nitrogen oxides, react in the presence of heat and sunlight. Human exposure to such a zone can produce shortness of breath and, over time, permanent lung damage. Research shows that ozone may be harmful at levels even lower than the current federal air standard. In addition, it can reduce crop yields. Finally, fossil fuel use also produces particulates, including dust, smoke, soot, and other suspended matter, which are respiratory irritants. In addition, particulates may contribute to acid rain nucleation. Coal mining also contributes to water pollution.

Characteristically, the material near coal deposits is acidic. After mining of this coal, the land remains barren unless special precautions are taken to ensure that the proper top soil is used when the area is replanted.[5] Materials other than coal are also brought to the surface in the coal mining process, and these are left as solid wastes. As the coal itself is washed, more waste material is left. Finally, as the coal is burned, the remaining ash is left as a waste product.[5]

Thus in order to meet the increasing energy demand in the near future, there is need to search for alternative energy resources. Three major options are at our disposal to tackle the 10 TW clean energy generation in the coming years. These include fossil fuel (use by controlling pollution), nuclear power, and renewable energy.[6] If we have to produce 10 TW energy using fossil fuels without affecting the environment, we need to find secure storage for 25 billion metric tons of CO_2 produced annually.[1] The increasing need for energy that has developed in the recent past has been further complicated by rapidly diminishing conventional resources, like oil and coal. The challenge faced by the developing nations including India, is to meet increasing energy needs while minimizing the damage to the environment. This is why, while working to bridge our

energy deficit, there is a need to increase the share of clean, sustainable, and renewable energy sources.

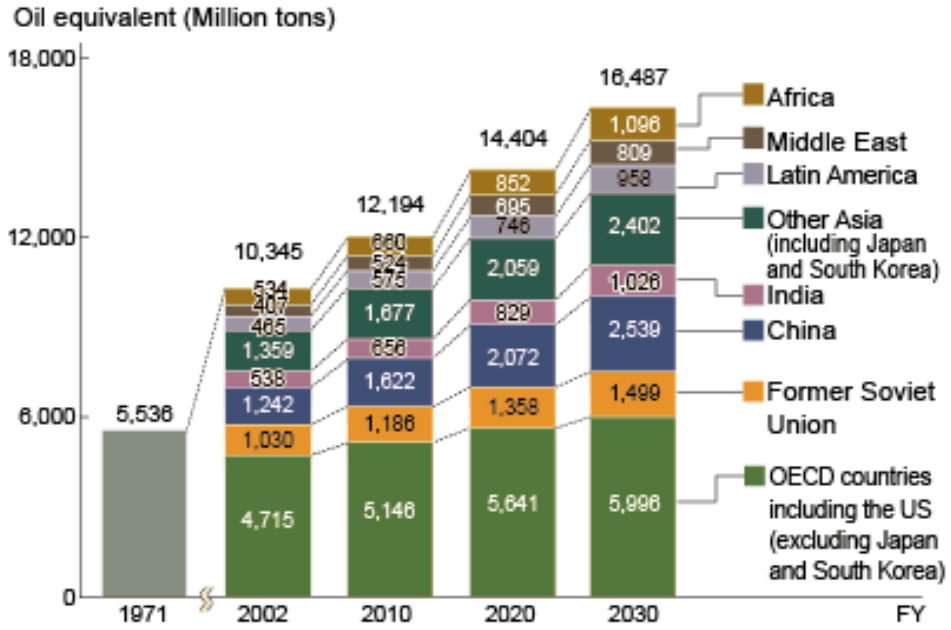

Figure 4. Global energy consumption (***Source:* OECD/IEA *World Energy Outlook* 2004**)

Nuclear power is one viable option. For nuclear power to be the alternate source of energy, we will require construction of a new 1 GW (giga watt)-electric nuclear fission plant everyday for the next 50 years somewhere on earth.[6] This is next to impossible. Also there are two important environmental concerns about nuclear power, both of which deal with its potential negative impact for human health. One involves the highly radioactive products produced by nuclear fission inside power reactors and their careful management at the reactor during and after disposal. The other concern revolves around the weapons-grade plutonium or uranium that might be secretly derived from the nuclear power fuel cycle to make bombs or other weapons of mass destruction by various nations. The routine (non-accidental) emissions of pollutants from the harvesting, processing, and conversion of nuclear fuels can also not be ignored.[6] As compared to

other energy technologies, these emissions are vulnerable to being enhanced by meager mismanagement. Even then the impacts of these emissions are significantly less than those involved with producing power with current coal technologies. Although involving different pollutants, routine emissions from nuclear power systems are probably no more dangerous than those from new natural gas power systems. If public concerns about reactor safety, proliferation, and waste disposal can be satisfied, nuclear power may be able to play a significant role in de-carbonizing the world energy system in the next 50 years.[7]

Renewable energy which is energy derived from the available sources can be tapped from sun, wind, ocean, hydropower, biomass, geothermal resources, biofuels and hydrogen derived from renewable resources. The sources of these energies are aptly called “renewable” as they can be derived from natural processes which can be constantly replenished within a short time span and not unlike fossil fuels which require millions of years for their formation. Renewable energy resources are available in wide geographical areas, in contrast to other energy sources, which are concentrated in a limited number of countries. Rapid deployment of renewable energy and technological diversification of energy sources would indeed result in significant energy security and economic benefits.

1.2. Types of Renewable Energy

1.2.1. Wind Energy

Figure 5. Wind farms for production of electricity

(http://sppiblog.org/tag/wind-energy ,(2014 Sire Studios Inc)

http://www.constructionweekonline.in/article-5858-conditions_favorable_for_wind_energy_growth/

(Published by & © 2014 ITP Business Publishing Ltd))

Of all the renewable energy sources the Wind energy is the oldest and most explored renewable energy source. It was first used to drive ships on the river Nile which is dated 7000 years ago. Today airflows are used to run wind turbines. Modern day wind turbines range from around 600 kW to 5 MW of rated power, although turbines with rated output of 1.5–3 MW have become the most common for commercial use. The power available from the wind is a function of the cube of the wind speed, hence as the wind speed increases, power output increases dramatically up to the maximum output for the particular turbine.[8] Areas where winds are stronger and more constant, such as offshore and high altitude sites, are preferred locations for wind farming. Globally, the long-term technical potential of wind energy is believed to be five times total current global energy production, or 40 times of the current electricity demand, if all practical barriers needed were to be overcome. This would require wind turbines to be installed over large areas, particularly in areas of higher wind resources e.g. offshore. The specific advantage of wind

power is that it does not have fuel cost. Thus the price of wind power is much more stable than any other energy source. The only drawback of electricity from wind is that the wind power is variable on several different timescales. The globally extractable wind power is estimated to be about 2-4 TW.[9]

1.2.2. Hydropower

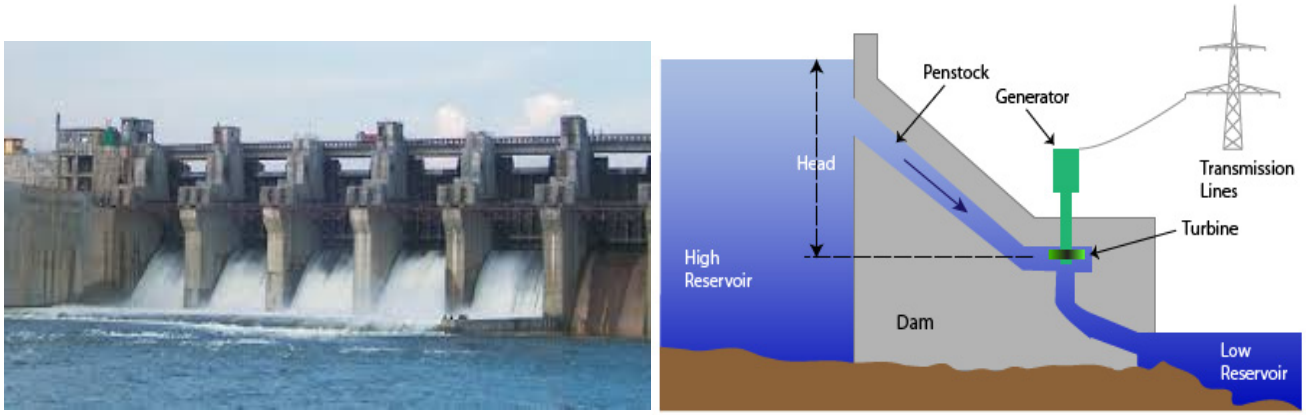

Figure 6. Hydro electric power station

(http://www.voith.com/en/markets-industries/industries/hydro-power/referenz-omkareshwar-4161.html

http://www.greenrhinoenergy.com/renewable/hydro.php (©2013 Green Rhino Energy Ltd))

Hydro-power is the power derived from the energy of falling water and running water, which may be harnessed for useful purposes. Water energy can be harnessed in various ways, namely,

- Hydroelectric energy, usually reserved for large-scale hydroelectric dams.
- Micro hydro systems which are hydroelectric power installations that typically produce up to 100 kW of power. They are often used in water rich areas as a remote-area power supply.
- Run-of-the-river hydroelectricity systems which derive kinetic energy from rivers and oceans without the creation of a large reservoir.

- Tidal power which converts the energy of tides into electricity.

The only drawback of hydropower is that it is a bit expensive. The globally extractable hydro power is estimated to be 2-3 TW.[10]

1.2.3. Geothermal Energy

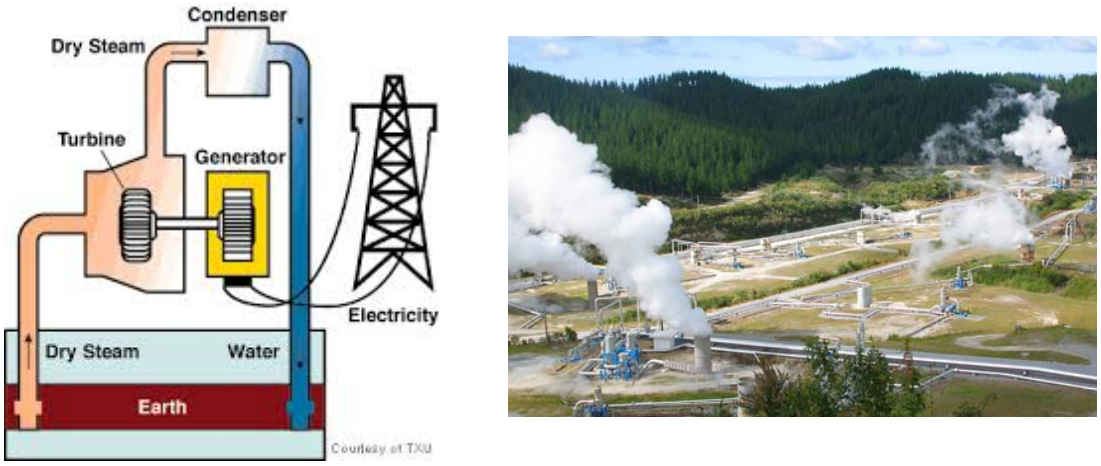

Figure 7. Geothermal energy plant

(http://www.treehugger.com/renewable-energy/hot-water-becoming-a-hot-topic-geothermal-in-india.html

http://www.luminant.com/responsibility/education/generation/geothermal.aspx (2014 Luminant))

Geothermal energy is from the thermal energy generated and stored in the Earth. Thermal energy is the energy that determines the temperature of matter. Earth's geothermal energy originates from the original formation of the planet (20%) and from radioactive decay of minerals (80%).[11] The heat that is used for geothermal energy can be from deep within the Earth, all the way down to Earth's core – 4,000 miles (6,400 km) down. At the core, temperatures reach over 9,000 °F (5,000 °C). Heat conducts from the core to surrounding rock. Extremely high temperature and

pressure cause some rock to melt, which is commonly known as magma. This magma then heats rock and water in the crust, sometimes up to 700 °F (371 °C).[12]

From hot springs, geothermal energy has been used for bathing since Paleolithic times and for space heating since ancient Roman times, but it is now better known for electricity generation. Geothermal energy integrated over all of the land area is estimated to be about 12 TW.[13]

1.2.4. Biomass and Biofuel

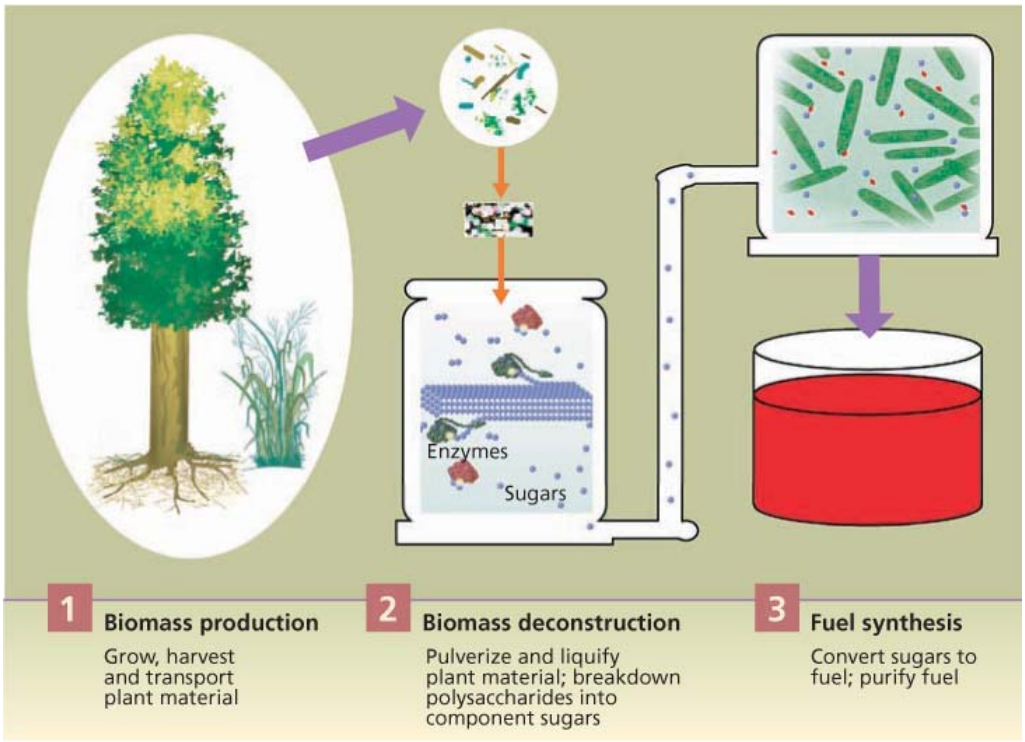

Figure 8. Steps involved in the production of biofuel from biomass

(http://genomics.energy.gov)

Biomass is biologically derived material obtained from living organisms or recently lived organisms. It usually refers to plant or plant derived materials. The energy from this biomass can be derived directly by burning to produce heat or indirectly by converting it to some form of fuel

referred as biofuel.[14] Wood is invariably the largest source of energy obtained from biomass. Dead trees, dead leaves, wood chips and various types of wastes from plants like eucalyptus, sugarcane, hemp etc. are also used as biomass for energy generation. Plant biomass can also be degraded from cellulose to glucose through a series of chemical treatments, and the resulting sugar can then be used as a first generation biofuel. Biofuel can be in solid, liquid and gaseous forms. Liquid biofuels include biodiesel and bioethanol whereas gaseous biofuel includes biogas. Biofuels provided 2.7% of the world's transport fuel in 2010.[15]

1.2.5. Solar Energy

Among all the renewable energy options solar energy stands out as the most viable choice to meet our energy demand as solar energy striking the earth is 120,000 TW per annum. The abundance of this energy reaching earth can be fruitfully utilized in various ways namely solar fuel, Solar Electricity (photovoltaics), Solar electricity (thermal e.g. thermoelectrics, CSP-steam turbine) and Solar Thermal solutions.

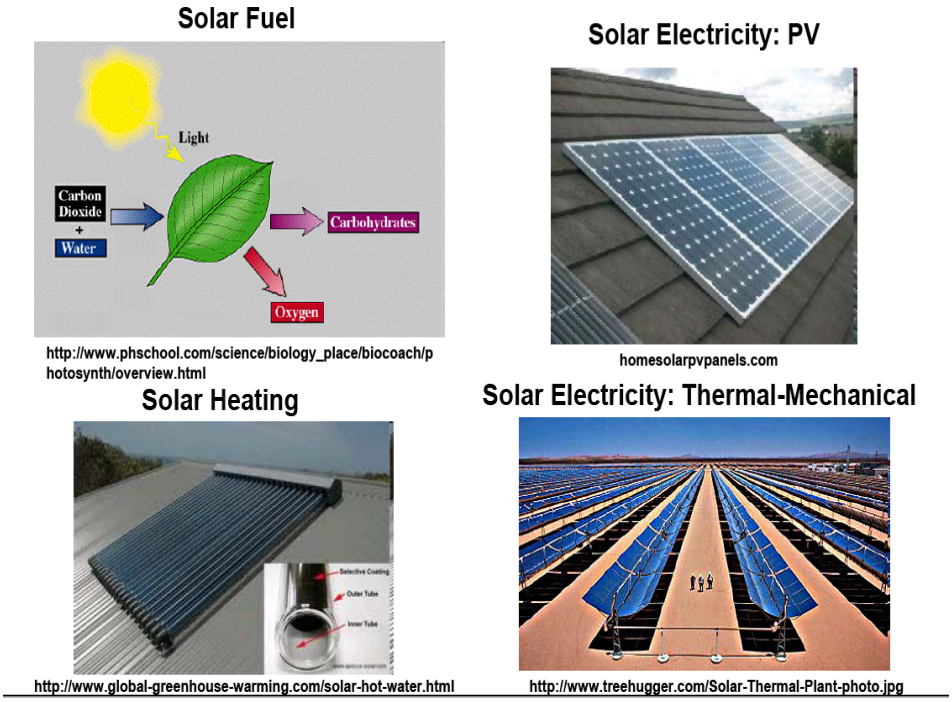

Figure 9. Solar energy utilization

1.2.5.1. Solar Fuel

It a fuel produced from sunlight using artificial photosynthesis. Here light is used as the energy source and thus solar energy is converted to chemical energy by reducing protons to hydrogen and carbon dioxide to organic compounds.[16] Various photocatalysts are being developed to carry out this conversion. Solar fuels can be produced by both direct and indirect processes. Direct processes harness the energy from sunlight to produce a fuel without intermediary energy conversions. However in the indirect process solar energy is converted to another form of energy first (such as biomass or electricity) and then the same can be used to produce a fuel. For example photochemical hydrogen generation and photochemical carbon dioxide reduction are the well studied branches where fuel is produced by using sunlight. The "artificial leaf" developed by Nocera and coworkers involves a combination of metal oxide-based catalysts and a semiconductor solar cell to produce hydrogen upon illumination, with oxygen as the only byproduct.[17]

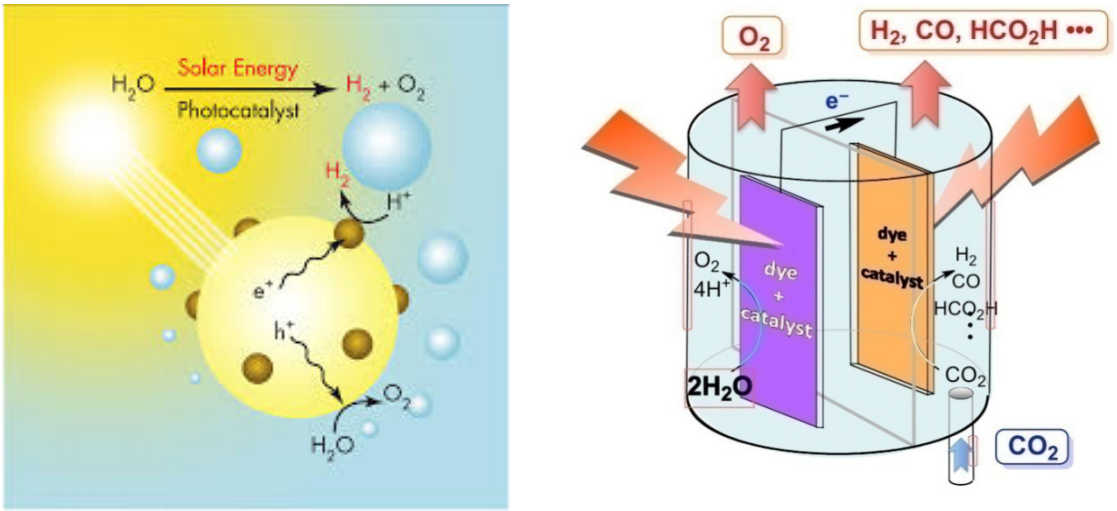

Figure 10. Solar fuels H_2 and CO_2

(http://wordlesstech.com/2011/06/27/solar-powered-water-splitter-to-produce-hydrogen/ (2014 wordlessTech))

1.2.5.2. Solar Heating and Cooling Operating at low temperatures

Solar heating and cooling (SHC) technologies collect the energy from the sun and use the corresponding heat to provide hot water, space heating, cooling, and pool heating for residential, commercial, and industrial applications.[18] These technologies displace the need to use electricity or natural gas for such functions. Solar heating systems can be easily installed at homes which consist of solar collector, insulating pipeline and hot water storage tank. A freeze protection system can be used for colder climates. The solar collector gathers the heat from the solar radiation and transfers the heat to potable water. This heated water flows out of the collector to a hot water tank, and is used as necessary. In colder climates an antifreeze solution, such as non-toxic propylene glycol, is heated in the solar collector and circulated to the hot water storage tank via a heat exchanger. The potable water in the storage tank is warmed by the hot, antifreeze-filled heat exchanger, and the heated water can then be used as necessary, while the cooled glycol is piped back to the solar collector to be heated again. With this system significant amount of hot water needs of a building can be satisfied.

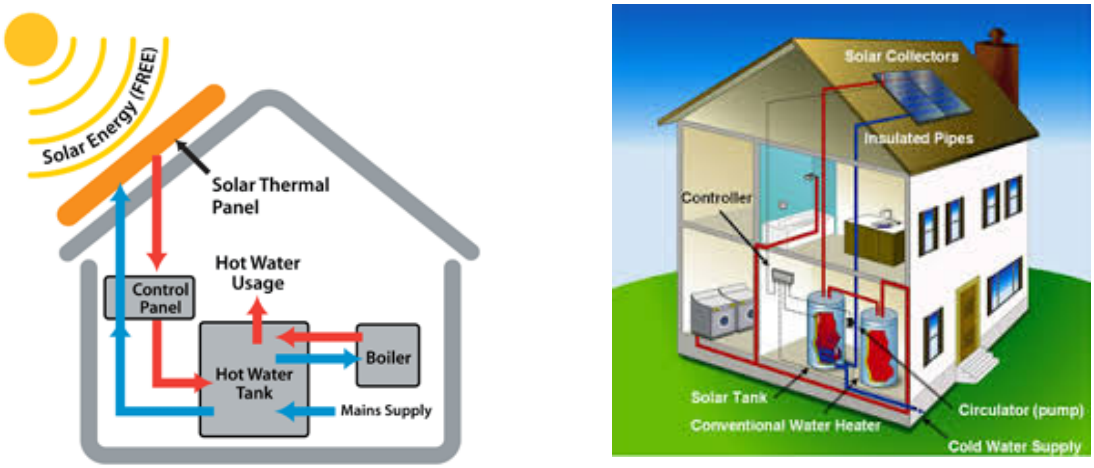

Figure 11. Solar Heating and cooling systems

(http://www.easyenergyweb.com/uncategorized/solar-thermal-right-business , (2013 EasyEnergy)

http://www.solartubs.com/solar-heating-system.html)

1.2.5.3. Solar Electricity-Thermal

The solar heat can be used in two ways with homes and businesses. One is to heat water for domestic hot water systems as seen in previous section, and another to achieve water temperatures to make steam and electricity by concentrating the power. Solar thermal plants are established to convert solar energy into electricity. These solar thermal power plants rely upon curved mirrored troughs that concentrate sunlight. The sun heats a liquid that creates steam to turn a traditional turbine. In a more efficient technology called the "stirling dish," an entirely new kind of engine is used to power the thermal plant.[19] Instead of the internal combustion engine, which relies upon an explosion inside the engine walls to turn pistons, the dish stirling engine relies upon the sun to heat tubes filled with hydrogen that turn the crankshaft. Solar electricity by thermal way is currently the most efficient method for utilization of solar energy.[20]

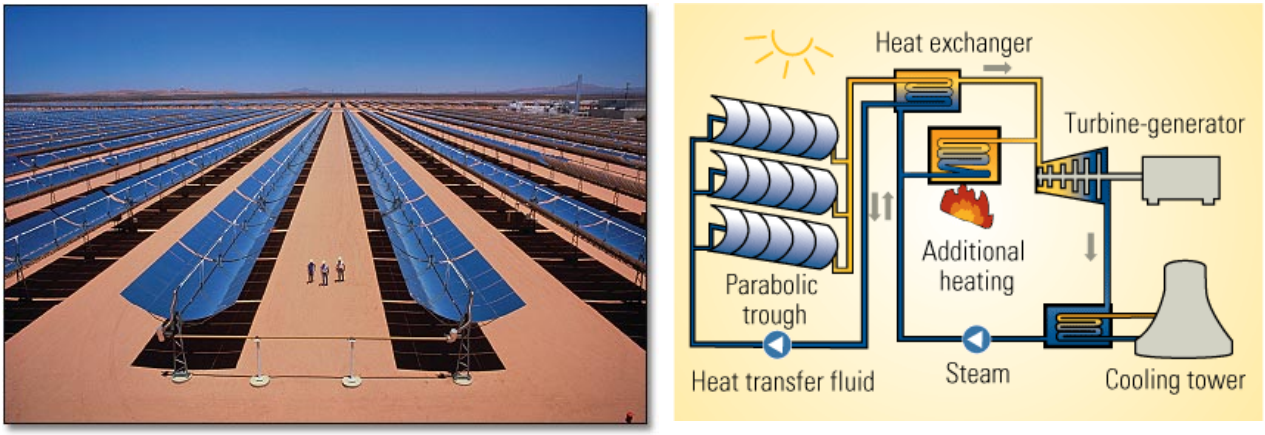

Figure 12. Solar concentrators and schematic of solar thermal plant

(http://www.greenenergyreporter.com/wp-content/uploads/2012/01/One-dimensional-parabolic-solar-thermal-plant.jpg

http://greenterrafirma.com/solar-thermal-for-electricity.html)

1.2.5.4. Solar Electricity - Photovoltaics

Photovoltaics (PV) is a technology of generating electrical power by converting solar radiation into direct current electricity using semiconductors. Photovoltaic power generation employs solar panels composed of a number of solar cells containing a photovoltaic material. Solar photovoltaics power generation has long been seen as a clean sustainable energy technology.[21] The direct conversion of sunlight to electricity occurs without any environmental emissions during operation and thus it is eco-friendly.

The basic requirements for operation of a photovoltaic cell are

- Broadband solar spectrum absorption and generation of electron and hole pairs (in some cases, excitons)
- Separation of the above generated charge carriers (in some cases exciton ionization and carrier separation)
- Extraction of these carriers to an external circuit

Depending upon the type of absorbing material used, manufacturing technique / process adopted, and type of junction formed etc., the solar cell technologies can be broadly classified as follows:[22]

(A) Wafer based crystalline silicon solar cells.

(B) Thin-film solar cells, which include, Copper Indium Gallium Diselenide (CIGS), Cadmium Telluride, Amorphous silicon (a-Si) etc

(C) Emerging technologies such as thin-film silicon, dye sensitized solar cells; polymer based organic solar cells and more recently perovskite cells etc.

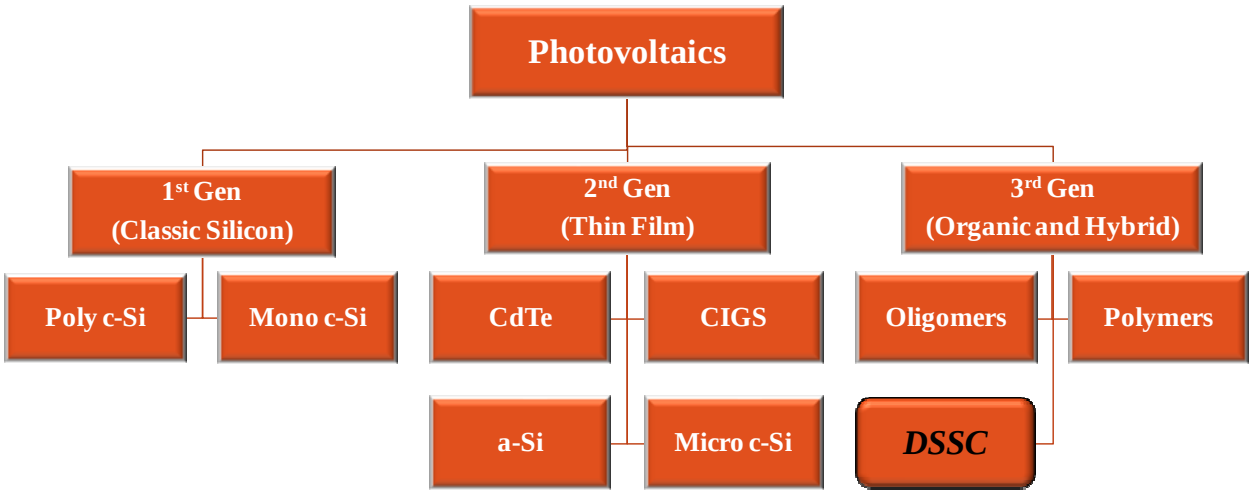

Figure 13. Classification of Solar cells

(A) Classic Silicon Cells

Wafer-based crystalline silicon solar cell technology:

The technology used to make most of the solar cells, fabricated so far, borrows heavily from the microelectronics industry; which is further classified into two categories as;

A.1 Single or Mono-crystalline silicon solar cell:

This is the most established, robust, and efficient solar cell technologies till date, which has a module level efficiency of 18-20%. The cell and module fabrication technology is well developed and reliable. These cells are manufactured from single silicon crystal, which are made by a process called Czochralski process.[23] During the manufacturing, c-Si crystals are cut from cylindrical ingots. The theoretical efficiency of these monocrystalline solar cells is ~ 29%. [24] The advantages of these solar cells are their high efficiency, longevity, greater heat resistance and ability to produce more electricity per square meter of installed panels. The disadvantage of these mono crystalline solar cells is their initial cost. As these mono crystalline solar cell panels are

made from single-cell silicon crystals the process of making them is one of the most complex and costly.

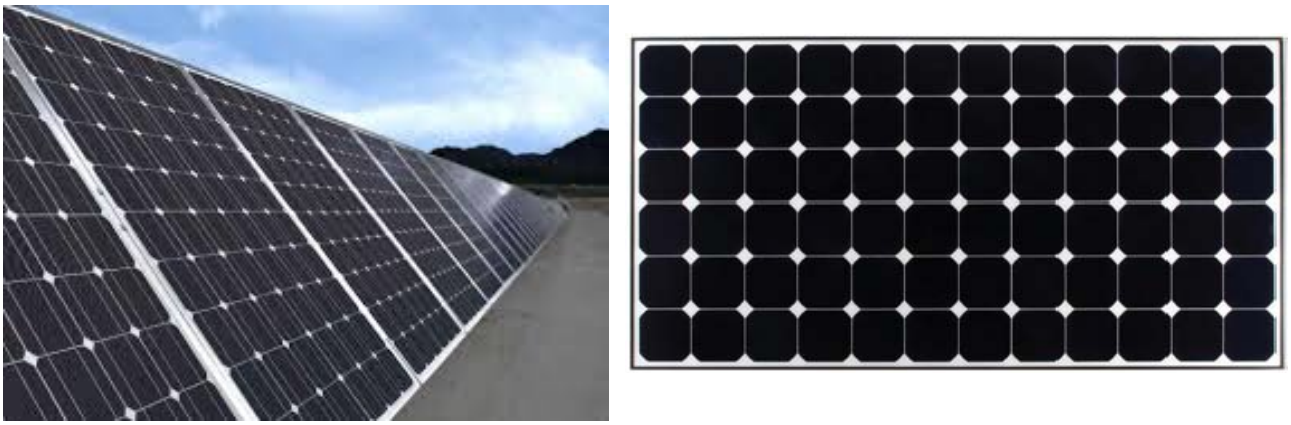

Figure 14. Monocrystalline solar cell panels

(http://www.solar-facts-and-advice.com/monocrystalline.html) (2010-2013 Alchemie Limited Inc)

A.2. Polycrystalline silicon solar cell

A polycrystalline solar cell wafer is cut from a multifaceted polycrystalline silicon ingot. Because the individual crystals are not necessarily all perfectly aligned together and there are losses at the joints between them, these cells are not as efficient as the monocrystalline solar cells. However, this misalignment of grains can help under certain circumstances, because the cells work better from light at all angles, in low light, etc. The cells of a polycrystalline solar panel tend to have a unique appearance due to optical reflectivity effects from surface facets, similar to that of shattered glass. The production of polycrystalline cells is more cost-effective and these are manufactured by cooling a graphite mould filled with molten silicon. In this process, liquid silicon is poured into blocks that are subsequently sawed into plates. During solidification of the material, crystal structures of varying sizes are formed, at whose borders defects emerge. These cells exhibit module level efficiency of around 12-14%. The advantage of

these polycrystalline solar cells is that they are cheaper than their monocrystalline counter parts and involve simpler methods for manufacturing. But the efficiency of this type of solar cells still remains an issue to address in the context of large scale implementation. But by increasing the purity and process tolerances this efficiency gap between monocrystalline and polycrystalline solar cells has been reducing over time.[25]

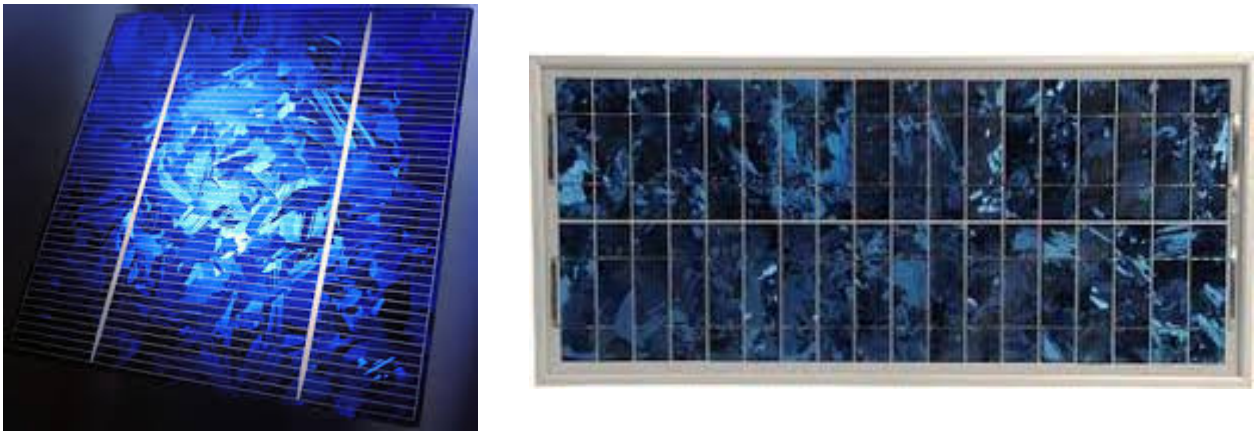

Figure 15. Polycrystalline solar panel

(www.adinex-service.ro)

B. Thin film Solar Cells

A thin-film solar cell is a solar cell that is made by depositing one or more thin layers (thin film) of photovoltaic material on a substrate. The thickness range of such a layer is wide and varies from a few nanometers to tens of micrometers. Many different photovoltaic materials are deposited with various deposition methods on a variety of substrates. Thin-film solar cells are usually categorized according to the photovoltaic material used:[26-27]

B.1. Amorphous Silicon Solar cells

Amorphous silicon is a disordered (non-crystalline) allotrope of silicon. It is used as photovoltaic material where the power requirement by the cell is rather low. More recently, improvements in a-Si construction techniques have made them more attractive for large-area solar cell

applications as well. The main advantage of these solar cells is that they use just 1% of silicon needed for manufacture of crystalline solar cells. This drastically reduces the cost of these solar cells. The efficiency of these solar cells at the module level is around 4-8%. The cause of this low efficiency for amorphous Silicon solar cells is their low quantum efficiency.

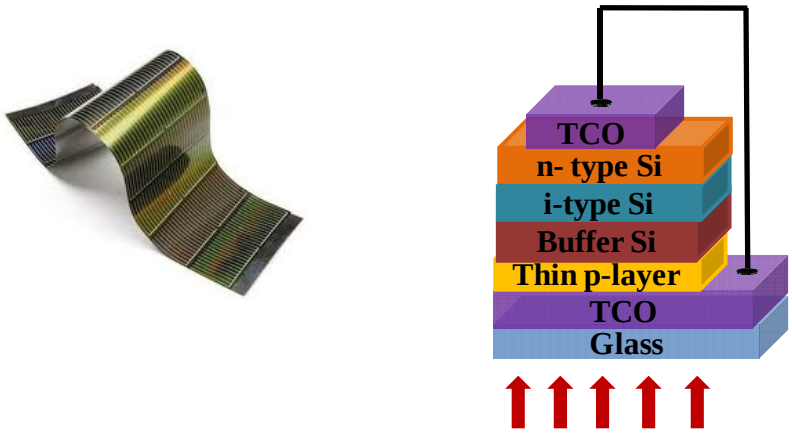

Figure 16. Amorphous Silicon Solar cells

(http://www.modernenviro.com/home-solar-energy-guide-part-3/) (2014 by ModernEnviro)

The quantum efficiency of thin-film solar cells is low due to reduced number of collected charge carriers per incident photon. To improve the efficiency of these cells a tandem and even triple layer devices that contain p-i-n cells stacked one on top of the other are used which has improved the efficiency of these amorphous silicon solar cells (> 10%).[26] These cells suffer from low efficiency as the amorphous silicon has disordered structure which leaves it with many dangling bonds. These dangling bonds act as defects which give rise to anomalous conductivity in this material. To passivate this issue hydrogenation is done where hydrogen bonds with the dangling bonds reduce its density. However, this hydrogenation process is associated with light induced degradation of material called Staebler Wronski effect.[28]

B.2. Cadmium Telluride solar cells

CdTe solar cells is a photovoltaic (PV) technology that is based on the use of cadmium telluride thin film, a semiconductor layer designed to absorb and convert sunlight into electricity.[29] Cadmium telluride PV is the only thin film photovoltaic technology to surpass crystalline silicon PV in cost for a significant portion of the PV market, namely in multi-kilowatt systems.[30]

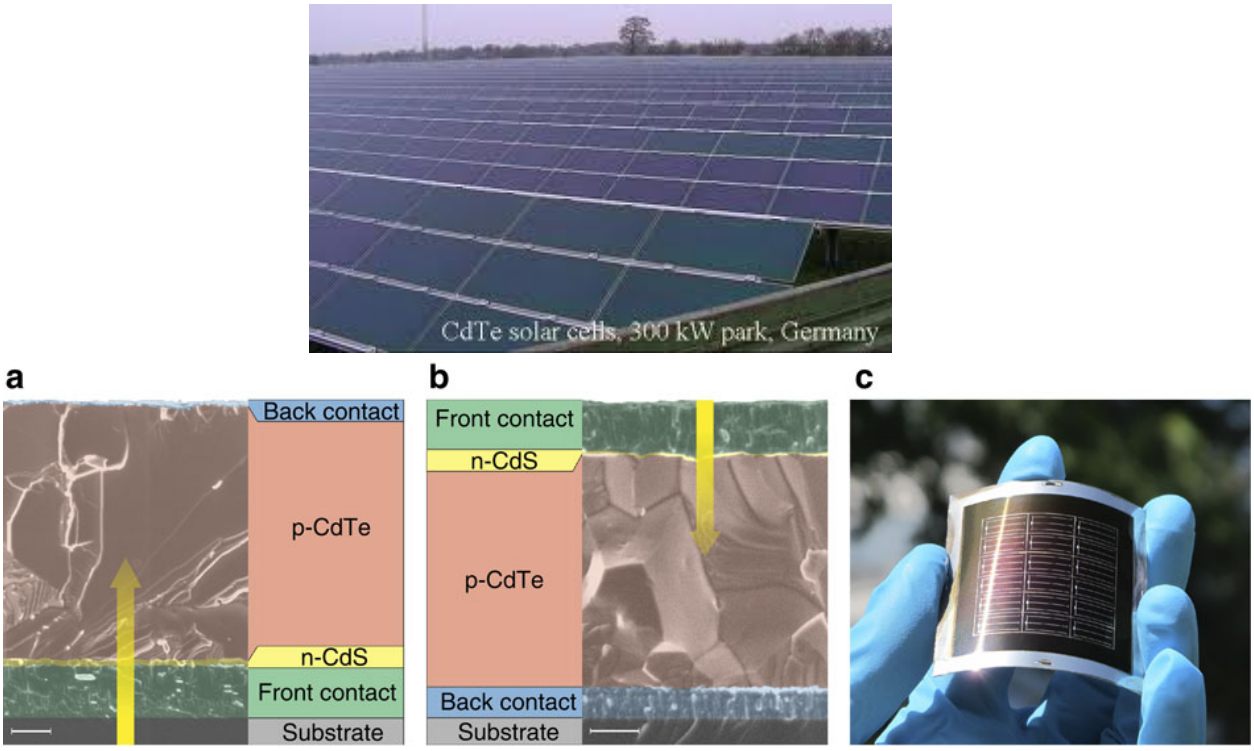

Figure 17. CdTe solar cell panel, superstrate and substrate configuration along with a flexible CdTe solar cell (http://www.tf.uni-kiel.de/matwis/amat/semitech_en/kap_8/backbone/r8_3_1.html and Nature Comm, 2013, 4, 1-7)

CdTe thin film technology is around more efficient than amorphous silicon, as its band gap is 1.4 eV and thus matches the solar spectrum very well. It is also much more adaptive to mass production, as the CdTe thin film can be deposited onto the substrate quickly and is a high-throughput technology. Each cell comprises a junction of n-doped cadmium sulfide, known as

the window layer on top of a p-doped layer of cadmium telluride, known as the "absorber." A transparent conductive front contact covers the cadmium sulfide, while the CdTe is in contact with a conductive rear surface substrate.

Thin-film CdTe/CdS heterojunction solar cells have been fabricated in two different configurations, referred to as substrate and superstrate.[31] In both configurations, light enters the cell through the transparent conducting oxide (TCO) and CdS films. But in the superstrate cell, the TCO, CdS, and CdTe layers are sequentially deposited onto a glass superstrate, which also serves as the mechanical support for the cell, and light must pass through the supporting glass before reaching the CdS/CdTe junction. In the substrate configuration, the CdTe film is typically deposited first onto a suitable substrate, followed by sequential deposition of CdS and the TCO. CdTe with laboratory efficiency as high as 20% have been developed and confirmed at NREL.[32]Availability of a large number of manufacturing techniques is the main advantage of these solar cells which are suitable for large scale production. Limited availability of cadmium and toxicity/pollution problem associated with cadmium is the main concern about this technology.

B.3. Copper Indium Gallium Selenide (CIGS) solar cells

This is a semiconductor material comprising copper, indium, gallium and selenium which is used for solar cell manufacturing. The CIGS absorber is deposited on a glass or plastic backing, along with electrodes on the front and back to collect the photo-generated current. Because the material has a high absorption coefficient and strongly absorbs sunlight, a much thinner film is required than those of other semiconductor materials. It is one of the most promising thin film technologies due to the high attained efficiency and low material costs. Amongst thin film solar

cells, the advantage of CIGS solar cell is its extended operational lifetime without significant degradation. The inherent properties of CIGS also provide an opportunity for maximizing the efficiency. The laboratory scale efficiency of CIGS solar cells is around 20% while on module scale the efficiency obtained is about 18%.

The basic structure of CIGS solar is shown in figure 18. The most common substrate is soda-lime glass of 1–3 mm thickness. This is coated on one side with molybdenum (Mo) that serves as the metal back contact. The hetero-junction is formed between the semiconductors CIGS and ZnO, separated by a thin layer of CdS and a layer of intrinsic ZnO. The CIGS is doped p-type from intrinsic defects, while the ZnO is doped n-type to a much greater extent through the incorporation of aluminum (Al). This asymmetric doping causes the space-charge region to extend much further into the CIGS than into the ZnO. Absorption is minimized in the upper layers, called window, by the choice of larger band gap materials like ZnO = 3.2 eV and CdS = 2.4 eV. The doped ZnO also serves as the front contact for current collection. Laboratory scale devices, typically 0.5 cm^2 in size, are provided with a Ni/Al-grid deposited onto the front side to contact the ZnO.[33]

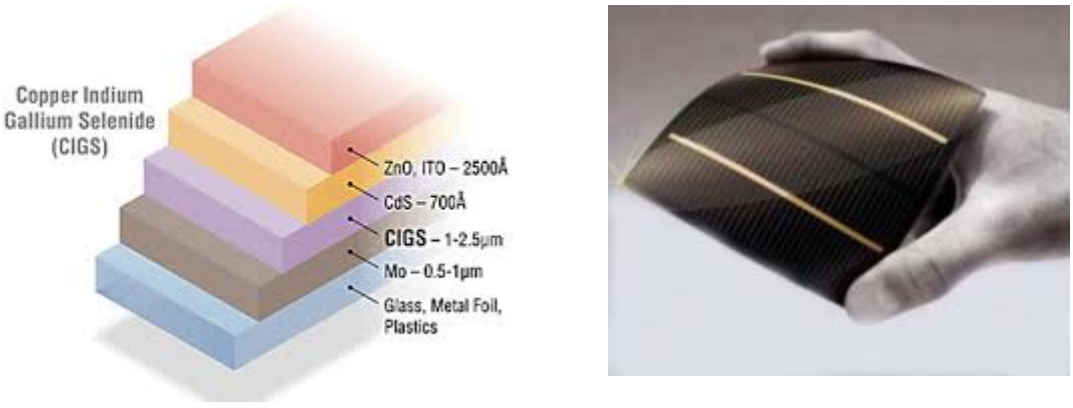

Figure 18. Schematic diagram of CIGS solar cell and commercially available Flexible CIGS solar cell

(http://www.nrel.gov/pv/thinfilm.html, http://www.solarserver.com/solarmagazin/newsa2006_01_e.html)

B.4. Microcrystalline silicon solar cells

Microcrystalline silicon is almost similar to amorphous silicon as it also has amorphous phase but where they both differ is that, in the microcrystalline solar cells small grains of crystalline silicon are embedded in an amorphous matrix. Microcrystalline Silicon has many useful advantages over amorphous silicon. One important advantage is that if grown properly it can have higher electron mobility, due to the presence of the silicon crystallites. It also shows increased absorption in the red and infrared wavelengths, which make it an important material for use in a-Si solar cells. One of the most important advantages of microcrystalline silicon, however, is that it has increased stability over a-Si, one of the reasons being its lower hydrogen concentration. Although it currently cannot attain the mobility that poly-Si can, it has the advantage over poly-Si that it is easier to fabricate, as it can be deposited using conventional low temperature a-Si deposition techniques such as PECVD, as opposed to laser annealing or high temperature CVD processes in the case of poly-Si.[34] The efficiency obtained for these type of solar cells is ~11%.

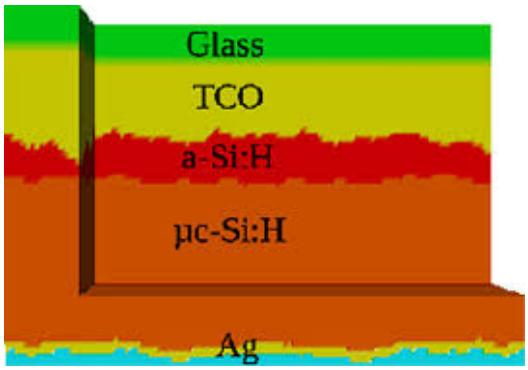

Figure 19. Microcrystalline solar cell

(http://spie.org/x87098.xml) (2014 SPIE)

C. Organic and Hybrid Solar cells

C.1. Organic Solar Cells

Organic solar cells are a type of polymer solar cells which use conductive organic polymers or small organic molecules for light absorption and charge transport to produce electricity from sunlight by the photovoltaic effect. A common characteristic of both the small molecules and polymers used in photovoltaics is that they are large conjugated systems. A conjugated system is formed where carbon atoms covalently bond with alternating single and double bonds. Compared to silicon-based devices, polymer solar cells are lightweight (which is important for small autonomous sensor applications), potentially disposable and inexpensive to fabricate (sometimes using printed electronics), flexible, and customizable on the molecular level. Moreover, they have lower potential for negative environmental impact. The disadvantages of polymer solar cells are also quite serious: they offer about 1/3 of the efficiency of hard materials, and they are relatively unstable toward photochemical degradation. For these reasons, despite continuing advances in semiconducting polymers, the vast majority of solar cells rely on inorganic materials.[35] Polymer solar cells suffer from a lack of enough efficiency for large scale applications and stability problems but their promise of extremely cheap production and eventually high efficiency values has led them to be one of the most popular fields in solar cell research.[36-37] Highest efficiency of these organic solar cells is around 8%. [38]

These organic cells are mainly of three types as described briefly below.

C.1.1. Single layer

These cells are made by sandwiching a layer of organic electronic materials between two metallic conductors, typically a layer of indium tin oxide (ITO) with high work function and a layer of low work function metal such as Al, Mg or Ca. The basic structure of such a cell is

illustrated in figure 20. The difference of work function between the two conductors sets up an electric field in the organic layer. When the organic layer absorbs light, electrons will be excited to the LUMO and leave holes in the HOMO, thereby forming excitons. The potential created by the different work functions helps to separate the exciton pairs, pulling electrons to the positive electrode (an electrical conductor used to make contact with a non-metallic part of a circuit) and holes to the negative electrode. An example of such organic cells is the work by Karg et al. [39] where the device was ITO/PPV/Al which gave efficiency of 0.1% but a Voc of 1V. The major drawback of this type of cell is low quantum efficiency leading to poor power conversion efficiency. A major problem with them is that the electric field resulting from the difference between the two conductive electrodes is seldom sufficient to break up the photogenerated excitons. Often the electrons recombine with the holes rather than reach the electrode. To deal with this problem, the multilayer organic photovoltaic cells were developed.

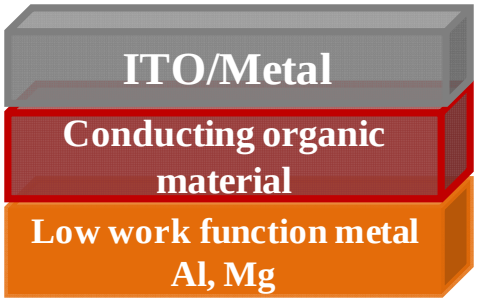

Figure 20. Schematic showing single layer organic solar cell

C.1.2. Bilayer Organic solar cells

In this type of cell two different layers are sandwiched between the conductive electrodes as shown in Figure 21. These two layers of materials have differences in electron affinity and ionization energy, therefore electrostatic forces are generated at the interface between the two

layers. The materials are chosen properly to make the differences large enough, so these local electric fields are strong, which may break up the excitons much more efficiently than the single layer photovoltaic cells do. The layer with higher electron affinity and ionization potential is the electron acceptor, and the other one is the electron donor. This structure is also called a planar donor-acceptor heterojunction.[40] Example of this type of cell is use of C60 which has high electron affinity as electron acceptor and MEH-PPV as electron donor which gave very poor efficiency.[41] Later using C60/PPV as bilayer an efficiency of 1% was reported.[42] The cause of this low efficiency is the diffusion length of excitons in organic electronic materials is typically on the order of 10 nm. For most excitons to diffuse to the interface of layers and break up into carriers, the layer thickness should be in the same range as the diffusion length. However, a polymer layer typically needs a thickness of at least 100 nm to absorb enough light. At such a large thickness, only a small fraction of the excitons can reach the heterojunction interface. To address this problem, a new type of heterojunction photovoltaic cells is designed, which is the dispersed heterojunction photovoltaic cells.

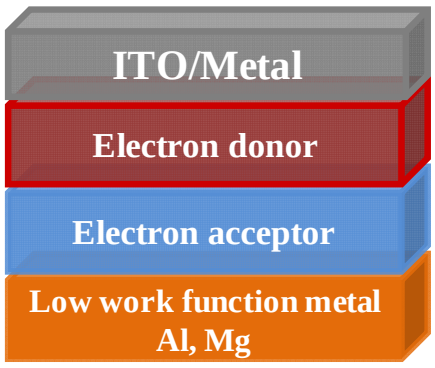

Figure 21. Schematic showing bilayer organic solar cell

C.1.3. Bulk hetrojunction Solar Cells

In this type of solar cell the electron donor and acceptor are mixed together, forming a polymer blend. Figure 22 shows a typical structure of bulk heterojunction solar cell. If the length scale of the blend is similar to the exciton diffusion length, most of the excitons generated in either material may reach the interface, where excitons break efficiently. Electrons move to the acceptor domains and are carried through the device and collected by one electrode, and holes are pulled in the opposite direction and collected at the other side.[43] Example of bulk heterojunction solar cells is silicon nanorod as acceptor and Spiro as a donor with efficiency of 10.3%

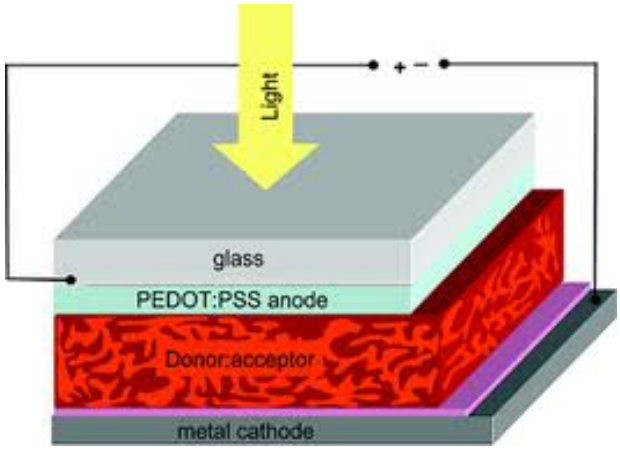

Figure 22. Schematic showing Bulk heterojunction solar cells

(http://www.nature.com/nphoton/journal/v8/n5/full/nphoton.2014.55.html)

C.1.4. Graded/Ordered heterojunction solar cells

In this type of photovoltaic cell, the electron donor and acceptor are mixed together, like in the bulk heterojunction, but in such a way that the gradient is gradual. This architecture combines the short electron travel distance in the dispersed heterojunction with the advantage of the charge gradient of the bilayer technology.[44]

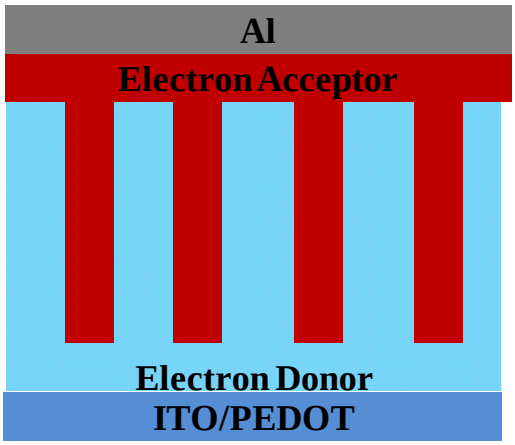

Figure 23. Ordered bulk heterojunction solar cells

C.2. Hybrid Solar cells

This type of solar cell takes advantage of both organic and inorganic semiconductors. Here the organic material is mostly conjugated polymer which can absorb light and also help in transport of holes. The inorganic part is mainly used as electron transport material. In hybrid solar cells, an organic material is mixed with a high electron transport material to form the photoactive layer.[45]The two materials are assembled together in a heterojunction-type photoactive layer, which can have greater power conversion efficiency than a single material.[45] The efficiency of these solar cells depends on how efficient these organic-inorganic interfaces are made. These hybrid solar cells are mainly of two types; Polymer-nanocomposite hybrid solar cell and Dye Sensitized Solar Cell.

C.2.1. Polymer Nanocomposite Hybrid Solar Cell

In this type of solar cell the photoactive layer is made by mixing nanomaterials into the polymer matrix. Here the advantage of nanoparticles is their large surface to volume ratio which helps in increased surface area for charge transfer processes. These cells are similar to polymer solar cells

where fullerene acceptor material is replaced by nanoparticles. The advantages of use of nanoparticles are,

- Simple and low temperature process required for the synthesis of these nanoparticles,
- Compared to organic systems like fullerene these nanoparticles are more stable, and
- Band gap of nanoparticles can be tuned so as to improve the light absorption.

The polymers used for these type of solar cells should have hole mobility greater than electron mobility, thus this polymer phase is used to transport holes. The nanoparticles present in the matrix help to transport electrons to the electrode.[46] The interface area between the polymer phase and the nanoparticles have to be large. This is achieved by dispersing the particles throughout the polymer matrix. However, the nanoparticles need to be interconnected to form percolation networks for electron transport, which occurs by hopping of electrons.[46]

The nanoparticle aspect ratio, geometry, and volume fraction directly affect the performance of these types of solar cells. Nanoparticle structures include nanocrystals, nanorods, and hyper-branched structures.[47] Different structures change the conversion efficiency by effecting nanoparticle dispersion in the polymer and providing pathways for electron transport. The nanoparticle phase is required to provide a pathway for the electrons to reach the electrode. By using nanorods instead of nanocrystals, the hopping events from one crystal to another can be avoided which helps give more efficient solar cell devices.[47] For the fabrication of nanoparticle polymer matrix these two materials are simply mixed in a solution and spin coated onto a substrate or are made by usual sol-gel methods. Most of these methods do not involve high-temperature processing. Annealing increases order in the polymer phase, increasing conductivity. However, annealing for too long is to be avoided as it causes the polymer domain size to increase, eventually making it larger than the exciton diffusion length and possibly allowing

some of the metal from the contact to diffuse into the photoactive layer, reducing the efficiency of the device.[46-47] The nano-materials used in these type of cells are usually CdS, CdSe, TiO_2 nanoparticles (size range 6-20nm) etc. and common polymers used are P3HT, MEH-PPV etc. which have extended conjugation and are also hydrophobic.

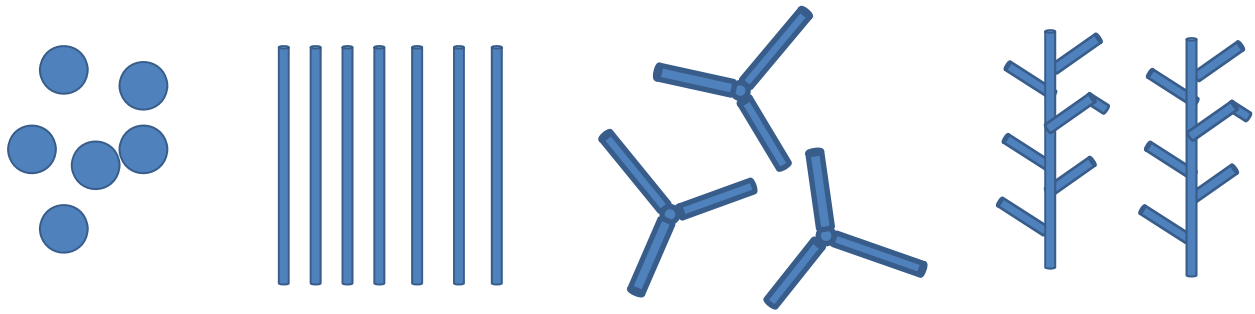

Figure 24. Different morphologies of nanoparticles used in hybrid polymer-nano composite solar cells

C.2.2. Dye Sensitized Solar Cells (DSSCs)

DSSCs are solar cells, belonging to third generation of solar cells, were discovered by Grátzel and O'Regan in 1991. They are based on Nature's principles of photosynthesis. DSSCs are composed of a porous layer of titanium dioxide nanoparticles, covered with a molecular dye that absorbs sunlight very similar to the chlorophyll in green leaves. The titanium dioxide is immersed under an electrolyte solution, above which is a platinum-based catalyst which acts as a counter electrode. This chemical way of assembling the cell architecture allows facile and cost effective processing which makes these cells front runners in the view of the basic design novelty and potential for low cost manufacturing.[48]They involve use of low-tech fabrication techniques such as roll-to-roll printing. Figure 25 shows basic dye sensitized solar cell architecture.

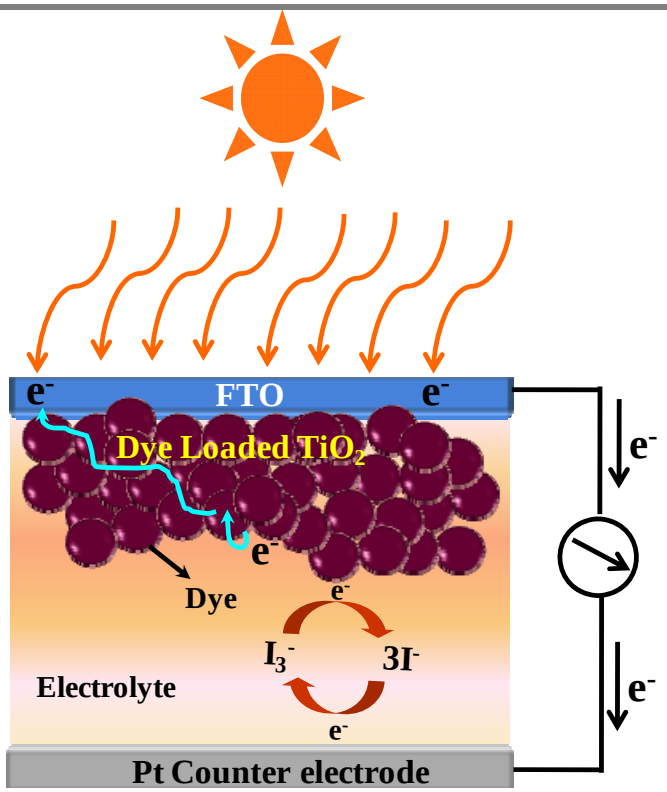

Figure 25. Schematic of basic DSSC

One of the efficient DSSCs devices uses ruthenium-based molecular dye, e.g. Ruthenium dye (N719), that is anchored to the photoanode via carboxylate ligands. The photoanode consists of 12 µm thick film of transparent 10–20 nm diameter TiO_2 nanoparticles covered with a 4 µm thick film of much larger (400 nm diameter) particles that scatter photons back into the transparent film. The excited dye rapidly injects an electron into the TiO_2 after light absorption. The injected electron diffuses through the sintered particle network to be collected at the front side transparent conducting oxide (TCO) electrode, while the dye is regenerated via reduction by a redox shuttle, I_3^-/I^-, dissolved in a solution. Diffusion of the oxidized form of the shuttle to the counter electrode completes the circuit.

The significant collective efforts by the scientific community over the past 20 years have not only pushed the efficiencies higher but have brought out several new ways of making robust and durable DSSC cells fairly affordably with good efficiencies. This has included intense work on various inorganic oxide morphologies,[49-52] sensitizers,[53-55] co-adsorbers,[56-57] co-sensitization,[58-59] new counter electrodes,[60] new redox electrolytes [61-62] etc. Till now the best efficiency recorded by these cells is ~13% using co-sensitization of dyes and cobalt redox shuttle as electrolyte.[61] But a major problem of these type of solar cells is the use of liquid electrolyte which evaporates as it contains volatile solvents. Higher temperatures cause the liquid to expand, making sealing of the modules a serious problem. Hence efforts are being made to replace this liquid electrolyte with gel electrolyte [63] or solid hole transporting material (HTM).[64]

C.2.2.1. Solid State DSSC

A solid-state electrolyte is considered to be an alternative to the liquid electrolyte, because it could achieve a better mechanical stability and simplified fabrication processes. It is an essentially simple idea that replaces the liquid electrolyte with inorganic p-type semiconductors or organic hole transporting materials to eliminate the evaporation and leakage of liquid electrolyte. A suitable hole-transport material must have a band gap structure compatible with the highest occupied molecular orbital (HOMO) level of the dye on one hand and the conduction band of TiO_2 on the other to drive the charge-transfer process. The main difficulty in realizing such a solid-state electrolyte device is to form an intimate contact at the p–n junction interfaces. The first p-type semiconductors acting as hole-transport materials (HTM) were CuSCN and CuI, introduced by Tennakone *et al*. [65] and O'Regan and Schwartz [66]. In their first step, they could achieve an overall efficiency of less than 1% due to the formation of unfilled voids in the TiO_2. As for p-type organic semiconductors, spiro-OMeTAD has proven to be the most successful one.

It was initially presented by Bach *et al.* in 1998, and since then the conversion yield of the corresponding devices has been increasing and has reached about 4%.[64]Very recently Kanatzidis used $CsSnI_3$ as a p-type perovskite material in the place of liquid electrolyte to get an efficiency of 10%. [67] As discussed later this has opened up several new opportunities for cell designs.

The conversion efficiency of DSSCs using solid electrolyte is generally lower than liquid electrolyte based cells, typically less than 5%. This is due to the poor contact at the TiO_2/electrolyte interface and the low conductivity of these materials. [68] In order to overcome these drawbacks, an alternative solution is proposed and attempted where both liquid and solid electrolytes can be combined to form a quasi-solid electrolyte, or gel electrolyte.[69] Apparently, there are several advantages of using a gel electrolyte: (i) relatively high ambient ionic conductivity (6–8 $mS\text{-}cm^{-1}$), (ii) intimate interfacial contact with TiO_2, and (iii) remarkable electrolyte stability. At the initial step, the solvent with a low viscosity penetrates the TiO_2 mesopores to form a good contact. After gelation volatile liquid solvent is encapsulated within a gel network that prevents the rapid electrolyte evaporation and leakage.

C.2.2.2. Perovskite Solar Cells

Very recently, a major path-breaking advancement has been reported in the domain of solid state sensitized solar cells with the introduction of organometal halide perovskites as efficient alternatives to liquid electrolyte based DSSC.[70-71]The early efforts by Miyasaka and coworkers[72] and Park and coworkers[73] on the use of organometal halide perovskite in solar cells were mainly focused on their use as sensitizer in liquid electrolyte based sensitized solar cells which could give power conversion efficiencies up to 5-6%. Subsequently, a remarkable efficiency of 9.7% was reported by Park and coworkers[74] using $CH_3NH_3PbI_3$ as a light absorber deposited on a sub-micrometer thick (0.6 μm) mesoporous TiO_2 film and spiro-OMeTAD as Hole Transporting

Material (HTM). These devices however suffered from poor fill factor due to poor charge transport properties of Spiro-OMeTAD. Grätzel and coworkers[70] later introduced p-type dopant in the form of a cobalt complex to improve the charge transport properties of Spiro-MeOTAD. Snaith and coworkers[71] showed a record efficiency of 10.9% with V_{oc} of 1.1 V by replacing the mesoporous TiO_2 with an insulating mesoporous Al_2O_3. The mesoporous Al_2O_3 acted as a scaffold for a few-nanometer thin layer of $CH_3NH_3PbI_2Cl$ transporting electronic charges out of the device through FTO anode, while the spiro-OMeTAD collected the holes. Here mixed halide perovskite $CH_3NH_3PbI_2Cl$ was used, which acted as both a light absorber as well as an electron transporter. Liu et al.[75] have recently shown room temperature processed ZnO based perovskite solar cells with a robust and reproducible efficiency of 15.7%.

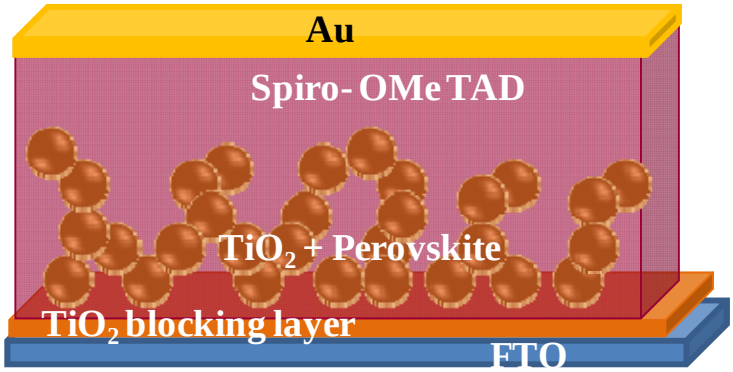

Figure 26. Typical Perovskite solar cell

These perovskite solar cells are thus considered as advancement over DSSCs where the photoanode thickness is reduced to a few microns, dye is replaced by superior light absorbing organo-metal halide perovskite, and a hole transporting layer which can be deposited directly over this cell architecture. These new systems have already shown efficiency values of about 15-16% and hold great promise for even higher efficiency (20%) at lower cost.[70-71] High absorption

coefficient[76] spanning the full visible spectrum, a sharp absorption edge,[74] and very low recombination losses[74] in organometal halide perovskite are regarded as the main reasons for the high efficiency values realized by these type of cells. Research is still in early stages for these perovskite solar cells. Commercialization and industrial production of this technology may take a few years, but it appears that this perovskite technology, if used in combination with other established solar cell technologies, can help solve the problem of energy generation for the coming years.

1.3. The market scenario

Wafer based silicon solar cell technology is dominating the current photovoltaic market and it will continue to do so for the next 8-10 years thanks to reduction in silicon prices. In 2010, 87% of global PV sales were attributed to crystalline silicon technologies.[77] Silicon PV being a well established and mature technology, continued cost reductions are expected to be achieved through improvements in materials and manufacturing processes, provided the market continues to grow, thereby developing a number of high-volume manufacturers. In such a case the non-silicon thin film solar cells mainly the Dye Sensitized Solar Cells can prove to be able competitors to traditional silicon solar cells as they have the advantage of both, the low cost and physical flexibility.

Today the non silicon PV market is growing rapidly and its share in the global PV market is around 20%.[77] This increase in demand for non-silicon PV, mainly Dye Sensitized Solar Cells, is attributed to its simple fabrication process which involves roll to roll production scheme. For example G24i team has developed a next generation commercial roll to roll manufacturing plant for DSSCs. The advantage of this technology is that the coating of DSSCs can be easily done on

flexible substrates at low temperature, low capital, low energy and it requires no new or sophisticated machinery. G24i has also developed innovative self powering products which make use of third generation DSSC Technology. G24i's DSSC is declared as the world's most powerful indoor photovoltaic module.[78] DSSCs can perform well in diffuse light as well which means more power can be generated using this PV technology. Majority of solar cell testing is done under standard test conditions (STC) conditions with intensities of 1000W/m^2. But the indoor lighting conditions are significantly different. When tested under indoor or low light conditions the DSSCs perform better than the a-silicon or any other thin film solar cells.

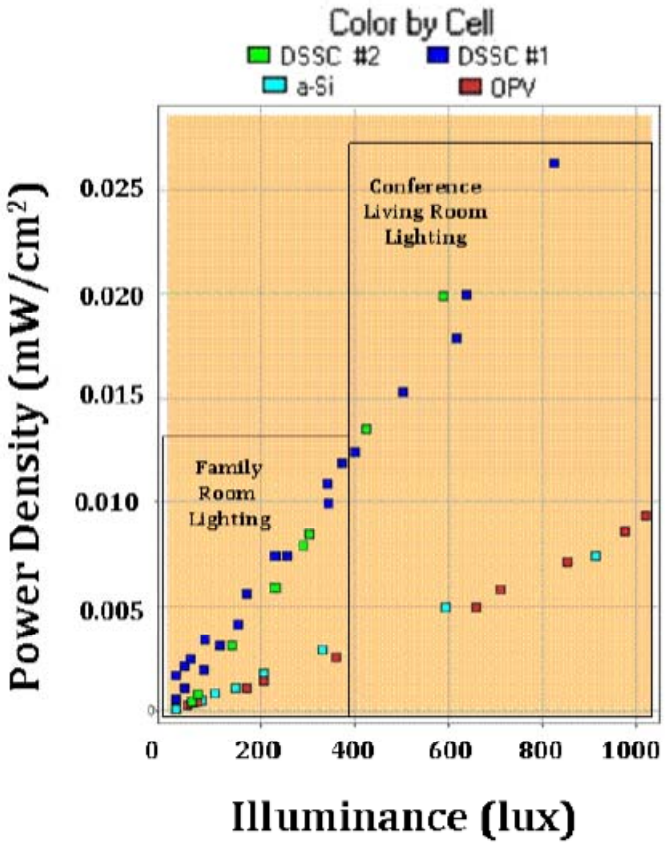

Figure 27. Plot of power density Vs Illuminance for different types of solar cells

(http://gcell.com/wp-content/uploads/Appendix-2-a_study_of_dssc_under_indoor_low_level_light_texas_instruments.pdf)

Certified DSSC efficiency of above 12% has been reported for single junction DSSCs[78] and an efficiency of 15% is demonstrated for tandem version of these solar cells.[79] G24i has also shown an efficiency of 7.1% on flexible substrates.[80] These lightweight flexible DSSC modules which perform well under different light conditions are used in solar powered smoke detectors, calculators, keyboards, window blinds etc. DSSCs can also be used outdoor applications like mobile charger and other portable consumer electronics.

Figure 28. Indoor and Outdoor applications of Dye sensitized solar cells

(Commercialization of Dye Sensitized Solar Cells, K.G. Chettibabu G24i Power Ltd.)

Thus DSSCs can be a good alternative energy source for remote sites and mobile applications.

1.4. Outline of Thesis

This thesis mainly describes a detailed work on the second type of third generation solar cells i.e the Dye Sensitized Solar Cells (DSSCs). The second chapter describes the basic aspects of

DSSCs in more details along with the other related experimental procedures. The third chapter thoroughly describes the fabrication protocol for making high efficiency DSSCs. Some statistical data along with the use of different TiO_2 morphologies is highlighted in this chapter. The forth chapter gives the details of special characterization techniques used for DSSC characterization such as the electrochemical impedance spectroscopy, cyclic voltammetry, Tafel polarization plots etc. The fifth chapter presents work on the use of natural dye extracted from flowers of "flame of forest" as sensitizer in DSSC. Details of extraction, purification of this dye along with its solar cell efficiency and stability are described in this chapter. The sixth chapter gives detailed procedure for fabrication of DSSCs entirely by a newly developed room temperature process. Here the recipe for preparation of the room temperature solar paint, realization of a good solar cell efficiency using this solar paint, and detailed characterization using impedance spectroscopy are described. Also results on our efforts towards flexible and large area DSSCs are presented in the same chapter. The concluding chapter seven describes the future scope for this present research work. The appendix of the thesis describes some interesting ongoing work on solid state DSSCs using $CsSnI_3$ p-type material as hole conductor instead of a liquid electrolyte.

1.5.References

1. U.S. Energy Information Administration
2. http://www.ucsusa.org/clean_energy/our-energy-choices/coal-and-other-fossil-fuels/the-hidden-cost-of-fossil.html
3. World Energy Assesment: Energy And The Challenge of sustainability , Chapter 3
4. Harvard School of public health http://chge.med.harvard.edu/category/nature-health-built-environment
5. http://www.california-solar.org/inform/hazards-of-burning-fossil-fuels.php

6. European Commission, The Energy Challenge of the 21st Century: The role of Nuclear Energy, http://europa.eu.int/comm/research/rtdinfo en.html
7. Renewables 2013 Global Energy Report
8. K. Grogg, Harvesting the Wind :The Physics of wind Turbines, 2005, http://digitalcommons.carleton.edu/pacp/7
9. Global Wind Statistics, http://www.gwec.net/wp-content/uploads/2013/02/GWEC-PRstats-2012_english.pdf
10. Chapter 3, Perspectives on Sustainable Energy for the 21st Century
11. D.L. Turcotte, G. Schubert, G., "4", Geodynamics (2 ed.),2002, Cambridge, England, UK: Cambridge University Press, 136–137, ISBN 978-0-521-66624-4
12. Geothermal capacity , About BP , BP Global, Bp.com
13. I.B. Fridleifsson , *Renewable and Sustainable Energy Reviews*., **2001**, *5* ,3.
14. Global Trends in Sustainable Energy Investment report 2013, www.fs-unep-centre.org.
15. REN21, Renewables 2011: Global Status Report, 2011.
16. S. Styring, *Faraday Discuss*., **2012**,*155*, 357-376
17. S.Y. Reece, J.A. Hamel, K.; Sung, T.D. Jarvi, A.J. Esswein, J.H. Pijpers, D.G. Nocera, *Science*, **2012**, *334*, 645–648.
18. http://solarheatcool.sustainablesources.com/
19. Stirling Energy Systems Inc. - Solar Overview. Stirlingenergy.com
20. Sandia, Stirling Energy Systems set new world record for solar-to-grid conversion efficiency" (Press release). Sandia National Laboratories. **2008**-02-12
21. J. M .Pearce., *Futures*,**2002**,*34*, 663-669.
22. http://sovoxglobal.com/cell_classification.html

23. T. Surek, *J. Cryst. Growth*, **2005**, *275*, 292

24. Georgia Tech, SmartTech Search

25. C.Becker, *J. Appl. Phys.*, **2009**, *106*, 084506

26. A.G. Aberle, *Thin Solid Films.,* **2009**, *517*, 4706–4710

27. K. L. Chopra, P. D. Paulson, V. Dutta, *Prog. Photovolt: Res. Appl.,* **2004**,*12*,69–92

28. C. R. Wronski, J.M. Pearce, J. Deng, V. Vlahos, R.W. Collins, *Thin Solid Films*, **2004**,*451,* 470-475.

29. "Publications, Presentations, and News Database: Cadmium Telluride". National Renewable Energy Laboratory.

30. Further mention of cost competitiveness: "Solar Power Lightens Up with Thin-Film Technology", Scientific American, April **2008**.

31. C. Routray, A. Panda, S. P. Singh ,U. P. Singh, *Invertis Journal of Renewable Energy*, **2011**,*1*, 75-82.

32. M. Gloeckler, I. Sankin, Z. Zhao, *IEEE Journal of Photovoltaics*, **2013**, 3 , 1389–1393.

33. H.S. Ullal, "*Polycrystalline Thin Film Solar Cell Technologies*". National Renewable Energy Laboratory Colorado U.S.A.

34. S. Gupta, *Understanding Of Nano Science And Technology*., **2006**, Global Vision Publishing Ho.

35. J. Luther, M. Nast, M. N. Fisch, D.Christoffers, F.Pfisterer, D. Meissner, J. Nitsch , *Ullmann's Encyclopedia of Industrial Chemistry*, *Solar Technology* , **2000**,33,528-575

36. R. Poa, C. Carboneraa, A. Bernardia, F. Tintib, N. Camaioni, *Solar Energy Materials and Solar Cells*, **2012**,*100*, 97-114.

37. M. C. Scharber, D. Mühlbacher, M. Koppe, P. Denk, C. Waldauf, A. J. Heeger, C. J. Brabec, *Adv. Mater.*, **2006**, 18, 789–794

38. L. Dou, J. You, J. Yang, C.-C. Chen, Y. He, S. Murase, T. Moriarty, K. Emery, G. Li, Y. Yang, *Nat Photonics*, **2012**, 6, 180–185 .

39. S. Karg, W. Riess, V. Dyakonov, M. Schwoerer, *Synthetic Metals*, **1993**, *54*, 427-433.

40. D.G. McGehee, M.A.Topinka, *Nature Material*, **2006**, *5* , 675–676.

41. N. S. Sariciftci, D. Braun, C. Zhang, V. I. Srdanov, A. J. Heeger, G. Stucky , F. Wudl, *Appl. Phys. Lett.*, **1993**, *62*, 585

42. J. J. M. Halls, K. Pichler, R. H. Friend, S. C. Moratti, A. B. Holmes, *Appl. Phys. Lett.*, **1996**, *68*, 3120.

43. J.J.M. Halls., R.H. Friend, M.D., Archer, R.D.Hill, *Clean electricity from photovoltaics. London: Imperial College Press.* pp. 377–445.ISBN 1860941613.

44. "Organic Photovoltaic Solar Cells using Graded Heterojunction Technology". University of Minnesota.

45. S. E. Shaheen, D. S. Ginley , G.E. Jabbour, *MRS Bulletin*, **2005**,*30*,10-19

46. A. Ueda, R. Mu, M. H. Wu, *Semiconductor Quantum Dot Based Nanocomposite Solar Cells".Organic Photovoltaics: Mechanisms, Materials, and Devices. Organic Photovoltaics,* **2005,** doi:10.1201/9781420026351.ch14 CRC Press.

47. B.R. Saunders, M.L. Turner, *Advances in Colloid and Interface Science*, **2008**, *138*, 1–23.

48. B. O'Regan, M. Gràtzel. *Nature*, **1991**, *353*, 737 – 740.

49. S.Muduli, O.Game, V.Dhas, A.Yengantiwar, S. B.Ogale, *Energy Environ. Sci.*, **2011**, *4*, 2835-2839.

50. D. Chen, F .Huang, Y-B.Cheng, R. A.Caruso, *Adv. Mater.,* **2009**, *21*, 2206–2210.

51. D. Kim, A.Ghicov, S. P. Albu, P. Schmuki, *J. Am. Chem. Soc.,* **2008**, *130*, 16454–16455.

52. E.Ghadiri,N. Taghavinia, S.M. Zakeeruddin,M.Gràtzel, J-E.Moser, *Nano Lett.*, **2010**, *10*, 1632–1638.

53. F.Gao,Y. Wang, D. Shi, J. Zhang, M.Wang, X. Jing , R. Humphry-Baker, P. Wang, S.M. Zakeeruddin, M. Gràtzel, *J. Am. Chem. Soc.*, **2008**, *130*, 10720–10728.

54. S.Ito, S. M. Zakeeruddin, R. Humphry-Baker, P. Liska, R. Charvet,P.Comte, M. K. Nazeeruddin, P. Péchy, M .Takata,H. Miura, S. Uchida,M.Grätzel, *Adv. Mater.* , **2006**, *18*, 1202–1205.

55. R. Argazzi , N-Y-M.Iha, H. Zabri,F.Odobel, C. A. Bignozzi, *Coordinat Chem. Rev.*, **2004**, *248*,1299–1316.

56. R. Y.Ogura, S.Nakane, M.Morooka,M.Orihashi, Y. Suzuki, K. Noda, *Appl. Phys. Lett.* **2009**, *94*, 073308.

57. N.A. Allegrucci, A.J. Lewcenko, L. Mozer, P.Dennany, D.L. Wagner, K. Officer, S. Sunahara, L.Mori, Spiccia. *Energy Environ. Sci.,* **2009**, *2*, 1069–1073.

58. D.Kuang, P.Walter, F.Nüesch, S. Kim, J. Ko, P. Comte, S.M. Zakeeruddin, M.K. Nazeeruddin , M.Grätzel. *Langmuir*, **2007**, *23* , 10906–10909.

59. Y. Chen, Z. Zeng, C. Li, W. Wang, X. Wang, B. Zhang, *New J. Chem.*, **2005**, *29*, 773-776.

60. M. Wu, X. Lin, T. Wang, J. Qiu, T. Ma, *Energy Environ. Sci.* **2011**.

61. A.Yella, H-W. Lee,H.N.Tsao, C. Yi, A.K. Chandiran, M.K. Nazeeruddin, E.D. Wei-Guang,C-Y.Yeh, S.M. Zakeeruddin, M. Grätzel, *Science* , **2011**, *3344*.

62. M. D. McGehee, *Science*, **2011**, *334*, 607-608.

63. Kron G, Egerter T, Werner J H, Rau U., *J. Phy. Chem. B.,* **2003**, *107*, 3556–64.

64. G R A Kumara, S. Kaneko, M. Okuya, K.Tennakone, *Langmuir*, **2002**, *18* , 10493–5.

65. K. Tennakone, G R A . Kumara, A R .Kumarasinghe, K.G.U. Wijayantha, P M.Sirimanne, *Semiconductor Science and Technology*, **1995**,*10*,1689–93.

66. B. O'Regan, D T.Schwartz, *Chem. Mater.,* **1995**,7 , 1349–54.

67. I. Chung, B. Lee, J. He, R. P. H. Chang , M. G. Kanatzidis, *Nature* , **2012**, 485, 486.

68. U . Bach, D . Lupo, P. Comte, J. E. Moser, F. Weissortel, J. Salbeck, H. Spreitzer, M. Gratzel, *Nature*, **1998**,*395*,583–5.

69. G. Kron, T. Egerter, J H. Werner, U. Rau, *J. Phys. Chem.B* , **2003**,*107*,3556–64.

70. M. M. Lee, J.Teuscher, T. Miyasaka, T. N. Murakami, H. J. Snaith, *Science*, **2012**, *338*,643.

71. J. Burschka, N. Pellet, S-J Moon, R. Humphry-Baker, P. Gao1, M. K. Nazeeruddin, M. Gratzel, *Nature*, **2013**, *499*,316.

72. A.Kojima, K.Teshima, Y. Shirai, T. Miyasaka, *J. Am. Chem. Soc.,* **2009**, *131*, 6050-6051.

73. J. H. Im,; C. R. Lee, J.W. Lee, S.W. Park, N.G. Park, *Nanoscale,* **2011**, *3*, 4088-4093.

74. H. S.Kim, C. R. Lee, J. H. Im, K. B. Lee, T. Moehl, A. Marchioro, S. J.Moon, R.H Baker, J.H. Yum, J.E. Moser, M. Grätzel, N.G. Park, *Sci Reports* **2012**, 2, 591.

75. D. Liu, T.L. Kelly, *Nature Photonics,* **2014**, *8,* 133-139.

76. H. J. Snaith, *J. Phys. Chem. Lett.*, **2013**, *4*, 3623

77. M.D. Archer, R. Hill, *Series on Photoconversion of Solar Energy, Volume 1: Clean Electricity from photovoltaics*, Imperial College Press **2001**.

78. Solar Energy Production jumps 50% in **2007**

79. http://www.earth-policy.org/indicators/C47/solar_power_2007

80. Commercialization of Dye Sensitized Solar Cells, K.G. Chettibabu G24i Power Ltd.

Chapter 2

Basics of DSSCs and other related Experimental Methods

This chapter presents the basic working principles of Dye sensitized solar cell (DSSC). It highlights the important parameters which determine the DSSC solar conversion efficiency. The various DSSC components and the basics of their fabrication processes are discussed in detail in this chapter. Also, different methods for the synthesis of TiO_2 nanomaterials used in the doctoral work such as hydrothermal, sol-gel and solvothermal are discussed in detail in this chapter. This is followed by the discussion of various experimental tools employed to characterize the structural, optical and electrical properties of the synthesized nanomaterials.

2.1. Introduction

Developing affordable and highly efficient photovoltaic technologies has always been a cherished goal of materials scientists and device community. Exploring non-silicon alternatives based on the novel scientific opportunities afforded by the emergence of nanotechnology (the so-called third generation cells) has gained significant momentum in this respect during the past two decades. Towards this end the discovery of Dye Sensitized Solar Cells (DSSC) in 1991 by Grátzel and co-workers stands out as one of the front runners in view of the basic novelty of the concept derived from nature's principles and the chemical way of assembling the cell architecture which allows facile and cost effective processing alternatives.[1] The significant collective efforts by the scientific community over the past 20 years have not only pushed the efficiencies higher but have brought out several new ways of making robust and durable DSSC cells fairly affordably with good conversion efficiencies. This has included intense work on various inorganic oxide morphologies,[2-5] sensitizers,[6-8] co-adsorbers,[9-10] co-sensitization,[11-12] new counter electrodes,[13] new redox electrolytes [14-15] etc.

2.2. The basic working principle of DSSCs

As with all solar cells, DSSC converts solar energy directly into electric current (power). Figure 1 shows the basic components of DSSC along with its working mechanism. The parts include:

1. A transparent anode made up of a glass sheet treated with a transparent conductive oxide layer;
2. A mesoporous oxide layer (typically,TiO_2) deposited on the anode to activate electronic conduction;

3. A monolayer dye covalently bonded to the surface of the mesoporous oxide layer to enhance light absorption;
4. An electrolyte containing redox mediator in an organic solvent effecting dye-regeneration; and
5. A cathode made of a glass sheet coated with a catalyst (typically, platinum) to facilitate electron collection.

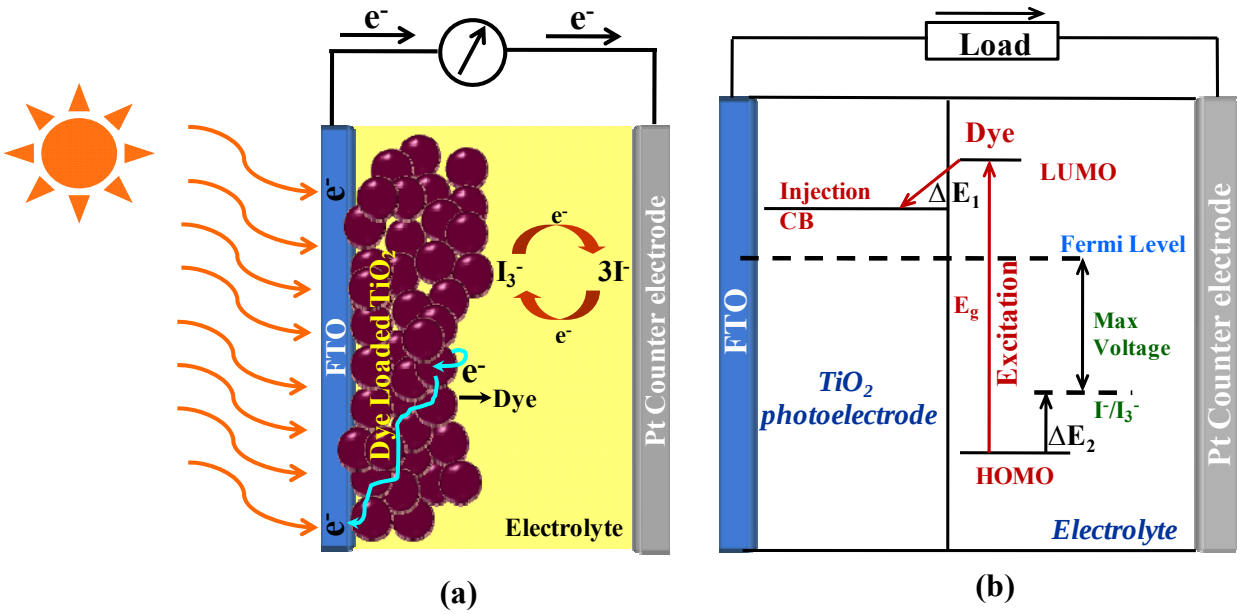

Figure 1. Schematic of DSSC and basic working mechanism of DSSC

Transfer of electrons during cell operation involves the following steps:

$TiO_2|\ S + h\nu \rightarrow\ TiO_2|S^*$ Excitation of dye upon irradiation (1)

$TiO_2|\ S^* \rightarrow\ TiO_2|S^+ + e^-$ Oxidation of dye due to injection of electrons into TiO_2 (2)

$TiO_2|\ S^+ + e^- \rightarrow\ TiO_2|S$ Dye recovers its original ground state (3)

$TiO_2|\ S^+ + 3/2I^- \rightarrow\ TiO_2|S + 1/2I_3^-$ Oxidization of the electrolyte (4)

$1/2I_3^- + e^- \rightarrow 3/2I^-$ Restoration of electrolyte at the counter electrode (5)

$I_3^- + 2e^- \rightarrow 3I^-$ Redox reaction (6)

S: Dye sensitizer; S*: excitation upon irradiation; S^+: Oxidized dye

When exposed to sunlight, the dye sensitizer gets excited from which an electron is injected into the conduction band of the mesoporous oxide film. These generated electrons diffuse to the anode and are utilized at the external load before being collected by the electrolyte at the cathode surface to complete the cycle. In order to enhance electrical conductivity and light transmittance, conducting glass is used as the substrate. There are mainly two types of conducting glass: indium-doped tin oxide (ITO) and fluorine-doped tin oxide (FTO). The semiconductor electrode is usually a layer of nano-crystalline titanium dioxide (TiO_2), a thin film deposited on the conducting glass film with the thickness ca. 10-15 micrometers, which plays an important role in both the exciton separation and the electron transfer process. The porosity and morphology of the TiO_2 layer are dominant factors that determine the amount of dye molecules absorbed on its surface which can provide an enormous area of reaction sites for the dye molecule monolayer to harvest incident light.

The overall performance of the solar cell can be evaluated in terms of cell efficiency (η) and fill factor (FF) expressed as

$$FF = \frac{\text{Imax Vmax}}{Jsc\ Voc}$$

$$\eta = \frac{\text{Jsc Voc FF}}{\text{Pin}} \text{ x } 100$$

Where J_{sc} is the short-circuit current density (mA/cm^2), V_{oc} the open-circuit voltage (V) and P_{in} the incident light power. J_{max} and V_{max} correspond to current and voltage values, respectively; at which the maximum power output is derivable as shown in Figure 2.

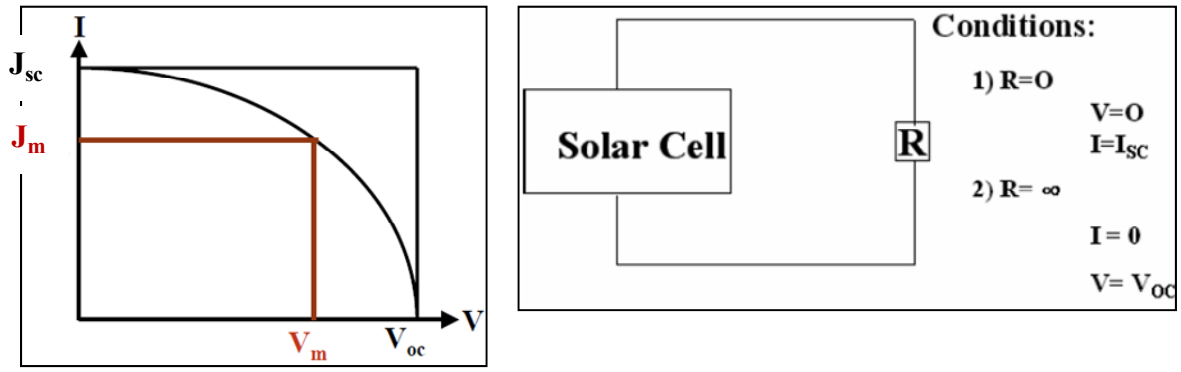

Figure 2. Important parameters of Solar cell

2.2.1. Short Circuit Current (J_{SC})

It is the current obtained from the cell when it is short circuited or in other words when the load resistance is zero. It largely depends on the photon generated electrons and the interfacial recombination of the electrons and holes. Solar cell current is normally represented as current density, J_{sc} , $J_{sc}=I_{sc}/A$ (mA/cm^2), Where, A is the effective area of the solar cell. It is a function of the solar illumination, optical properties and charge transfer probability of the cell.

2.2.2. Open-Circuit Voltage (V_{OC})

Open-circuit voltage is the maximum voltage obtainable from a solar cell and is obtained when a load with infinite resistance is attached to its terminals. It is determined by the difference

between the redox potential of the electrolyte and Fermi level of electrons in the semiconductor namely TiO_2. Check figure 1 (b).

For DSC the V_{oc} is given by:

$$V_{oc} = E_{CB}/q + kT/q \ln(n/N_{CB}) - E_{redox}/q \qquad \text{(volts)}$$

where, n is the number of electrons in the TiO_2 conduction band and N_{CB} is the effective density of states. The first two terms define the quasi-fermi level of TiO_2 and E_{redox} is the Nernst potential of the redox mediator.

2.2.3. Series Resistance (R_s)

Series resistance, R_S in a solar cell, is the result of the contact resistance and charge transfer resistance in the semiconductor material. Series resistance reduces the fill factor of the device and thus affects the maximum device power output, while excessively high value of R_S can also reduce the short-circuit current. The open-circuit voltage is not affected by R_s, since at V_{oc} the total current flow through cell itself is zero and hence through the series resistance is zero. An approximate value of the series resistance can be determined from the slope of the I-V curve at the open-circuit voltage point.

2.2.4. Shunt Resistance (R_{sh})

Low shunt resistance provides an alternate current path for the photo-generated current causing significant power loss. Low shunt resistance reduces the fill factor and lowers the open-circuit voltage, thereby affecting the maximum power output. The short-circuit current is not affected by shunt resistance unless for its very low value, since at J_{SC} the total current flows through the

outer path and hence through the shunt resistance is low. An approximate value of the shunt resistance can be obtained from the slope of the I-V curve at the short circuit current point.

2.2.5. Fill Factor (FF)

The fill factor (FF) is a measure of the maximum power output from a solar cell. It represents the squareness of the I-V curve and is defined as the ratio of the maximum power to the product of V_{OC} and J_{SC} for the solar cell:

$$FF = V_m * J_m / V_{oc} * J_{sc}$$

where, V_m and J_m are the voltage and current values at maximum power point. Fill factor, being a ratio of the same physical parameters, has no unit. Fill factor is a function of the series and shunt resistances of the solar cell. For DSSC, it reflects the extent of electrical and electrochemical losses during cell operation. To obtain higher fill factor improvement of the shunt resistance and decrement of the series resistance are required.

2.2.6. Power Conversion Efficiency

The power conversion efficiency of a solar cell is defined as the ratio of the maximum electrical energy output to the energy input from the sun. Thus the mathematical definition of efficiency is,

$$\eta = (V_{oc} * I_{sc} * FF) / P_{in}$$

where, P_{in} is the power input from the sunlight. Efficiency is generally expressed in percentage. Besides the solar cell performance itself, it depends on the incident light spectrum and intensity as well as operating temperature. The internationally recognized standard condition for the efficiency measurement of solar cells is under 'AM1.5 Global' solar irradiation and at a temperature of 25°C.

2.2.7. Quantum Efficiency or Incident Photon to Current Conversion Efficiency (IPCE)

Quantum efficiency (QE) or 'External Quantum Efficiency (EQE)', sometimes also referred to as Incident Photon to Current Conversion Efficiency (IPCE) is a measure of how efficient a solar cell can create photo-generated charges at a given wavelength. It is defined as the ratio of the number of incident photons to the number of charge carriers generated and is a function of the excitation wavelength:

$$IPCE\ (\lambda) = 1240 * J_{sc} / \lambda * \phi$$

where, J_{SC} is the short circuit current (mA/cm^2), λ is the wavelength (nm) and ϕ is the incident radiative light flux (W/m^2).

For DSSC, the term is defined as:

$$IPCE\ (\lambda) = LHE(\lambda) * \phi(inj) * \eta(coll)$$

where, LHE(λ) is the light-harvesting efficiency for photons at wavelength λ, ϕ(inj) is the electron injection quantum yield for the excited sensitizer to the semiconductor oxide conduction band and η(coll) is the fraction of injected charges that is able to reach the back contact.

The shape of the I-V plot can be fitted with a basic diode equivalent circuit model of solar cells. To achieve a larger output voltage and current, the series resistance is expected to be the smaller, while the parallel resistance should be greater. Correspondingly, in the I-V plot, the slope at V= V_{oc} should be steep and at J= J_{sc} be flat.

The difference between the quasi-Fermi level of the TiO_2 layer and the electrolyte redox potential determines the maximum voltage generated under illumination. J_{sc} can be calculated by integrating the product of incident photon to current efficiency (IPCE) and incident photon flux (P_{in}) over the spectral distribution.

2.3. The detailed structure of DSSC

The dye sensitized solar cell consists of five main components: transparent conductive oxide (TCO) coated substrate, metal oxide coating, dye, electrolyte and counter electrode material.

2.3.1. The TCO glass substrate

The transparent conducting substrate plays an important role in dictating the DSSC's performance. It functions as a current collector and a support of the semiconductor layer in DSSC. It has two important features: the high optical transparency which allows natural sunlight to pass through to the beneath of the active material without unwanted absorption of the solar spectrum, and low electrical resistivity which facilitates the electron transfer process and reduces the energy loss. Current transparent conducting oxides used in industry are primarily n-type conductors.

Transparent conducting coatings for photovoltaic applications have been fabricated using both inorganic and organic materials. Inorganic films typically are made up of a layer of transparent conducting oxide (TCO),[16] generally in the form of indium tin oxide (ITO), fluorine doped tin oxide (FTO), and doped zinc oxide. Organic films are being developed using carbon nanotube networks and graphene, which can be fabricated to be highly transparent to infrared light, along with networks of polymers such as poly(3,4-ethylenedioxythiophene) and their derivatives. The most efficient TCO material widely used in photovoltaic application is ITO or FTO coated glass substrate. However, the only concern with ITO is that its conductivity decreases during the calcinations process in the DSSCs fabrication. Therefore FTO is the preferred transparent conducting material for DSSCs.TCO films are deposited on a substrate through various deposition methods, including metal organic chemical vapour deposition (MOCVD), spray

pyrolysis, and pulsed laser deposition (PLD), however the most efficient technique is magnetron sputtering of the film.[17]

2.3.2. Metal Oxide Coating

The metal oxide nanoparticulate porous coating is generally deposited on the top of the TCO by doctor blade method or screen printing method. This coating provides a surface for the dye adsorption, it accepts electrons from the excited dye, and conducts electrons to the TCO. The choice of metal oxide can be made between different n-type oxides such as TiO_2,[18] ZnO,[19-20] SnO_2 [21-22] and other ternary oxide like Zn_2SnO_4 [23] etc. TiO_2 is the work horse material for DSSCs. It exists in three forms namely anatase, rutile and brookite. Of the three forms rutile is the most stable phase but it suffers from slow electron transfer rate leading to low current in DSSC. Anatase TiO_2 is widely used as a photo-anode material which renders conversion efficiency of 12% due to greater electron transport properties and high surface area. Zinc oxide (ZnO) is a promising alternative to TiO_2 because it has a similar band structure and relatively high electron mobility (1–5cm^2 V^{-1} s^{-1}).[24] However it is not stable in the most efficient dyes containing acidic groups which are required for anchoring of the dye on the metal oxide surface. Alternatively tin oxide (SnO_2) is an attractive option but it shows poor photovoltaic performance due to faster recombination dynamics and lower isoelectric point leading to poor dye loading on its surface.[25] Thus in this thesis work TiO_2 nanoparticle films are used as the working electrode.

2.3.2.1. Synthesis procedures of TiO_2 Nanoparticles: Need for 15-20 nm sized TiO_2 nanoparticles

Over the past decade a wide variety of techniques and methods are developed to synthesize nano materials of different sizes, shapes and forms. These have been well documented in several reviews in the literature.[26] It important to note here that the particle size of the TiO_2 particles is

also very important in order to have good DSSC efficiency. This is because the charge transport properties within the TiO_2 network largely depend on the TiO_2 particle size.[27] The morphological analysis of the TiO_2 network as shown by Cao *et al*[28] revealed that the particle size and surface area exert an impact on the charge transport properties, while the coordination number and neck diameter seemed to be consistent with the nanoparticle size. Thus the electron transport along with the TiO_2 network is mainly affected by the particle size in terms of the mean free path; the bigger particle size provides both long travel distance and less collision chance with the boundary. Surface area also exerts a strong influence on the recombination when it is in contact with an electrolyte. Accordingly the largest TiO_2 particles with low transport resistance, high recombination resistance, and low chemical capacitance, should exhibit longest diffusion length (Ln) and thus greater efficiency. However, highest efficiency is observed in 15 nm TiO_2 nanoparticle photoanode suggesting that there should be a balance between morphological factors of the TiO_2 governing the light harvesting capability of the entire network and the charge collection efficiency which is governed by the particle size of TiO_2. Thus the synthesis of 15nm sized TiO_2 nanoparticles is a crucial task. The main focus of this section is to describe the specific methods employed for synthesis of TiO_2 nanoparticles in the present thesis work. These include the known hydrothermal synthesis, sol gel method and solvothermal synthesis for nearly monodispersed nanoparticles.

(I) Hydrothermal Synthesis

The hydrothermal technique is one of the most important synthesis methods for advanced materials processing, particularly due to its advantages in the processing of nanostructural materials for a wide variety of technological applications such as electronics, optoelectronics, catalysis, ceramics, magnetic data storage, biomedicine, biophotonics, etc. The

hydrothermal technique not only helps in processing monodispersed and highly homogeneous nanoparticles, but also acts as one of the most attractive techniques for processing nano-hybrid and nanocomposite materials. The term 'hydrothermal' comes from the earth sciences, where it implies a regime of high temperature and water pressures. Generally, conditions ranging from the boiling point of water (100°C, 0.10 MPa) up to the critical point (374.3°C, 22.11 MPa) can be considered as hydrothermal. For a typical hydrothermal process, one needs a high temperature, high-pressure apparatus called 'autoclave' or 'bomb'. A great deal of early experimental work was done using the Morey bomb[29,30] and Tuttle-Roy[31] test tube bomb (Tem-Press) . Hydrothermal synthesis involves use of water both as a catalyst and occasionally as a component of vapour phases in the synthesis at elevated temperature (> 100°C) and pressure (> a few atmosphere). Now-a-days, one can get many kinds of autoclaves to cover different p–t ranges and volumes.

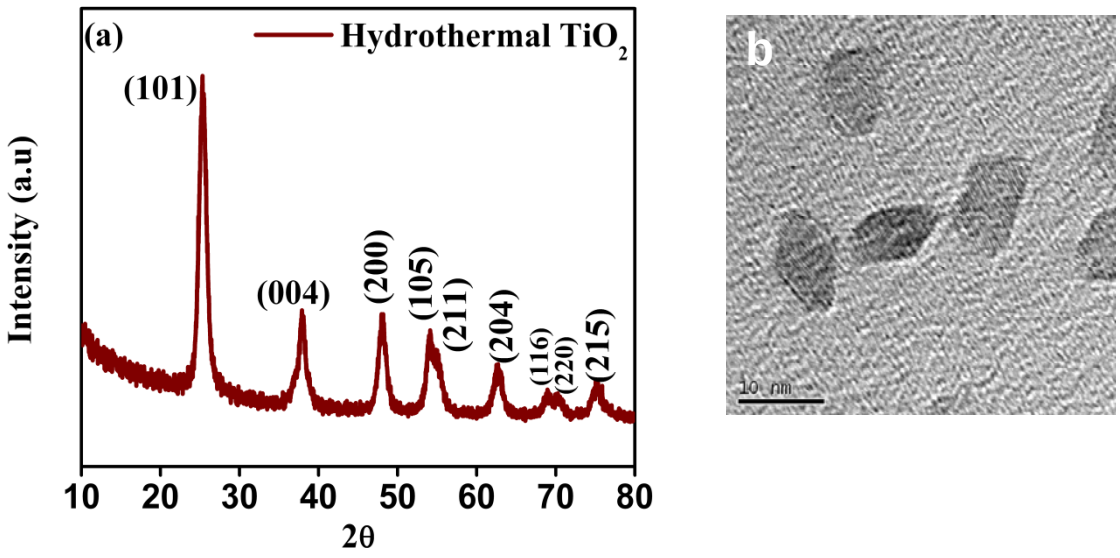

Figure 3. (a) XRD data and (b) TEM image of hydrothermally synthesized TiO_2 nanoparticles

A typical hydrothermal synthesis procedure involves hydrolysis of Titanium isopropoxide (2 mL) using sufficient amount of deionized water followed by sonication for 5 min. The solution is

then transferred to Teflon lined autoclave vessel along with 3 mL of H_2SO_4 (1 M). This autoclave vessel is kept at 175 ^{0}C for 24 h. The resulting product is washed thoroughly with de-ionized water and dried at 50^{0}C in a dust proof environment to produce white powder of TiO_2 nanoparticles.

Figure 3 (a) and (b) show the XRD and TEM images, respectively, of hydrothermally synthesized TiO_2 nanoparticles respectively. The peaks in Figure 3 (a) at positions 25.4(101), 38.1 (004), 48.1 (200), 54.2 (105), 55.0 (21 1), 62.8 (204), 69.1 (11 6), 70.3 (220) and 75.4 (215) (PCPDFWIN#211 272) clearly represent pure anatase TiO_2 phase. The TEM image in Figure 3 (b) shows the TiO_2 nanoparticles size of around 8-10 nm.

(II) Sol gel Synthesis

The sol-gel technique is one of the most widely used soft chemical methods and mainly applied for the synthesis of metal and semimetal oxides. In this process, oxides are synthesized by the formation of an oxide network directly in the solution by hydrolysis of alkoxides, followed by gelation and finally removal of the solvent.[32] In contrast to the solid-state method, a wet chemical synthesis can provide homogenous nano-sized oxides of high purity at lower reaction temperatures. Sol-gel and aerogel processes are the most widely used routes and involve a colloidal sol which is converted into a gel during aging.[33,34] The main principle of the classical sol-gel process is the controlled hydrolysis of metal-organic compounds (alkoxides) in an organic solvent. The sol-gel process involves olation (formation of hydroxyl bridges) and oxolation (formation of oxygen bridges) reactions during hydrolysis (reactions 2.1-2.3). The oxolation condensation reaction is responsible for the formation of colloidal agglomerates, and the olation addition reaction is responsible for their aggregation into a polymeric gel.

$\equiv M\text{-}OR + H_2O \rightarrow \equiv M\text{-}OH + HOR$ (Hydrolysis)..... (2.1)

≡M-OH + RO-M≡ → ≡M-O-M≡ + HOR (Condensation)..... (2.2)

2 (≡M-OH) → ≡M-O-M≡ + H_2O (Addition)..... (2.3)

Where R is alkyl group and M is metal or semi-metal.

The gel formation depends on different parameters including the nature of starting material, kind of solvent, precursor concentration in the solvent, alkoxy to water ratio, temperature of the reaction, pH, kind of catalyst, stirring and aging time. Metal alkoxides serve as starting materials and can be hydrolyzed by water. During hydrolysis, alkoxy groups are replaced by strong OH- nucleophiles, and condensation and addition steps lead to the formation of oxide chains. The sol-gel synthesis goes through the formation of a sol of colloidal particles or units in a solution, gelation of the sol by the agglomeration of these particles or sub-units into a big gel network structure, removing of the solvent, and heat treatment to transfer gel into solid. Depending on reaction conditions, the sol particles may grow further or form gel. The drying of the sol gives powders. The removal of the solvent by drying causes the shrinking of the gel and significant reduction in the volume due to increasing capillary forces. The high capillary pressure in the pores causes the collapse of the gel network structure and the production of less porous powder (xerogel).

A typical synthesis procedure followed is as follows:

5ml (4.8gm) of Titanium Isopropoxide is dissolved in 25ml ethanol. Hydrolysis is done using a mixture of minimum amount of distllled water (2 ml) and ethanol (8 ml) with few drops (40 µl) of conc HCl, which is added slowly with stirring. This is an important step as we do not want faster hydrolysis. After addition of hydrolysis mixture, the solution is stirred for 15 min till it starts getting viscous. Then this viscous liquid (sol) is poured in petri dish for formation of gel. Gel formation takes place within 2-3 hrs and gel converts to xerogel (dried solid) by 48 hrs.

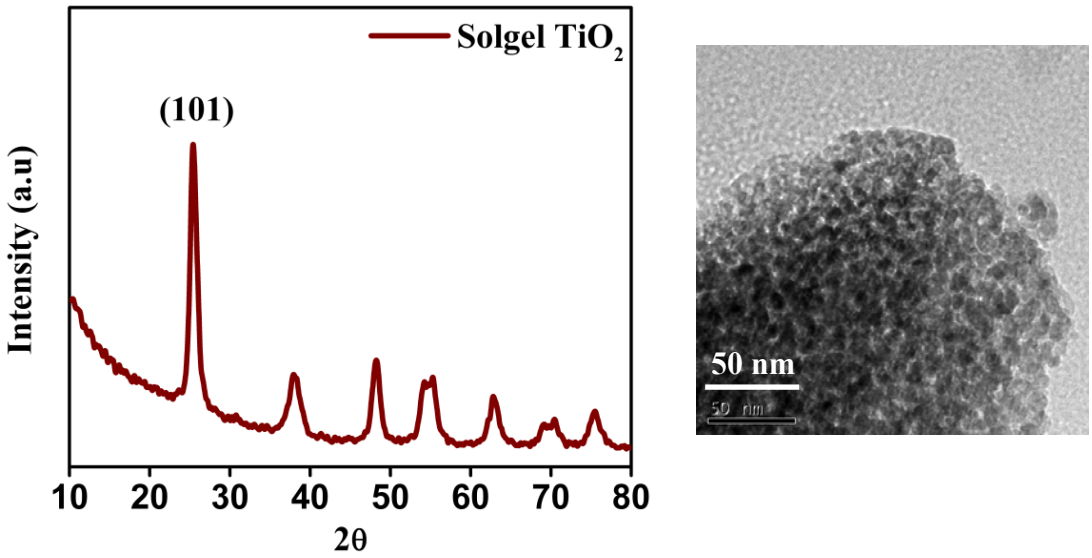

Figure 4. (a) XRD data and (b) TEM image of solgel synthesized TiO_2 nanoparticles

This Xerogel is clear and transparent, which on crushing becomes a white powder and on cacination at 400^{o}C for 2h gives TiO_2 nanoparticles. Figure 4 (a) shows the XRD for these solgel TiO_2 nanoparticles. Like hydrothermally synthesised TiO_2 nanoparticles sol gel synthesized TiO_2 Nps are also in pure anatase phase [JCPDS 21-1272].. The crystallite size calculated using Scherrer formula is around 8-10 nm which is in good agreement with the TEM image as seen in Figure 4(b).

(III) Solvothermal Synthesis

Solvothermal synthesis is a chemical method used for the synthesis of various compounds. It is similar to the hydrothermal route (where the synthesis is conducted in a stainless steel autoclave), the only difference being that the precursor solution is usually not aqueous. Using the solvothermal route gains one the benefits of both the sol-gel and hydrothermal routes.[26] The solvothermal synthesis allows for the precise control over the size, shape distribution, and crystallinity of metal-oxide nanoparticles or nanostructures. These characteristics can be altered

by changing certain experimental parameters, including reaction temperature, reaction time, solvent type and the precursor type.

The typical procedure followed for synthesis of TiO_2 nanoparticles is as follows:[35]

An amount of 12 g (0.2 moles) of acetic acid is added all at once to 58.6 gm (0.2 moles) of titanium iso propoxide under stirring at room temperature. The modified precursor is stirred for about 15 min and poured into 290 ml water as quickly as possible under vigorously stirring (700 rpm). A white precipitate is instantaneously formed. One hour of stirring is required to achieve a complete hydrolysis reaction. After adding a quantity of 4 ml of concentrated nitric acid, the mixture is heated from room temperature to 80 °C within 40 min and peptized for 75 min. Water is then added to the cooling liquid mixture to adjust the volume to a final 370 ml. The resultant mixture is kept in a 570 ml titanium autoclave and heated at 250 °C for 12 h. Following this step, 2.4 ml of 65% nitric acid is added and the dispersion is treated with a 200W ultrasonic titanium probe at a frequency of 30 pulses every 2 s.

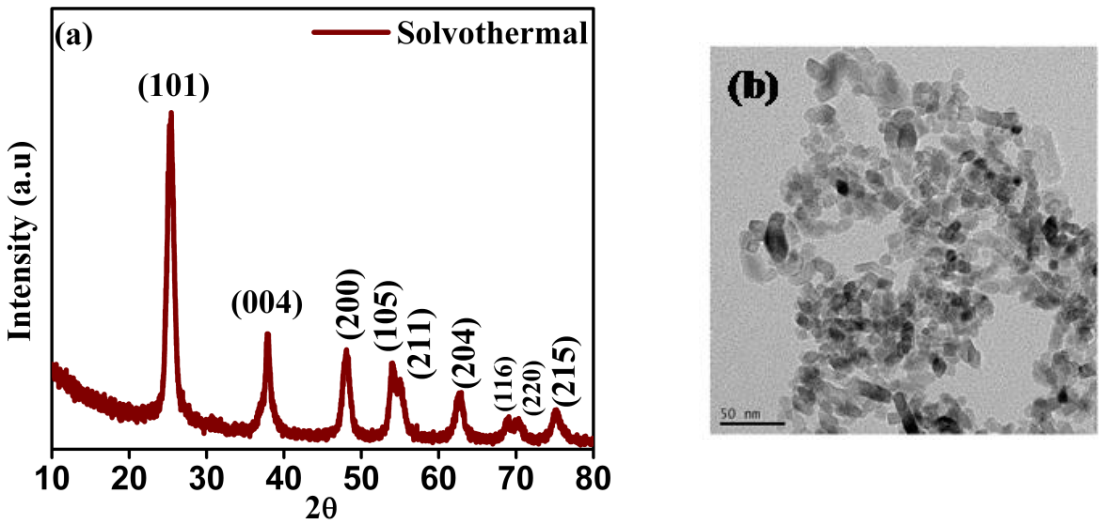

Figure 5. (a) XRD data and (b) TEM image of solvothermally synthesized TiO_2 nanoparticles

The resultant colloidal solution is concentrated with a rotary-evaporator to contain 13 wt.% TiO_2. Finally, it is triply centrifuged to remove nitric acid and washed with ethanol three times to produce a white precipitate containing 40 wt.% TiO_2 in ethanol and only trace amounts of water. Figure 5 (a) shows XRD data of solvothermally synthesized TiO_2 nanoparticles. The size of these particles is around 15-20 nm as calculated using Scherrer formula and as required for DSSC application. The TEM image in Figure 5(b) also confirms the same size of the TiO_2 nanoparticles. It is clear from the TEM image that these particles are well dispersed with very little agglomerates unlike sol gel synthesized ones. Such well dispersed particles are required for making transparent TiO_2 photoanodes for DSSCs.

The efficiencies trends obtained for the particles synthesized by the above three ways are Solvothermal > Solgel ≥ Hydrothermal.

2.3.3. The Sensitizer

The ideal sensitizer used in DSSC has to meet several requirements that guide effective molecular engineering : (i) the sensitizer should be able to absorb all incident light below the near-IR wavelength of approximately 920 nm; (ii) it must carry a carboxylate or phosphonate group to anchor on the surface of the semiconductor oxide; (iii) the lowest unoccupied molecular orbital (LUMO) of the sensitizer must match the edge of the conduction band of the oxide to minimize the energetic potential losses during the electron transfer reaction; (iv) the highest occupied orbital (HOMO) of the sensitizer must be sufficiently low to accept electron donation from an electrolyte or a hole conductive material; (v) it should be stable.

The sensitizer, or dye monolayer, is the layer which interacts with the sunlight and therefore is a very important part of the DSSC. Typically the metal oxide films are immersed in the dye

solution for 12 to 24 hrs so that the dye molecules get adsorbed on the surface of the metal oxide nanoparticles.

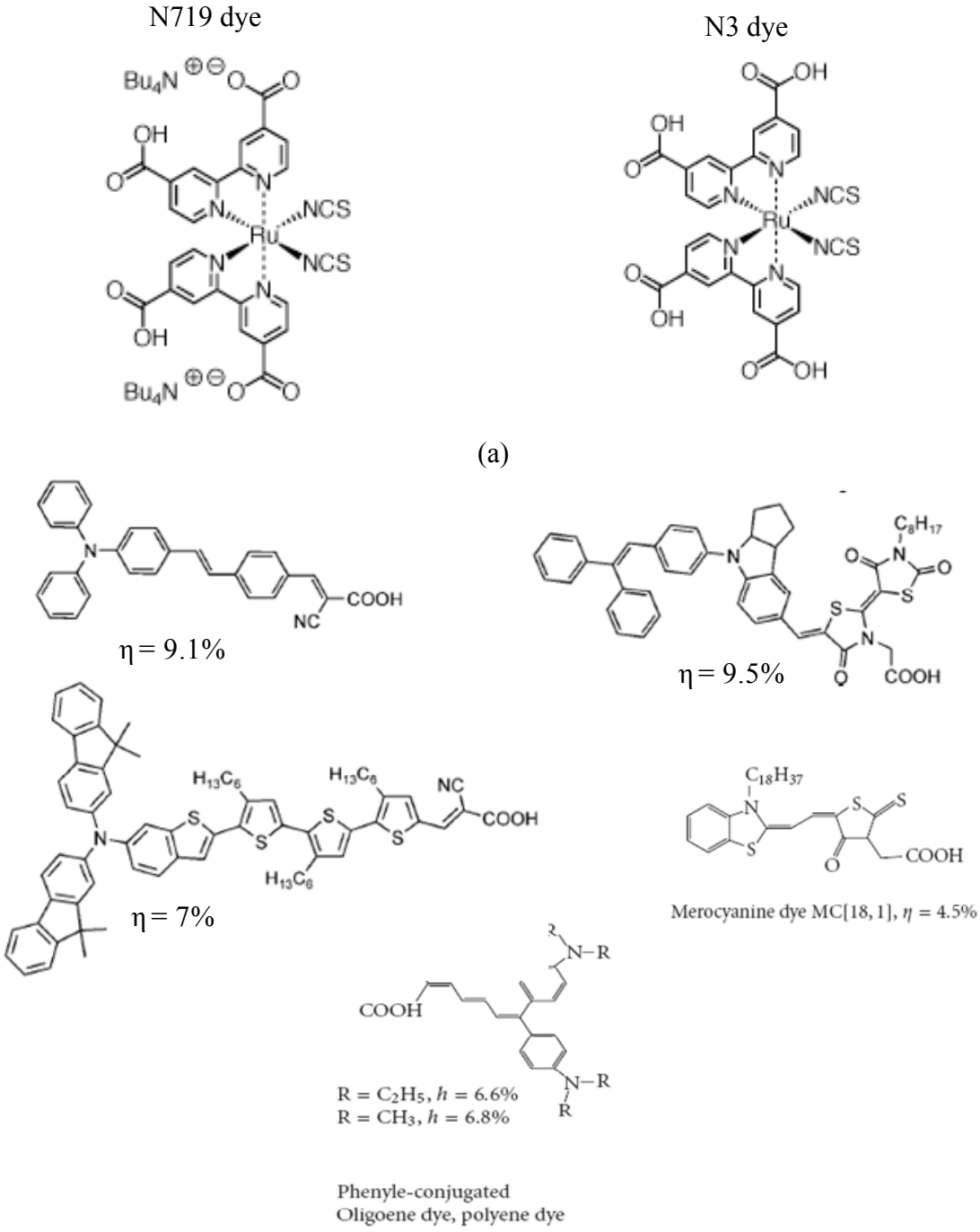

Figure 6. (a)Ruthenium dyes (b) Different forms of Organic dyes [36-40]

Ruthenizer 535-bisTBA (also known as N719) and Ruthenizer 535 (also known as N3 dye) (Figure 6 (a)) in the literature, have been so far the most efficient sensitizers in Dye Solar Cells which sensitize wide band-gap oxide semiconductors, like titanium dioxide, very efficiently up to a wavelength of 750 nm. The photovoltaic performance of black dye is expected to be superior to all other known charge-transfer sensitizers in terms of the whole range of light absorption. But the high cost, the limited abundance and availability of noble metals, and also the sophisticated synthesis and purification steps have pushed the scientific community to search for some metal free organic dyes and even natural dyes as well.[41]

Figure 6 (b) shows various metal free organic dyes used in DSSCs. Yella *et al.* [14] synthesized a donor-p bridge-acceptor zinc porphyrin dye (YD2-o-C8) which suppresses the interfacial electron back transfer from the nano-crystalline TiO_2 film to the oxidized cobalt mediator, and leads to a strikingly high power conversion efficiency of 12.3% under simulated air mass 1.5 global sunlight.

2.3.4. The Electrolyte

The electrolyte is a key component of dye-sensitized solar cells (DSSCs). It functions as charge carrier collecting electrons at the cathode and transporting the electrons back to the dye molecule. The most commonly used liquid electrolyte, namely iodide/ triiodide (I^-/I_3^-), works well mainly due to its kinetics. Figure 7 shows the kinetics of I^-/I_3^- redox couple with Ru-N719 dye. The electron injection into the TiO_2 conduction band occurs in the femto second time scale which is much faster than the electron recombination with I_3^-, and the oxidized dye preferably reacts with I^- than combining with the injected electrons. In the electrolyte, the I_3^- diffuses to cathode to harvest electrons and in turn produce I^- which diffuses in the opposite direction

towards the TiO_2 electrode to regenerate the dye molecules. The diffusion coefficient of I_3^- ions in the porous TiO_2 structure is about 7.6 x10^6 cm^2/s.[42] It is found that recombination can be suppressed by introducing additives to the electrolyte such as 4-tert-butylpyridine (4TBP) [38], guanidiumthiocyanate [43], and methylbenzimidazole (MBI) [44]. The most probable mechanism is that these additives, when absorbed by theTiO_2 surface, block the reduction sites to keep electron acceptor molecules away from contact.

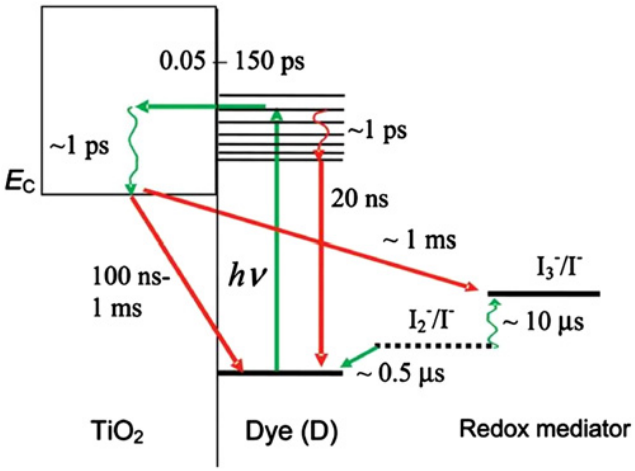

Figure 7. Kinetics of the cis- $Ru(dcbpy)_2(NCS)_2$- (N719) sensitized TiO_2 solar cell with I^-/I_3^- redox mediator [42]

The overall conductivity of this electrolyte can also be increased by using different ionic liquids containing imidazolium salts.[45] Depending on the alkyl chains attached to these imidazolium salts the performance of the electrolyte can be varied. These additives can thus improve the efficiency and stability, though they do not participate in the fundamental photo-electrochemical processes. Lithium iodide is added in the electrolyte as it acts as a source of iodide ions required for redox couple in electrolyte. Also the Lithium ions screen the negative charge in the semiconductor, and increases charge conductivity in the electrolyte.[46]In absence of these cations

on the surface the conduction band of semiconductor shows a downward shift which gives lowers the V_{oc} of the cell. [46] But the concentration of this LiI must not be very high as the small Li cations can intercalate with the TiO_2 matrix and act as recombination centers thus lowering the device performance.[46] In theory, the maximum voltage generated in DSSCs is determined by the difference between the quasi-Fermi level of the TiO_2 and the redox potential of the electrolyte, about 0.7 to 0.8 V under solar illumination conditions. In order to obtain a higher open circuit voltage and control the corrosion of I^-/I_3^- redox couple, a variety of alternative redox couples have been introduced in DSSCs such as Br^-/Br_3^-, $SCN^-/(SCN)_2$, $SeCN^-/(SeCN)_3^-$, $Fe(CN)_6^{3-/4-}$ [47] and Co(II)/Co(III)complex. In this thesis work liquid I^-/I_3^- redox electrolyte with suitable additives is used as the electrolyte. The composition details are described in the next chapter.

2.3.5. The Counter electrode

Usually Pt nanoparticle-coated FTO obtained by thermal decomposition,[48] sputtering [49] or chemical reduction [50] is used as the counter electrode. Pt counter electrode is very efficient in I^-/I_3^- redox regeneration (the conversion of I_3^- to I^- occurs on the surface Pt) which in turn helps in the regeneration of oxidized dye. Thus, platinum acts as catalyst for the charge transfer reaction occurring between iodide and tri-iodide.[51] However in view of the high cost and less natural abundance of Pt, in recent years significant efforts are directed towards the replacement of this Pt catalyst with other inexpensive and earth abundant materials.[52]

The pre-requisites for an efficient catalyst in DSSC are that it should be easily available, low cost, stable in the cell architecture ambient and certainly with a very good catalytic activity. Carbon is one of the leading candidates in this respect. Till today various carbon forms like CNTs,[53] functionalized graphene,[54] mesoporous carbon,[55] carbon fibers,[56] laser synthesized

carbon[57] etc. have been successfully used as counter electrodes in DSSCs with efficiency comparable to or even exceeding that of platinum. But the main problem of carbon counter electrodes is adhesion of these carbon materials to the substrate surface and its opaque nature. Inorganic materials like sulphides, carbides, nitrides and some organic/inorganic composites can also be used as the counter electrode materials.[58] In this thesis work drop casted and thermally deposited Pt is used as counter electrode.

The next section describes the important characterization tools used for nanoparticle characterization in this thesis.

2.4. Nanomaterials Characterization techniques

2.4.1. X-Ray Diffraction

X-ray diffraction (XRD) technique is used to realize structural properties of materials and get information like crystal structure/phase, lattice parameters, crystallite size, orientation of single crystals, preferred orientation of polycrystals, defects, strains and so on.[59] This technique is suitable for thin films, bulk and nanomaterials. In the case of nanostructures, the change in lattice parameter w. r. t. bulk gives an idea of nature of strain present in the film. In XRD, a collimated monochromatic beam of X-rays is incident on the sample for diffraction to occur. A constructive interference occurs only for certain θ*'s* correlating to those (hkl) planes, where path difference is an integral multiple (n) of wavelength. Based on this, the Bragg's condition is given by

$$2d\sin\theta = n\lambda$$

Where, λ is the wavelength of the incident X-ray, d is the inter-planer distance, 'θ' is the scattering angle and n is an integer-called order of diffraction. In nanostructures, X-rays are diffracted by the oriented crystallites at a particular angle to satisfy the Bragg's condition. Having known the value of θ and λ, one can calculate the inter-planer spacing. The XRD can be taken in various modes such as θ - 2θ scan mode, θ - 2θ rocking curve, and ϕ scan. In the θ - 2θ scan mode, a monochromatic beam of X-rays is incident on the sample at an angle of θ with the sample surface. The detector motion is coupled with the X-ray source in such a way that it always makes an angle 2θ with the incident direction of the X-ray beam (Figure 8). The resulting spectrum is a plot between the intensity recorded by the detector versus 2θ.

$$\textit{Angle of Incidence } (\theta_i) = \textit{Angle of Reflectance } (\theta_r)$$

This is done by moving the detector twice as fast in (θ) as the source. So, only where $\theta_i = \theta_r$, will be the intensity of the reflected X-rays to be measured. Nanomaterials have smaller sized

crystallites and significant strains due to surface effects, causing considerable peak broadening and shifts in the peak positions w.r.t standard data.

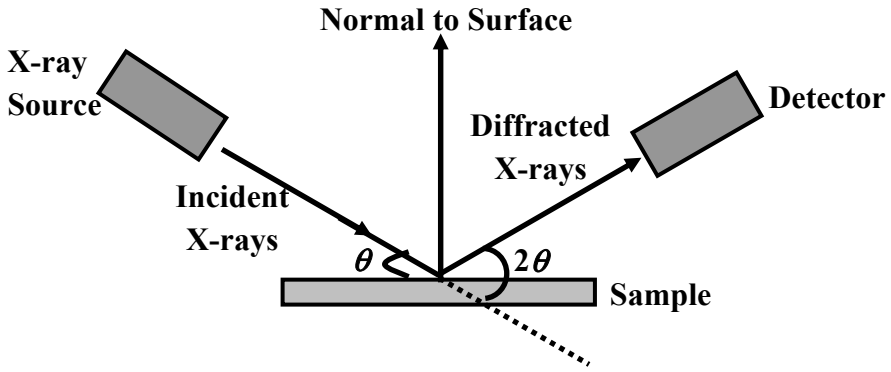

Figure 8. Representation of X-ray Diffraction

The θ-2θ scan maintains these angles with the sample, detector and X-ray source. Only planes of atoms that share this normal will be seen in the θ-2θ scan. From the shifts in the peak positions, one can calculate the change in the d-spacing, which is the result of change of lattice constants under strain. The crystallite size (D) is calculated using Scherrer's formula:

$$D = k \lambda / \beta \cos\theta$$

Where, k = Scherrer's Constant ≈ 0.9, β = Full Width at Half Maximum (FWHM). The only disadvantage of XRD is its less sensitivity towards low-Z materials, thus usually high-Z materials can be better characterized. In such cases, electron or neutron diffraction is employed to overcome the low intensity of diffracted X-rays.

2.5. Microscopy Tools for nanoparticle characterization

2.5.1. Transmission Electron Microscopy (TEM)

Transmission electron microscopy (TEM) [60-61] is an imaging technique whereby a beam of electrons is focused onto a specimen causing an enlarged version to appear on a fluorescent screen or a layer of photographic film, or to be detected by a CCD camera. TEM operates on the same basic principles as the light microscope but uses electrons instead of light. The line diagram of a typical TEM column is shown in Figure 9. The column consists of a source of electrons, electrodes for electron acceleration, electromagnetic focusing and deflecting lenses and the electron detection system such as a CCD array. By using electron energy of several hundred kilovolts the de Broglie wavelength associated with the electron can be reduced to a small fraction of nanometer and hence atomic resolution imaging becomes feasible. Virtually, TEM is useful for determining size, shape and arrangement of the particles which make up the specimen. Moreover, it is highly useful for the determination of the lattice planes and the detection of atomic-scale defects localized in areas of few nanometers in diameter with the help of selected area electron diffraction (SAED) technique. The *d*- spacing between lattice planes of crystalline materials can be calculated from a SAED pattern using the relationship:

$$dr = \lambda L$$

where, L is the distance between the specimen and the photographic plate, λL is known as the camera constant and r is the radius of diffracted rings. It is easy to measure r directly from the photographic plate, and λL can be established from the instrument by calibrating it with a standard material (usually Ag), and hence one can easily get d values. Since, each d value corresponds to a specific lattice plane for a specific crystal structure; description of the crystal structure of a crystalline specimen can be obtained from SAED pattern. In some cases SAED

pattern is more helpful as compared to XRD, due to the limited detection limit of XRD instrument. Also, the XRD generally gives global information.

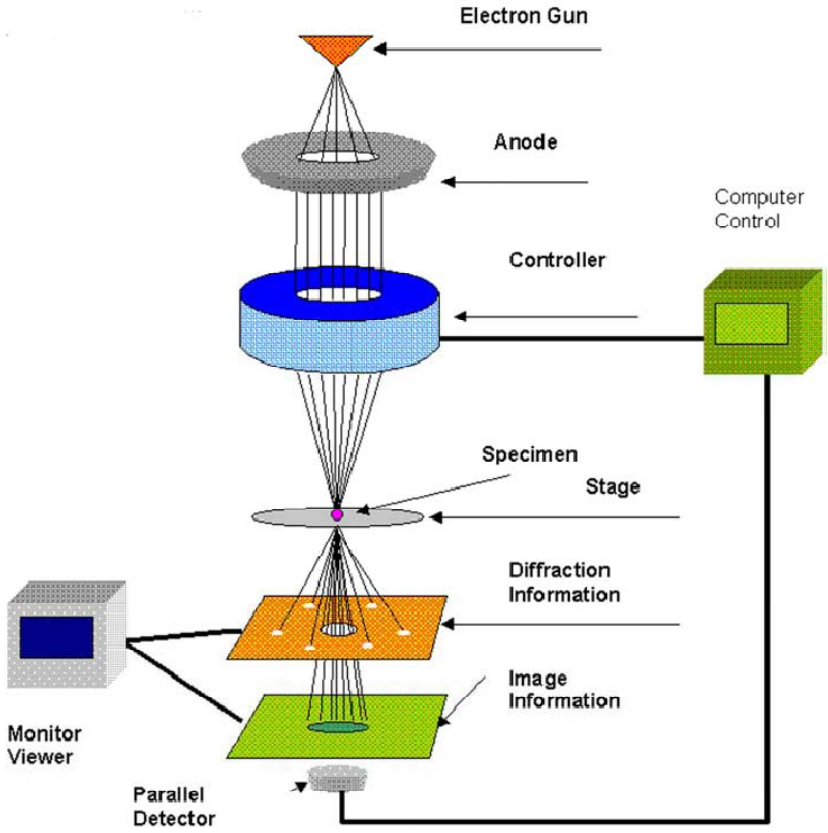

Figure 9. Schematic diagram of the Transmission Electron Microscope
(Ref: http://www.rpi.edu/dept/materials/COURSES/NANO/shaw/Page5.html)

The TEM measurements in the present work were performed on a JEOL JEM-1200EX instrument operating at 300 kV, camera length of 80 cm and field limited aperture of 100 µm. Prior to TEM measurements, the samples were dispersed in a suitable organic solvent (isoamyl acetate, methanol, acetone, toluene, etc.) and a drop of the solution was poured on carbon-coated copper grid of 400 mesh size. The film formed on the TEM grids was allowed to dry for 2 minutes following which the extra solvent was removed using a blotting paper and the TEM and

SAED measurements were performed. The image and diffraction analysis were performed under an accelerating voltage of 300 kV. Experimental electron diffraction patterns of various samples were compared with the simulated electron diffraction patterns of the corresponding phases. Electron diffraction ring patterns were simulated using the computer program JECP/PCED.

2.5.2. Scanning Electron Microscope (SEM)

It uses a beam of electrons focused to a diameter spot of approximately 1nm in diameter on the surface of the specimen and scanned back and forth across the surface (beam energy of 200kV). The surface topography of a specimen is revealed either by the reflected (backscattered) electrons generated or by electrons ejected from the specimen as the incident electrons decelerate secondary electrons. A visual image, corresponding to the signal produced by the interaction between the beam spot and the specimen at each point along each scan line, is simultaneously built up on the face of a cathode ray tube similar to the manner by which a television picture is generated. The best spatial resolution currently achieved is of the order of 1nm.

The scanning electron microscope (SEM) [62-63] is a very useful instrument to get information about topography, morphology and composition information of materials. A typical schematic of a SEM is shown in Figure 10. It is a type of electron microscope capable of producing high resolution images of a sample surface. Due to the manner in which the image is created, SEM images have a characteristic three-dimensional appearance and are useful for judging the surface morphology of the sample.

The SEM has an ability to image a comparatively large area of a specimen and also to image bulk materials. Topology of the powder samples in the present study was carried out using a FEI, Model Quanta 200 3D scanning electron microscope.

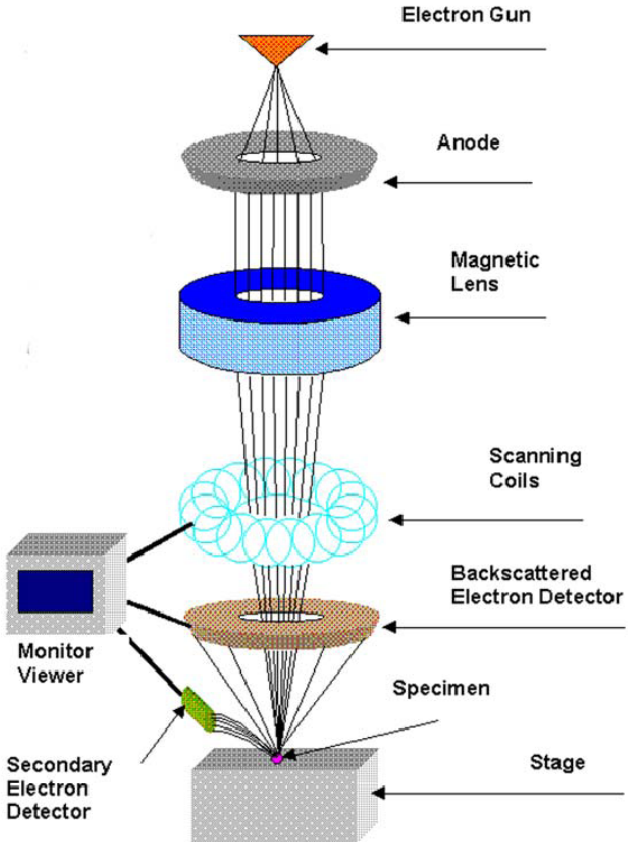

Figure 10. Schematic diagram of the Scanning Electron Microscope
(Ref: http://www.rpi.edu/dept/materials/COURSES/NANO/shaw/Page5.html)

2.6. Spectroscopy Tools

2.6.1 UV-VIS Spectroscopy

UV-VIS Spectroscopy deals with the recording of absorption signals due to electronic transitions. In semiconductors, when the incident photon energy exceeds the band gap energy of the materials, absorption takes place and signal is recorded by the spectrometer whereas in metals when the surface free electrons vibrate coherently with the incident frequency then resonant absorption takes place.

Such a spectrometer can operate in two modes (i) transmission and (ii) reflection mode. In transmission mode usually thin films and colloidal NPs well-dispersed in solvent are used. The optical measurements for opaque thin films and those NPs which are not dispersible in solvents are done in diffuse reflectance (DRS) mode.

Instrument: Figure 11 shows the block diagram of UV-Vis spectrophotometer. The light from the source is alternatively split into one of two beams by a chopper; one beam is passed through the sample and the other through the reference. The detector, which is often a photodiode, alternates between measuring the sample beam and the reference beam. Some double beam instruments have two detectors, and the sample and reference beam are measured at the same time. In other instruments, the two beams pass through a beam chopper which blocks one beam at a time.

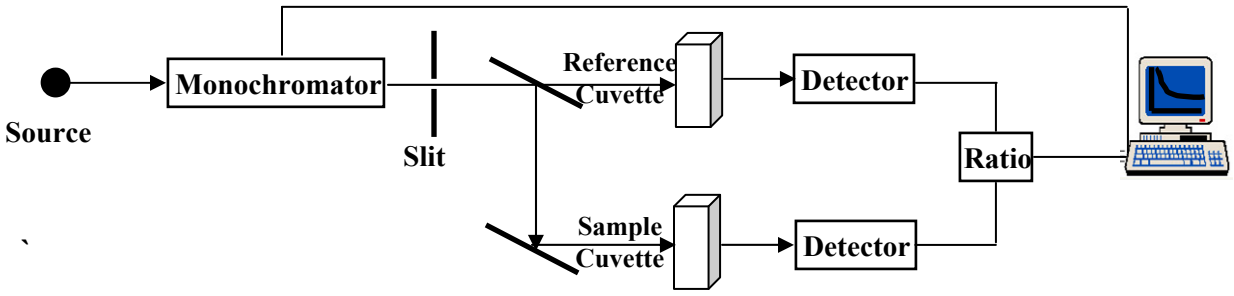

Figure 11. Schematics of UV-VIS Spectrophotometer in Transmission Mode

Broadening of spectral transitions: The possible sources for the signal broadening: (a) Doppler Broadening : Random motion of NPs in the liquids and gaseous samples causes their absorption and emission frequencies to show a Doppler shift and hence the spectrum lines are broadened. This effect is more pronounced in liquids than gaseous samples due to significant collisions in solutions. In the case of solids, the motions of the particles are more limited in extent and less

random in direction, so that solid phase spectra are often sharp but show evidence of interactions by the splitting of the lines into two or more components; (b) Heisenberg's Uncertainty Principle: If a system exists in an energy state for a limited time 'δt' seconds, then the energy of that state will be uncertain (fuzzy) to an extent 'δE' and is given by $\delta E \times \delta t \approx h/2\pi \approx 10^{-34}$ J.s, where h = Planck's Constant. Usually life time of excited state is 10^{-8} sec, i.e. 10^{8} Hz uncertainty in the radiation frequency which is, in fact, small as compared to UV-Vis frequency regime ($10^{14} - 10^{16}$ Hz).

Intensity of Spectral lines: There are three main factors that decide the intensity of spectral lines: (i) *Transition probability*: The likelihood of a system in one state changing to another state which is usually governed by quantum mechanical selection rules; (ii) *Population of states*: The number of atoms/molecules initially in the state from which the transition occurs. It is governed by the equation: $N_{upper} / N_{lower} = \exp(-\Delta E/kT)$; Where, $\Delta E = E_{upper} - E_{lower}$, T= temperature (K), k = Boltzman's Constant = 1.38×10^{-23} J/K; (iii) *Concentration and path length*: Clearly since sample is absorbing energy from a beam of radiation, the more sample the beam traverses, the more energy will be absorbed from it. Besides the amount of the sample, the concentration of the sample is also deciding factor for the energy absorption. Based on this, Beer-Lambert law, which is often written as:

$$I / I_0 = \exp(-\kappa cl) \quad \text{or} \quad I / I_0 = 10^{-\varepsilon cl} = T$$

Where, κ = constant, for particular spectroscopic transition under consideration. Where T = transmittance = I / I_0 , ε = molar absorption coefficient.

Inverting above equation and taking logarithms,

$$I_0 / I = 10^{\varepsilon cl} \quad \text{Or} \quad \log(I_0 / I) = \varepsilon cl = A,$$

Where A = absorbance / optical density

Thus, absorbance is directly proportional to the concentration, where the path length and molar extinction coefficient is supposed to be constant for the particular measurement. The sources used for the UV and visible light are deuterium and tungsten lamps, respectively, and the detector used is usually a photomultiplier tube (PMT).

In the present study, UV-Vis spectroscopy measurements were carried out on a Jasco UV-Vis spectrophotometer (V570 UV-VIS-NIR) operated at a resolution of 1 nm at National Chemical Laboratory, Pune, INDIA.

2.6.2. Photoluminescence Spectroscopy

Photoluminescence (PL) is the spontaneous emission of light from a material under optical excitation. The appropriate excitation energy and intensity is required to choose to probe the sample's discrete electronic states accurately. When light of sufficient energy is incident on a material, photons are absorbed, electrons get excited and electronic transitions occur. Eventually, these excitations relax and the electrons return to the ground state. If radiative relaxation occurs, the emitted light is called PL. This light can be collected and analyzed to yield a wealth of information about the photo-excited material. The PL spectrum provides the transition energies, which can be used to determine electronic energy levels, defects and impurity states in the sample. The PL intensity gives a measure of the relative rates of radiative and non-radiative recombination. Please refer Figure 12 (a) to (d).

PL is divided into two categories, fluorescence and phosphorescence, depending upon the electronic configuration of the excited state and the emission pathway. Fluorescence is the property of some atoms and molecules to absorb light at a particular wavelength and to subsequently emit light of longer wavelength after a brief interval, termed the fluorescence

lifetime. The process of phosphorescence occurs in a manner similar to fluorescence, but with a much longer excited state lifetime. PL is a simple, versatile, and non-destructive measurement technique. The PL signal itself is characterized by two essential features: peak energy and intensity. The excitation energy and optical intensity can be chosen properly in order to yield more accurate information on the energy levels available to electrons in the material. The PL signal often depends on the density of photo-excited electrons and the intensity of the incident beam. The intensity of the PL signal depends on the rates of radiative and non-radiative events, which depend in turn on the density of non-radiative interface states.

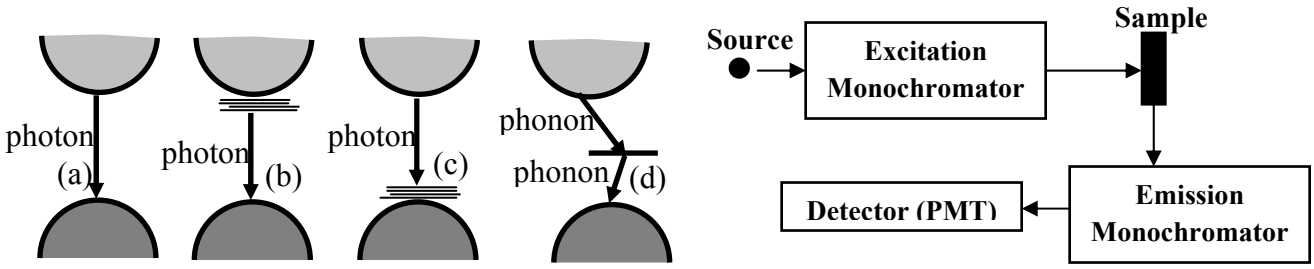

Figure 12. (a) CB to VB direct transition, (b) Donor states to VB, (c) CB to acceptor states, (d) Non-radiative recombination via intermediate states and Figure at right side shows: Schematic Layout of PL Set-up

Usually, defects and impurities break the periodicity of the lattice and perturb the band structure locally. This perturbation is attributed to the discrete energy levels lying within the band gap. Depending on the defect or impurity, the state acts as a donor or acceptor of electrons in the lattice. Surfaces and interfaces contain a high concentration of impurity or defect states. Dangling bonds at a semiconductor surface or defects give rise to electronic states within the

band gap. These mid-gap states fill up to the Fermi level with electrons that originate in the bulk of the material. The fundamental limitation of PL analysis is its reliance on radiative events. Materials with poor radiative efficiency, such as low-quality indirect band gap semiconductors, are difficult to study via ordinary PL. The PL measurements in this work were performed using LS 55 spectrophotometer at National Chemical Laboratory, Pune, INDIA.

2.6.3. Raman Spectroscopy:

When a beam of visible light is passed through a transparent substance, a small amount of the radiation energy is scattered, the scattering persisting even if all other extraneous matter are rigorously excluded from the substance. If monochromatic radiation is used, if the scattered energy will consist almost entirely of radiation of the incident frequency then it is so-called *Rayleigh scattering* but, in addition, certain discrete frequencies above and below that of the incident beam will be scattered, it is referred to as *Raman scattering*.

According to quantum theory of radiation, when photons having energy 'hν' undergo collisions with molecules, and if the collision is perfectly elastic, they will be deflected unchanged. A detector placed to collect energy at right angles to an incident beam will thus receive photons of energy 'hν', i.e. radiation of frequency 'ν'. However, it may happen that energy is exchanged between photon and molecule during the collision: such collisions are 'inelastic'. The molecule can gain or lose amounts of energy only in accordance with the quantam laws; i.e. its energy change, ΔE joules, must be the difference in energy between two of its allowed states. That is to say, ΔE must represent a change in the vibrational and/or rotational energy of the molecule. If the molecule gains energy ΔE, the photon will be scattered with the energy hν-ΔE and the equivalent radiation will have a frequency ν- ΔE/h. Conversely, if the molecule loses energy ΔE, the scattered frequency will be ν+ ΔE/h. Radiations scattered with a frequency lower than that of

the incident beam is referred to as Stokes' radiation, while that at higher frequency is called anti-Stokes' radiation. Since the former is accompanied by an increases in molecular energy (which can always occur, subject to certain selection rules) while the latter involves a decrease (which can only occur when the molecule is originally in an excited vibrational /rotational state). Stokes' radiation is generally more intense than anti-Stokes' radiation. Figure 13 shows schematic of Raman spectrometer.

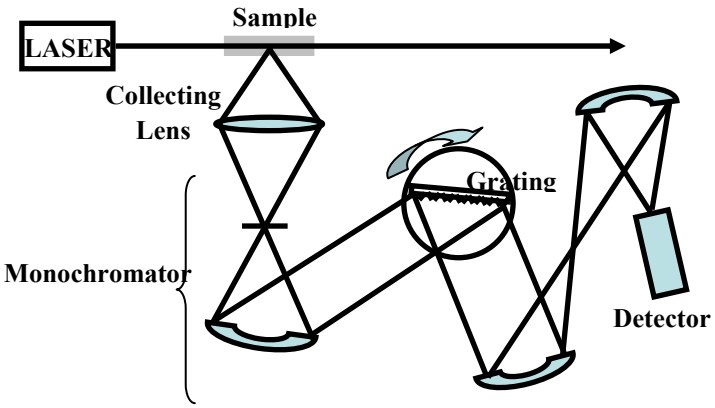

Figure 13. Schematic of Raman Spectrometer

A typical Raman Spectrometer consists of Laser beam (very narrow, monochromatic, coherent and powerful) which when passed through the cell, usually a narrow glass or quartz tube filled with the sample, light get scattered sideways from the sample, which is collected by a lens and passed into a grating monochromator. The signal is measured by a sensitive PMT and after amplification; it is usually processed by a computer which plots the Raman spectrum.

Raman spectroscopy measurements in the present work were done on Horiba Micro Raman at National Chemical Laboratory, Pune, India.

2.7. Dye sensitized solar cells characterization

2.7.1. Solar Simulator

A solar simulator (also known as artificial sun) is a device that provides illumination approximating natural sunlight. The purpose of the solar simulator is to provide a controllable indoor test facility under laboratory conditions used for the testing of solar cells, plastics, and other materials and devices.

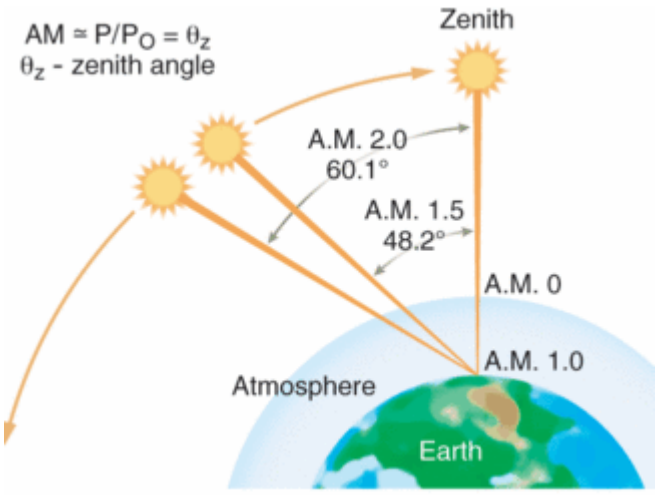

Figure 14. Air-Mass calculations for 1 Sun measurements

[http://www.optoiq.com/index/photonics-technologies-applications/lfw-display/lfw-rticle-display/286515/articles/laser-focus-world/volume-43/issue-3/features/photovoltaics-nhancements-enable-solar-simulators-to-shed-light-on-new-photovoltaic-designs.html]

The simulator starts with a xenon arc lamp with various output powers, with the illumination area ranging from 2 × 2 inch to 8 × 8 inch. For example, a 300 W, 2 × 2 in. solar simulator can provide output densities of up to 2800 W/m^2, or nearly three times the typical solar irradiance level at sea level with an AM equivalent of 1.0.

In Figure 14 the air-mass value AM 0 equates to isolation at sea level with the Sun at its zenith. AM 1.0 represents sunlight with the Sun at zenith above the Earth's atmosphere and absorbing oxygen and nitrogen gases. AM 1.5 is the same, but with the Sun at an oblique angle of 48.2º, which simulates a longer optical path through the Earth's atmosphere; AM 2.0 extends that oblique angle to 60.1º.

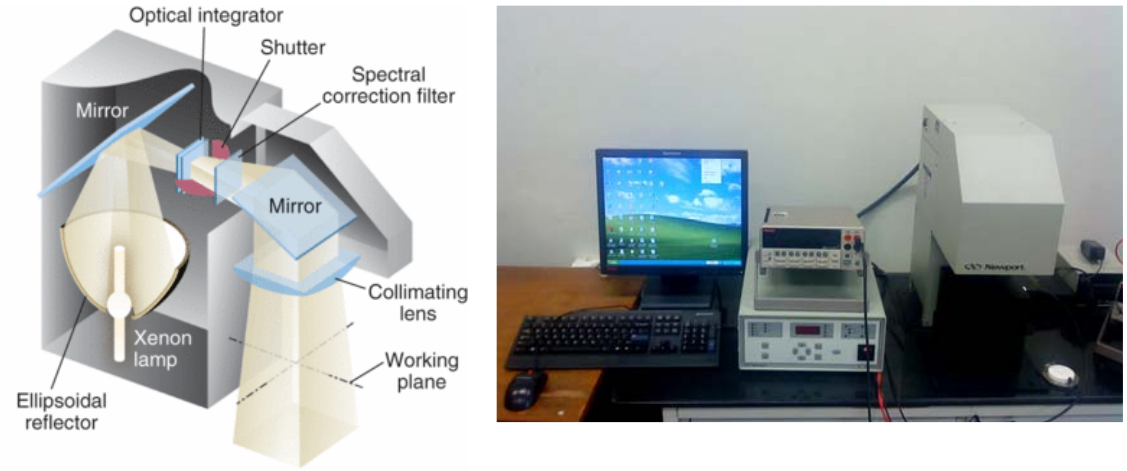

(a) (b)

Figure 15. (a) Schematic diagram of Solar Simulator and (b) Newport Solar Simulator with I-V measurement set up.
[http://www.optoiq.com/index/photonics-technologies-applications/lfw-display/lfw-rticle-display/286515/articles/laser-focus-world/volume-43/issue-3/features/photovoltaics-nhancements-enable-solar-simulators-to-shed-light-on-new-photovoltaic-designs.html]

The simulator also includes a control that allows the output levels to be increased or decreased while maintaining the proper spectral ratios necessary to simulate solar irradiance. An ellipsoidal reflector collects the lamp output, and a collection mirror directs the light through a single-blade shutter to an optical integrator that ensures uniformity variations of less than 2% across the

simulator's output beam. Beam uniformity is heavily dependent on two design considerations: proper alignment of the optical elements and the optical integrator. The integrator is a monolithic optic that effectively homogenizes the collimated light to within the uniformity values listed in international photovoltaic testing standards. The light then passes through the AM spectral-correction filter as shown in Figure 14.

I-V measurements-such as short-circuit current (I_{sc}), current density (J_{sc}), open-circuit voltage (V_{oc}), fill factor (FF), maximum output power (P_{max}) and current (I_{max}), voltage (V_{max}), and cell efficiency (η) require a reference-cell comparison to calculate the spectral-mismatch factors for different cells and test equipment configurations. A Newport Silicon Reference Cell is used as reference cell for optimization of solar simulator. The reference cell is connected to readout electronics that displays measured solar simulator irradiance and cell temperature. These values are entered as parameters in the I-V measurement software and are used to generate accurate and repeatable I-V performance. Proper integration between software, solar simulator, and reference cell is necessary to achieve accurate, repeatable data to calculate the solar cell efficiency. Once the solar simulator and other instruments are turned on and the cell is placed beneath the simulator, the software will open the solar-simulator shutter, sweep the voltage across the prescribed range, measure the current, and display the I-V curve. Then the software calculates the key solar cell parameters discussed previously, including the cell conversion efficiency.

2.7.2. Incident photon-to-current conversion efficiency (IPCE) Measurements

Another fundamental measurement of the performance of a solar cell is the "external quantum efficiency", which in the DSSC community is normally called the incident photon to current conversion efficiency (IPCE). The IPCE value corresponds to the photocurrent density produced

in the external circuit under monochromatic illumination of the cell divided by the photon flux that strikes the cell. From such an experiment the IPCE as a function of wavelength can be calculated from

$$IPCE = \frac{J_{SC}(\lambda)}{e\Phi(\lambda)} = \frac{1240\, J_{SC}(\lambda)\ [\mathrm{A\ cm^{-2}}]}{\lambda\ [nm] P_s(\lambda)\ [\mathrm{W\ cm^{-2}}]} \qquad (2.13)$$

where e is the elementary charge. IPCE values provide practical information about the monochromatic quantum efficiencies of a solar cell.

Figure 16. Newport IPCE setup

2.8. References

1. B. O'Regan, M. Gràtzel, *Nature*, **1991**, *353*, 737 – 740.
2. S.Muduli, O.Game, V.Dhas, A.Yengantiwar, S. B.Ogale, *Energy Environ. Sci*., **2011**, *4*, 2835-2839.
3. D. Chen, F .Huang, Y-B.Cheng, R. A.Caruso, *Adv. Mater.*, **2009**, *21*, 2206–2210.
4. D. Kim, A.Ghicov, S. P. Albu, P. Schmuki, *J. Am. Chem. Soc.* **2008**, *130*, 16454–16455.
5. E.Ghadiri,N. Taghavinia, S.M.Zakeeruddin,M.Gràtzel, J-E.Moser*, Nano Lett.,* **2010**, *10*, 1632–1638.
6. F.Gao,Y. Wang, D.Shi, J. Zhang, M.Wang,X. Jing , R. Humphry-Baker, P. Wang, S.M.Zakeeruddin, M. Gràtzel. *J. Am. Chem. Soc.*, **2008**, *130*, 10720–10728.
7. S.Ito, S. M. Zakeeruddin, R. Humphry-Baker, P. Liska, R. Charvet,P.Comte, M. K. Nazeeruddin,P. Péchy, M .Takata,H. Miura, S. Uchida, M.Grätzel, *Adv. Mater.*, **2006**, *18*, 1202–1205.
8. R. Argazzi , N-Y-M.Iha, H. Zabri,F.Odobel, C. A. Bignozzi*, Coordination Chem Rev*. **2004**, *248*,1299–1316.
9. R. Y.Ogura, S.Nakane, M.Morooka, M.Orihashi, Y. Suzuki, K. Noda, *Appl. Phys. Lett.*, **2009**, *94*, 073308.
10. N.A. Allegrucci, A.J. Lewcenko, L.Mozer, P. Dennany, D.L. Wagner, K. Officer, S. Sunahara, L. Mori, Spiccia, *Energy Environ. Sci.*, **2009**, *2*, 1069–1073.
11. D.Kuang, P.Walter, F.Nüesch, S. Kim, J. Ko, P. Comte, S.M. Zakeeruddin, M.K. Nazeeruddin, M.Grätzel, *Langmuir*, **2007**, *23*, 10906–10909.
12. Y. Chen, Z. Zeng, C. Li, W. Wang, X.Wang, B. Zhang, *New J. Chem.*, **2005**, *29*, 773-776.

13. M. Wu,X. Lin, T. Wang, J. Qiu, T. Ma, *Energy Environ. Sci.* **2011**.

14. A.Yella, H-W. Lee, H.N.Tsao, C. Yi, A.K. Chandiran, M.K. Nazeeruddin, E.D. Wei-Guang, C-Y.Yeh, S.M. Zakeeruddin, M. Grätzel, *Science,* **2011**, 3344.

15. M. D. McGehee , *Science*, **2011**, *334*, 607-608.

16. A. Stadler, *Materials***, 2012**, *5*, 661-683.

17. T. Minami, T.Miyata, T. Yamamoto, *Surface and Coatings Technology*, **1998**, *10*, 583–587.

18. B. O'Regan, M. Grätzel, *Nature*, **1991**, *353*, 737–740.

19. K Keis, E.Magnusson, H. Lindstrom, S.E. Lindquist, A. Hagfeldt, *Solar Energy Materials and Solar Cells* , **2002**,*73*,51–8.

20. M.Saito, S. Fujihara, *Energy Environ. Sci.,* **2008**, *1*, 280–3.

21. E. Ramasamy, J. Lee, *J. Phys Chem. C*, **2010**, ***114***, 22032–7.

22. G.A Parks., *Chem Rev*., **1965**, *65*,177–98.

23. L.Huang, L. Jiang, M. Wei, *Electrochem. Comm.*, **2010**, *12*, 319–22.

24. M. Law, L.E.Greene, J. Johnson, R. Saykally, P. Yang , *Nat Mater*, **2005**,*4*,455–9.

25. ANM. Green, E. Palomares, S.A Haque, J.M Kroon, J.R. Durrant., *J. Phy. Chem. B* **2005**,*109*, 12525–33.

26. X.Chen, S.S.Mao, *Chem. Rev.* , **2007**, *107*, 2891-2959.

27. P. Tiwana,; Docampo, M.Johnston, H. Snaith, L.M. Herz, *ACS Nano,* **2011**, *5*, 5158.

28. K. Park, Q. Zhang, D. Myers, G. Cao, *ACS Appl. Mater. Interfaces* **2013**, *5*, 1044−1052

29. G. W. Morey*, J. Am. Ceram. Soc.,* **1953**, *36*, 279.

30. L. G. Benning and T. M. Seward, *Geochim Cosmochim Acta* ,**1996**, *60*, 1849.

31. O. F. Tuttle, *Amer. J. Sci.*, **1948**, *246*, 628.

32. J. Gopalakrishnan, *Chem Mater*, **1995**, *7*, 1265.

33. L. G. Hubert-Pfalzgraf, S. Daniele, J.M. Decams, *J. Sol-Gel Sci. Technol.*, **1997**,*8*, 49.

34. X. Wang, Z. Zhang, S. Zhou, *Mater. Sci. Eng. B: Solid-State Mater. Adv. Technol*., **2001**, *B86*, 29.

35. S. Ito , T. N. Murakami , P. Comte, P.Liska, C. Grätzel ,M. K. Nazeeruddin, M. Grätzel, *Thin Solid Films*, **2008**, *516* ,4613–4619

36. S. Hwang, J. H. Lee, C. Park, H. Lee, C. Kim, C. Park, M.-H.Lee, W. Lee, J. Park, K. Kim, N.-G. Park, C. Kim, *Chem.Comm*. **2007**, 4887.

37. S. Ito, H. Miura, S. Uchida, M. Takata, K. Sumioka, P. Liska, P.Comte, P. Pechy, M. Gratzel, *Chem. Comm*. **2008**, 5194

38. H. Choi, C. Baik, S. O. Kang, J. Ko, M.-S. Kang, M. K. Nazeeruddin, M. Gratzel, *Angew. Chem*. **2008**, 120, 333

39. S.-L. Li, K.-J. Jiang, K.-F. Shao, L.-M. Yang, *Chem. Comm*., **2006,** 26, 2792–2794.

40. K. Hara, M. Kurashige, S. Ito, A. Shinpo, S. Suga, K. Sayama, H. Arakawa, *Chem. Comm*., **2003**, 2, 252–253.

41. G. Calogero, G.D. Marco, S.Caramori, S.Cazzanti, R. Argazzi, C. Bignozzi, *Energy Environ. Sci.*, **2009**, *2*, 1162–1172.

42. S Y Huang, G Schlichthorl, A J Nozik, M Gratzel, A.J Frank, *J. Phy Chem B.*, **1997**,*101*, 2576–82.

43. N .Kopidakis, N.R. Neale, A.J.Frank, *J. Phy Chem B.,***2006**, *110*, 12485–9.

44. E. Figgemeier, A. Hagfeldt., *Inter. J. Photoenergy.,* **2004**,*6*,127–40.

45. Z. Zhang, N.Evans, S.M. Zakeeruddin, R. Humphry-Baker, M. Gratzel, , *J. Phy Chem C* **2007**,*111*,398–403.

46. S.M. Zakeeruddin, M.Gratzel, *Adv.Funct. Mat.* , **2009**, *19*, 2187–202.

47. S. R. Raga,E. M. Barea, F. Fabregat-Santiago *, J. Phys. Chem. Lett.* **2012**, *3*, 1629−1634

48. T. Daeneke, Y. Uemura, N.W.Duffy, A.J. Mozer, N. Koumura, U. Bach, L.Spiccia, *Adv.Mater*, **2012**.

49. N. Papageorgiou, W. F. Maier, M. Gratzel, *J. Electrochem. Soc.* , **1997**, *144*,876

50. M. Ikegami, K. Miyoshi, T. Miyasaka , K. Teshima, T. C. Wei,C. C. Wan, and Y. Y. Wang, *Appl. Phys. Lett.* , **2007**, *90*, 153122.

51. Y. Jun, J. Kim, M. G. Kang, *Sol. Energy Mater. Sol. Cells*, **2007**, *91*, 779.

52. M. Wu , T. Ma, *ChemSusChem* , **2012**, *5*, 1343 – 1357.

53. M. Wu, X. Lin, T. Wang, J. Qiu , T. Ma, *Energy Environ. Sci.*, **2011**, *4*, 2308–2315.

54. W. J. Lee, E. Ramasamy, D. Y. Lee, J. S. Song, *ACS Appl. Mater. Interfaces* , **2009**, *1*, 1145.

55. J. D. Roy-Mayhew, D. J. Bozym, C. Punckt, I. A. Aksay, *ACS Nano*, **2010**,*4*, 6203.

56. E. Ramasamy, J. Lee, *Carbon*, **2010**, *48*, 3715

57. Arango A C, Johnson L R, Bliznyuk V N, Schlesinger Z, Carter S A, Horhold H H, *Adv Mater*, **2000**,*12*,1689–92.

58. Calandra P, Calogero G,Sinopoli A, Gucciardi P G, *Catalyst,* **2010**;*3*:4a.

59. H.K. Mulmudi,S. K. Batabyal, M. Rao,R. R. Prabhakar, N. Mathews, Y- M Lam and S. G. Mhaisalkar, *Phys. Chem. Chem. Phys*., **2011**, *13*, 19307–19309

60. D. Dijkamp, T. Venkatesan, X. D. Wu, S. A. Shaheen, N. Jisrawi, Y. H. Min-Lee, W. L. McLean, M. Croft, *Appl. Phys. Lett*., **1987**, *51*, 619.

61. B. D. Cullity, *Elements of X-ray Diffraction*, 2nd ed., *Addison-Wesley*,**1978**.

62. G. Thomas, *Transmission Electron Microscopy of Metals*, John Wiley & Sons

Inc., New York **1972**, 274.

63. X. Z. Li, *Ultramicroscopy*, **2004**, *99*, 257.

Chapter 3

DSSC Device Fabrication: Development of Methodology for the realization of high conversion efficiency

This chapter deals with making of small area DSSC devices. The full DSSC device fabrication protocol, including making of slurry used for photoanode construction, photo-anode fabrication, dye loading, electrolyte preparation and incorporation, making of counter electrode, is explained in detail. The best efficiency achieved in laboratory on a 0.25 cm^2 device using the above mentioned materials is demonstrated to be 9.4%. Use of different morphologies for the DSSC photoanode and the corresponding implications for the performance are also highlighted. Finally, the scaling up issues for large area solar cells and the related different device architectures are discussed and illustrated.

3.1. Introduction

Fairly efficient photovoltaic conversion combined with ease of manufacturing and low production costs makes the DSSC technology an attractive approach for small as well as large-scale solar energy conversion.[1] The fundamental research work on the improvement of DSSC performance involves making of highly porous electronically interconnected nano-crystalline TiO_2 films, employing high molar extinction coefficient dyes as sensitizers, application of light harvesting layer on the top for full utilization of the incident light, reducing recombination effects between the photo-generated electrons and holes, reducing various interface resistances etc.

Fabrication of an effective dye sensitized solar cell architecture, which involves several steps, is central to the realization of a high solar cell performance. This chapter elaborates on this fabrication process that is developed in the laboratory as part of this thesis work to optimize the performance of the dye sensitized solar cells by examining and fine tuning the various aspects pertaining to the cell architecture.

3.2. Preparation of Photoanode

3.2.1. Choice of substrate. FTO coated glass

The bottom electrode substrate used is a transparent conducting oxide (TCO) coated glass. TCO material usually used is Fluorine doped Tin Oxide (FTO) or tin doped indium oxide (ITO). FTO substrate is preferred over ITO for photoanode due to its better thermal stability (stable upto 500^{o}C). The FTO substrate chosen should have low sheet resistance (10-15 Ω /□) as this is where the electrons reach after travelling through TiO_2 nanoparticle network. Along with the conductivity, transparency of this substrate is also very crucial. Light has to pass through this

substrate and reach TiO_2 active layer which loaded with dye molecules which in turn generates photo-electrons. The transmittance of this FTO substrate is > 80%. Thus transparency and conductivity of this substrate are crucial while making the choice of substrate.

3.2.1.1. FTO Glass Cleaning. FTO glass was cut into 2x2 cm square pieces. Cleaning of these FTO substrates is important in order to remove any organic or inorganic contaminants on its surface which in turn enhances the adhesion of subsequent layers to be deposited over it. The cleaning protocol pursued is as follows:

- Sonicate in soap solution for 15 minutes
- Rinse with deionized water
- Sonicate in deionized water for 15 minutes
- Sonicate in ethanol for 15 minutes

3.2.2. Blocking layer of TiO_2.

The photoanode made of nanoporous TiO_2 active layer provides high surface area that is important for efficient photon-to-electricity conversion as it enhances dye loading and solar light absorption.[2] However, unfortunately it also provides abundant openings through the active layer to the bare FTO substrate, where the photo-injected electrons may recombine with I_3^-species in the redox electrolyte ($2e^- + I_3^- \rightarrow 3I^-$).[3-4] This recombination will cause the loss of the photocurrent thus decreasing the solar cell performance. The introduction of a compact layer between the interface of FTO and nanoporous TiO_2 has been proven theoretically and practically to be effective in blocking the electron recombination via this undesirable indirect route.[5-7] This compact layer is thus much denser than the nanoporous TiO_2 active layer. Semiconductors such

as TiO_2,[8] Nb_2O_5,[9] ZnO [10] etc. have been effectively used as blocking layer materials in DSSCs. Amongst them, the compact TiO_2 layer is the most suitable candidate. Besides the blocking effect, higher density of the compact layer, together with larger contact area and improved adherence between the TiO_2 layer and FTO surface provides more electron pathways from TiO_2 to FTO for photo-generated electrons, which facilitates electron transfer and subsequently improves the electron transfer efficiency. The procedure for making this blocking layer is described in detail here.

The cleaned substrate is heated for 15 min at 450ºC to remove the residual organic contaminants and then the blocking layer is deposited. The deposition of the blocking layer involves two steps:

1. Preparation of blocking layer solution: To prepare blocking layer solution, Titanium tetraisopropoxide (TIP, Aldrich) (1 mL) is added in the mixture of ethanol (5 mL) and acetic acid (0.5 mL) and sonicated for 5 minutes.
2. Spin coating and annealing: Washed FTOs are masked at both ends with scotch tape leaving the desired area in between as open. Blocking layer solution is spin coated on the exposed area at 2500 rpm for 1 minute. The scotch tape is removed and the films are then sintered at 450°C for 1 hour, which results in the formation of the compact TiO_2 layer.

3.2.3. TiO_2 paste making Protocol

In the beginning a doctor blading paste making protocol (**Protocol 1**) was followed which gave an efficiency of the range 4-6%. Blade coating of the film was followed by a post $TiCl_4$ treatment to improve the adhesion of the film and also to increase the surface roughness of the TiO_2 particles. But in order to further increase the efficiency of the DSSCs, the Screen printing

paste making protocol (**Protocol 2**) was subsequently followed. This gave us an efficiency of ~9-10%.[11] In the course of working on these two procedures we developed some of our protocols independently in order to match our experimental conditions. To master the art of film making and assembly of the cell, we first worked with the commercially available Degussa P25 TiO_2 powder. Later the same process was extended to the lab-made hydrothermal or solvothermal TiO_2 powders.

3.2.3.1. Protocol I

Degussa P25 powder contains a mixture of 70% anatase and 30% rutile TiO_2 nanoparticles. The primary particle size of the nanoparticles is around 25 nm, but they form aggregates of > 100 nm size. To prepare the slurry this powder (0.5g) was ground in an agate mortar with small amount of water (0.5ml) and dilute acetylacetonate (Merck) (~0.8ml) to prevent re-aggregation of the particles. Other additives such as dilute acid (dilute (0.05M) HNO_3 0.25ml) to modify the TiO_2 surface with H^+ ions and binding agents (Polyethylene glycol 0.25gm of molecular weight 10,000, Aldrich) were found to be suitable as well. Small amount of Triton X-100 (Merck) (about 50µl) which is a very good surfactant (and which lowers the surface tension between the solvents used and TiO_2 nanoparticles) was also added to facilitate the spreading of the colloid on the substrate. To produce uniform films from this paste, "Doctor Blade" coating method was used. In this method, first an FTO coated glass substrate is masked with two scotch tapes (~25-30 micrometer thick). This creates an area as well as controls the thickness of the TiO_2 film. The remaining, non-coated part of the substrate provides area for electrical contact. The prepared slurry is applied to one of the edges of the conducting glass and is spread over to the other end using a glass side or blade. The coated film is allowed to air dry for 10 minutes and then heated

for 10 min at 450 ^{0}C. The resulting film thickness is around 6-7 µm. This process is repeated to get a film of 12-15 µm thickness. After air drying the electrode is fired for 60 min at 450 ^{O}C.

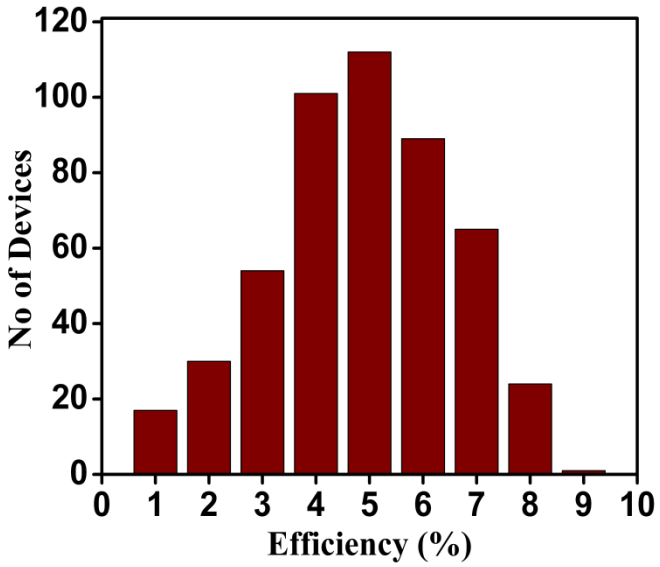

Figure 1. Graph showing statistics of efficiency vs number of devices for solvothermally synthesized TiO_2 NPs cell prepared by protocol 1

This is followed by post $TiCl_4$ treatment that which is discussed in the next section. The doctor bladed films are soaked in a dye solution for 24 hrs giving rise to a dyed, purple color film which is then assembled with the cathode and later with the electrolyte for solar cell characterization. The dye used here is Ruthenium based N719 dye and electrolyte is iodide /tri-iodide. Figure 1 shows the statistics for efficiency of cells prepared by this method. It is clear from the graph that this efficiency is in the range 4-6%.

3.2.4. Post $TiCl_4$ treatment

For post $TiCl_4$ treatment, blade coated TiO_2 films annealed at 450^oC are dipped in 40mM $TiCl_4$(Spectrochem) solution (0.55ml of $TiCl_4$ in ice made from 100ml DI water, ice is allowed to melt to a get a colorless $TiCl_4$ solution in water.) at 70^oC for 30mins. The films are washed with water and ethanol and then dried in air. After this they are again annealed at 450^0C for 30min. The effect of this $TiCl_4$ treatment was studied in detail using various characterization techniques. FESEM was used to study the surface modifications; the Current Perpendicular to Plane (CPP) measurement was performed to study the inter-particle connectivity as well as adhesion of the TiO_2 film onto the conducting substrate. AFM study was used to study the nanoscale morphology of the film after $TiCl_4$ treatment. To study the effect of $TiCl_4$ treatment on various interfaces of DSSC Electrochemical Impedance Spectroscopy (EIS) measurements were also performed. However, this part is discussed in detail in chapter 4.

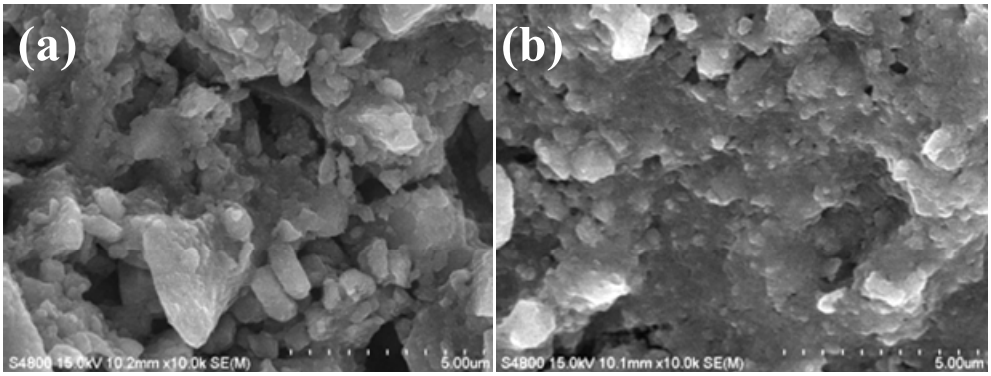

Figure 2. The FESEM images of the untreated and $TiCl_4$ treated films.

The FESEM images in Figure 2 explain that after $TiCl_4$ treatment there is a coating of a layer of TiO_2 on the already existing TiO_2 which gives the film a compact nature and induces good necking between the TiO_2 particles. This reduces the porosity of the film but at the same time

improves the interconnectivity between particles so as to reduce hopping of electrons within film. Solar cell characterization results of the films with and without $TiCl_4$ treatment are shown in Figure 3(a). The efficiency for the $TiCl_4$ treated films is considerably higher as compared to untreated ones. The open circuit voltage for the treated film is high showing lower rate of recombination in this case as compared to the untreated film. The current density shows a drastic increase from 10 mA/ cm^2 to16.5 mA/cm^2 in case of with $TiCl_4$ treated films.

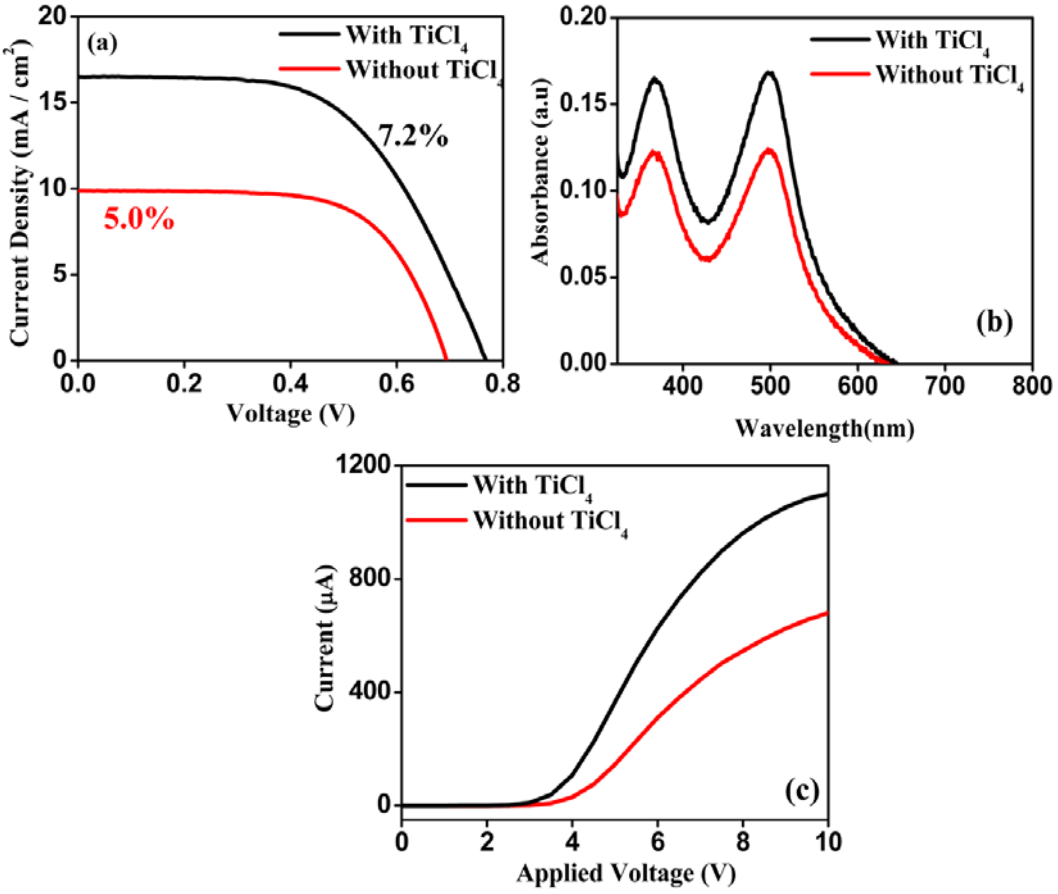

Figure 3. (a) IV Data, (b) Dye Loading Data, and (c) Current Perpendicular to Plane (CPP) I-V measurement results

This is attributed to improved dye loading seen in treated films. The calculated dye loading from the optical data is shown in Figure 3(b). It is found to be 6×10^{-8} and 5×10^{-8} mol/cm^2 for the

treated and untreated films, respectively. The significant enhancement in dye loading for $TiCl_4$ treated case is attributed to increased surface area and roughness factor due to formation of the additional thin layer of tiny TiO_2 nanoparticles on and within the film.[12]

To study the effect of $TiCl_4$ treatment on the overall conductivity of the film, Current-perpendicular-to-plane (CPP) conductivity measurements of films were done before dye loading (i.e. after annealing at 450 ^{0}C) using aluminium top electrode as shown in Figure 3 (c). The voltage was swept from 0 V to 10 V in steps of 0.5 V and a delay of 0.5 sec. It was seen that for the films treated with $TiCl_4$ the current is almost twice compared to the untreated case. This shows that $TiCl_4$ treatment improves the necking between the particles, thereby reducing the recombination during hopping of electrons and also the grain boundary defects which act as recombination centers for the same. The thin layer of TiO_2 formed by the $TiCl_4$ treatment within the working electrode as well as on the surface is highly pure which contains no impurities.[13] It also masks the impurities within the film if present thus helping in improving the overall conductivity of the cell.

Figure 4 shows the results if scanning probe microscopic studies on bare and $TiCl_4$ treated TiO_2 film. These measurements were carried in high vacuum conditions (10^{-6} torr) using SPM 100 (RHK Technologies.) The AFM studies were carried in contact mode using a cantilever of spring constant 0.2 N/m. The force distance (F-D) curve for $TiCl_4$ treated films resembles the F-D curves commonly observed on firm surfaces compared to diffused curve observed on untreated films. These results clearly indicate surface modification with a fair increase in surface properties leading to higher compactness after $TiCl_4$ treatment.

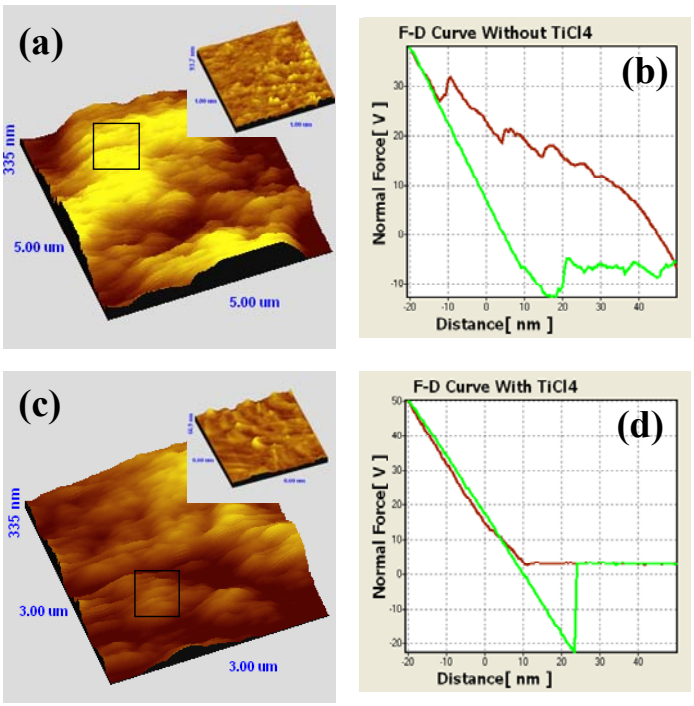

Figure 4. (a, b) AFM Topography of untreated and treated films (c, d) F-D Curves for untreated and treated films

Thus the $TiCl_4$ treatment mainly helps in improving the surface quality (in terms of compactness an adhesion) and area, as well as electrical quality of the TiO_2 films, thereby improving the dye loading and the current density of the cells as well.

In order to further improve the efficiency of DSSCs a new protocol for making of TiO_2 pastes was followed. Seigo Ito et al. have developed the screen printing paste making procedure to develop good quality films.[14] This is referred to as Protocol II which is discussed next section.

3.2.3.2. Protocol II

This procedure involves using of ethyl cellulose (Viscosity 100.000cps, Aldrich) and alpha terpineol (97+%, ACROS) as binder and surfactant, respectively, instead of PEG and Triton – X.[5] In our optimization work using this protocol the commercially available TiO_2 was used (TiO_2 Nanopowder, 21nm particle size, >= 99.05% trace metal basis, Aldrich). Below is the flow chart showing the procedure details.

Mix TiO_2 powder (6gms) and acetic acid (1ml) in agate mortor for 15 mins

↓

Add D.I water (1ml) to it and grind for 1 min, repeat this step for 5 times

↓

Add ethanol (1ml) to it and grind for 1 min, repeat this step for 15 times

↓

Again add acetic acid (1ml) in agate mortor for 3-4 mins

↓

Add ethanol (2.5ml) and grind for 1 min, repeat this step for 6 times

↓

Transfer paste into a beaker add 100ml ethanol to it

↓

Stir using magnetic stirrer for about 2 hours

↓

Sonicate using ultrasonic horn 5 seconds work and 5 seconds rest x 30 times

↓

Add 21.34ml terpeniol

↓

Stir on magnetic stirrer for 20 mins followed by
Sonication using ultrasonic horn 5 seconds work and 5 seconds rest x 30 times

↓

Add 3gm ethyl cellulose dissolved in 30ml ethanol

↓

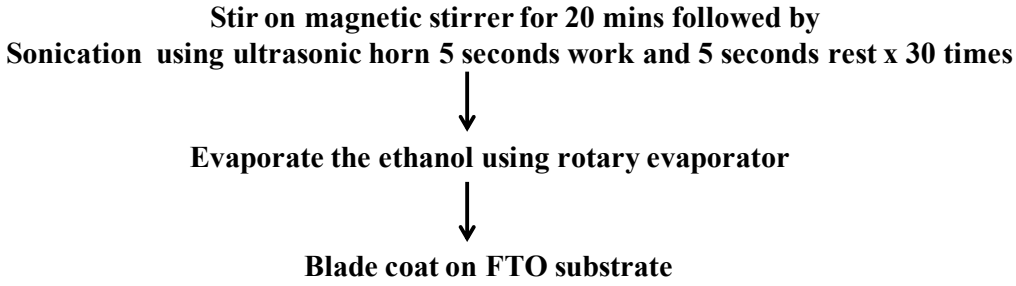

Figure 5. Flow chart showing protocol II

In this procedure the heating protocol followed was also slightly different. A slow programmed heating procedure was followed.

200^0C for 10 min ⟶ 325^0C for 5 min ⟶ 375^0C for 5 min ⟶ 450^0C for 15 min ↓ 500^0C for 15 min

This was followed by usual post $TiCl_4$ treatment (heating at 70^oC for 30min and annealing at 450^oC for 30 min). The films made by this protocol are transparent / semitransparent with improved adhesion with the FTO substrate. Images in Figure 6 show the DSSC photoanode made from this protocol. Figure 7 shows the statistics for efficiency of cells prepared by this method. It is clear from the graph that the efficiency achieved with this protocol is in the range 7-9%. It would be worth to mention that DSSCs made with protocol 2 but with P25 powder also gave good efficiency of 7%.

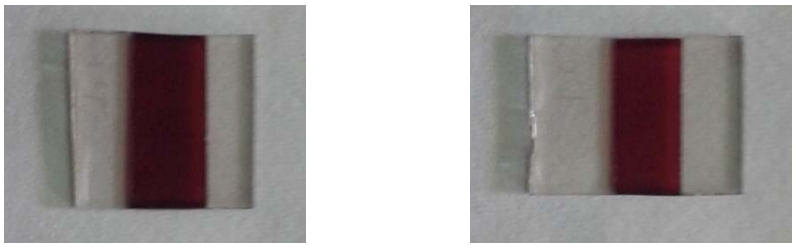

Figure 6. Dye loaded TiO_2 photoanodes

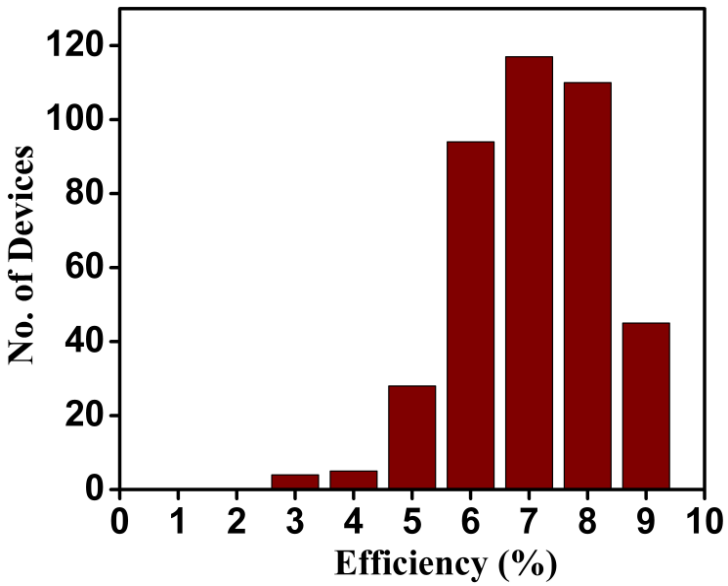

Figure 7. Graph showing statistics of efficiency vs number of devices for solvothermally synthesized TiO_2 NPs cell prepared by protocol 2

3.2.5. Preparation of Dye

Various Ru-metal based (e.g. N3, N719 or black dye) and organic dyes (phenothiazine based, C101 dye) can be used as sensitizers.

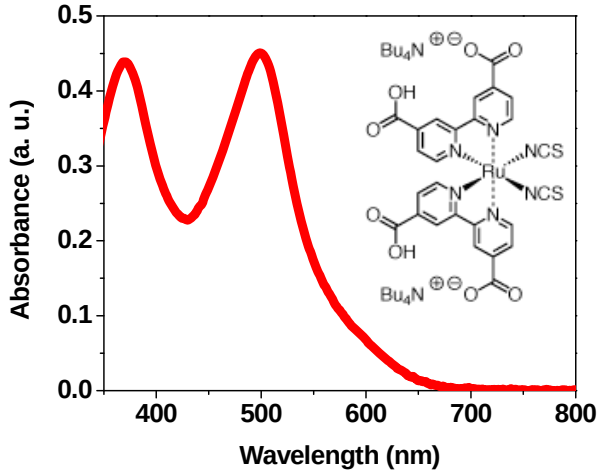

Figure 8. UV –Vis absorption spectra of N719 dye along with its structure

But the most efficient and easy to use is the ruthenium N719 dye. Ruthenium N719 dye was used as a sensitizer in all the thesis work. Dye solution was prepared in tertiary butyl alcohol and acetonitrile solvents (50/50 ratio v/v). Concentration of the dye solution was 0.5mM. The dye was procured from Solaronix.

3.2.6. Calculations for dye loading

The amount of dye loaded on the TiO_2 film is very important as it directly affects the cell performance. It mainly depends on the TiO_2 film thickness, the surface properties of TiO_2 nanoparticles, its surface area, morphology etc. The amount of dye loaded on a TiO_2 film can be quantitatively determined by detaching this dye using KOH (10^{-3}M) solution and recording a simple UV-Vis data of that solution.[15] Dye loaded film is dipped in above mention KOH solution for 12 hours so as to detach all the dye. Finally the dye loading is calculated using the formula

$A = \varepsilon cl$ equation, we can calculate the dye loading,

Where A= Absorbance

ε = Molar extinction coefficient (14×10^3 $M^{-1}cm^{-1}$ for N719 dye)

l = UV-Vis cell length (generally 1cm)

c = concentration of dye in solution to be found out

3.2.7. Preparation of electrolyte

The electrolyte used was I^-/I_3^- redox shuttle. The typical concentration of the electrolyte is as follows: 1(M) 1-propyl-2, 3-dimethyl-imidazolium iodide, 0.05 (M) LiI, 0.05 (M) I_2, and 0.5 (M) 4-tertbutylpyridine in acetonitrile/valeronitrile solution (v/v 1:1). Care should be taken to avoid any moisture contamination. As discussed in the previous chapter the concentration of various

components involved in the electrolyte is crucial. The above mentioned concentrations are optimized for our set of experiments.

3.2.8. Preparation of counter electrode

Counter electrodes in dye sensitized solar cells (DSSCs) are key players in determining the efficiency of energy conversion and thus a lot of efforts are put into the designing of such electrodes. Till date Pt is considered as the best candidate for counter electrode material. For this thesis work counter electrode was prepared by drop casting 0.6M H_2PtCl_6 ethanolic solution on FTO. It was allowed to dry for few minutes and then fired at 450^0C for 15min.

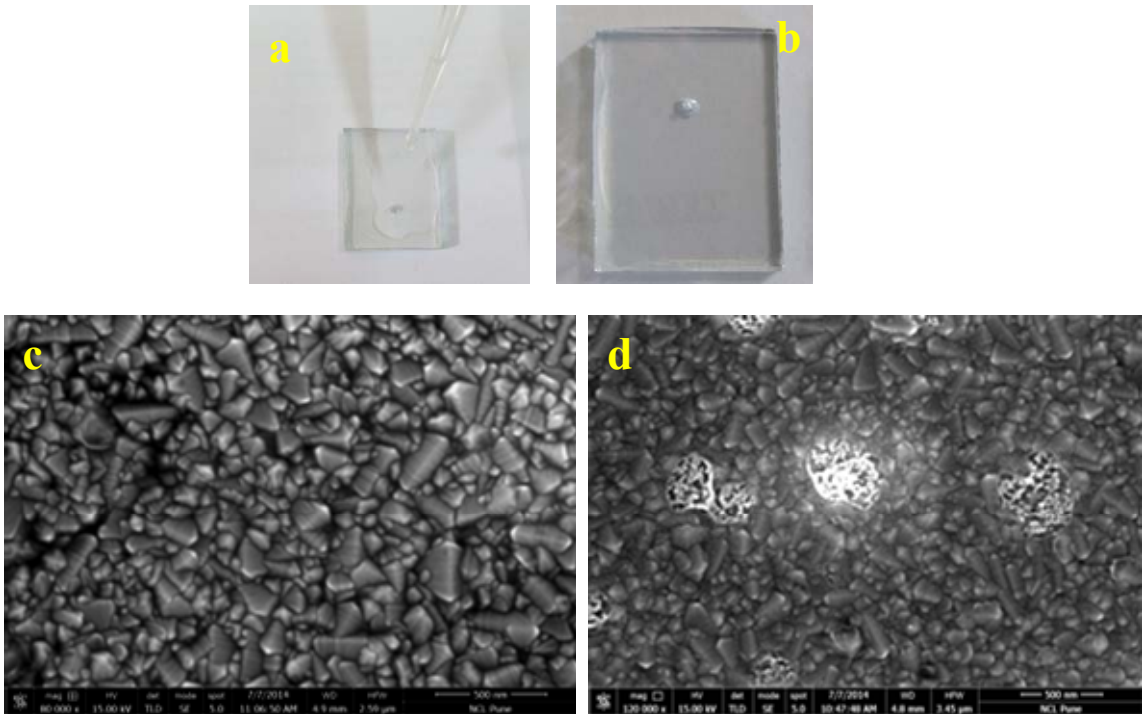

Figure 9. Images of Pt counter electrode (a,b) and FESEM images of (c) bare FTO and (d) Pt coated FTO.

3.3. Use of light harvesting over-layer

In DSSCs, the porous electrode composed of anatase phase TiO_2 nano-crystals (~20 nm) is essential due to its high internal surface area which maximizes the uptake of the dye molecules, thereby giving rise to DSSCs with large current density and high photon-to-current conversion efficiency.[16-18] However, such TiO_2 nano-crystal films usually show high transparency and negligible light scattering due to the small particle size and this results in poor light-harvesting capability.[19-21]An approach to enhance this capability of the TiO_2 electrodes, without sacrificing the accessible surface for dye loading, sub micrometer-sized TiO_2 particles with abundant mesopores are used.[22]

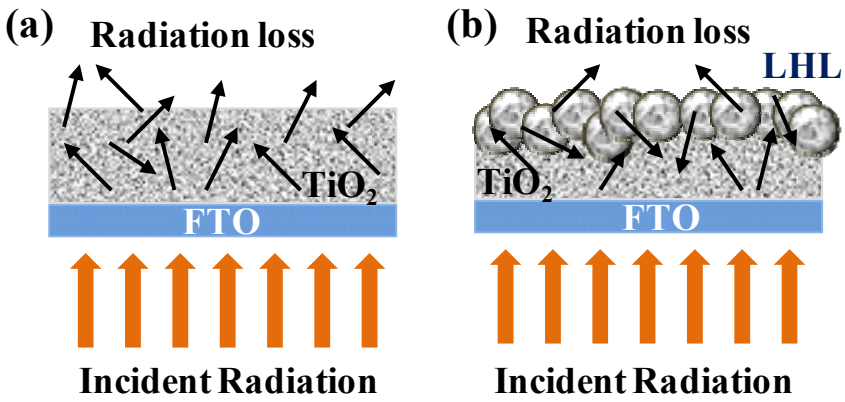

Figure 10. Effect of Light Harvesting Layer

Figure 10 shows the advantage of using the light harvesting layer (LHL) in the fabrication of DSSC photoanode. According to Mie theory the scattering of light by spherical particles largely depends on the particle size and wavelength of incident radiation. The resonant scattering of light may occur when the particle size is comparable to the wavelength of incident light. The submicron sized TiO_2 morphologies can therefore scatter light more efficiently thereby

increasing the light harvesting ability of the entire photoanode. The light scattering by these submicron sized particles extends the distance that light travels within the photoanode film and provides the photons with more opportunities to be absorbed by the dye molecules i.e the path length of light is increased.

3.3.1. TiO_2 Nanobeads (NBs) as light harvesting over-layer

3.3.1.1. Experimental.

TiO_2 nanobeads were synthesized by following the work of Curaso *et al*.[23] which involved sol gel process followed by solvothermal synthesis. In brief, Hexadecylamine (HDA) was used as a surface directing agent which was added to titanium butoxide to yield high surface area porous beads. HDA was dissolved in ethanol, followed by the addition of KCl solution (0.1 M). TIP was added to this solution under vigorous stirring at ambient temperature. The resulting white TiO_2 suspension was kept static at the same temperature for 18 h, The TiO_2 beads were then collected by centrifugation, washed with ethanol three times and dried in air at room temperature. In order to obtain the mesoporous TiO_2 beads with a highly crystalline framework, a solvothermal process was used. Few grams quantity of the amorphous TiO_2 beads was dispersed into a mixture of (2:1) ethanol and deionized water, and then different amounts of 25% ammonia solution were added. The mixtures were sealed within a Teflon-lined autoclave (50 mL) and heated at 160^0C for 16 h. The solid products were collected by filtration, washed with ethanol, and dried in air at room temperature. The resultant powders were calcined at 500^0C for 2h in air to remove organic components.

3.3.1.2. Characterization of TiO_2 Nanobeads

FESEM and TEM images were recorded for the determination of morphology. The above synthesized TiO_2 nanobeads were used for further characterization. Figure 10 (a), (b) show the FESEM images of TiO_2 nanobeads. The FESEM images of the nanobeads show the individual bead size of 200-300 nm made up of granular 10-20 nm sized TiO_2 nanoparticles. The TEM images seen in Figure 10 (c) to (e) also show that the beads are made up from interconnected small granular TiO_2 particles (10-20 nm) exhibiting their porous nature.The lattice fringes in the Figure 10 (e) show the crystalline nature of the nanoparticles forming the nanobeads.

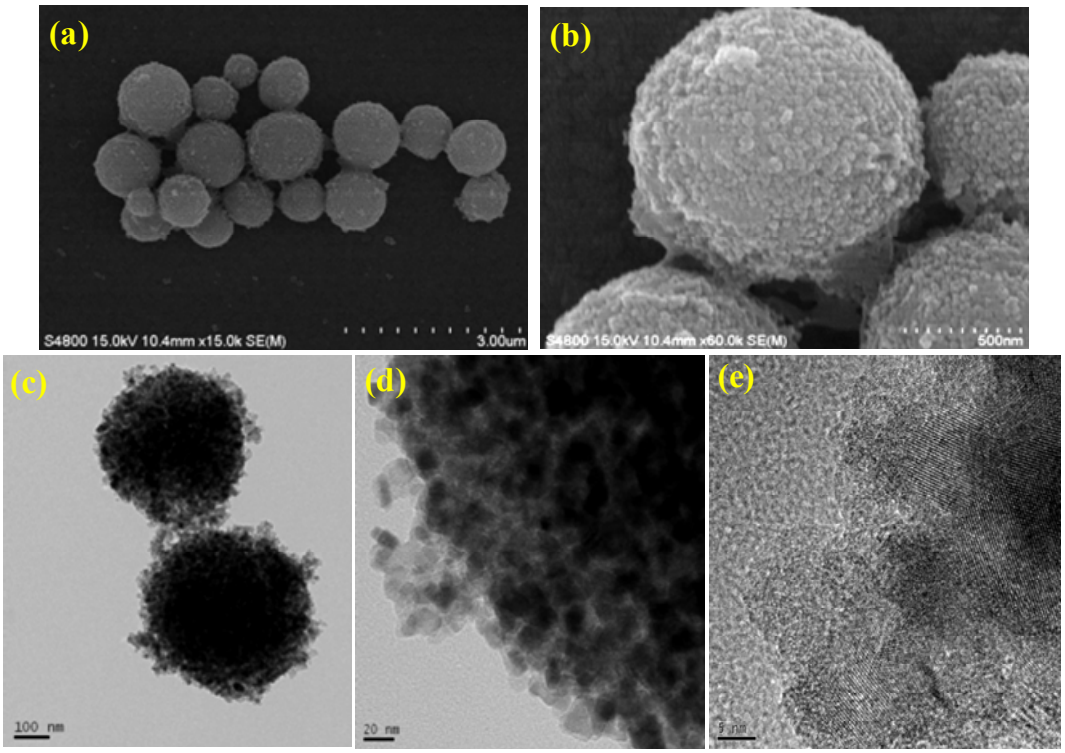

Figure 11. FESEM images (a) and (b), TEM images (c), (d) and (e) of TiO_2 nanobeads

3.3.1.3.XRD

The x-ray diffraction (XRD) pattern of the TiO_2 nanobead powder shows pure anatase phase as seen in Figure 12. The crystal size estimated from the full width at half maximum of the (101)

peak using the Scherrer equation indicates that these TiO_2 nanocrystals are (10-12nm) in diameter, in a good agreement with that measured from TEM images.

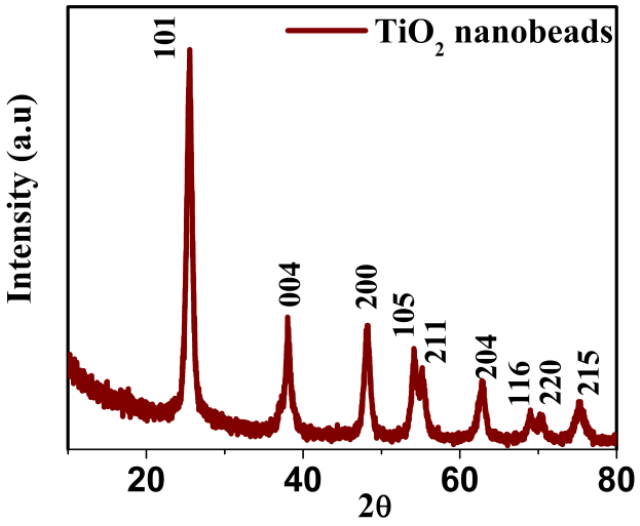

Figure 12. XRD data of TiO_2 nanobeads

3.3.1.4. Solar Cell Characterization

A paste of these nanobeads was prepared by using protocol II. These TiO_2 nanobeads (NBs) are used as light harvesting overlayer, over the transparent 10-12 micron thick layer of 20 nm sized TiO_2 nanoparticles (Nps) making the final thickness in both the cases (i.e with and without light harvesting layer) to 15 microns. In order to study the effectiveness of these TiO_2 nano-beads as light harvesters % R (Diffuse reflectance) measurements were made for the films coated with only transparent TiO_2 paste, only nanobeads, and transparent TiO_2 NP layer with nanobeads as overlayer. Figure 13 shows the reflectance data for all the three cases. TiO_2 nanoparticle film being transparent shows very little reflection as almost all the light is transmitted through the film. Compared to TiO_2 Nps, the films composed of meso-porous TiO_2 NBs exhibit better reflection capabilities in the visible and near infrared regions (from 450 to 800 nm) indicating

that the incident light is significantly scattered within the film of mesoporous TiO_2 beads due to the bead size being comparable to the wavelength of visible light. These NBs can thus be used to make a film as a light harvesting overlayer on Nps to improve the performance of the DSSC, as shown in Figure 14.

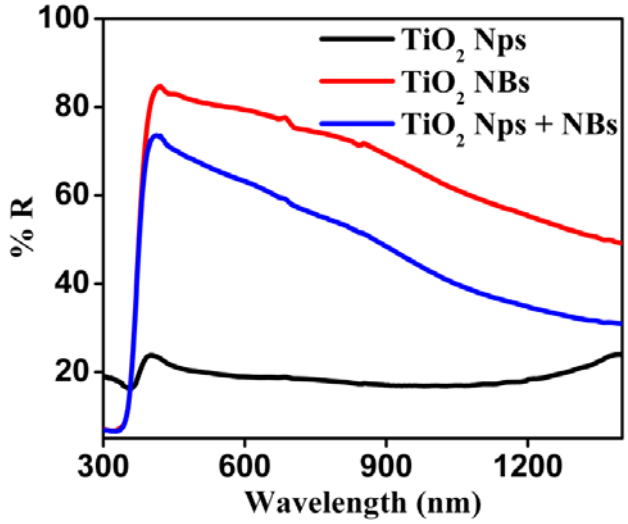

Figure 13. %R (Diffuse Reflectance) data for TiO_2 Nps, TiO_2 NBs and TiO_2 Nps+NBs

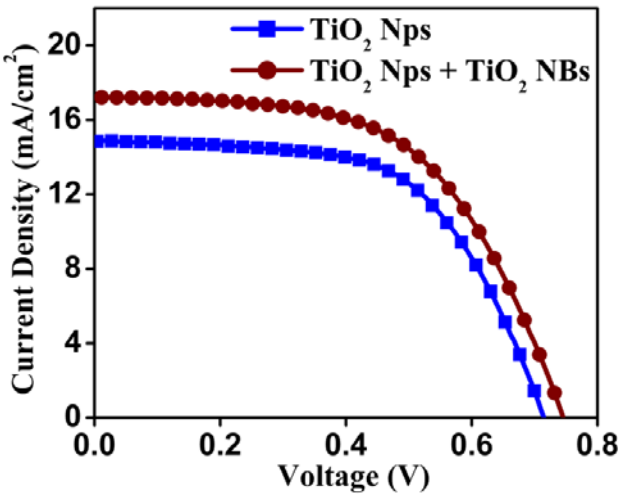

Name	V_{oc} (V)	J_{sc} (mA/cm²)	FF (%)	η (%)
Nps	0.71	14.8	59.3	6.3
Nps+ NBs	0.76	17.7	54.5	7.3

Figure 14. I-V data and table for solar cell parameters of TiO_2 Nps and TiO_2 Nps + TiO_2 NBs

Thus the use of TiO_2 nanobeads as LH layer enhances the DSSC performance by improving the solar cell parameters, namely the short circuit current density and open circuit voltage by almost 20%. This enhanced current density is attributed to the improved light harvesting capabilities (thereby increased absorption) of TiO_2 nano-beads.

Further improvement in DSSC efficiency was achieved through use of TiO_2 nanoflowers (NFs) as light harvesting overlayer instead of TiO_2 nanobeads.

3.3.2. TiO_2 Nanoflowers (NFs) as light harvesting overlayer

3D TiO_2 nanoflowers (NFs) were synthesized by following work by Fu *et al.*[24] The advantage of TiO_2 NFs over TiO_2 NBs is that these flowers are branched structures while being porous with high surface area. These branched structures are more efficient in harvesting light at the same time they provide easily accessible area for electrolyte and dye. The branched structures have self-similar configurations with hierarchical levels of size and thereby scattering length scales. Hence they can be effective light harvesters over a broad wavelength range.

3.3.2.1. Experimental.

3D hierarchical TiO_2 flowers were prepared by simple hydrothermal method followed by calcination at 450^0C. Briefly the procedure is as follows: Tetrabutyl titanate and glycerol are mixed together by stirring. This solution is then added to ethanol under constant stirring. Further this mixture is transferred to Teflon autoclave and heated at 180^oC for 24hrs. The product is centrifuged and washed with ethanol followed by drying at room temperature. The dried product is then calcined at 450^0C in air for 3 hours to remove the organic content.

3.3.2.2. Characterization of TiO_2 Nanoflowers

FESEM and TEM images were recorded for the determination of morphology and microstructure. Figure 15 (a) and (b) shows the FESEM images of the TiO_2 NFs. From the images it is clear that these nanostructures have many petals like outgrowths which are all arranged in clusters. From the TEM images seen in Figure 15 (d) to (e) it is clear that the individual flowers are of ~600±150 nm in size. The petals of these flowers are made up of granular TiO_2 nanoparticles of size ~20 nm. The lattice fringes in Figure 15 (e) show that the TiO_2 nanoflowers are crystalline in nature.

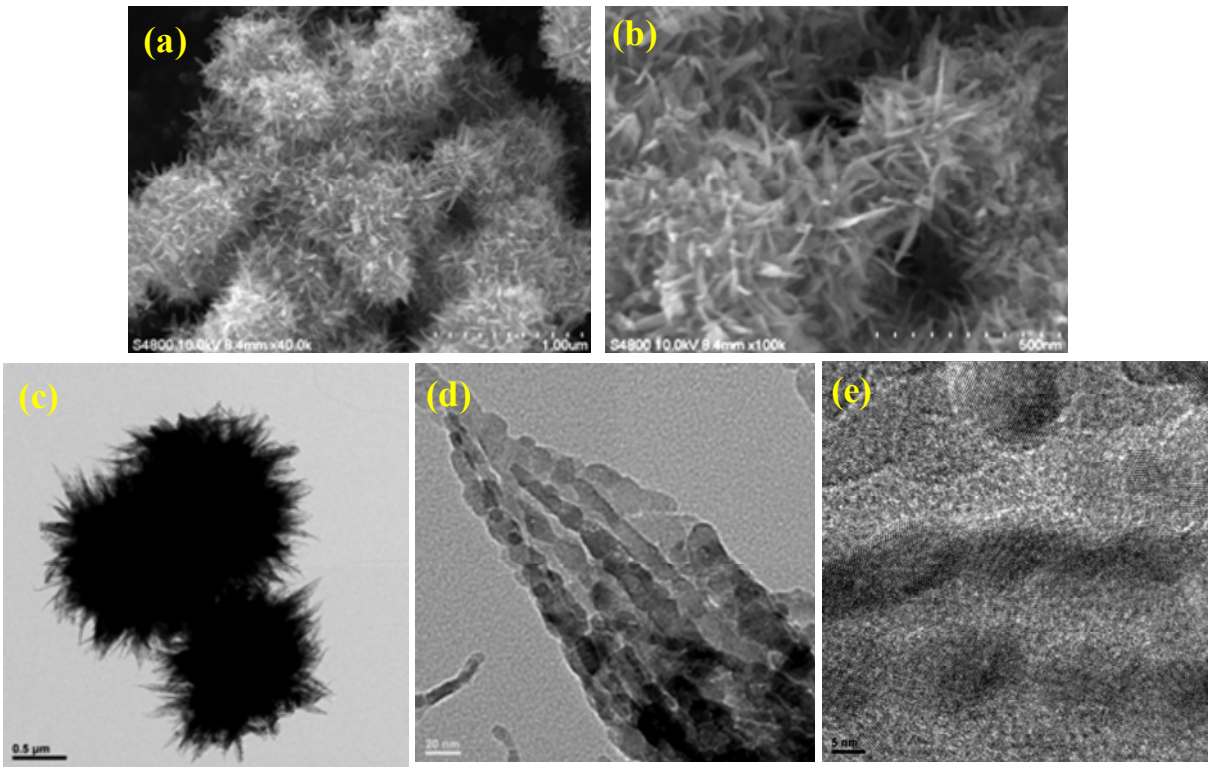

Figure 15. FESEM images (a) and (b), TEM images (c), (d) and (e) of TiO_2 nanoflowers

3.3.2.3. XRD

The XRD data shown in Figure 16 shows mainly anatase phase with some impurity of rutile phase. The crystal size estimated from the full width at half maximum of the (101) peak using

the Scherrer equation indicates that these TiO_2 nanocrystals are (15-20) nm in diameter, in good agreement with that measured from TEM images.

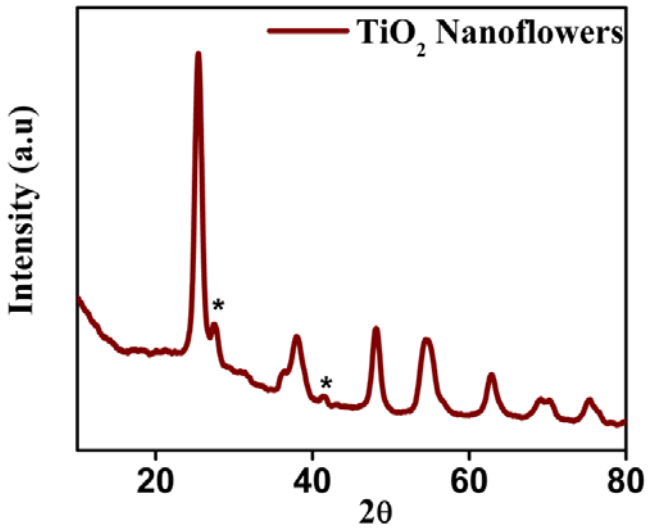

Figure16. XRD data for TiO_2 Nanoflowers

A paste of these nanoflowers was prepared by using protocol II. These TiO_2 nanoflowers (NFs) were used to make a coating of the light harvesting overlayer over the transparent 10-12 micron thick layer made of 20 nm sized TiO_2 nanoparticles (Nps).

3.3.2.4. Solar Cell Characterization

I-V Data: Figure 17 shows the I-V data for TiO_2 nanoparticle film case without light harvesting layer and similar TiO_2 Np film coated with the light harvesting layer made of TiO_2 nanoflowers. Here as well the thickness in both cases is kept at ~15 microns. The corresponding solar cell parameters are given in Table 17. Clearly a very significant enhancement in efficiency of 21 % is noted. The increase in efficiency in the case of the light harvesting overlayer is mainly due to

increase in current density as clearly seen in Figure 17. Interestingly, in this case the V_{oc} is almost the same as against the case of nanobeads discussed earlier.

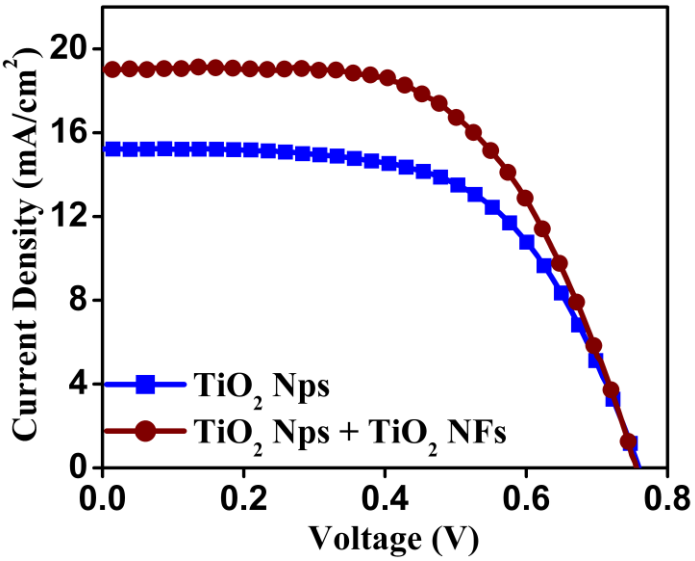

Name	V_{oc} (V)	J_{sc} (mA/cm^2)	FF (%)	η (%)
Nps	0.76	15.2	59.7	6.9
Nps + NFs	0.76	19.0	58.6	8.4

Figure 17. I-V data and table for solar cell parameters of TiO_2 Nps and TiO_2 Nps + TiO_2 NFs

IPCE data: In order to see verify this effect Incident Photon to Current conversion Efficiency (IPCE) measurement was performed. IPCE is related to the short circuit current density by the equation

$$IPCE\ (\%) = 1240 J_{sc}/\lambda\ P_{in}$$

where J_{sc} is the short-circuit current density, λ is the wavelength of the incident light, and P_{in} is the power of the incident light.

In simpler terms IPCE is the number of photons generated at a particular wavelength. Figure 18 shows the IPCE data for Np film case and Np + NF film case.

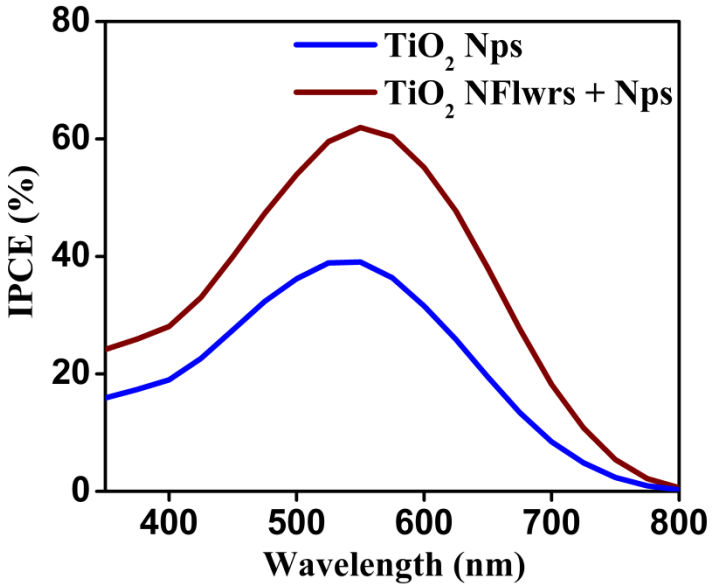

Figure 18. IPCE data for the Nps and Nps + NFs

By addition of light harvesting overlayer the peak IPCE value is seen to have improved significantly for the Nps + NFs case. This confirms the significant optoelectronic benefits of the light harvesting layer in the cell design and is reflected in the significant efficiency enhancement.

3.4. Fabrication of Large Area DSSCs

After achieving an efficiency of above 9% for small area DSSC the next target was to scale up the area and prepare a solar cell module. For any application, large area (~ 5 cm^2 or more) DSSCs are required. They can be connected in series or parallel to make a solar panel depending on the requirement of higher voltage or higher current density, respectively. The large area DSSC technology needs to address the following points:

- Internal electrical interconnection of individual cells
- Large area deposition of uniform TiO_2 layers
- Dye degradation at elevated temperature
- Electrolyte leakage and Stability
- Efficient module design

Most points can be addressed once a proper module design is fabricated. Hence selection of a proper large area DSSC module design is very important. There are different types of module designs as shown below: [25-28]

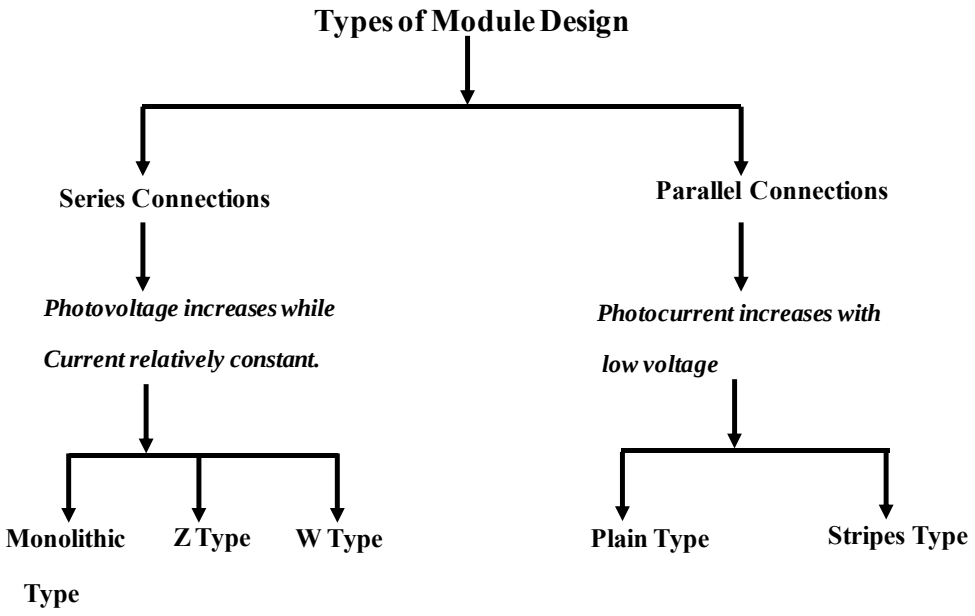

Figure 19. Types of solar cell module design

From a detailed literature review, it was clear that the **'parallel stripe type'** design is most favorable and hence was chosen that for our large area solar cell module. The main advantages of this design are

- Ease of fabrication
- Less ohmic losses due to metal contacts between the stripes
- Better charge collection due to reduced recombination, hence higher fill factor

Figure 20 below shows a typical stripes type cell.

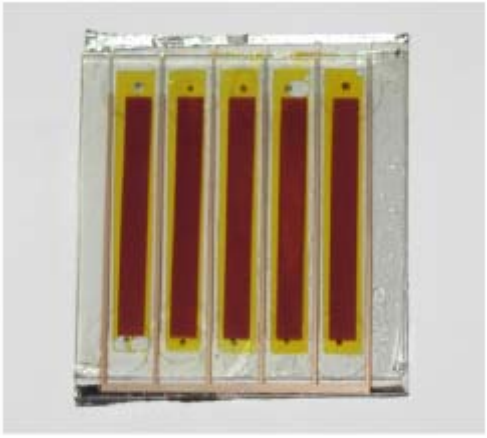

Figure 20. Parallel Stripes type cell

The cell area was gradually increased from 0.25 cm^2 to ~3 cm^2. The paste was prepared by protocol II. The films were coated using doctor blading method followed by programmed heating and $TiCl_4$ treatment. In order to have efficient charge collection silver contacts were thermally deposited on the working as well as the counter electrodes, as shown in Figure 21. Initially the cell efficiency was checked without making any silver connections but this gave a low fill factor. After depositing silver connections, the fill factor improved considerably with better charge collection. The silver contact films were deposited by thermal evaporation method. The film thickness was tuned to around 150 nm. An efficiency of over 3% was obtained.

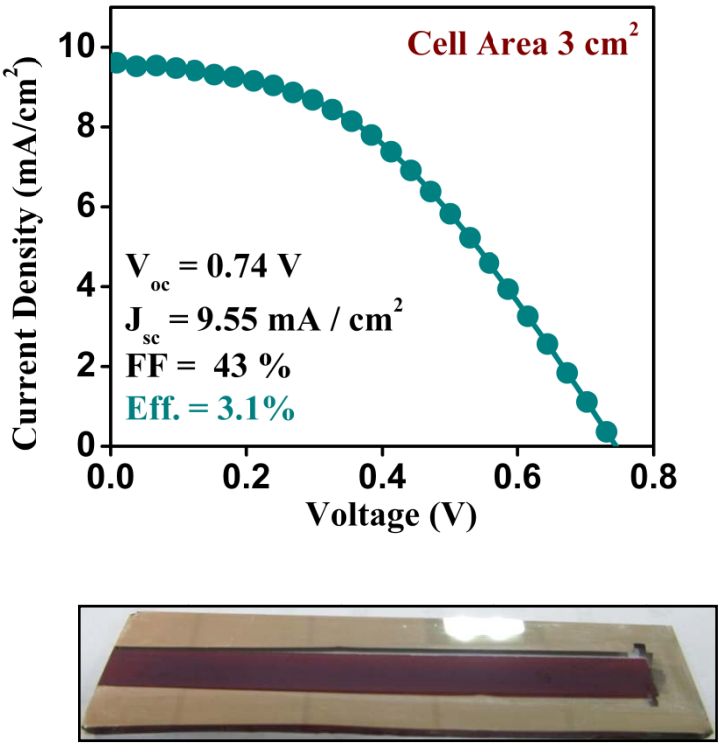

Figure 21. I-V data for large area DSSC along with an image of large area DSSC

In figure 21 the cell dimensions are 5 cm x 0.6 cm (L x W). The Large area device shows low efficiency and the reason of this low efficiency is clearly seen in low fill factor of the device. It should be noted that the silver contacts for this device were made only on the photoanode and not on the counter electrode. This increased the series resistance (~300 Ohms should be ideally few ohms) of the cell and also lowered its shunt resistance (30,000 ohms which should be ideally in lakhs) which reduced the fill factor of the device drastically. Further work was carried out to improve the device performance. This work shows the initial results of our attempt to make large area DSSCs although today in our lab at CSIR-NCL, Pune we get good efficiencies exceeding 5% for large area (5 cm^2) DSSC devices (with proper sealing and silver deposition on both the electrodes) it is not a part of this thesis.

3.5. References

1. G. Smestad, *Sol. Energy Mater. Sol. Cells*, **1994**, *32*,259
2. I. Kartini, D. Menzies, D. Blake, J.C.D. da Costa, P. Meredith, J.D. Riches, G.Q. Lu, *J. Mater. Chem*. **2004**,*14*,2917.
3. J.R. Durrant, S.A. Haque, E. Palomares, *Coord. Chem. Rev.*, **2004**, *248*, 1247.
4. K. Kalyanasundaram , M. Gratzel, *Coord. Chem. Rev.*, **1998**,*177*, 347.
5. K. Zhu, N. Kopidakis, N.R. Neale, J. Lagemaat, A.J. Frank, *J. Phys. Chem. B* **2006**,**110**, 25174.
6. S.A. Haque, E. Palomares, B.M. Cho, A.N.M. Green, N. Hirata, D.R. Klug, J.R. Durrant, *J. Am. Chem. Soc.*, **2005**,*127*, 3456.
7. N. Kopidakis, K.D. Benkstein, J. Van de Lagemaat, A.J. Frank, *J. Phys. Chem. B* **2003**,*107*,11307.
8. R. Hattori , H. Goto, *Thin Solid Films*, **2007**,*515*, 8045.
9. J. Xia, N. Masaki, K. Jiang, S. Yanagida, *J. Phys. Chem. C* , **2007**,*111*, 8092.
10. S.-J. Roh, R.S. Mane, S.-K. Min, W.-J. Lee, C.D. Lokhande, S.-H. Han, *Appl. Phys. Lett.,* **2006**,*89*, 253512/1.
11. S. Ito, T.N. Murakami , P. Comte, P. Liska, C. Grätzel, M. K. Nazeeruddin, M. Grátzel, *Thin Solid Films*, **2008**, *516*,4613–4619
12. B. O'Regan, J.R. Durrant, P. M. Sommeling and N. J. Bakker, *J. Phys. Chem. C,* **2007**, *111,* 14001-14010
13. N.-G. Park, G. Schlichthorl, J. Lagemaat , H. M. Cheong, A. Mascarenhas, J. Frank, *J. Phys. Chem. B.,* **1999,** *103,* 3308-3314.
14. S. Ito, P.Chen, P. Comte, M. K. Nazeeruddin, P. Liska, P.Pechy, M. Grátzel, *Prog. Photovolt: Res. App. l*, **2007**

15. Elisa Dell'Orto, Luisa Raimondo, Adele Sassella, Alessandro Abbotto, *J. Mater. Chem.*, **2012**, *22*, 11364

16. C. J. Barbe, F. Arendse, P. Comte, M. Jirousek, F. Lenzmann, V. Shklover, M. Grátzel, *J. Am. Ceram. Soc.* , **1997**, *80*, 3157.

17. T. P. Chou, Q. F. Zhang, B.Russo, G. E. Fryxell, G. Z. Cao, *J. Phys. Chem. C*, **2007**, *111*, 6296.

18. D.Cahen, G. Hodes, M. Gra¨tzel, J. F. Guillemoles, I. Riess, J. *Phys. Chem. B* , **2000**, *104*, 2053.

19. M. Graetzel, *Inorg. Chem.,* **2005**, *44*, 6841.

20. S. Hore, C. Vetter, R. Kern, H. Smit, A. Hinsch, *Sol. Energy Mater.Sol. Cells,* **2006**, *90*, 1176.

21. Y. Chiba, A. Islam, R. Komiya, N. Koide, L. Y.Han, *Appl. Phys. Lett.,* **2006**, *88*, 223505.

22. J-H. Park, S-Y Jung, R. Kim, N-G Park, J. Kim, S-S. Lee, *Journal of Power Sources*, **2009**, *194*, 574-579.

23. D.Chen, F. Huang, Y-B. Cheng , R. A. Caruso,*Adv. Mater.* , **2009**, *21*, 2206–2210

24. G. Tian, Y. Chen, W. Zhou, K. Pan, C. Tian, X-r Huang and Honggang Fu, *Cryst Eng Comm*, **2011**, *13*, 2994.

25. J. M. Kroon, N. J. Bakker, H. J. P. Smit, P. Liska, K. R. Thampi, P. Wang,S. M. Zakeeruddin,M. Gratzel, A. Hinsch, S. Hore, U. Wurfel, R. Sastrawan, J. R. Durrant, E. Palomares, H. Pettersson, T. Gruszecki, J. Walter, K. Skupien and G. E. Tulloch, *Prog. Photovolt: Res. Appl.*, **2007**, *15*,1–18

26. E. Ramasamy, W. J Lee, D -Y. Lee, J-S Song, *Journal of Power Sources*, **2007**, *165* , 446–449

27. R. Sastrawan, J. Beier, U. Belledin, S. Hemming, A. Hinsch, R. Kern, C. Vetter,F. M. Petrat, A. Prodi-Schwab, P. Lechner , W. Hoffmann, *Prog. Photovolt: Res. Appl*, **2006**, *14*,697–709

28. Michael Grätzel, *Prog. Photovolt. Res. Appl.,* **2000**, *8*, 171-185

Chapter 4

Important characterization techniques for DSSCs

This chapter deals with a detailed discussion about some such key characterization techniques that can be effectively used to understand, improve and optimize the DSSC device performance. These techniques include the impedance measurement that is used to measure the internal impedances of the various components of the solar cell, the cyclic voltammetry analysis for the determination catalytic properties of counter electrode and to determine the energy levels of the dye or electrolyte, and finally the Tafel polarization method for determining the properties of counter electrode. Employing these techniques together helps elucidate the key reasons behind a specific nature of performance realized in a given device.

4.1 Introduction. The DSSC device represents a complex architecture of functional inorganic and organic materials in nanometric and thin films forms configured as an intricate assembly. Moreover it works under optical excitation and involves several phenomena such as exciton formation, exciton ionization, charge separation, recombination, and transport. Electronically speaking these effects finally manifest themselves in terms of resistances and capacitances or impedances which control the voltages and currents. Elucidation of these factors by direct experimental measurements can throw light on a number of aspects pertaining to the cell architecture and can therefore help identify and solve the related problems so as to get the best performance parameters. Indeed, in view of the existence of several complex and interconnected events in the overall solar cell performance, isolating effects across different interfaces and in different components of the cell design is necessary to understand what is going right and what may be going wrong. This chapter deals with a detailed discussion about some such key characterization techniques that can be effectively used to understand, improve and optimize the DSSC device performance. These techniques include the impedance measurement that is used to measure the internal impedances of the various components of the solar cell, the cyclic voltammetry analysis for the determination catalytic properties of counter electrode and to determine the energy levels of the dye or electrolyte, and finally the Tafel polarization method for determining the properties of counter electrode. Employing these techniques together helps elucidate the key reasons behind a specific nature of performance realized in a given device.

4.2. Electrochemical Impedance Spectroscopy (EIS)

The J-V (Current density-Voltage) measurement of a solar cell is the basic measurement which tells us about the overall performance of the device in terms of its efficiency, but it gives very

little information about the limiting factors and resistances of individual sub-components of the architecture that hinder the device performance. Electrochemical impedance spectroscopy (EIS) is an advanced technique that can be used to study the charge transfer resistance and interfacial capacitances that are present in a DSSC internal equivalent circuit including contact resistances. Time constants can also be measured by using the EIS equivalent circuit parameters in order to determine the mechanism of electron transport through the semiconductor.

4.2.1. What is impedance?

Electrical resistance can be defined as the ability of a circuit element to resist the flow of electrical current. Ohm's law (Equation (i)) defines resistance in terms of the ratio between voltage, V, and current, I.

$$R = V/I \quad \text{..... (i)}$$

However, the well known Ohm's law has its limit. It can only be used for systems with only one circuit element, i.e. an ideal resistor which must have several properties such as:

- It obeys Ohm's law at all current and voltage levels.
- It shows resistance that is independent of frequency.
- AC current and voltage signals though resistors are always in phase with each other

In real device systems, the circuit elements show much more complex behavior which implies that we have to rely on 'impedance', a more complex circuit parameter which basically represents the collective response of the device elements to an electronic current or voltage stimulus. Like a resistance, impedance is also a measure of the ability of a circuit to offer a specific response to the flow of electrical current, but it is not limited to only the properties listed above. While impedance is a general term applicable to a combination of resistances,

capacitances and inductances, due to the specific hybrid character of the DSSC device, herein we have to primarily deal with the electrochemical impedance. Electrochemical impedance is usually measured by applying an AC potential to an electrochemical cell and measuring the current through the cell. If we apply a sinusoidal potential excitation, the response to this potential is an AC current signal which can be analyzed as a sum of sinusoidal functions. Electrochemical impedance is normally measured using a small excitation signal in order to maintain the response of the cell in the pseudo-linear regime. The characteristic of a pseudo-linear system is that the sine wave current response to a sine wave applied potential will also be a sine function observed at the same frequency but may be shifted in phase.

An expression for impedance (Z) of the system can be derived similar to the Ohm's law with potential and current functions as:

$$Z = E_t/I_t = E_o \text{ Sin } (\omega t)/ I_o \text{ Sin } (\omega t + \varphi) = Z_o \text{ Sin } (\omega t)/ \text{ Sin } (\omega t + \varphi) \quad \text{…….. (ii)}$$

The impedance can be expressed in terms of a magnitude, Z_o, and a phase shift, φ. If the impedance is represented as a complex function, the potential is described as,

$$E_t = E_o \exp (j\omega t) \quad \text{……. (iii)}$$

And the current response as,

$$I_t = I_o \exp (j\omega t - \varphi) \quad \text{……. (iv)}$$

The impedance (Z) is represented as a complex number,

$$Z(\omega) = E/I = Z_o \exp (j\varphi) = Z_o (\cos \varphi + j \sin\varphi) \quad \text{……. (v)}$$

In the impedance measurement the system is normally kept in a steady state followed by applying an AC potential and measuring the AC current through the cell. The universally accepted method allows for complex impedance and the phase shift measurements at a particular frequency. Using model equivalent circuits (which could have different alternatives based on

dissecting an actual device into component structures), impedance parameters can be assigned for individual internal components of the cell. In addition to the scanning frequencies, the EIS parameters can also be obtained under various conditions of the steady state i.e. different bias voltages or illumination intensities, in order to generate a thorough knowledge on the trend of behavior of the various elements. The impedance data can be represented in various forms like the Nyquist plot and Bode plot.

4.2.2. The Nyquist plot

The expression for Z (ω) in equation (v) has a real and an imaginary part. If the real part is plotted on the x-axis and the imaginary part on the y-axis of a chart, we get a Nyquist plot.

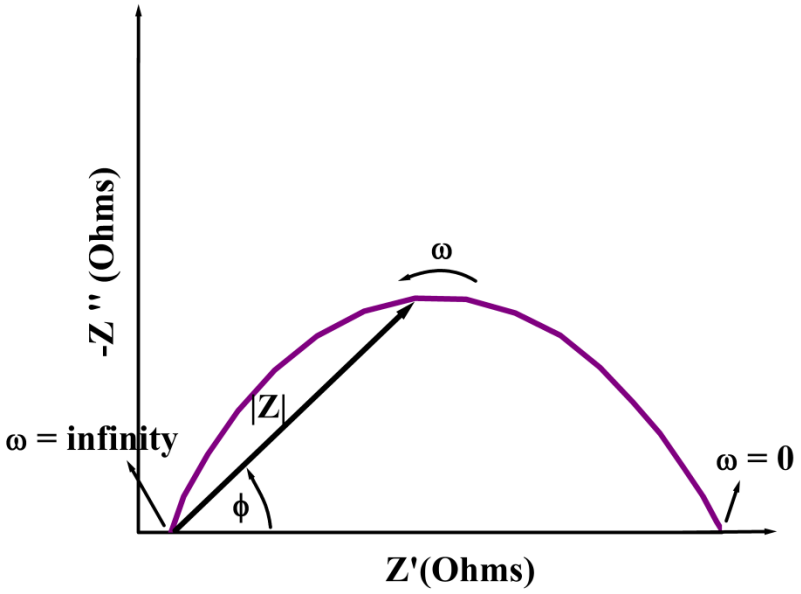

Figure 1. A typical Nyquist plot

The y-axis is negative (capacitative impedance) and each point on the Nyquist plot is the impedance at one frequency. On this plot the impedance can be represented as a vector (arrow)

of length |Z|. The angle between this vector and the x-axis is commonly called as the phase angle, φ. The semicircle on a Nyquist plot is characteristic of a single time constant. Electrochemical impedance plots often contain several semicircles. But these Nyquist plots have one major limitation: they do not give the complete information on the exact frequency that was used to record one point.

4.2.3. The Bode plot

Another important representation of the EIS measurement is the Bode phase plot. The impedance is plotted with log frequency on the x-axis and the phase-shift on the y-axis. Unlike the Nyquist plot, the Bode plot gives the complete frequency information.

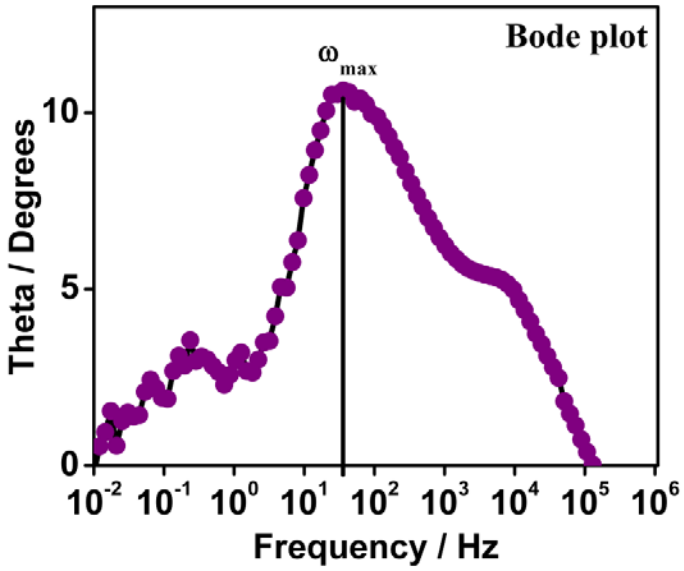

Figure 2. A typical Bode plot

4.2.4. Experimental details

The frequency range chosen in our work for the EIS measurements was from 10^{-2} Hz to 10^{6} Hz with ac amplitude of 10 mV.[1] The impedance spectrum of DSSC (Nyquist plot) mainly consists of three semicircles attributed to the impedances for the Pt| Electrolyte (Z_1), TiO_2|Dye

|electrolyte (Z_2) and the diffusion of I_3^- (Z_3) in the electrolyte, respectively. The semicircle at the high frequency region (kHz range) is related to the charge transfer at Pt|electrolyte interface, the middle frequency (1-100Hz) semicircle deals with electron transfer at TiO_2|dye|electrolyte interface and the low frequency region (mHz) deals with diffusion of I_3- into the electrolyte. The total internal resistance of the cell R_{total} is the sum of all the resistances at these interfaces.[1,2] For a high performance DSSC this internal resistance of the cell should be low. Different groups all over the world follow different conditions to record the impedance data, for example, at different bias voltage in dark or at different bias voltage under illumination.

4.2.5. Equivalent Circuit – The transmission line model. The electronic processes occurring in DSSCs are described well by transmission line model developed by Bisquert and co workers[3] which is suitable for porous electrodes. This transmission line equivalent circuit notation was earlier noted in solid state electronics and later even adopted in electrochemistry. Bisquert and coworkers used this transmission line model to study impedance of DSSCs governed by the diffusion and recombination processes.

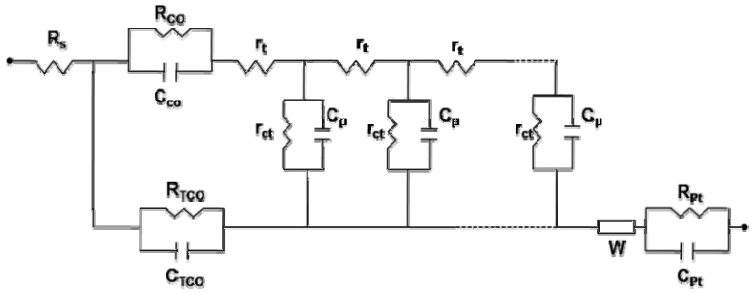

Figure 3. Equivalent circuit the transmission line model

The important parameters to be extracted from the Nyquist plot using the equivalent circuit[1,4] are described in details below:

a) R_s is the resistance at which the first semicircle starts. It is the sum of the sheet resistance of the TCO, the contact resistance between TCO and TiO_2, and the external contact resistance.

b) k_{eff} is estimated from the peak frequency ω_{max} of the central arc, which describes the rate of recombination of electrons in the film.

c) τ_{eff} is the inverse of k_{eff} which gives the information about the lifetime of electrons throughout the working electrode.

d) R_{ct} is the diameter of the central arc which gives the charge transfer resistance including recombination of electrons with I_3^- at the TiO_2 / electrolyte interface.

e) R_t is the resistance of electron transport in the photo-electrode film, consisting typically of the interconnected TiO_2 nanoparticles. The total transport resistance of the film is $R_t = r_t\, d$ (Ω m^2), where d is the film thickness.

f) D_{eff} is the effective diffusion coefficient of electrons is calculated as, $D_{eff} = (R_{ct}/R_t)L^2 k_{eff}$ Where L is the thickness of working electrode and for true circle $R_{ct} >> R_t$

g) R_D is the DC resistance for the diffusion of I_3^- in the electrolyte calculated from the diameter of the third arc (low frequency in the mHz range).

h) Con describes the charge transport resistance and its recombination rate along the entire thickness of working electrode and is calculated as $Con = R_{ct}\, L\, k_{eff}$.

Figure 4 shows a typical Nyquist plot for P25 film along with the parameters to be extracted from the plot. The impedance spectroscopy is used to compare the variation in all these parameters under different conditions so as to explain the reasons for high / low efficiency in DSSCs.

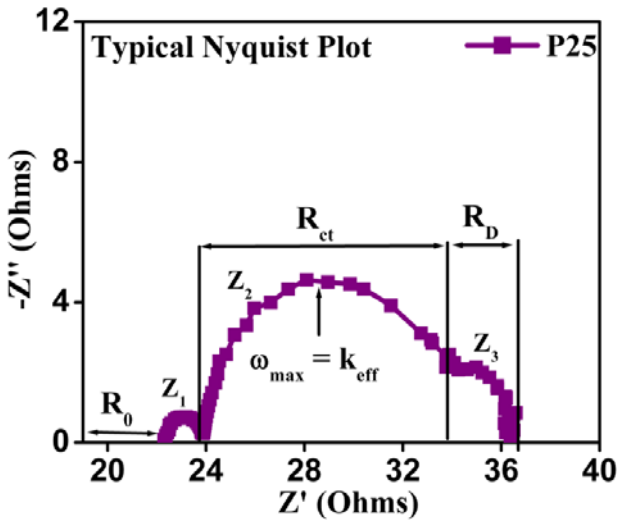

Name	k_{eff} (s^{-1})	τ_{eff} (s)	R_{ct} (Ω)	R_t (Ω)	D_{eff} (cm^2 s^{-1})	Con (Ω cm s^{-1})	R_D (Ω)
P25	11.76	0.014	10.45	1.07	$1.69x10^{-4}$	0.15	2.18

Figure 4. A typical Nyquist plot of P25 film along with the table of impedance parameters

4.2.6. Various Case Studies

In this section different case studies wherein impedance analysis aided to understand the effects of variations of different parameters on the overall performance and efficiency of DSSCs are discussed. Some of the works represented here is the thesis author's own original work while a few others are the works in which the author of the thesis has been a co-author. Indeed the role of the author of this thesis in the co-authored works was primarily to perform the impedance measurements and to analyze and extract the desired parameters by fitting various Nyquist plots using the NOVA software.

4.2.6.1. Effect of annealing temperature

In order to study the effect of annealing on the properties of photo-anode, P25 films were made by the routine procedure i.e. annealing at 450°C while others were made at room temperature without any heat treatment (binder free TiO_2 paste was prepared, details of this protocol are discussed in chapter 6). Impedance data of these two cases were recorded (Figure 5). It is observed that the electron transport resistance R_t increases substantially in the no heat treatment case. This can be attributed to the poor necking between the TiO_2 particles which hampers the transport of electrons through the TiO_2 network.[5] Figure 2 shows the Nyquist plots for these two cases along with the parameters enlisted in the table. This justifies the cause of high efficiency of 7% in 450°C annealed case as compared to 3% in the no heat treatment case.

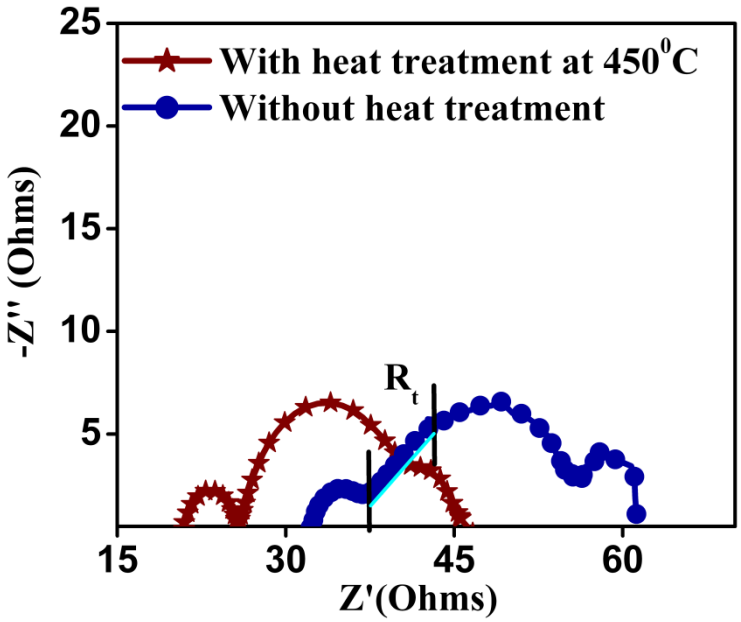

Name	k_{eff} (s^{-1})	τ_{eff} (s)	R_{ct} (Ω)	R_t (Ω)	D_{eff} (cm^2s^{-1})	R_D (Ω)
450°C Annealed	9.76	0.016	15.0	1.08	1.63×10^{-4}	4.1
Room Temperature	17.03	0.009	10.77	7.74	0.34×10^{-4}	6.84

Figure 5. Nyquist plot for 450°C annealed and Room temperature prepared DSSC along the table for various parameters

4.2.6.2. Effect of post $TiCl_4$ treatment

In order to study the effect of $TiCl_4$ treatment on the various interfaces of DSSC architecture impedance measurements were carried out. The parameters of specific interest for dye sensitized solar cells were then calculated (Fig. 6 and the table). It was found that k_{eff} which describes the rate of recombination of electrons in the film, estimated from the peak frequency ω_{max} of the central arc, is ~1.5 times smaller in the case of films treated with $TiCl_4$ than those not treated. The life time of electrons throughout the film (τ_{eff}) which is equal to the inverse of k_{eff} is seen to have increased in the case of $TiCl_4$ treated films. It was found that the total resistance R_{total} for the $TiCl_4$ treated cell was reduced considerably as compared with the ones without $TiCl_4$ treatment.

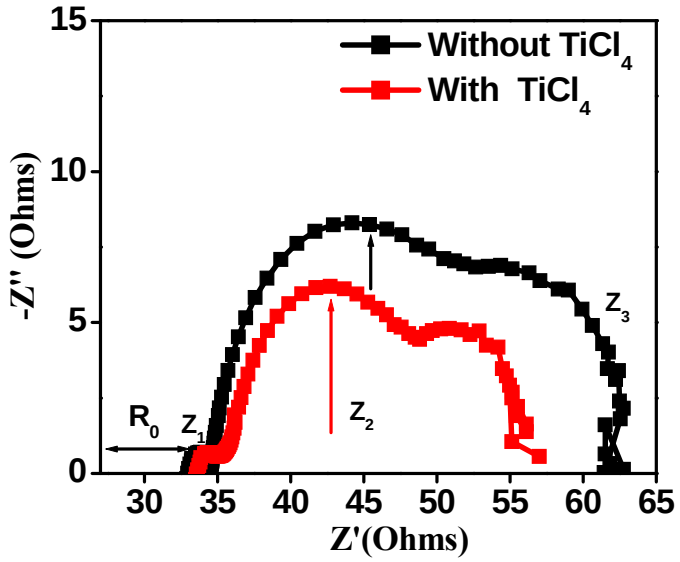

Name	K_{eff} (s^{-1})	τ_{eff} (s)	R_{ct} (Ω)	R_t (Ω)	D_{eff} (cm^2 s^{-1})	Con (Ω cm s^{-1})	R_D (Ω)
Without $TiCl_4$	5.59	0.178	14.98	1.77	$0.68x10^{-4}$	0.1122	10.84
With $TiCl_4$	3.85	0.259	12.18	0.59	$1.14x10^{-4}$	0.0589	7.29

Figure 6. Nyquist plot for cases with and without $TiCl_4$ treatment along with table showing different parameters

R_t the electron transport resistance within the TiO_2 film was less than half for the $TiCl_4$ treated film confirming better connectivity between the TiO_2 particles. R_D, the DC resistance for the diffusion of I_3^- in electrolyte calculated from the diameter of the third arc (low frequency in the mHz range) is also low i.e. 7.4 Ω for films treated with $TiCl_4$ as compared to untreated i.e.10.8 Ω. Lastly, Con describes the charge transport resistance and its recombination rate along the entire thickness of working electrode and is calculated as product of R_{ct} L k_{eff}, where L is the thickness of the working electrode (here it is 12μm). This value has substantially decreased to half in the case of $TiCl_4$ treated films as compared to the untreated films. This shows that $TiCl_4$ treated films show effectively a better charge transport and greater electron density with low recombination rate.[6] Thus the essentials for efficient solar cell like high $\tau_{eff,}$ low k_{eff}, high R_k and low R_D are obtained after $TiCl_4$ treatment.

4.2.6.3. Effect of Au nanoparticles on the light harvesting properties of nanofibers

In one of our recent studies (Rounak Naphade et al. wherein the author of this thesis is a joint corresponding author) a significant enhancement in the performance of dye sensitized solar cells was observed by using in situ Au nanoparticle (Au NP) loaded TiO_2 nanofibers (Au:TiO_2 NFs) as the light harvesting (LH) layer as compared to the use of only TiO_2 nanofibers (NFs) as the LH layer.[7] The Au NP:TiO_2 nanofibers were prepared by electro-spinning of a precursor mixture whereby nano-structured porous TiO_2 nanofibers were formed and got *in situ* loaded with only 4–5 nm Au NPs. The presence of gold nanoparticles showed considerable improvements in light harvesting and the electrochemical properties of TiO_2 nanofibers. A remarkable enhancement in the efficiency by 25% was achieved with the Au NF LH layer (Efficiency of 7.7%) as compared to 12% with the NF layer (Efficiency of 6.76%), over the value without any light harvesting layer (Efficiency of 6.03%). To understand the role of Au NPs in the performance improvement,

electrochemical impedance spectra (EIS) were recorded and analyzed primarily by the author of this thesis at different applied bias voltages under 1 Sun illumination. The EIS spectra can be used to derive the information regarding interfacial and transport processes, and the kinetics of diffusion and recombination.

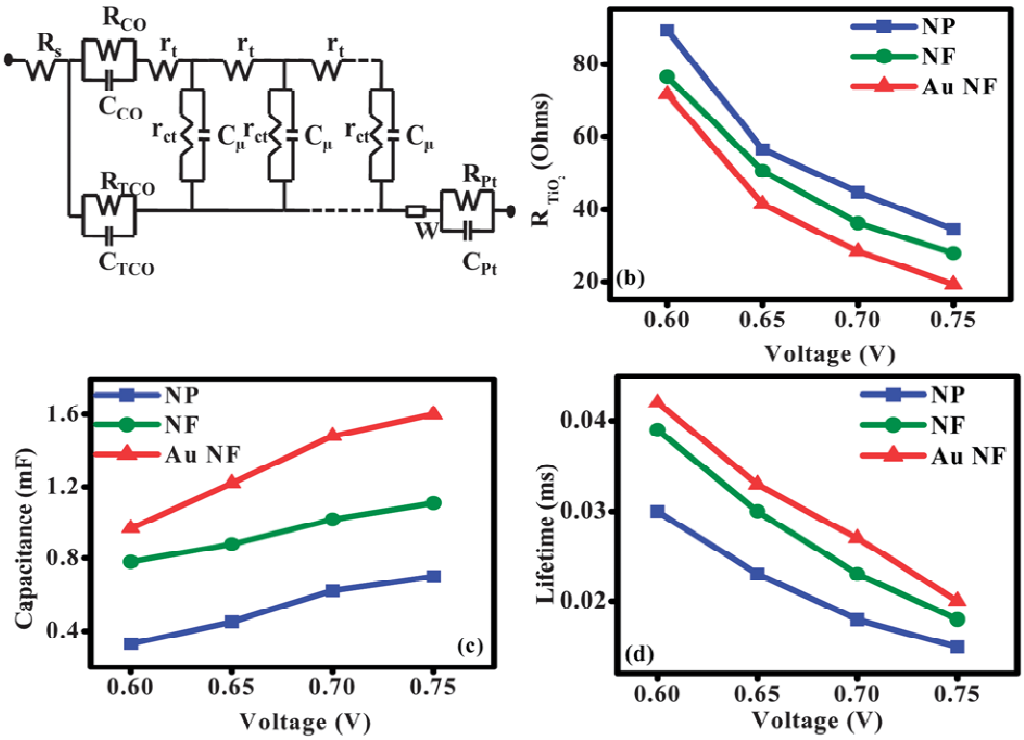

Figure 7. (a) shows the transmission line model used for fitting the EIS curves, (b) shows the variation of transport resistance (R_{TiO2}), (c) shows the variation of chemical capacitance (C) vs. applied bias voltage for the NP cell, NF cell and Au NF cell, (d) shows the life time obtained from the Bode phase plots over the applied bias range for the NP cell, NF cell and Au NF cell.

Figure 7 (a) shows the equivalent circuit used to fit the Nyquist plots. Figure 7(b) shows the graph of R_{TiO2} vs. applied bias voltage. The charge transport resistance (R_{CT}) is seen to decrease when the LH layer is employed over the entire range of applied bias potential. In the case of the

Au:TiO_2 NF LH cell the R_t is even lower as compared to the NF LH cell without Au NPs. This implies an increase in the charge transfer rate from dye to TiO_2 in the presence of the Au TiO_2 NF LH layer. This is consistent with the improvement in the fill factor which also suggests the lowering in the charge recombination process. From Figure 7(c) it can be clearly observed that in the presence of the Au:TiO_2 NF LH layer the chemical capacitance (C) in the photo-anode is enhanced. The capacitance observed in this study is mainly attributed to the total density of electronic states in the conduction band as well as in the band tail states.[8] The chemical capacitance also indicates the recombination with the electrolyte and the electron density in the active layer. Hence the enhancement in the capacitance in the LH layer employed devices indicates better charge storing ability of TiO_2 NFs and Au: TiO_2 NFs. These nanofibers are composed of assembled TiO_2 nanoparticles where the grain boundaries of TiO_2 nanoparticles are connected thus electrons can be rapidly driven from one end to another in the TiO_2 nanofibers as compared to the TiO_2 nanoparticle cell. The grain-connected TiO_2 nanoparticles in nanofibers can carry higher number of charge carriers as compared to the randomly connected nanoparticles; hence the capacitance in the case of nanofibers is greater as compared to the only nanoparticle cell.[9] But in the Au:TiO_2 NF LH cell the capacitance is even higher than the TiO_2 NF cell. The enhancement in the capacitance can be attributed to formation of randomly distributed Au:TiO_2 Schottky barriers in the Au:TiO_2 NFs. These Schottky barriers can store the charge effectively leading to an enhancement in the life time. The Fermi energy level of gold nanoparticles is below the conduction band of TiO_2. Hence such Au/TiO_2 interfaces form the charge trapping centers leading to higher electrochemical capacitance.

The overall capacitance is enhanced almost by 90% as compared to the TiO_2 NP case with Au:TiO_2 NFs and by 40% with the TiO_2 NFs. The enhancement in the capacitance is in good

agreement with the enhanced life time of the charges. The frequency maximum (ω_{max}) of the middle semicircle in the Nyquist plot represents the life time of photo generated charges. Figure 7(d) shows that the life time of photo-generated charges is enhanced by employing the light harvesting layers. In the presence of gold nanoparticles the life time is higher as compared to the only TiO_2 NF case over the entire range of applied bias potentials. This ensures better performance of the devices even under ambient light conditions.

4.3. Impedance measurements to elucidate the catalytic properties of counter electrodes.

4.3.1. Experimental. Impedance measurements for the studies of counter electrode related effects were performed using a symmetric cell assembly in dark under zero bias. In the symmetric cell assembly case two counter electrodes are sandwiched together with the electrolyte in between.[10] The electrolyte used is the same as the one which we use to measure J-V curves of DSSCs. The frequency range used is 10^5 Hz to 10^{-1} Hz with an AC amplitude of 10V. Nova 1.7 software is used to fit the above Nyquist plots.

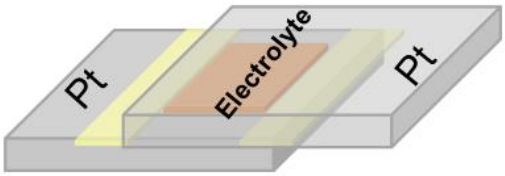

Figure 8. Symmetric cell assembly for counter electrode impedance

The Nyquist plot the case of counter electrodes in the symmetric cell assembly shows mainly two semicircles. The high-frequency intercept on the *x*-axis corresponds to the series resistance (R_s) which describes the Ohmic resistance of the counter electrode along with the adhesion of

counter electrode material to the substrate. The left semicircle in the high-frequency region arises from the charge transfer (R_{ct}) and the corresponding capacitance (C_{μ}) at the electrode/ electrolyte interface, whereas the other semicircle in the low-frequency region arises from the Nernst diffusion impedance (Z_N) of the tri-iodide/iodide in the electrolyte. The R_{ct} determines the catalytic activity of the counter electrode. [10]

The importance of these parameters can be summarized as

- Smaller the R_{ct} more efficient is that counter electrode towards reduction of I^-/I_3^-.
- The capacitance C_{μ} should be more which implies increased specific surface area of counter electrode i.e the catalyst.
- The Nernst diffusion impedance should also be small which helps in faster diffusion of the tri-iodide/iodide in the electrolyte.

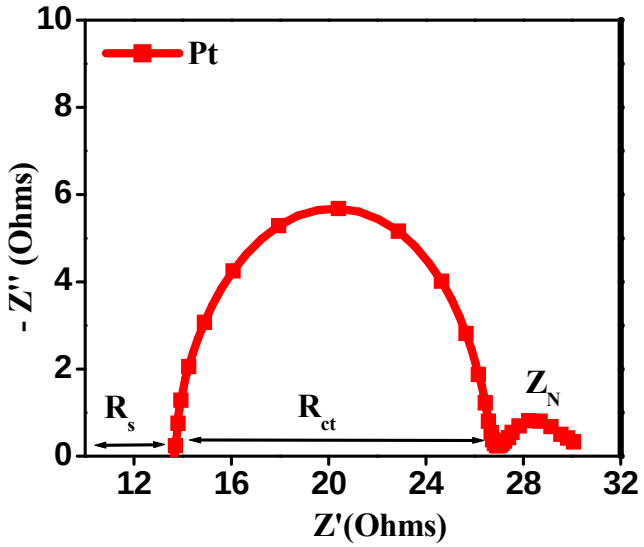

Figure 9. Typical Nyquist plot for Pt counter electrode

In the following section also additional representative case studies are discussed where impedance analysis is used to characterize different materials for their use as counter electrodes

in DSSCs. Once again, in these co-authored studies the role of the author of this thesis was EIS measurements and analysis.

4.3.2. Carbon cloth counter electrode for DSSCs: Impedance analysis

In one of our recent works (Thathavadekar et al. wherein the author of the thesis is a joint corresponding author) a conducting carbon cloth obtained by one-step pyrolysis of easily available cellulose fabric was seen to compete favorably with the commonly employed expensive platinum/FTO system as a counter electrode for dye sensitized solar cell (DSSC).[11] In view of the low carbonization temperature (1000°C) which forbids full graphitization, the nature of carbon in this case is represented by topologically randomly assembled nanoscale graphene units (turbostratic carbon). This morphology has high density of edge states and oxygen containing surface groups rendering multitude of catalytic sites for the reduction of I_3^-. Moreover the cloth is permeable to the dye and/or liquid electrolyte and its absorption properties also help retain the electrolyte. A fairly high efficiency of 5.8% is achieved using such cloth as a counter electrode as against 7% with the conventional Pt/FTO system (Figure 10 (a)). Moreover, the permeable property of the cloth eliminates a complete step of drilling hard TCO substrates for final dispensing of electrolyte into the device and the sealing process is therefore also facile.

Figure 10 (b) shows the Nyquist plot obtained from impedance measurements with the equivalent circuits used to fit the respective graphs. The parameters to be extracted from the Nyquist plot are: R_s, R_{ct}, C and the Warburg diffusion constant W. R_s is the series resistance of the electrolyte and the electrodes in a symmetric cell assembly, R_{ct} is the charge transfer resistance at the electrolyte electrode interface, C is the capacitance of the double layer and W is

the Warburg diffusion. Due to the absorption of electrolyte by the carbon cloth counter electrode the Warburg parameter for diffusion of ions was not employed in the equivalent circuit.[12]

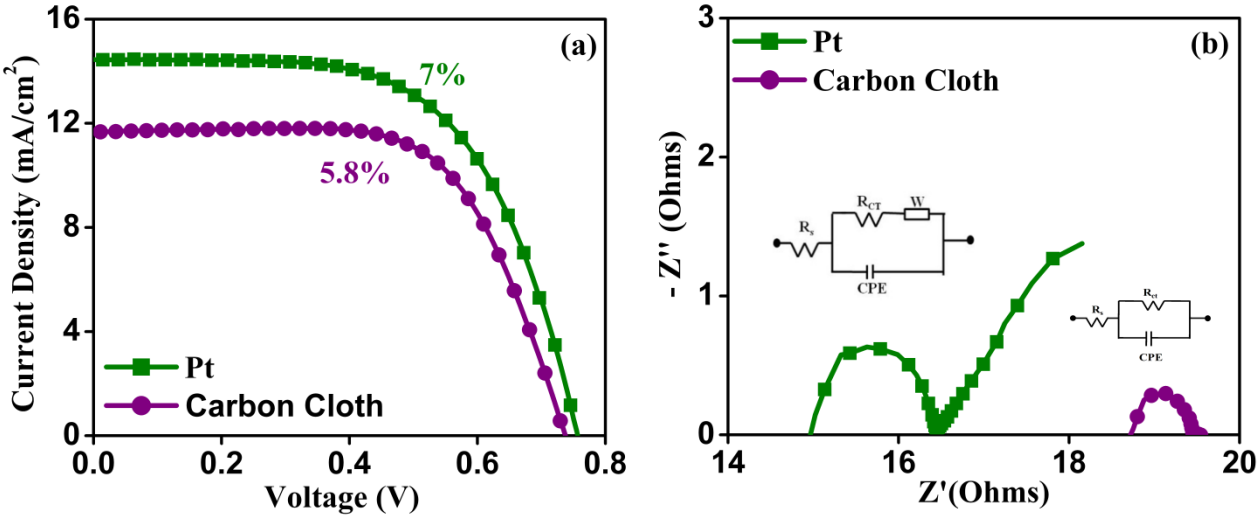

Figure 10. IV and impedance data for carbon cloth as counter electrode

R_{ct} which is the charge transfer resistance has an inverse relation to the catalytic reduction of $I_3^-$is less for the carbon cloth counter electrode (0.71 Ω) than the Pt electrode (1.3 Ω). This highlights the better catalytic activity of carbon counter electrode towards reduction of I_3^-. The series resistance for Pt counter electrode is 15.1 Ω which is less than that of carbon cloth counter electrode with R_s of 18.7 Ω. The cause for higher series resistance in the carbon cloth counter electrode lies in the current way of device fabrication. In the carbon cloth case we have just used a mechanical press contact between the cloth and ITO conducting substrate through a layer of epoxy adhesive dispensed over the edges. This contact in the current design is thus not ideal and efficient as in the other case where Pt is thermally deposited directly on FTO substrate.

4.3.3. Nickel Cobalt Sulfide (NCS) as Counter electrodes in DSSCs: Impedance analysis

This work on sulfide growth was performed by Abhik Banerjee et al. and the work on the solar cell fabrication, testing and impedance measurements/analysis was done by the author of this thesis.[13] Self supported nickel cobalt sulfide (NCS) nano-needles were directly formed on FTO glass substrates by sulphurization of nickel cobalt oxide ($NiCo_2O_4$ or NCO) nano-needles (grown by a hydrothermal method) in the presence of a hydrogen sulfide and argon gas mixture.

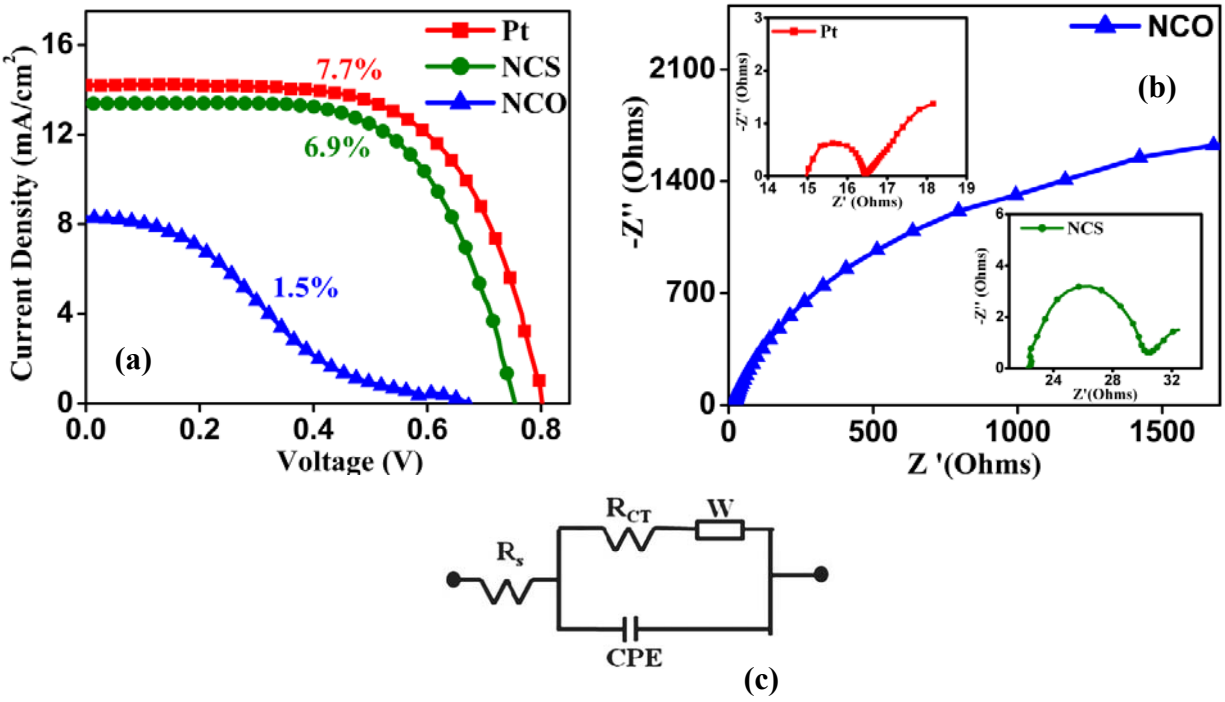

Figure 11. Solar cell characteristics and impedance data for Pt, NCS and NCO counter electrodes along with equivalent circuit used for modeling.

These NCS nano-needles when used as a counter electrode for dye sensitized solar cells (DSSCs) showed an efficient catalytic activity towards the I^-/I_3^- redox couple, and lead to an impressive efficiency of 6.9%, compared with 7.7% obtained with a Pt electrode in similarly constructed

devices (see data in Figure 11(a)). Figure 11 (b) shows the Nyquist plots for the Pt, NCS and NCO counter electrodes. The R_{ct}, i.e. the charge transfer resistance related to the catalytic activity, is 1.35 Ω for the Pt electrode while it is higher for the NCS electrode (7.71 Ω). The R_{ct} value for the NCO electrode is in kilo-ohms, which correlates with its poor catalytic properties and low efficiency. The series resistance for the NCS electrode is 22.4 Ω, while that of Pt is 15.1 Ω. This resistance depicts the 'electronic' adhesion of the material on the FTO along with its sheet resistance. Higher R_{ct} and higher R_s appear to be the reason for the slightly lower efficiency in the case of the NCS electrode. Thus it is clear that NCS is superior as a counter electrode for DSSCs as compared to NCO.

4.3.4. Laser synthesized Carbon as counter electrode for DSSCs: Impedance analysis

Recently Rohan Gokhale *et al.* introduced concept of UV-laser induced photochemical stitching to obtain conducting super-hydrophobic carbon coatings on FTO-coated glass substrates with unique, hierarchical and process-tunable broccoli-type morphology.[14] This unique feature and the properties were used to examined the viability of this material for DSSC application and it yielded excellent results for solar conversion efficiency. The author of this thesis performed studies on impedance measurements and analyses.

Nyquist plots were obtained for the carbon counter electrodes synthesized with different values of process parameters by applying bias voltage varying from 0V to 0.8V. Figure 13(a) shows plot of R_s and R_{ct} versus laser irradiation time and the inset is the equivalent circuit used to fit the Nyquist plots. Figure 13 (b) shows the plot of log R_{ct} versus applied voltage for different laser formed counter electrodes. R_s,which is the series Ohmic resistance reflecting the adhesion of carbon film on the substrate was found to have a value between 25-35 Ω for all the laser formed

counter electrodes. This indicates that all laser formed counter electrodes have fairly good adhesion with the substrate.

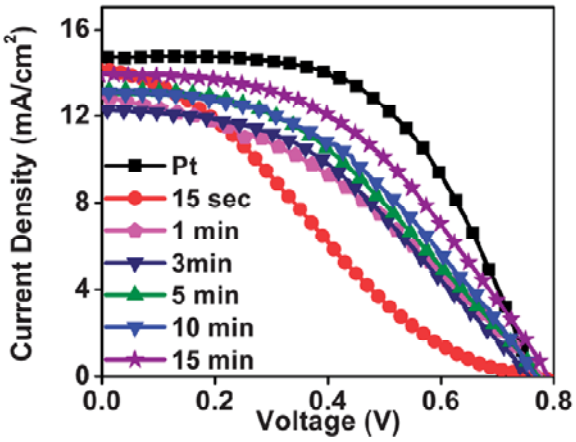

Name	V_{oc} (V)	J_{sc} (mA cm^{-2})	FF (%)	η (%)
Pt CE	0.76	14.7	55.6	6.2
15 s	0.77	14.11	25.39	2.8
1 min	0.78	12.82	37.7	3.8
3 min	0.75	12.22	42.5	3.9
5 min	0.77	13.14	41.4	4.2
10 min	0.77	13.02	44.3	4.4
15 min	0.79	13.86	46.1	5.1
20 min	0.66	8.37	53.7	2.9

Figure 12. Solar cell characteristics for laser formed carbon counter electrode. [14]

All the laser formed films were seen to follow proper trend where R_{ct} was found to decrease with increase in the applied bias voltage and the Nernst diffusion impedance showed an increase, as seen in figure 13(b). From Figures 13(a and b) it is seen that catalytic charge transfer resistance, R_{ct} decreases with irradiation time and is lowest for 15 min laser formed film. It shows an increase for 20 min laser irradiated case as there is gradual loss of carbon by laser ablation due to prolonged exposure to laser photons. This matches well with the high efficiency performance of 15 min laser formed counter electrode compared to the other laser formed counter electrodes. 15 min laser formed counter electrode showed a good catalytic activity and better charge transfer properties at the electrode electrolyte interface. Figures 13(c-d) show Nyquist plots for the 15 min laser formed counter electrodes at different bias voltages.

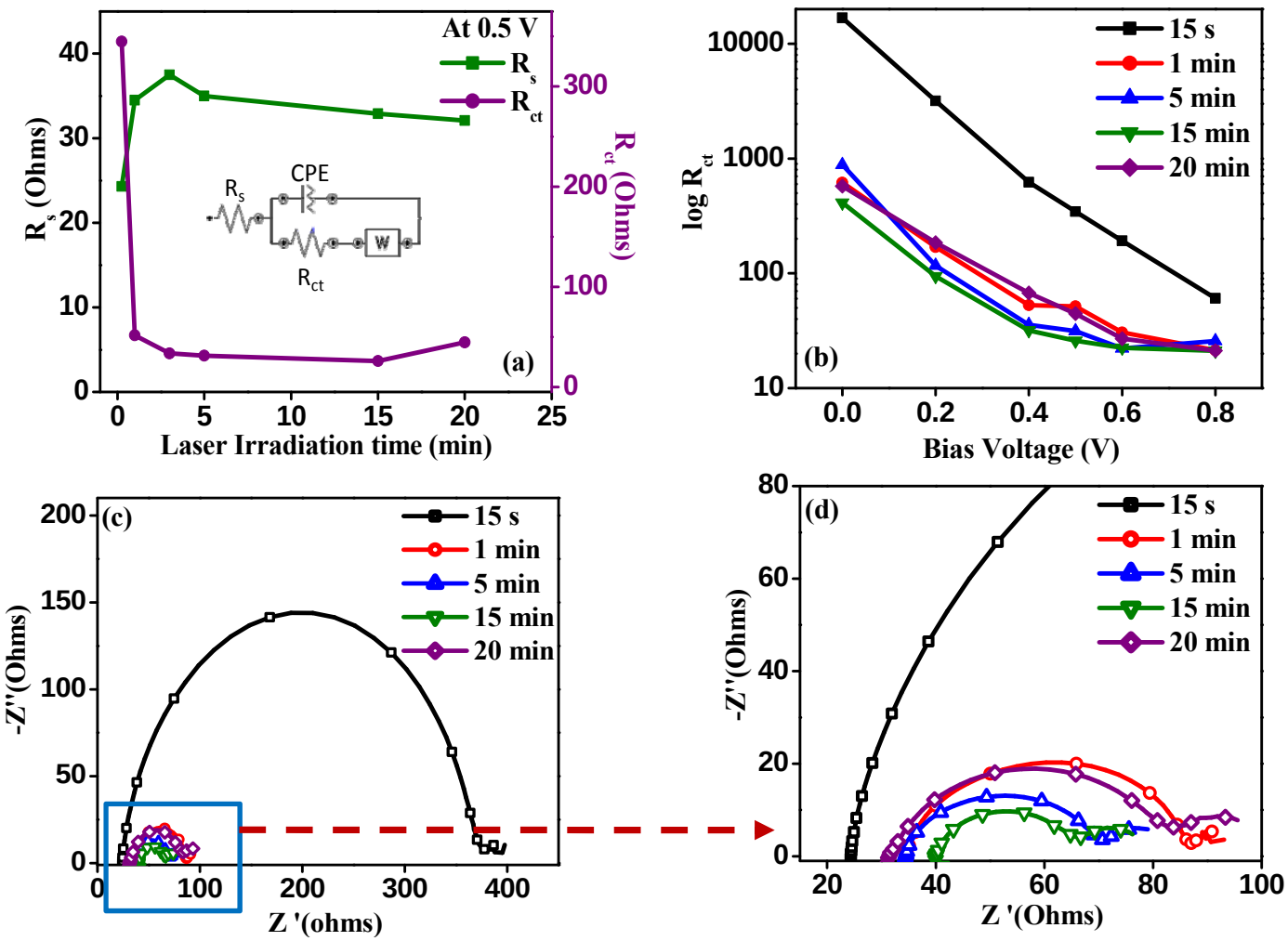

Figure 13. a) Plot of R_s and R_{ct} vs Laser irradiation time, b) Plot of Log R_{ct} vs bias voltage for 15s, 1 min, 5 min, 10 min and 20 min laser formed Counter electrode, c) Nyquist plots for various counter electrodes as bias voltage 0.5V, d) zoomed version of (c).

4.4. Cyclic Voltammetry

Cyclic voltammetry or CV is a type of electrochemical measurement which is performed by varying the potential. In a cyclic voltammetry experiment the working electrode potential is increased linearly with time similar to linear sweep voltammetry. Unlike linear sweep voltammetry which ends when working electrode reaches a set potential, in cyclic voltammetry, when the working electrode reaches a set potential the direction of potential scan is inverted. The current at the working electrode is plotted versus the applied voltage to give the cyclic voltammogram. Cyclic voltammetry is generally used to study the electrochemical properties of an analyte in solution. It is widely used to study a variety of redox processes, for obtaining stability of reaction products, the presence of intermediates in oxidation-reduction reactions,[15-16] and electron transfer kinetics, [17] and the reversibility of a reaction.[18] CV can also be used to determine the electron stoichiometry of a system, the diffusion coefficient of an analyte, and the formal reduction potential, which can be used as an identification tool.[19] Cyclic voltammetry can be applied for DSSCs to study the redox properties of the counter electrode which involves electron transfer from counter electrode to the electrolyte namely for reduction of tri-iodide ions which thus help in regeneration of oxidized dye. It can also be extended find the HOMO-LUMO levels of dye and redox potential of the electrolyte as discussed in next sections.

4.4.1. Cyclic voltammetry for analysis of catalytic properties of counter electrode

Cyclic voltammetry measurements are performed to measure and compare the catalytic activity of different counter electrodes. Typically, a three electrode system is used with at a scan rate of 100 mV/s and over the voltage range from -1 V to 1.2 V. Thermally deposited Pt or any other potential counter electrode is used as working electrode with an area ~1 cm^2, Ag/AgCl as a

reference electrode, and Pt foil as a counter electrode. The electrolyte used for this study is 10 mM LiI, 1 mM I_2 and 0.1 M $LiClO_4$ in acetonitrile. The CV data display two sets of peaks which relate to the redox peaks of I^- / $I_3^-$and I_2 / I_3^-.The redox reactions taking place at the counter electrode surface are as follows:

$$I_3^- + 2e^- \leftrightarrow 3I^- \quad (1)$$

$$I_3^- \leftrightarrow I_2 + I^- \quad (2)$$

For an efficient counter electrode material, the process of hole extraction from electrolyte should be faster. The kinetics of conversion of $I_3^-$to I^- decides the performance of the counter electrode.[20] The peak at around -0.13 V is assigned the reduction reaction of I_3^- to I^-. The peak currents and peak to peak separation are important parameters for determining the catalytic activity of counter electrodes. The rate constant of a redox reaction is inversely proportional to its peak separation (E_{pp}).[21] E_{pp} is calculated using the formula:

$$E_{pp} = |E_p \text{ (anodic)} - E_p \text{ (cathodic)}|$$

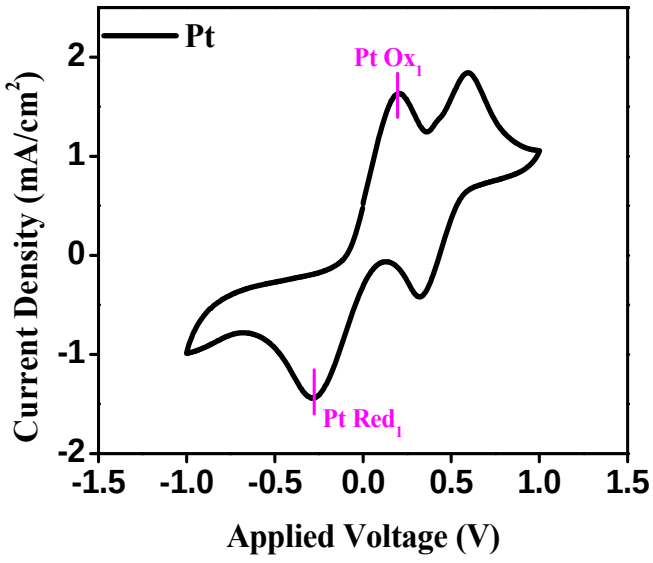

Figure 14. Cyclic voltammogram of Pt counter electrode

Figure 14 shows the cyclic voltammogram of drop-casted and thermally deposited Pt counter electrode. The E_{pp} value for this Pt counter electrode is ~560mV. This E_{pp} value is used for comparison with other counter electrodes which helps to decide the catalytic properties of the counter electrode.

4.4.2. Nickel cobalt Sulphide (NCS) and Nickel cobalt Oxide (NCO) as counter electrodes in DSSC: Cyclic Voltammetry analysis

We discuss the methodology with reference to our studies on NCS and NCO systems.[13] As the counter electrode used for DSSC is responsible for the reduction of I_3^- to I^- , the more negative pair of peaks is our main focus.

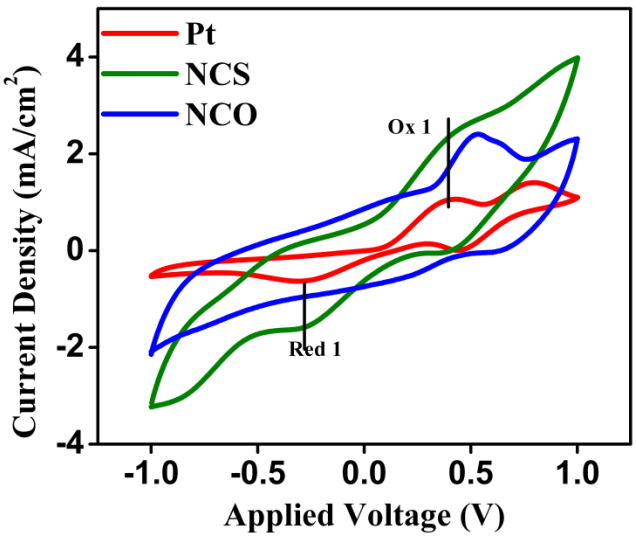

Figure 15. The cyclic voltametry data for Pt , NCS and NCO

From the data shown in Figure15 it is seen that, like Pt, NCS and to some extent NCO also are catalytically active for the reaction to regenerate the redox couple. The current density obtained for the NCS and NCO electrodes are higher than that of Pt. The higher current density may be

due to the high porosity of NCS and NCO films as compared to Pt. Due to the higher thickness, good porosity and elongated structures, there is intimate contact between the electrolyte and the catalyst which leads to a capacitive behaviour in these two cases, giving rise to a higher current. The peak currents and peak to peak separation are important parameters for determining the catalytic activity of counter electrodes. The rate constant of a redox reaction is inversely proportional to its peak separation (E_{pp}). As stated before, in a DSSC context the peak of interest is the peak towards the more negative side. Therefore this peak is used for E_{pp} calculations. The E_{pp} for the NCS counter electrode is ~671 mV and for NCO, it cannot be well defined. Thus, it is clear that both the NCS and Pt drop-casted counter electrodes are catalytically more active towards the reduction of I_3^- to I^- than NCO

4.4.3. Carbon cloth as counter electrode in DSSC: Cyclic Voltammetry analysis

We discuss the methodology with reference to our studies on carbon cloth as counter electrode for DSSCs.[11] The peak at around -0.14V is assigned the reduction reaction of I_3^- to I^-. From the CV data seen in Figure 16 (a) it is clear that the carbon cloth shows good catalytic activity towards the reduction reaction of the I_3^-. The current density observed for the carbon cloth is higher than that for Pt which is due to its higher thickness, porosity and absorption properties. There is an intimate contact of this carbon cloth counter electrode with the electrolyte which gives rise to a capacitive behaviour leading to higher current. Also the catalytic activity of the carbon cloth and Pt counter electrode were compared by determining the peak to peak separation (ΔE_{pp}) values. ΔE_{pp} for Pt and carbon cloth counter electrode were found to be 560 mV and 480 mV respectively with iodide/tri iodide electrolyte. As ΔE_{pp} is inversely proportional to the catalytic activity of counter electrode material, carbon cloth proves to be superior counter electrode due to presence of oxygen containing groups as well as defects in its network. Catalytic

activity of this carbon cloth was also tested for a cobalt redox shuttle and compared with Pt counter electrode as seen in **Figure 16(b)**. The cobalt shuttle used for this study is Chlorophenylterpyridine Cobalt Complex.[22] The electrolyte composed of 0.001M Co^{+2}, 0.0001 M Co^{+3} and 0.01M $LiClO_4$ in acetonitrile. Here Pt wire was used as working electrode, Ag/AgCl as a reference electrode and Pt foil as a counter electrode at a scan rate of 50mV/s ranging from 0 to 0.8V. The oxidation potential for cobalt electrolyte is around 0.38V while the reduction potential is at 0.3V. Thus the $E_{1/2}$ for this cobalt electrolyte in acetonitrile vs Ag/AgCl reference electrode is 0.34V. The carbon cloth shows catalytic activity towards redox reaction of the cobalt shuttle as well due to presence of oxygen containing groups on its surface. The peak to peak separation i.e ΔE_{pp} in cobalt electrolyte for carbon cloth is 200mV while it is 80mV for thermally deposited Pt counter electrode used routinely in DSSCs. Thus this pyrolyzed carbon cloth with surface oxygen containing groups is an efficient catalyst even for cobalt redox shuttle.

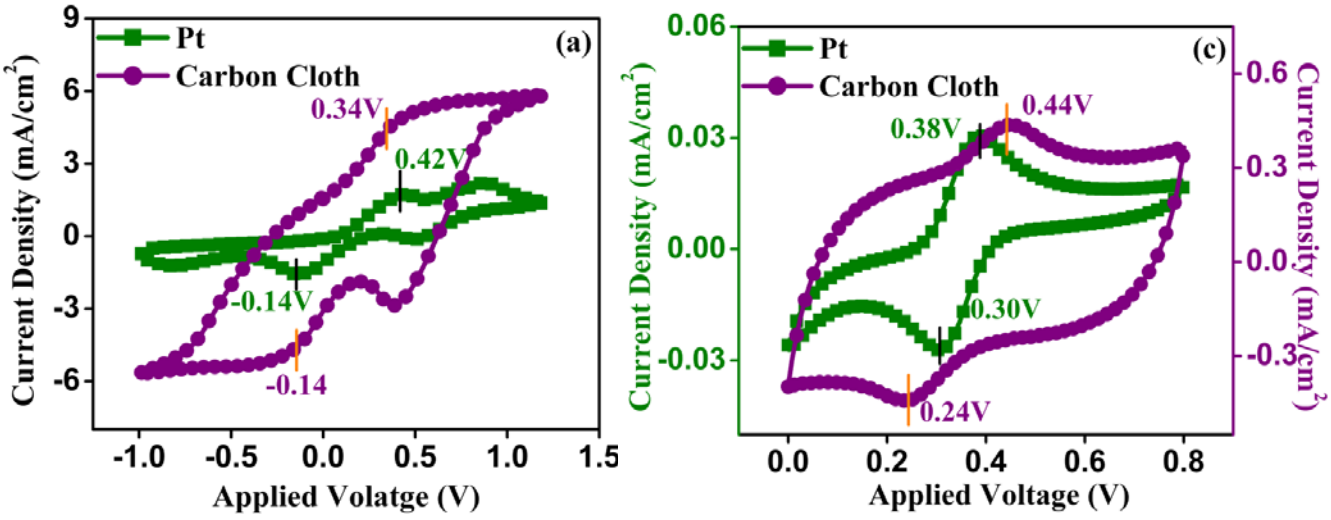

Figure 16. Cyclic voltametry data for Pt and carbon cloth as counter electrodes in (a) iodide tri-iodide electrolyte and (b) cobalt redox shuttle electrolyte.

4.5. Tafel polarization curve

Tafel equation is an electrochemical equation relating the rate of electrochemical reaction to its over-potential. The tafel equation can be written as

$\varepsilon = a + b \log J$ where,

ε is the potential (overpotential), J is the current density and a is empirical constant while b is the tafel slope. A plot of log J (current density) vs the applied potential (V) is known as a Tafel plot. It is useful in evaluating kinetic parameters.[23] Primarily the tafel plot is used to measure the corrosion properties of the electrode. The corrosion resistance and the exchange current density are the parameters extracted from the tafel plot. The exchange current is the current at equilibrium, i.e. the rate at which oxidized and reduced species transfer electrons with the electrode. Thus the Tafel plot can be used to study the electron transfer reactions between the electrodes and the electrolyte. This concept can be extended to counter electrode DSSCs where tri-iodide ions from the electrolyte are reduced to iodide ions by the counter electrode. These iodide ions in turn help in regeneration of the oxidized dye. Thus the conversion of I_3- to I- is a crucial step which can be monitored using the tafel plot. The following section describes the use of tafel plot to determine the performance of various counter electrodes in DSSCs.

4.5.1. Tafel polarization curve for counter electrode in DSSCs

Tafel measurements are also performed in a symmetric cell assembly as described in section 4.3. A cyclic voltammetry program is run but with a slow scan rate of 10-50V/s. Tafel plot usually consists of three parts. The portion of the curve over the lower potential range is the polarization zone, the curve in the middle portion with a steep slope is the Tafel zone (which determines the catalytic properties of electrode) and the third at the higher voltage regime is the diffusion

region.[25] In the Tafel zone the intersection of the tangent to the cathodic branch with the equilibrium (zero) potential ordinate is J_o, which is the exchange current density.[24]

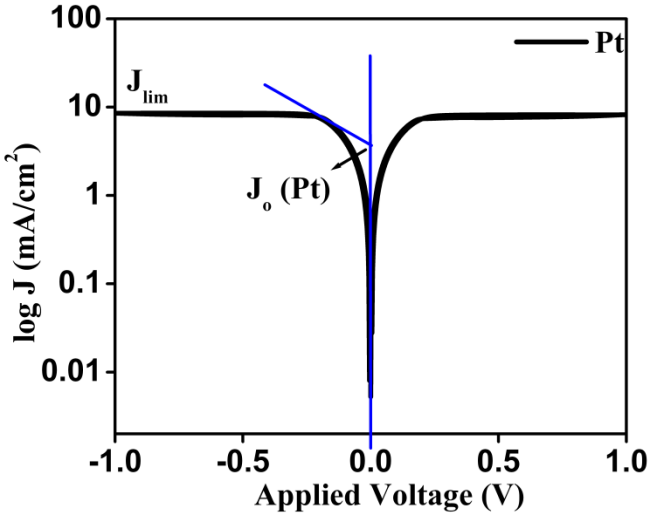

Figure 17. Tafel polarization curve for Pt counter electrode

Thus to analyze the catalytic properties of the counter electrode, Tafel polarization measurements are carried out on counter electrodes in a symmetric cell assembly with iodide/tri-iodide electrolyte. In our experiments the scan rate used was 10 mV/sec.

A high value of J_o indicates higher catalytic activity for reduction of I_3^-. J_o is inversely proportional to R_{ct} from the equation:

$$J_o = RT/nFR_{ct} \ldots\ldots\ldots \quad (vi)$$

Where R is constant, T is temperature, n is the number of electrons involved in reaction, and R_{ct} is the charge transfer resistance.

Another important parameter that can be extracted from this Tafel graph is J_{lim} which is the limiting diffusion current density. J_{lim} for any counter electrode must be higher which implies

better diffusion of electrolyte within counter electrode. It guarantees good contact of electrolyte with the counter electrode.

4.5.2. Nickel cobalt sulphide (NCS) as counter electrode in DSSC: Tafel analysis

In order to illustrate the strength and implications of Tafel analysis we discuss the case of the use of NCS as a counter electrode alluded to earlier.[13]

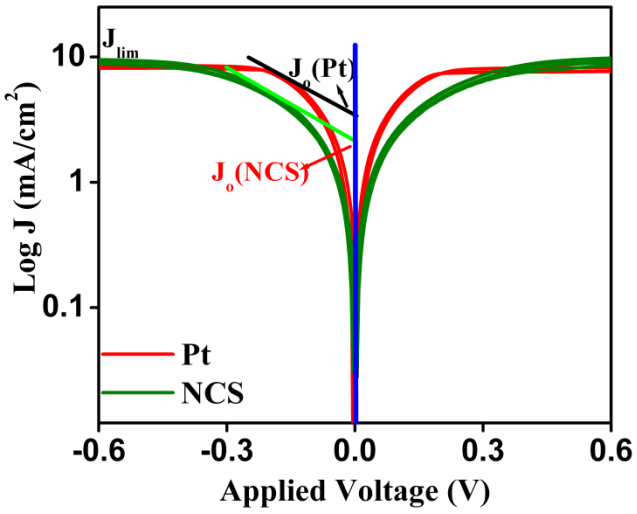

Figure 17. Tafel plot for Pt and NCS counter electrode

Figure 17 shows the tafel plot for Pt and NCS counter electrodes. From the graph obtained it is seen that Pt has higher J_o value than NCS, which indicates that it is more effective in catalyzing the reduction of I_3^-. J_o is inversely proportional to the R_{ct} as seen in equation (vi).This trend is well reflected in the solar cell characteristics of these two as counter electrodes where NCS counter electrode gave an efficiency of 6.9% compared to 7.7% for Pt counter electrode. J_{lim} is the limiting diffusion current density which relates to the easily accessible areas for electrolyte diffusion in counter electrode. J_{lim} for NCS is slightly higher than that of Pt. This may be due to

the porous nature of NCS counter electrode. Thus NCS can be a potentially useful candidate to replace Pt as counter electrode in DSSCs.

4.5.3. Copper Indium sulphide (CIS) and CIS/CuS composite as counter electrode in DSSC: Tafel analysis

We discuss the methodology with reference to our studies on copper indium sulphide (CIS) as counter electrode for DSSCs.[25] Figure18. shows the Tafel plot for Pt, CIS/CuS composite and pristine CIS. These measurements were also carried out in a symmetric cell assembly at a scan rate of 50mV/s.

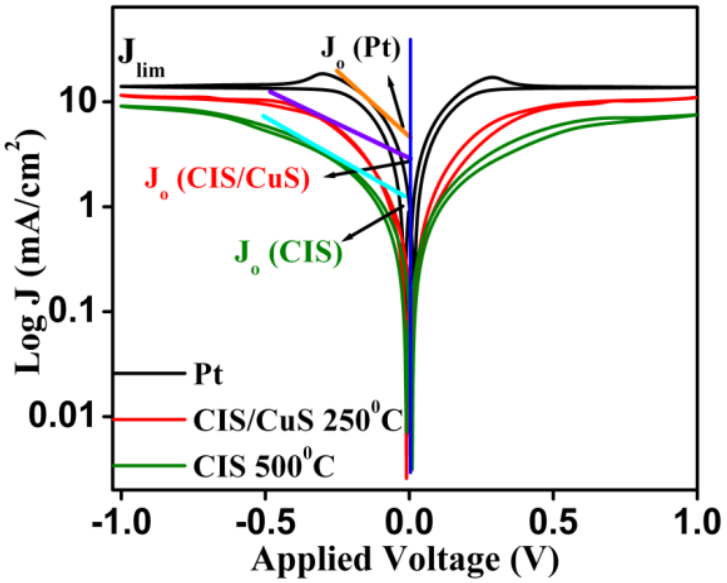

Figure 18. Tafel curve for Pt, CIS/CuS and CIS counter electrodes

A higher J_o for Pt and CIS/CuS counter electrodes implies a better catalytic activity towards I^-/I_3^- redox reaction. Another parameter to be extracted from Tafel plot is the limiting current density

J_{lim} which describes the diffusion of I_3^- ions in the counter electrode. From the graph it is clear that the diffusion of I_3^- ions in the CIS/CuS composite is higher than that of pristine CIS.

4.6. Cyclic voltametry for determination of energy levels of dye

Since DSSC architecture has many components and interfaces which are involved in charge transfer and which dictate the final performance parameters obtained, such as J_{sc} and V_{oc} etc., knowledge about the bands or electronic state distributions of different components in the multilayered hetero-structure assembly is key to understanding and optimization of the device. Towards this end cyclic voltammetry method bears significance. For instance, the HOMO-LUMO band alignment of dye or electrolyte can be calculated using cyclic voltammetry. Here again a three electrode system is used comprising of Pt foil as counter electrode, Pt wire as working electrode and Ag/AgCl as the reference electrode. These three electrodes are dipped in solvent containing the compound for which the HOMO-LUMO levels have to be determined. A routine cyclic voltammetry (CV) scan is run to get the oxidation and reduction peaks of the sample. The concentration of the sample is ~10^{-4}M, while that of supporting electrolyte is at least 10 times higher than that of the sample. The role of supporting electrolyte is to enhance the current so as to give more accurate values for the oxidation and reduction reactions. The solvent used is one in which the sample, the ferrocene standard (ferrocene is used as standard as it undergoes one-electron oxidation at a low potential and that too reversiblely, the oxidation of ferrocene gives ferrocinium ion), and also the supporting electrolyte all have good solubility. Using the standard protocol the electrode potential in non-aqueous solutions was measured against the potential of ferrocenium /ferrocene (Fc^+ /Fc) redox couple. The potential of Ag/AgCl reference electrode was internally calibrated by using the ferrocene / ferrocenium redox couple (Fc/Fc^+), which has a known reduction potential of – 4.8 eV. The highest occupied molecular

orbital (HOMO) was calculated from the onset oxidation potential ($E_{oxidation\ onest}$) using the formula equation (vii).[26]

$$HOMO = -(E_{ox\ onest\ vs\ Fc+/Fc} + 4.8)\ (eV) \qquad (vii)$$

$$E_{ox,\ onset\ vs\ Fc+/Fc} = E_{ox\ sample} - E_{1/2}\ of\ Fc^{+}/Fc$$

The LUMO level is calculated from the UV-Vis absorption maxima. The absorption maxima is converted to eV by using the formula

$$E = 1240/\lambda_{max} \qquad (viii)$$

4.6.1. Determination of HOMO-LUMO levels of organic phenothiazine dye

The solvent used for measurement in this system is a 1:1 v/v mixture of DCM and Methanol. Ferrocene which dissolves in this mixture is used as standard while Lithium perchlorate is used as supporting electrolyte. The concentration of dye was 10^{-4} M and that of supporting electrolyte is 10^{-3} M. First the CV for standard ferrocene is run in the solvent and the E1/2 of Ferrocene is thus calculated from the plot using simple formula

$$E_{1/2} = E_{ox} + E_{red}/\ 2 \qquad (ix)$$

Figure 19 shows CV of pure ferrocene in DCM-MeOH solvent with Lithium perchlorate as supporting electrolyte. The $E_{1/2}$ thus calculated from the plot comes out to be 0.43V. This value is used to calculate the HOMO level of the phenothiazine dye using the formula (vii). Figure 20 shows the CV of phenothiazine dye in the same solvent and with the same supporting electrolyte.

The onset oxidation potential for phenothiazine dye is at 0.57V. Thus $E_{ox,\ onset\ vs\ Fc+/Fc}$ for this phenothiazine dye is ~ 0.14V. Thus the HOMO of this dye can be calculated as -4.94eV wrt vacuum using the formula as stated in equation (vii).

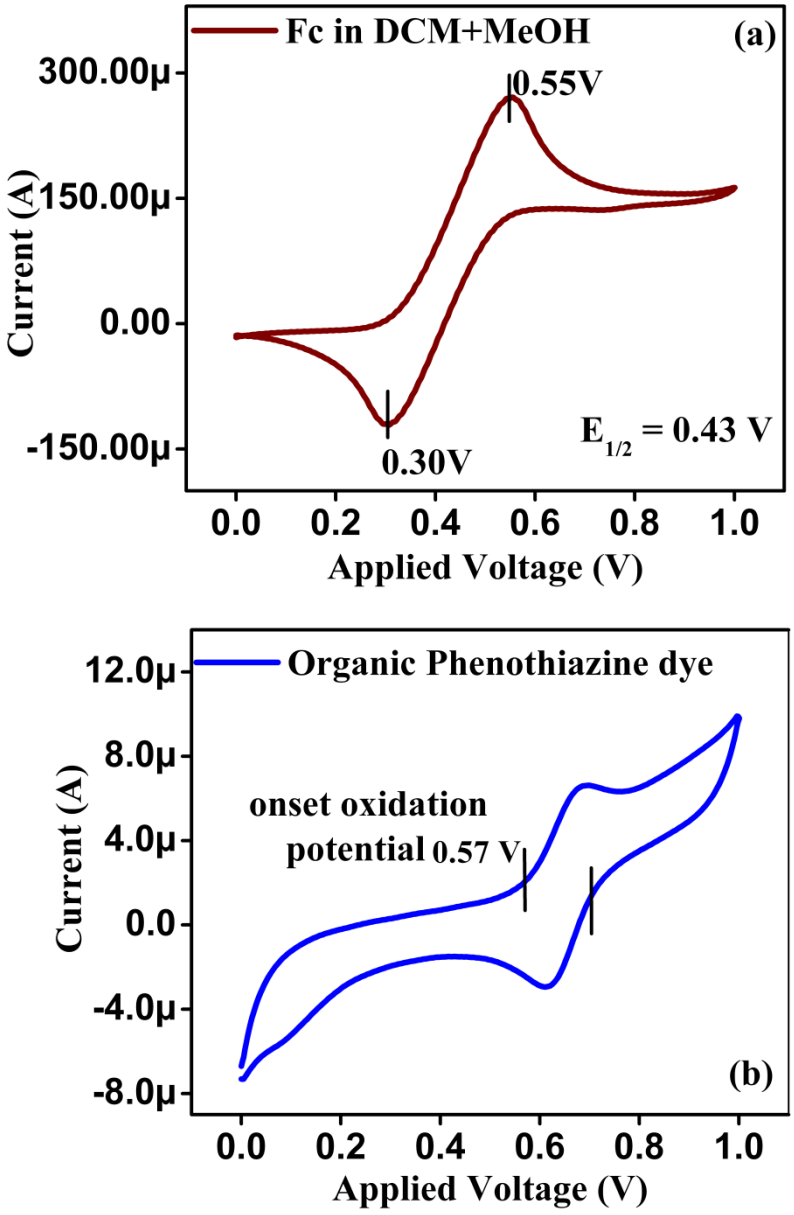

Figure 19. (a) CV of standard Ferrocene and (b) CV of phenothiazine dye in in DCM + MeOH solvent

The LUMO of this dye was calculated from the UV-Vis absorption spectra by using formula (viii). Figure 20 shows the UV-Vis data for phenothiazine dye with λ_{max} value of 274nm. Thus the LUMO can be calculated as ~ 2.6 eV.

Thus the HOMO – LUMO values for phenothiazine dye are -4.92eV and -2.6eV respectively.

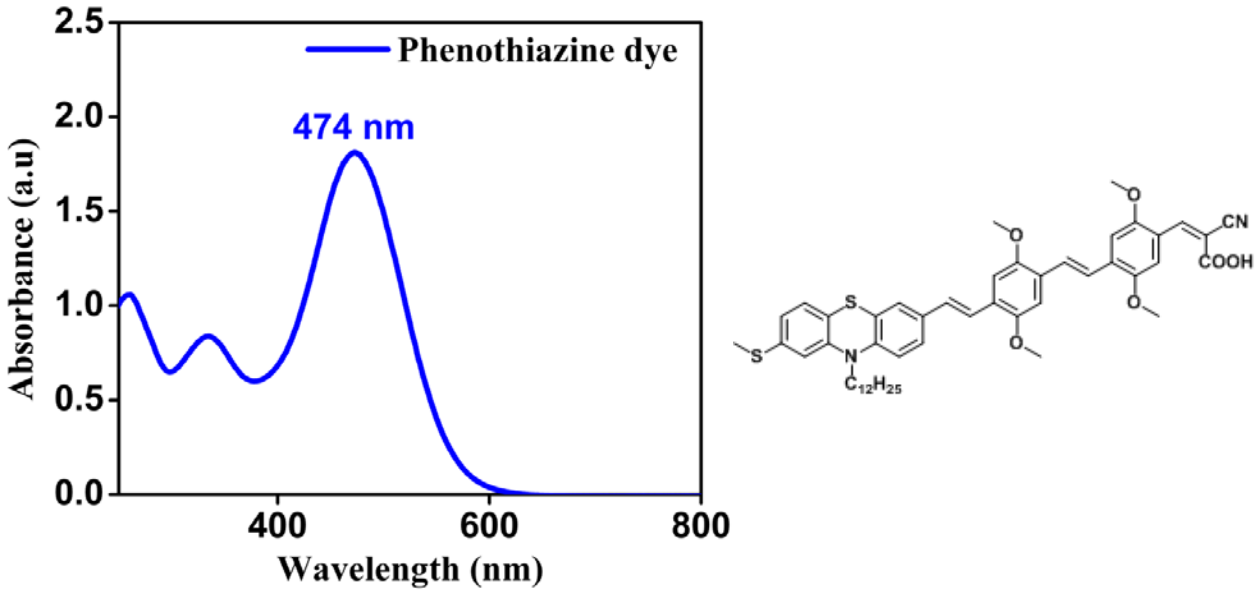

Figure 20. UV-Vis data for Phenothiazine dye along with its structure

Cyclic voltammetry can thus be used to determine the energy levels of various dyes as well as redox electrolyte.

4.7. References

1. Adachi M., Sakamoto M., Jiu J., Ogata Y.; Isoda S, . *J Phys. Chem. B.* **2006**, 110, 13872-13880.
2. R. Kern , R. Sastrawan, J. Ferber, R. Stangl, J. Luther, *Electrochimica Acta* **2002**, *47* 4213/4225
3. Juan B., *J. Phys. Chem. B* **2002,** *106,* 325-333
4. F. Fabregat-Santiago, J.Bisquert, E. Palomares, L. Otero, D. Kuang, S. M. Zakeeruddin, M.Grátzel, *J. Phys. Chem. C* **2007**, *111*, 6550-6560.
5. J. Halme , P. Vahermaa , K. Miettunen and P. Lund, *Adv. Mater.* **2010**, *22*, E210–E234
6. J. R. Jennings, Y. Liu, F. Safari-Alamuti , Q.Wang, *J. Phys. Chem. C* **2012**, *116*, 1556–1562.
7. R. A. Naphade, M. Tathavadekar, J. P. Jog, S. Agarkar, S. Ogale, *J. Mater. Chem. A* **2014**, *2*, 975-984
8. Brian C. O'Regan, James R. Durrant, Paul M. Sommeling and Nicolaas J. Bakker, *J. Phys. Chem. C* **2007**, *111,* 14001-14010.
9. J. Bisquert, *Phys. Chem. Chem. Phys*., **2003**, *5*, 5360–5364.
10. K. Mukherjee, T. H. Teng , R. Jose, *Appl. Phys. Lett.*, **2009**,*95*, 012101
11. M.Tathavadekar, M. Biswala Shruti Agarkar, Lingamallu Giribabu, Satishchandra Ogale, *Electrochimica Acta* , **2014**, *123* , 248–253.
12. M. Wu,. X. Lin, Y. Wang, L.Wang, W.Guo, D.Qi, X. Peng,A. Hagfeldt, M. Grätzel, T.Ma, *J. Am. Chem. Soc.* **2012**, *134*, 3419−3428.
13. A. Banerjee, K. Kumar Upadhyay, S Bhatnagar, M. Tathavadekar, U. Bansode, S. Agarkar and S.B. Ogale, *RSC Adv*., **2014**, *4*, 8289.

14. R. Gokhale, S. Agarkar, J.Debgupta, D.Shinde, B. Lefez, A.Banerjee, J.Jog, M. More, Beatrice Hannoyer , S. Ogale, *Nanoscale*, **2012**, *4*, 6730.
15. Y.-H. Lai, C.-Y. Lin, H.-W. Chen, J.-G. Chen, C.-W. Kung, R. Vittal, K.-C. Ho, *J. Mater.Chem* , **2010**, *20*, 9379.
16. S- H.DuVall , R. L. McCreery , *Anal. Chem.*, **1999**, *71*, 4594–4602.
17. R. S. Nicholson, *Anal. Chem.*, **1965**, *37*, 1351–1355
18. B. J. Sanghavia, S. M. Mobina, P. Mathurb, G.K. Lahirib, A. K. Srivastava, *Biosensors and Bioelectronics*, **2013**, *39*,124–132.
19. F. Gong, X. Xu, Z. Li, G. Zhou, Z-S. Wang, *Chem. Commun.*, **2013**, *49*, 1437-1439.
20. W. J. Lee, E. Ramasamy, D. Y. Lee and J. S. Song, *ACS Appl.Mater. Interfaces*, **2009**, *1*, 1145.
21. Understanding Voltammetry, ed. R. G. Compton and C. E. Banks, World Scientific Publishing Co. Pte. Ltd, **2007**
22. P. Salvatori, G. Marotta, A. Cinti, E. Mosconi, M. Panigrahi, L. Giribabu, M.K.Nazeeruddin, F. De Angelis, *Inorganica Chimica Acta* , **2013**,*406* ,106–112.
23. B. Zhang, D. Wang, Y. Hou, S. Yang, X-H. Yang, J-H. Zhong, J. Liu, H-F. Wang, P.Hu, H-J. Zhao, H-G. Yang, *Sci Rep.* **2013**, *3*,1836.
24. Chung-Wei Kung, Hsin-Wei Chen, Chia-Yu Lin, Kuan-Chieh Huang, R. Vittal and Kuo-Chuan Ho, *ACS Nano*, **2012**, *6*, 7016-7025.
25. R. K. Bhosale, S. A. Agarkar, I. Agrawal, R.A. Naphade and S. Ogale, *RSC Advances*, DOI: 10.1039/c4ra01740d
26. C. M. Cardona, W. Li, A.E. Kaifer, D. Stockdale and G. C. Bazan, *Adv. Mater.* **2011**, *23*, 2367–2371.

Chapter 5

Isobutrin from Butea Monosperma (Flame of the Forest): A Promising New Natural Sensitizer Belonging to Chalcone Class

In this work, we introduce a new class of sensitizers, i.e., Chalcones, for dye sensitized solar cells and possibly other optoelectronic applications. Chalcones belonging to the flavonoid group are aromatic ketones that form the central core of a variety of important biological compounds, and are known collectively by the said name. They exhibit a broad spectrum of biological activities. Butea monosperma (Fabaceae) is a medium sized deciduous tree found in South Asian countries with bright red orange flower clusters. It is commonly called as the "Flame of the Forest" due to its fire like appearance when in full blossom. The flowers of Butea monosperma contain various flavonoidal compounds such as are butein, isobutrin, butrin, palasitrin etc., of which isobutrin is one of the major constituents. Isobutrin is a bright yellow colored dye with M.P ~191^{o}C. In DSSCs, purified isobutrin yields very promising solar conversion efficiency of 1.8%. Interestingly the chelation of isobutrin to Ti shifts the optical absorption toward the visible (orange) making it effective in the DSSC operation.

Shruti A. Agarkar *et al* ***ACS Applied Materials and Interfaces***, **2011**, 3, 2440–2444.

5.1. Introduction

Solar energy is the most abundant, clean and green source of renewable energy and it can be harnessed via different routes in the interest of diverse applications. In many applications such as dye-sensitized solar cells (DSSCs), photocatalysis, solar to-chemical conversion, etc., sensitizers with good optical properties over the visible range are essential.[1] Although a number of molecular sensitizers in the form of organic dyes (including heavy metal ion incorporated ones) have been synthesized and are being used, the corresponding methods of synthesis, application and prolonged use are not eco-friendly. It is therefore highly desirable to explore sources of new natural dye systems that are stable, nontoxic (biocompatible), and with the desirable optoelectronic properties.[2]

In the case of DSSCs a number of factors such as the choice of the photo-anode, the dye, the bottom layer, the counter electrodes, etc., can limit the cell performance,[3] and a quantitatively significant stable electronic anchorage of the dye to the surface of the metal oxide nanostructure (e.g., TiO_2, ZnO) is a critical factor that determines the cell efficiency.[4] Among the various dyes that have been tested as sensitizers, ruthenium-based dyes have given the highest efficiency of ~11% on the laboratory scale.[5,6] The main advantage of Ru-based dyes is their efficient metal to ligand charge transfer.[4,7] However, their high cost due to complex synthetic procedures as well as environmental hazards posed by the presence of heavy metals invite search for safer and cheaper alternatives.[8] There have been some interesting explorations of natural dyes in the context of the dye-sensitized solar cell (DSSC) application using pigments obtained from biomaterials such as flowers, fruits and leaves.[9-16] The natural pigments commonly extracted from flowers and fruits are anthocyanins.[9-12] Anthocyanins give colors ranging from red to blue depending on the pH of the medium. The hydroxyl groups present in the anthocyanin molecule help in the binding of this

dye to the TiO_2 surface.[9] The maximum efficiency obtained by use of anthocyanins, i.e., juice obtained from Hibiscus sabdariffa, is 3.1%.[17] The problem with anthocyanins is that they are pH sensitive, i.e., good binding with TiO_2 occurs only if anthocyanin is present as flavylium ion species (which is stable) at pH around 1 to 3.2, but if pH is increased this ion gets hydrated to form quinoidal bases.[9] These quinoidal compounds are labile and can be transformed into colorless compounds.[18] If pH becomes more acidic <1 then the compound itself is leached out.[19] Maintaining the right pH is nontrivial and at the same time a very crucial step while extracting anthocyanins. They are also thermally unstable.[9] At high temperature the thermal degradation of anthocyanin takes place by loss of glycosyl moieties and α diketone formation. [20,21] If extracted at a temperature lower than 25^{o}C, then the issue of solubility of dye arises, which in turn leads to low efficiency of DSSCs. Porphyrins, which form the structural core of chlorophylls, the natural light harvesters, have also been examined as another class metal-porphyrin dyes that show conversion efficiency of 7.1%. In 1994, M. Grátzel studied the mechanism of photosensitization of TiO_2 solar cells by chlorophyll derivatives.[13] In 1986, Kamat and co-workers also explored the use of a chlorophyll analogue as a sensitizer for DSSCs.[14] Natural chlorophyll extracted from Shiso leaves was used as sensitizer by Kumara et al.,[23] which showed efficiency of 0.59%. Isolated chlorophyll was used along with shisosin (an anthocyanin) to realize a synergistic effect that gave efficiency of 1.31%. Betalain pigments extracted from red beet root were also used as dyes which gave efficiency of 0.19%.[24] More recently, Wang and co-workers have done interesting studies on the chlorophyll system and have also modified the dye with metal conjugation to enhance efficiency.[25]

In this work, we introduce a new class of sensitizers, i.e., Chalcones. Chalcones belonging to the flavonoid group are aromatic ketones that form the central core of a variety of important

biological compounds, and are known collectively by the said name. They exhibit a broad spectrum of biological activities. Butea monosperma (Fabaceae) is a medium sized deciduous tree found in South Asian countries with bright red orange flower clusters. It is commonly called as the "Flame of the Forest" due to its fire like appearance when in full blossom. The flowers of Butea monosperma contain various flavonoidal compounds such as are butein, isobutrin, butrin, palasitrin, etc., of which isobutrin is one of the major constituents. Isobutrin is a bright yellow colored dye with M.P ~191^{o}C.

5.2. Experimental

5.2.1. TiO_2 Sphere Synthesis. TiO_2 spheres were synthesized following the work of Caruso et al.[26] Trasparent TiO_2, which was used as bottom later, was purchased from Solaronix (Switzerland).

5.2.2. Characterization of Physical Properties. The sysnthesized nanoparticles were characterized using FTIR (Perkin-Elmer Instruments), UV-vis and DRS (Jasco Instruments), Transmission electron microscopy (FEI), and X-ray diffraction (Pan-Analytical).

5.2.3. Extraction and Purification of Isobutrin dye. Butea monosperma Flowers were collected from Mulshi, Pune, India. Petals (1400g) were separated and squeezed to acquire the juice. Residual pulp was extracted with methanol by cold maceration method to yield methanol extract, 65.1g (4.65% based on fresh petal weight). This juice (718 ml) was lyophilized (4.8%) and subjected to column chromatography on silica gel (100-200 mesh) using a gradient of methanol in chloroform (5 to 100%) as mobile phase to obtain two pigments A and B. Both pigments were tested as sensitizer of which B gave interesting results. The pigment B was found to be a mixture of two compounds in proportion 70-30 by ^{1}H and ^{13}C NMR. This mixture was again subjected to column chromatography on silica gel (100-200 mesh) using mobile phase

methanol: ethyl acetate: water (8:32:1) to separate one colorless compound and another yellow colored isobutrin. Isobutrin was isolated from methanolic extract by column chromatographic techniques as mentioned above. Isolated isobutrin was further purified by crystallization from methanol to obtain isobutrin with the yield of 2.5g, 0.18% (juice and pulp extract combined).

5.2.4. Fabrication and Testing of DSSCs. To make and study the DSSC solar cells, we employed the doctor blading method. After making the films they were annealed at 450^{o}C for 60 min. For sensitization, the films were dipped in samples viz. juice, separated fraction (aqueous methanol), and isobutrin (5 mM in methanol) for 24 h at room temperature (in separate experiments) and also with 0.5 mM N719 dye in ethanol for comparison. The samples were then rinsed with methanol to remove excess dye on the surface and air-dried at room temperature. This was followed by redox electrolyte addition and top contact of Pt coated FTO. The electrolyte used was 0.6M 1-propyl-2, 3 - dimethyl-imidazolium iodide, 0.1 M LiI, 0.05 M I_2, and 0.5 M 4-tertbutylpyridine in acetonitrile.[27] The I-V characteristics were measured under exposure with 100 mW/cm^2 (150W xenon lamp, Newport Instruments), 1 sun AM 1.5, simulated sunlight as a solar simulator. The current was measured using a Kiethley 2400 source. Measurements of the incident-photon-to-current conversion efficiency (IPCE) were performed by changing the excitation wavelength (Newport Instruments). In one set of experiments, the cells were heated to different temperatures up to 200^{o}C for 1/2 h and their efficiency was tested after cooling to the room temperature (for thermal stability of the dye).

5.2.5. Characterization of the Sensitizer. The ^{1}H, ^{13}C NMR and DEPT spectra were recorded on Bruker-AV 400 spectrometer operating at 400 and 100 MHz, respectively, in methanol-d4 (Sigma-Adrich) using TMS as the internal standard. The chemical shift values are reported in ppm (δ) units and the coupling constants (J) are in Hz. ESI-MS was recorded on API-QSTAR-

PULSAR mass spectrometer. The extract was subjected to column chromatography using silica gel (Spectrochem, India) having a 100-200 mesh size. All solvents were distilled prior to use. Isobutrin structure was confirmed by comparison of its physical constants and spectral properties (^{1}H and ^{13}C NMR and mass spectroscopy) with those reported in the literature.

Isobutrin: Yellow crystals (mp 191^{o}C). 1H NMR (400 MHz, methanol-d4, δ): 7.99 (d, J = 8.39 Hz, 1H; 60-H), 7.71 (d, J = 14.9Hz, 1H; β-H), 7.61 (d, J = 1.55 Hz, 1H; 2-H), 7.55 (d, J = 14.9 Hz, 1H, R-H), 7.27 (dd, J = 8.19, 1.55 Hz, 1H; 6-H), 6.83 (d, J = 8.19 Hz, 1H; 5-H), 6.62 (dd, J = 8.39, 2.22 Hz, 1H; 50-H), 6.6 (d, J = 2.22 Hz, 1H; 30-H), 3.17 to 5.13 (m, 14H, sugar H). 13C NMR (100 MHz, methanol-d4, δ): 192.58 (C = O), 163.59 (C-2'), 156.17 (C-40), 149.91 (C4), 145.71(C3), 144.86 (Cβ), 131.82 (C60), 127.00 (C1), 125.87 (C6), 117.45 (CR), 116.47 (C5), 116.10 (C50), 115.07(C10), 108.05(C2), 99.69(C30). MS (ESI, m/z): 619 $[M + Na]^{+}$.

The available binding sites in isobutrin for metal are the two phenolic –OH groups and one carbonyl group C=O which is in conjugation with the double bond. But the stearically favored Ti binding site is at the hydroxyl group on ring B of isobutrin as shown in Figure.1

Figure 1. Butea monosperma flower, isobutrin dye, and its structure elucidated from ^{1}H and ^{13}C NMR studies.

5.3. Results and Discussion

5.3.1. Extraction and Structure Elucidation. In this work we have extracted, isolated and characterized the isobutrin dye and studied its potential use as a sensitizer in DSSCs. We confirmed the structure of the extracted isobutrin by comparison of its physical constants and spectral properties (^{1}H, ^{13}C NMR and Mass Spectroscopy) with those reported in the literature,[28] as shown in Figure 1 and discussed in Experimental Section. The available binding sites in isobutrin for Ti are the two phenolic -OH groups and one carbonyl group C=O, which is in conjugation with the double bond.

5.3.2. FTIR Spectra. FTIR spectra were recorded for the cases of pure TiO_2, Isobutrin and TiO_2 - Isobutrin. The characteristic peaks of isobutrin are at wave numbers around 3338, 1641, 1561, 1362, 1218, 1075 cm^{-1}. Out of these the peak at 1641 cm^{-1} corresponds to C=O carbonyl group and 1362 cm^{-1} corresponds to phenolic -OH. Rest of all the peaks are the characteristic peaks of the aromatic ring as shown in Figure 2(a). The two phenolic -OH groups (rings A and B) are the potential sites for Ti conjugation. Ring A has the enone group, which is a chromophore. Ring B on the other hand is connected to this enone group through σ bond. In certain possible conformations of the molecule, ring B and the glucose molecule present a stearic hindrance for the -OH site on ring A, while in other possible conformations the hindrance is not presented. Thus, it is likely that both the phenolic -OH groups could be partially conjugated, although it is hard to determine the precise ratio of the contributions of the two. In any case, this should lead to a substantial reduction in the FTIR contribution of the phenolic -OH group, as observed (Figure 1 (b, c)). When we compare the intensity ratios of peak A2 (phenolic -OH signature) to peak A1 (carbonyl signature) in the cases of only isobutrin dye and the TiO_2 - isobutrin conjugate, it is clear that the A2/A1 ratio is significantly reduced in the case of TiO_2-Isobutrin.

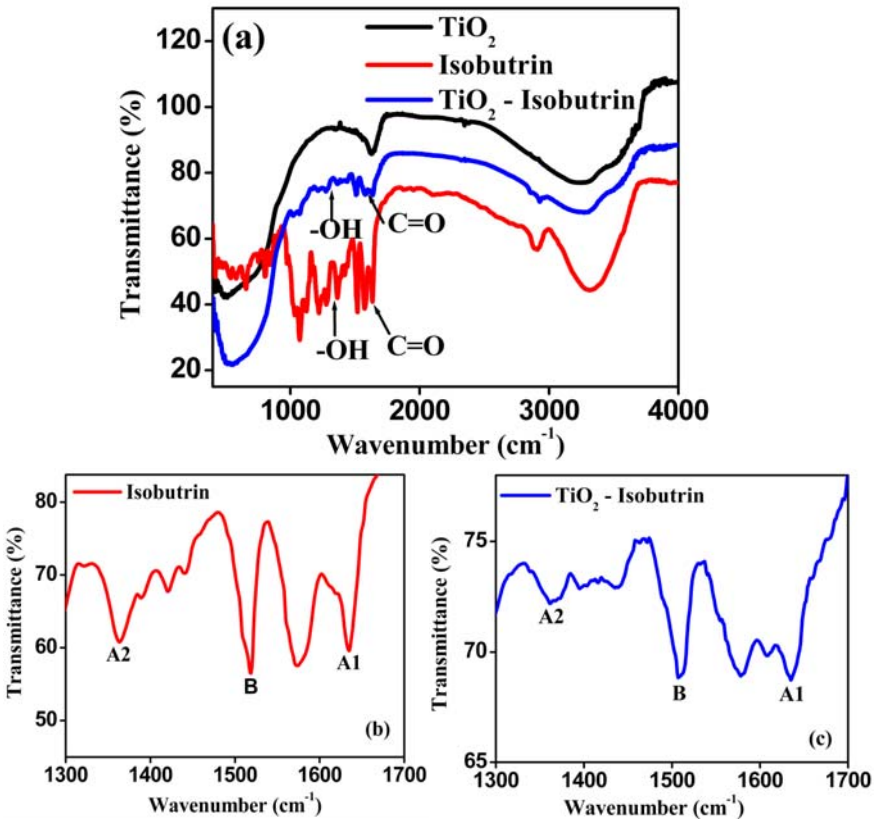

Figure 2. (a) FTIR spectra of pure TiO_2, isobutrin and TiO_2 – isobutrin, (b) Isobutrin (magnified) and (c) TiO_2 – Isobutrin (magnified).

5.3.3. UV-Vis and DRS spectra. From the UV-vis spectra of Figure 3(a), it is seen that the λ_{max} for the juice and the purified isobutrin (bright yellow color as shown in inset) is at ~370 nm. Because the absorption by isobutrin in the visible is only as an extended tail, one would think that this may not be effective for sensitization. However, we observed a very interesting aspect that its metal chelation shifts the absorption edge significantly toward the visible, as shown in Figure 3(b). The diffuse reflectance spectra (DRS) of Figure 3(c) bear out the proposition showing significant absorption over the visible range from 400 to 650 nm.

According to Yoon et al.,[29] chelation of organic ligands with Ti (IV) ions can lead to strong dye-TiO_2 charge transfer (DTCT) bands in the visible region. This falls under the category of type II

dyes where the electron injection occurs directly from the HOMO of the dye to the CB of TiO_2 by photoexcitation. The hydroxyl groups on the molecule bind strongly with TiO_2 giving rise to strong DTCT bands in the visible region.

Similarly, in our work, we have observed that isobutrin forms a chelate with Ti (IV) ions through -OH group(s), because of which its optical absorption shows a significant shift toward orange. Indeed, after removal of TiO_2 films from this dye following the 24 h dye loading process, its color changes to dark orange as shown in the inset of Figure 3(c).

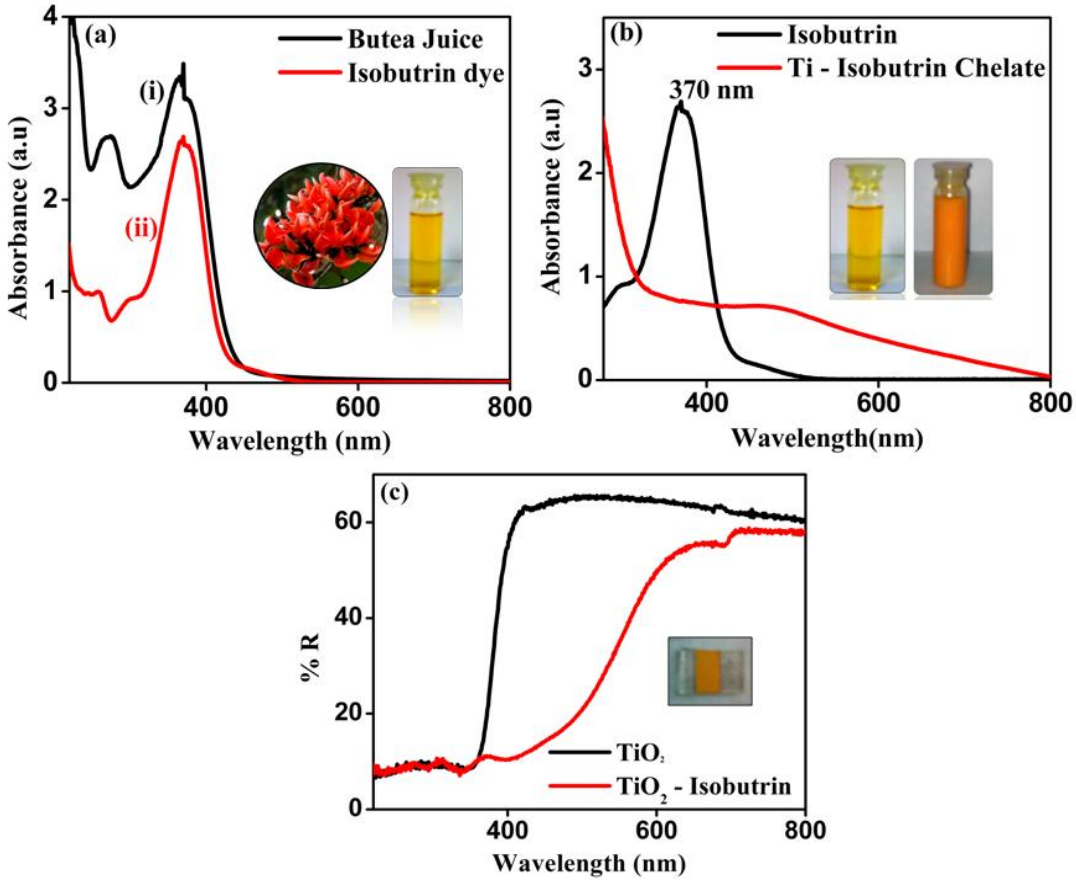

Figure 3. (a) UV-vis absorption spectra of butea juice and pure isobutrin, (b) UV-vis absorption spectra of pure isobutrin and Ti-isobutrin chelate, (c) diffuse reflectance spectra (DRS) of TiO_2 nanoparticle film and isobutrin dye-loaded TiO_2 film.

5.3.4. Benesei-Hildebrand Plot. We examined the evolution of the UV-vis absorption spectra as a function of the concentration of Ti (while keeping the concentration of Isobutrin constant) to reveal the formation steps of Ti-isobutrin chelate. In this experiment, Titanium Tetra Iso-propoxide (TIP) of various concentration was added (0.002-0.04M) to 5 mM isobutrin solution in methanol. UV-vis spectra of this solution were recorded and are presented in Figure 4(a). From the graph, it is clear that the addition of Ti to Isobutrin progressively shifts the absorbance toward the visible region (peak near 480 nm).

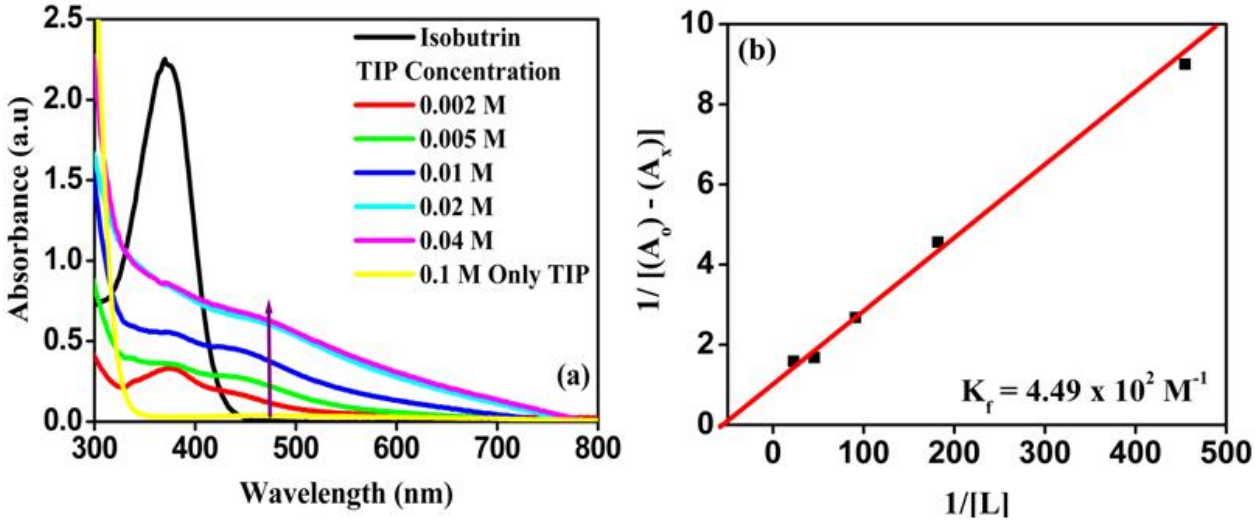

Figure 4. (a) UV-vis Spectra of Ti-isobutrin at various concentrations,

(b) B-H plot of Ti-isobutrin chelate.

As the concentration of Ti is increased, the peak at 370 nm (attributed to Isobutrin) is seen to disappear even at small concentrations of Ti and the spectral weight appears to shift to the visible region. The formation constant (K_f) and its stability can be calculated using the B-H (Benesi-Hildebrand) plot.[30, 31] Figure 4(b) shows the B-H plot for our case. From the graph the value of K_f is found to be ~4.49 x10^2 M^{-1} which testifies to the ease of its formation from equation.

$1/A_o-A_x = 1/(A_o-A) + 1/(A_o-A_x) \times [1/K_f \times 1/(L)]$ Where,

A_o = Abs when L (ligand) = 0 (i.e. only TiO_2); A_x = Abs with Ligand (TiO_2-Isobutrin chelate)

A = Abs when conc of L is high (isobutrin); K_f = Formation constant; L = Ligand (Isobutrin) conc. The formation constant K_f was calculated as K_f = slope/intercept.

5.3.5. DRS for Ti-Isobutrin Chelate. In order to explore the isobutrin-TiO_2 interaction further, we studied diffuse reflectance spectra (DRS) of the chelate with respect to concentration as shown in Figure 5. Here the concentration of isobutrin was varied keeping the concentration of TiO_2 constant.

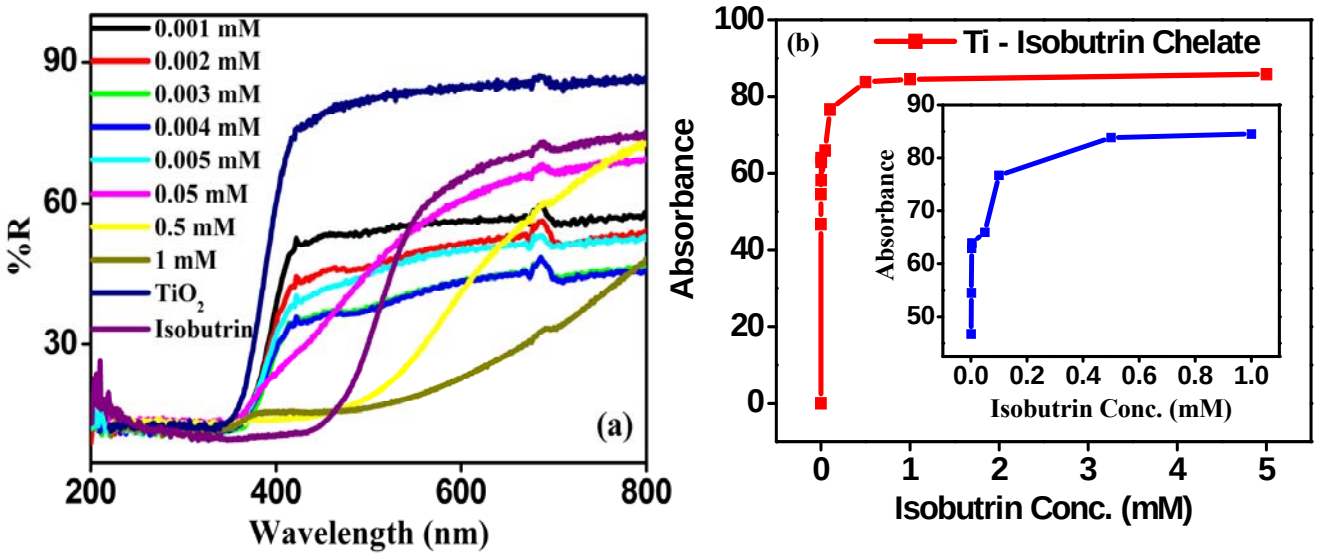

Figure 5. (a) Diffuse reflectance spectra of Ti-isobutrin at various concentrations (b) Graph of concentration of Isobutrin vs absorbance of chelate inset shows expanded scale to show saturation

From the DRS data it is seen that as the concentration of Isobutrin is increased from 0.001 mM to 1 mM the characteristic band of TiO_2 is modified due to chelation of isobutrin with Ti. The UV absorbing TiO_2 now shows prominent absorption in the visible region for the conjugate and

this absorption goes on increasing with the concentration of Isobutrin until it reaches saturation at ~0.5 mM.

5.3.6. Band Alignment. Figure 6 shows the results of HOMO-LUMO alignment of Ti-isobutrin chelate and pure isobutrin dye as calculated from cyclic voltametry using three electrode system as discussed in detail in chapter 4 section 4.6.

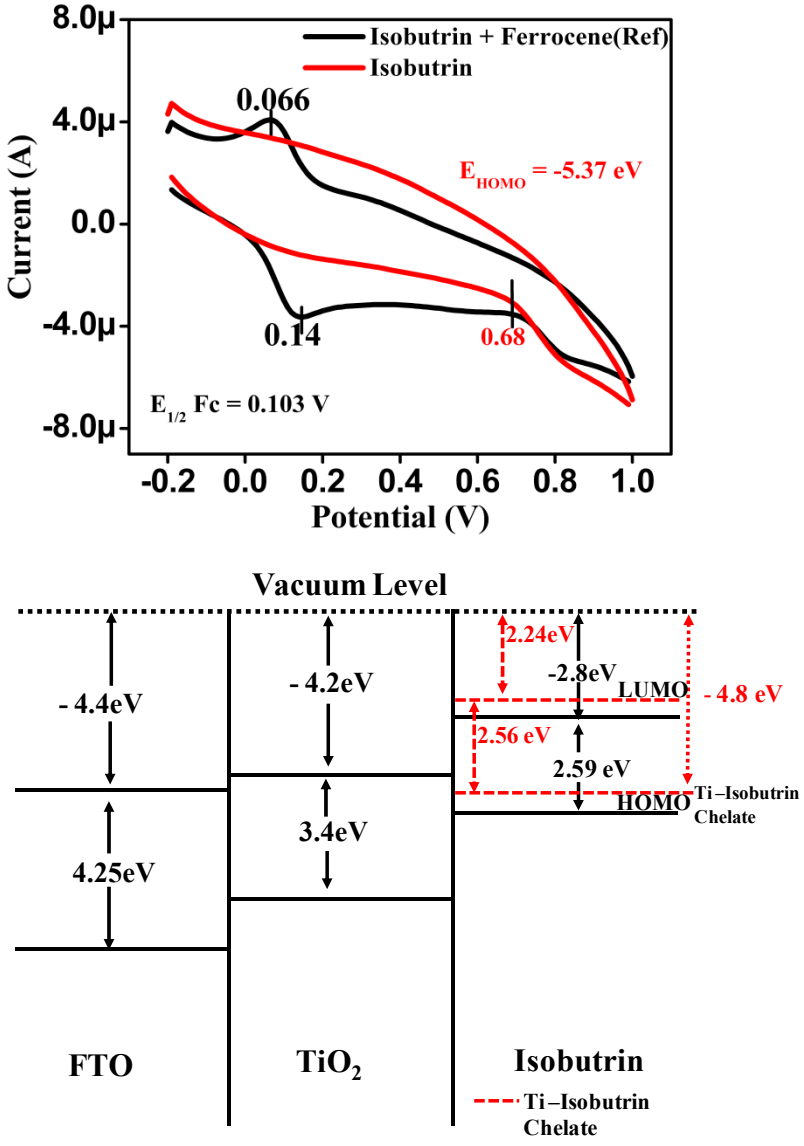

Figure 6. Cyclic Voltametry data of isobutrin dye and Band alignment of isobutrin dye with TiO_2

It is found that the HOMO of Ti-isobutrin chelate is at ~4.8 eV and that of pure isobutrin dye is at ~5.4 eV with reference to the vacuum level. Thus after chelate formation the HOMO of isobutrin has shifted by 0.6 eV toward the positive side. This gave us an insight of the electron transfer process occurring in this isobutrin natural dye-sensitized solar cell.

5.3.7. Fluorescence Lifetime Measurements. To monitor the charge-transfer (CT) process in the isobutrin-TiO_2 system, we performed fluorescence lifetime measurements. These were carried out for isobutrin dye and Ti-isobutrin chelate in methanol and the data are shown in Figure 7. The samples were excited by a 440 nm diode laser (IBH, UK, NanoLED-440 L). The fluorescence signal of 550 nm was collected in magic angle using CP-PMT (Hamamatsu, Japan) detector. The Instrument response function is ~120 ps.

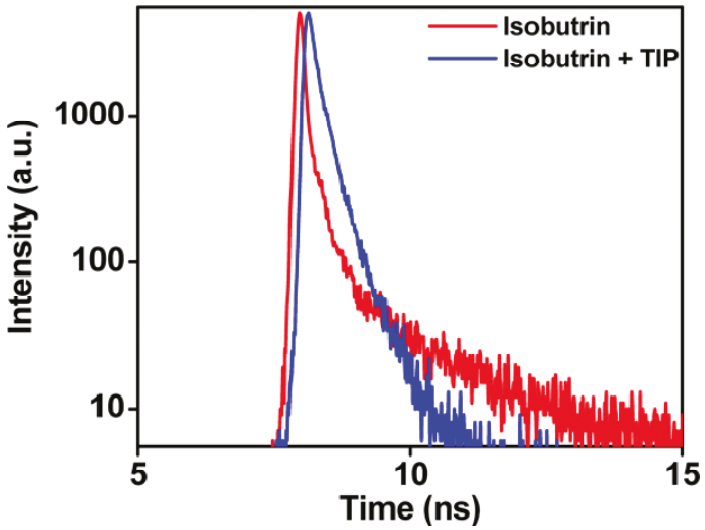

Figure 7. Florescence lifetime measurement of isobutrin and Ti-isobutrin chelate

It was found that chelation led to substantial quenching of the long lifetime component but the lifetime of the short lifetime component was seen to have increased. The τ_1 value for isobutrin was found to be 0.04 ns, while that for the chelate case to be 0.095ns. This change can be attributed to the conformational changes taking place in isobutrin during chelation and related

hybridization changes. These observations are a testimony to the fact that chelation influences the electronics states and the attendant optical effects significantly. More work is clearly needed to elucidate these matters further.

5.3.8. Photoluminescence Spectra. The photoluminescence spectra (PL) of Isobutrin dye and its Ti-chelate are shown in Figure 8. The isobutrin dye shows emission at 550 nm (2.545 eV) and the maximum in the excitation is at 453 nm (energy ~ 2.74 eV).

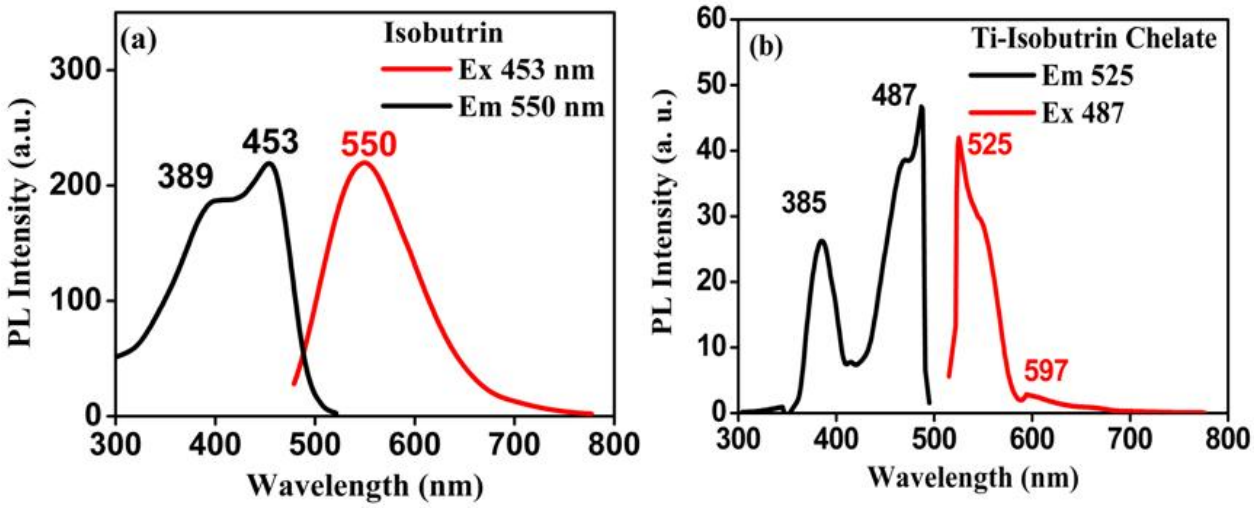

Figure 8. Photoluminescence Spectra of (A) Isobutrin Dye and (B) Ti- Isobutrin Chelate

Thus the e-h binding energy is ~0.19 eV. It may be seen that the absorption becomes notable above ~ 475 nm or 2.6 eV, which matches very well with the HOMO-LUMO difference in Schematic 1. In the case of the Ti-chelate the excitation maximum is red shifted to 487 nm (2.54 eV) which also matches rather correctly with the corresponding level difference depicted in the band alignment. The chelation can be seen to render the electronic states more compact and of course red-shifted.

5.4. Solar Cell Characteristics

5.4.1. I-V data at different stages of isobutrin dye purification. Figure 9 (a) shows the I-V data for the case of anatase TiO_2 nanoparticle films using isobutrin dye at different stages of purification. It is seen that the juice gave a low total conversion efficiency of ~0.3%. This is because the self-extracted juice contains fatty material, high amount of sugars and polysaccharides as well as other pigments which might compete for the binding sites, thereby hindering the process of adequate and effective anchorage of the dye on TiO_2 particles.

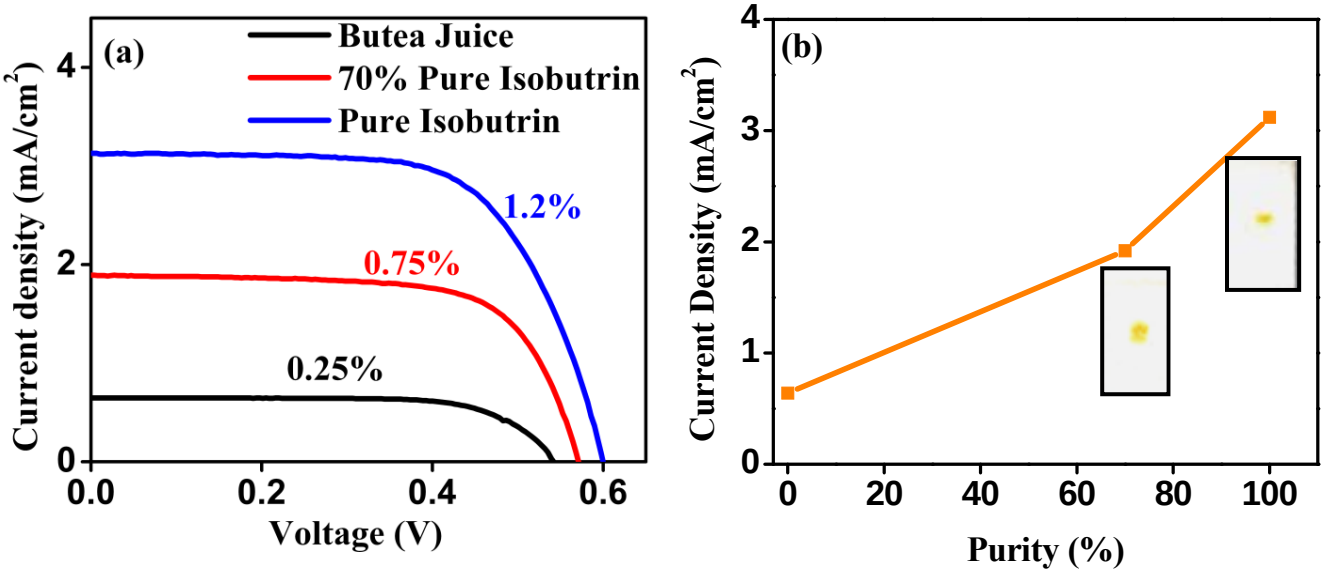

Figure 9. (a) Solar cell characteristics for the case of anatase TiO_2 nanoparticle films using isobutrin dye at different stages of purification (b) Current density in isobutrin sensitized TiO_2 with respect to the stages of purification.

Figure 9 (b) shows the TLC plates showing the cases of purified dye and the 70% purified dye which is seen to contain 2 compounds. Pure isobutrin binds well to TiO_2 as there is no competition anymore for the binding sites. Hence the short circuit current value increases gradually from 0.16 mA to 0.7 mA (current density from 0.6 mA/cm^2 to 2.8 mA/cm^2) as we go

from the juice to pure Isobutrin as shown in figure 9 (a) and (b). The open circuit voltage also increases for pure Isobutrin as compared to juice as here the rate of back electron transfer is minimized. This increase in open circuit voltage (V_{oc}) and current density (J_{sc}) is responsible for increase in efficiency from 0.3% for the juice to 1.2% for pure Isobutrin. We note that this efficiency value is obtained without any light harvesting over layer.

5.4.2. Effect of film thickness on I-V data. Figure 10 shows the I-V data for the case of anatase TiO_2 nanoparticle films using pure Isobutrin dye. Here, light harvesting (LH) architecture was used. Wherein a highly transparent (HT) TiO_2 layer of thickness varying from 2 to 6 micrometers was used as a bottom layer followed by a light harvesting layer of TiO_2 spheres of thickness ~6 μm (each sphere of diameter around 400 nm).

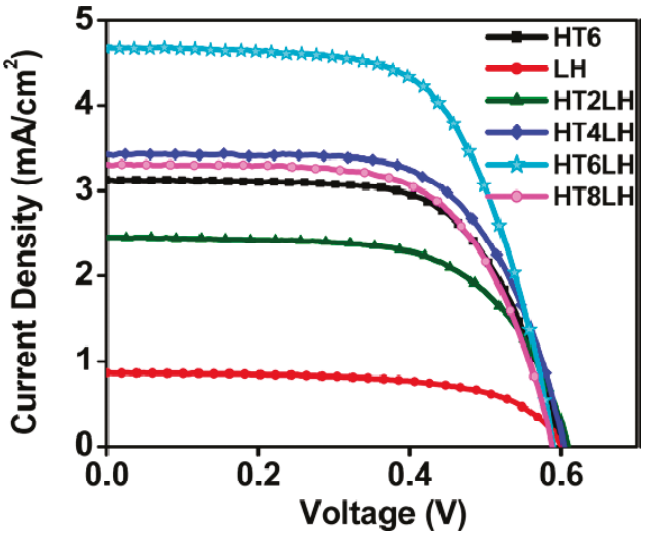

Name	V_{oc} (V)	J_{sc} (mA/cm²)	FF (%)	η (%)
HT6	0.6	3.12	65.5	1.2
LH	0.6	0.86	62.3	0.32
HT2LH	0.6	2.44	63.8	0.95
HT4LH	0.6	3.42	64.8	1.3
HT6LH	0.58	4.67	64.1	1.8
HT8LH	0.59	3.31	64.4	1.3

Figure 10. Solar cell characteristics for the case of anatase TiO_2 nanoparticle + light harvesting layer along with I-V parameters table.

Table 1 shows the data for various thickness values of the bottom layer with constant thickness of LH layer. The optimum thickness of HT was found to be 6 μm, which gave short circuit

current density of 3.12 mA/cm^2 and open circuit voltage of 0.6 V, which gave efficiency of 1.2%. By using LH layer of 6 μm thickness over this optimized thickness of HT layer, current density increased to 4.67 mA/cm^2 and gave a conversion efficiency of 1.8%.

5.4.3. Incident Photon to Current Conversion Efficiency. Figure 11 shows the IPCE spectra as a function of the wavelength for TiO_2 sensitized with Isobutrin. It was calculated from the equation: IPCE (%) = 1240 J_{sc} / λ P_{in} where J_{sc} is the short-circuit current density, λ is the wavelength of the incident light, and P_{in} is the power of the incident light.

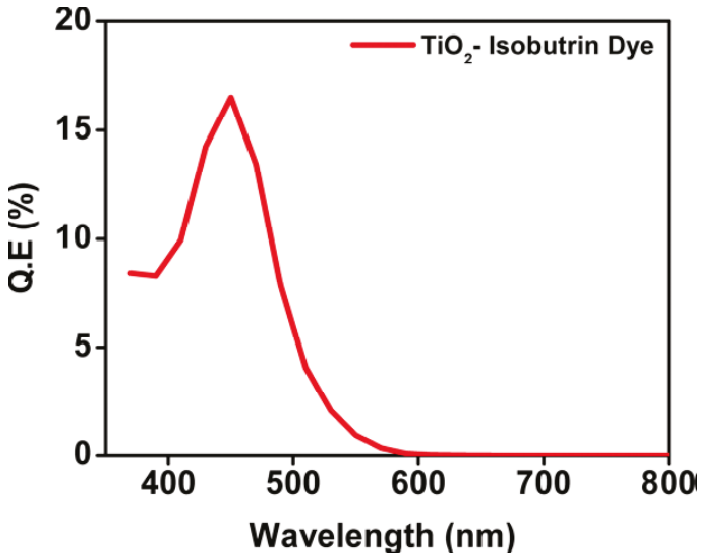

Figure 11. IPCE measurement of isobutrin dye-loaded TiO_2 film

5.4.4. Stability Data. To explore the thermal stability of natural Isobutrin Vis a Vis the N719 dye, we performed heat treatment study on the sensitized TiO_2 cells, the results being shown in Figure 10. Note that the efficiency was measured at room temperature after heating the cells to a specific temperature for ½ h. It is observed that in the case of Ru based dye the total conversion efficiency (at room temperature) starts decreasing for heat treatment above 50^{o}C while for Isobutrin dye it is stable for heat treatment up to 100^{o}C. For Ru based dye the efficiency

decreases from 5% to less than 0.3% at 200 ^{0}C after interval of 30 min at every step from room temperature to 200^{0}C. On the other hand in the case of isobutrin the total conversion efficiency remains ~ 1% up to 160^{0}C. This proves that isobutrin chelate is thermally stable as compared to Ru based dyes at higher temperature.

.

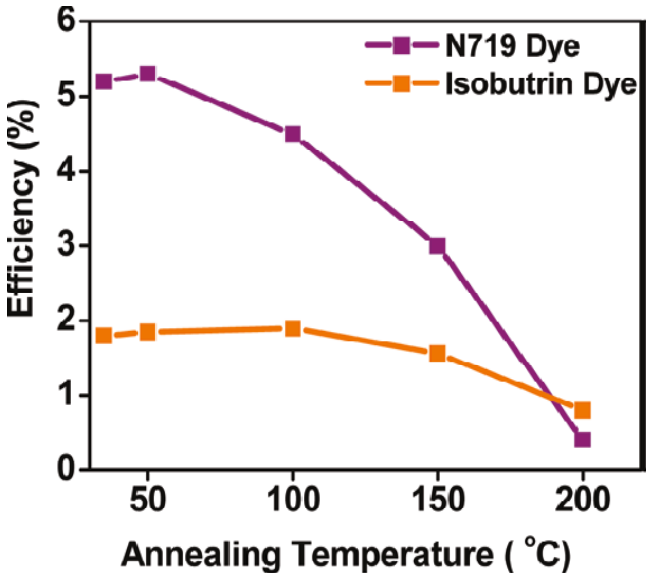

Figure 12. Solar conversion efficiency with respect to cell processing temperature

The reason for better thermal stability of isobutrin compared to N719 dye lies in its basic structure. N719 adsorbed on the TiO_2 electrode is not stable, as it can react with I_3^- in the electrolyte and be desorbed or get photodegradated under illumination, which leads to the decrease of electron injection efficiency. Moreover, high temperature accelerates the exchange reaction rate wherein the N719 dye loses its SCN ligands which are important in reduction of the oxidized dye.

$$Ru(dcbpy)_2(SCN)_2^{2-} + I_3^- \leftrightarrow Ru(dcbpy)_2 I_2^{2-} + I_2SCN^-$$

The loss of SCN^- ligand thereby suppresses the dye regeneration thus reducing the short-circuit current density and thereby efficiency of the cell.[32]

5.5. Conclusion

In summary, a new natural (metal free) sensitizer belonging to chalcone class, namely isobutrin, is extracted from a natural flower source Butea Monosperma (Flame of the Forest) for possible use in dye sensitized solar cells as well as other optoelectronic applications. In DSSCs, purified isobutrin yields very promising solar conversion efficiency of 1.8%. Interestingly the chelation of isobutrin to Ti shifts the optical absorption toward the visible (orange) making it effective in the DSSC operation. The formation constant of this chelate is found using B-H plot, which brings out the ease of its formation. The band alignment of this chelate is established using cyclic voltametry.

5.6. References

1. R. Argazzi, N.Y.Murakami Iha, H. Zabri, F. Odobel, C.A. Bignozzi, *Coord. Chem. Rev.* **2004**, *248*, 1299–1316.
2. G. Calogero,G.D. Marco, S. Caramori, S. Cazzanti, R. Argazzi, C.A. Bignozzi, *Energy Environ. Sci.,* **2009**, *2*, 1162–1172.
3. A. K. K. Kyaw, X.W. Sun, J.L. Zhao, J.X. Wang, D.W. Zhao, X.F.Wei, X.W. Liu, H.V. Demir, T.J. Wu, *Phys. D: Appl. Phys.,* **2011**,*44,* 045102.
4. N. Robertson, *Angew. Chem., Int. Ed.* , **2006**, *45*, 2338–2345.
5. B. O'Regan ,M. Gratzel, *Nature* , **1991**, *353*, 737–740.
6. M. K. Nazeeruddin.A. Kay, I. Rodicio, R. Humphry-Baker, E. Muller, N. Vlachpoulos, M. Gratzel, *J. Am. Chem. Soc.* **1993**,*115*, 6382–6390.
7. F. Sauvage, M.K.R. Fischer, A. Mishra, S.M. Zakeeruddin, M.K. Nazeeruddin, P. Bauerle, M. Gratzel, *ChemSusChem* ,**2009**,*2*, 761–768.
8. Y.Amao,T. Komori, *Biosens. Bioelectron.* **2004**, *19*, 843–847.

9. K.Wongcharee,V. Meeyoo, S. Chavadej, *Sol. Energy Mater. Sol.Cells,* **2006**, *11*, 566–572.

10. Q.Dai, J. Rabani, *Chem. Commun*. **2001**, 2142–2143.

11. A.Polo, N. Yukie, M. Iha, *Sol. Energy Mater. Sol. Cells* , **2006**, *90*, 1936–1944.

12. C.Garcia, A. Polo, N. Yukie, M. Iha, *J. Photochem. Photobiol*., **2003**, *160*, 81–91.

13. A Kay,R. Humphry-Baker, M. Gratzel, *J. Phys. Chem.*, **1994**, *98*, 952–959.

14. P. V. Kamat, J-P. Chauvet, R.W. Fessenden, *J. Phys. Chem*., **1986**, *90*, 1389–1394.

15. Y. Amao, Y. Yamada, K. Aoki, *J. Photochem. Photobiol. A:Chem.*, **2004**, *164*, 47–51.

16. S. Ito, T. Saitou, H. Imahori, H. Ueharad, N. Hasegawa, *Energy Environ. Sci.,* **2010**, *3*, 905–909.

17. J. Simiyu, B.O. Adula, J.M. Mwabora, *Prog. Colloid Polym. Sci,* **2004**, *125*, 34–37.

18. A. Bakowska, A.Z. Kucharska, Z. Oszmianski, *J. Food Chem.,* **2003**, *81*, 349.

19. S. Hao, J. Wu, L. Fan, Y. Huang, J. Lin, Y. Wei, *Sol. Energy Mater. Sol. Cells*, **2004**, *76*, 745–750.

20. M. Rubinskiene, P. Viskelis, I. Jasutiene, R. Viskeliene, C. Bobunas, *Food Res. Int.* **2005**, *38*, 867.

21. J.B. Adams, *J. Sci. Food Agri.* **1973**, *24*, 747–762.

22. W.M.Campbell, K.W. Jolley, P. Wagner, K.Wagner, P.J. Walsh, K.C. Gordon, L.S-Mende, M.K. Nazeeruddin, Q. Wang, M. Gratzel, D.L. Officer, *J. Phys. Chem. C* **2007**, *111*, 11760–11762.

23. G. R. A.Kumara, S.Kaneko, M. Okuya, B. Onwona-Agyeman, A. Konno, K. Tennakone, *Sol. Energy Mater. Sol. Cells* **2006**, *90*, 1220–1226.

24. D. Zhang, S.M. Lanier, J.A. Downing, J.L. Avent, J. Lum, J.L. McHale, *J. Photochem. Photobiol. A: Chem.*, **2008**, *195*, 72–80.

25. X-F Wang,C-H Zhan, T. Maoka, Y. Wada, Y. Koyama, *Chem.Phys. Lett.* , **2007**, *447*, 79–85.

26. D. Chen, L. Cao, F. Huang, P. Imperia, Y-B. Cheng, R.A. Caruso, *J. Am. Chem. Soc.* **2010**, *132*, 4438–4444.

27. S. Muduli, W. Lee, V.Dhas,S. Mujawar, M. Dubey, K. Vijayamohanan, S.H. Han, S. Ogale, *ACS Appl. Mater. Interfaces* , **2009**, *1*, 2030–2035.

28. A. K.Saxena,B.D. Gupta, B.K. Kapahi, S. Muthiah, D.M. Mondhe, G.N. Qazi, V. Kumar, G. Mathan, U.S. Patent 2006/0280817 A1.

29. E.L. Tae, S.H. Lee, J.K. Lee, S.S. Yoo, E.J. Kang, K.B. Yoon, *J. Phys. Chem. B* , **2005**, *109*, 22513–22522.

30. H.A. Benesi, J.H. Hildebrand, *J. Am. Chem. Soc.* **1949**, *71*, 2703–2707.

31. D. Kim, E. Shin, *Bull. Korean Chem. Soc.,* **2003**, *24*, 1490–1495.

32. G. Xue, Y. Guo, T. Yu , J. Guan, X. Yu, J. Zhang, J. Liu, Z. Zou, *Int. J. Electrochem. Sci*., **2012**, 7, 1496 – 1511.

Chapter 6

Room temperature processable Solar Paint for DSSCs

In this work we report the development of a room temperature curable titania-nanoparticle based paint which can be applied by doctor blading, screen printing or even hand-held paint-brush and gives a remarkable conversion efficiency of 3.6% on FTO/glass substrates. It involves a fully room temperature processing that can be easily used for smart windows. The paint cures quickly saving time in the cell fabrication process. Even on a flexible ITO/PET substrate efficiency of 2.4% was achieved. We present and analyze the results of described materials and device property characterizations.

Shruti A. Agarkar *et al* ***RSC Advances***, **2012**, 2, 11645-11649.

6.1. Introduction

The concept of Dye Sensitized Solar Cells (DSSC) discovered by Grátzel and coworkers stands out as one of the front-runners in developing efficient photovoltaic technologies. The chemical method of assembling the corresponding cell architecture enables facile and cost effective processing.[1] Over the past 20 years intense work has been pursued on this design including use of various inorganic oxide morphologies,[2–5] sensitizers,[6–8] co-adsorbers, [9,10] co-sensitization schemes,[11,12] new counter electrodes[13] new redox electrolytes[14,15] etc. For large scale implementation of the technology however it is considered essential that the cells are made on polymeric flexible substrates which are not stable above ~150 ^{0}C. [16] Low processing temperatures are also desirable for flexible metal ribbon type substrates to avoid oxidation and diffusion effects. Unfortunately low temperatures fail to establish good necking between the inorganic nanoparticles with adverse consequences for carrier transport and recombination lifetime. Several interesting strategies have been pursued to render non-thermal energy supplements to achieve good necking and fairly good efficiency[17–31] such as UV processing, EPD deposition of TiO_2 on the substrate followed by heating at 150 ^{0}C, to name a few.[32–34] Arakawa *et al.* in the year 2007 reported an impressive efficiency of 7.4% under room temperature processing but by application of high pressure (100 MPa).[35] Very recently, Liu *et al*. has shown an efficiency of 2.05% for an as prepared TiO_2 film dried at 85 ^{0}C, while its compression at a pressure of 1 ton showed efficiency of 5.86% with an organic dye on a plastic substrates.[36] Lindström *et al*. used compression but with heat treatment to get efficiency of 5.4%.[37] Zaban *et al.* has shown an efficiency of 5.1% using a double shell of TiO_2/MgO coating on a mesoporous TiO_2 film prepared by drying at 150 ^{0}C.[38] There appears to be a solitary report by Liu et al. on the use of ammonia treatment for surface activation of ZnO photo-electrodes to achieve an

efficiency of 4.5%.[39] Wu and co-workers applied this protocol for DSSCs on metal substrates yielding an efficiency of 1.5–2%.[40] Unfortunately ZnO is known to be an unstable system in a dye environment. In a recent interesting paper Kamat and coworkers have shown feasibility of a quantum-dot based titania solar paint, but their cells on FTO glass are processed at 200 ^{0}C and the efficiency achieved is about 1%.[41] In this work we report the development of a room temperature curable titania- nanoparticle based paint which can be applied by doctor blading, screen printing or even hand-held paint-brush and gives a remarkable conversion efficiency of 3.6% on FTO/glass substrates that can be easily used for smart windows.

6.2. Experimental

6.2.1.Making of Room Temperature TiO_2 photoanodes. Commercially available Degussa P25 was used and the paint was prepared using tertiary butyl alcohol (tBA) and water as solvents. The TiO_2 paint was prepared using tertiary butyl alcohol (tBA) and water as solvents. Small amount of dilute acid (pH ~2) was also added to this mixture. Various weight ratios of tBA: TiO_2 were examined for optimization. After adding the desired amount of TiO_2 to this solvent system it was continuously stirred for several hours to get a viscous paste. The TiO_2 paint thus formed was coated on FTO/glass substrates as well as ITO-PET substrates using doctor blading technique. Application of the paint on the substrate by using a paint brush was also examined. Both the substrates were properly cleaned prior to paint application. TiO_2 layers with different thicknesses were realized by multiple application of the paint. After drying the films at room temperature they were soaked in 0.5mM N719 solution. Solar cells made with top electrode (Pt catalyst on FTO) and iodide-tri-iodide electrolyte were then made and tested for energy conversion efficiency and solar cell parameters. Impedance measurements were also carried out to examine the various resistances involved in the equivalent circuit.

6.2.2. Materials and Methods. Commercially available TiO_2 (Degussa, P25) was procured and used for making the solar paint. The N719 dye and Fluorine doped SnO_2 (FTO) electrodes (sheet resistance 15 ohm/square) were procured from Solaronix Co. The electrolyte used was 0.5 M 1, 2-dimethyl-3-propyl imidazolium iodide, 0.05 M LiI, 0.05 M I_2, and 0.5 M 4-tert-butylpyridine in acetonitrile/valeronitrile (v/v 1:1). The I–V characteristics were measured using a solar simulator (Newport) at 100 mW/cm^2 (1 sun AM 1.5). Standard Silicon solar cell (SER NO. 189/PVM351) from Newport, USA was used as reference cell. The measurements of incident-photon-to-current conversion efficiency (IPCE) were done using Quantum Efficiency Setup (Newport Instruments). Diffused Reflectance Spectroscopy (DRS, Jasco V-570 spectrophotometer), Field emission scanning electron microscopy (FE-SEM HITACHI S4800) and Electrochemical Impedance Spectroscopy (EIS, Autolab PGSTAT30 (Eco-Chemie)) were used to characterize the samples. The impedance measurements were performed at room temperature.

6.3. Results and Discussion

6.3.1. The Scheme. The weight ratio between tBA and TiO_2 nanoparticles is key to the success of the reported binder-free room temperature paste protocol. Optimally hydrated TiO_2 particles connect with each other through hydrogen bonding as shown in Scheme 1. Several groups have reported the use of tBA and water as solvents for making binder free TiO_2 pastes leading to a well-connected TiO_2 network,[22] the water formed as a byproduct is removed by annealing above 120 ^{0}C. Our case differs distinctly from these other works in its use of H^+ ions by the addition of acid dil HNO_3 (pH ~2) during the formation of the binder-free paste. The role of H^+ ions is to catalyze this TiO_2 network formation in the first step with water obtained as a side product.[42] From this we get a proper viscous paste which is formed in a few hours compared to the earlier

reports where 4–5 days is typically required. The next step builds on the first by the formation of a tBA–water complex, which occurs as soon as the side product water molecules surround the excess tBA molecules see Scheme 1.[43] In all cases the water quantity was half the quantity of tBA. The complex can therefore be easily and efficiently removed at room temperature

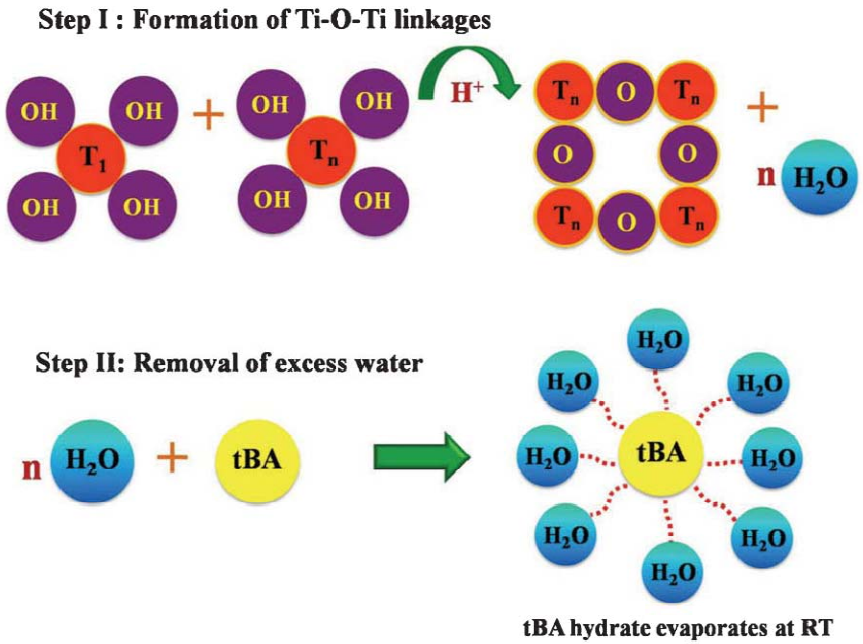

Scheme 1. Mechanism for the formation of titania photoanode at room temperature

6.3.2. FTIR Spectra. Figure 1 shows FTIR data of the solar paint taken in the ATR (Attenuated Total Reflection) mode at different time intervals. The as-formed paint shows characteristic peaks of tBA at 3375, 2970, 1650, 1360, 1200 and 900 cm^{-1} corresponding to OH bending, CH_3 anti symmetric stretching, OH bending, CH_3 deformation, C_3C–O anti symmetric stretching and CH_3 rocking modes, respectively.[44] These peaks begin to vanish quickly and progressively within a few minutes of forming film on the substrate and vanish completely after about 15 mins, suggesting that no organic matter remains in the film. This idea is central to the realization of

high quality photoanodes at room temperature. The details of the paste optimization are given in figure 2.

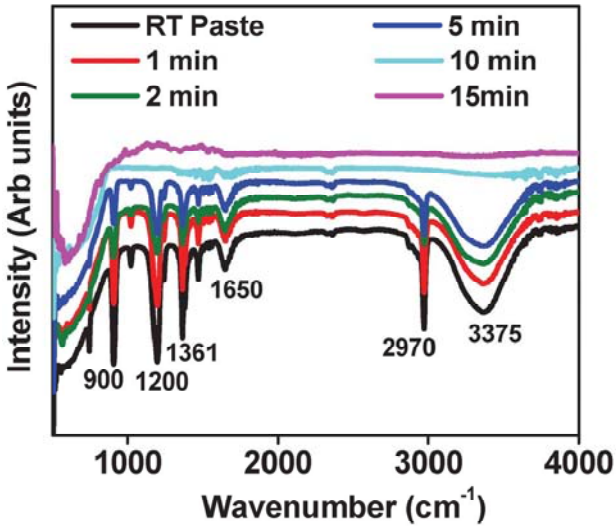

Figure 1. FTIR data of the as prepared paint taken at different time intervals at room temperature

6.3.3. Paste Optimization. It can be seen that when the weight ratio between tBA and TiO_2 nanoparticles is small (Figure 2 (a2)) the film does not have a uniform texture and agglomerates are seen. It is also clear from Figure 2 (a1)) that the paste formed is too thick to be properly blade-coated or painted on a substrate. Also there is no proper necking between the particles. When the ratio is increased, the film formed is of good quality maintaining proper porosity for dye loading as well as rendering good necking between the particles (Figure 2 (b2)). The slurry/paste formed using this ratio forms a uniform coating on the side walls of glass vial when tilted as seen in Figure 2 (b1). When the ratio is further increased a uniform film is formed but there is slight decrease in film porosity (see Figure 2 (c2)). As seen from Figure 2 (c1) this paste also forms a coating on the walls of glass vial when tilted. When the concentration of tBA is very high compared to TiO_2 the film shows scattered clusters as seen in Figure 2 (d2). Also the slurry

formed is not homogeneous and it separates out from the solvent as seen in Figure 2 (d1). Figure 3 (a-d) shows magnified FESEM images of all four cases.

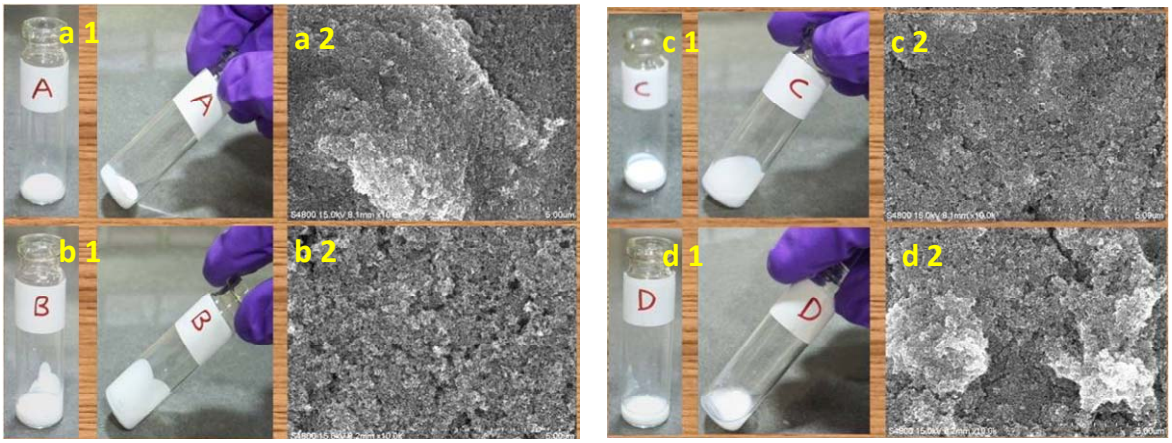

Figure 2. Shows the actual images and the FE-SEM images of the TiO_2 paint as the tBA: TiO_2 ratio is varied from low (2) to high (8). The (a1, a2), (b1, b2), (c1, c2), (d1, d2) cases correspond to the values of the ratio as 2, 4, 6, and 8, respectively.

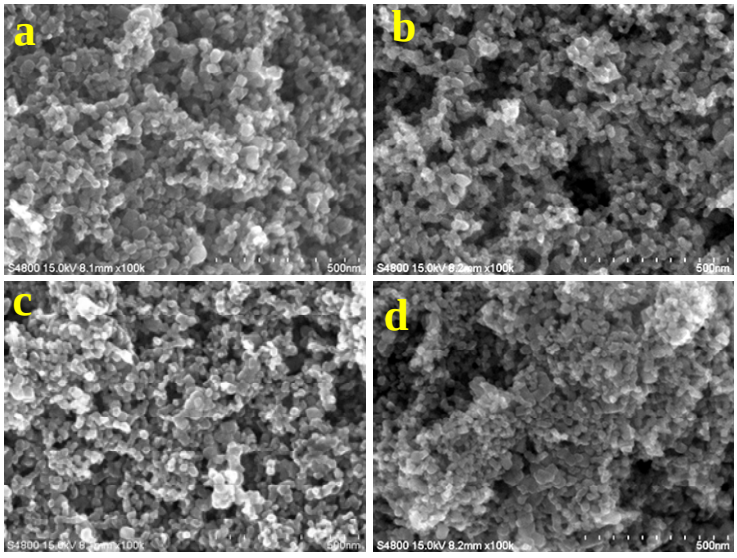

Figure 3. Magnified FE-SEM images for all the four cases with tBA: TiO_2 ratio 2 (a), 4 (b), 6 (c) and 8 (d).

6.4. Solar Cell Characteristics.

6.4.1. I-V Characteristics: Effect of variation of tBA: TiO_2 ratio. Figure 4A shows the I–V data for three different cases (tBA: TiO_2 ratio changing from 2 to 6) with all cells processed fully at room temperature. Table 1 gives the solar cell parameters. The electron micrographs shown in Figure 3 reveal changes in film morphology and microstructure with changing tBA : TiO_2 ratio (a ratio of tBA : TiO_2 of 8 shows a very rough film with large microcracks hence solar parameters are poor and not shown).

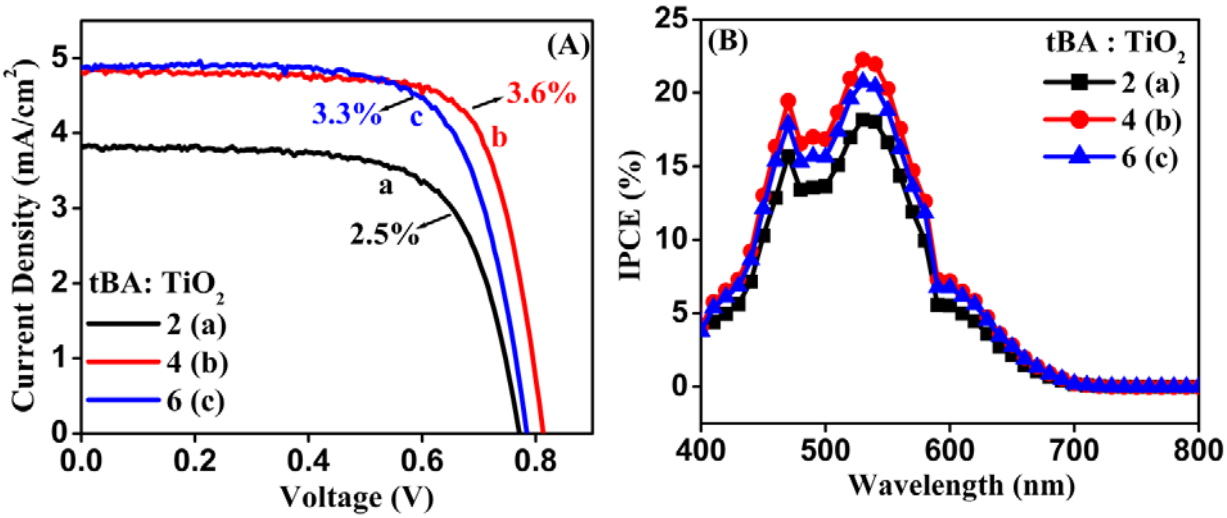

Table 1 Solar cell parameters for different systems of interest

tBA:TiO_2	V_{oc} (V)	J_{sc} (mA cm^{-2})	*FF* (%)	η (%)
2	0.77	3.82	68.74	2.5
4	0.81	4.82	73.76	3.6
6	0.78	4.88	70.1	3.3

Figure 4. (A) I–V data and (B) IPCE data for tBA : TiO_2 ratio of (a) 2 (b) 4and (c) 6.

The data for optimization purposes were recorded only with a single point edge contact. The intermediate ratio of ~4 yielded the highest efficiency at 3.6%. For a ratio of 6 the efficiency is close to the best case i.e. 3.3% while for a ratio of 2 the efficiency is low at 2.5%. Although the

dye loading for tBA : TiO_2 ratio of 2 is ~10% higher than that for ratio 4, the cause of the low efficiency is the high degree of agglomeration in the TiO_2 network which affects the interconnectivity between the TiO_2 particulate system which leads to a higher degree of recombination. The interconnectivity is reflected by the transport resistance value across the active layer (as is mentioned in Figure 6). Agglomeration tends to make mesoscale morphological features with nanoparticles attached to each other. The connectivity within the nanoparticles in a mesoscale object is good enough, but between such objects it is poorer, giving an overall higher transport resistance. An optimum tBA : TiO_2 ratio of 4 clearly shows best efficiency due to improved necking between the particles. This in turn improves the fill factor (FF) and the open circuit voltage (V_{oc}). For the tBA : TiO_2 ratio of 6 the current is high but V_{oc} and FF decrease due to presence of larger TiO_2 clusters which increase the recombination by increasing the resistance to electron flow. Figure 4B shows the incident photon to current conversion efficiency (IPCE) data for different cases. It follows the same trend as seen for the I–V data where the current density is highest for the ratio value of 4.

6.4.2. I.V Characteristics: Thickness Variation. In addition to the ratio of solvent precursors, another important parameter that is required to be optimized for the best performance of the titania electrode for DSSC is film thickness. The effective optical absorption length, internal light scattering, series resistance etc. all depend on the thickness and morphology in a fairly complex way. This is all the more important for room temperature processing because the electronic grain connectivity, which is a critical parameter governing the optoelectronic performance has no thermal assistance in this case. Indeed the solvent evaporation under ambient temperature and pressure through an evolving grain constitution defines the final nano (micro) structure; its vertical (grain compaction and connectivity gradient) and lateral (stress, micro-

cracking) uniformity. The lateral non-uniformity can result from drying shrinkage and the vertical one due to fluid density gradient. For very thin initial layers the effects of substrate-film interaction are important. Because of these factors we performed a detailed study of film thickness dependence and the relevant data are presented below. The I–V data for films of different thicknesses for our best efficiency case i.e. tBA : TiO_2 ratio 4 are shown in Figure 5. It can be seen from Table 2 that the 12 µm thick film gives the best result with better FF and Voc. It may be noted that the current density begins to drop for much thicker films.

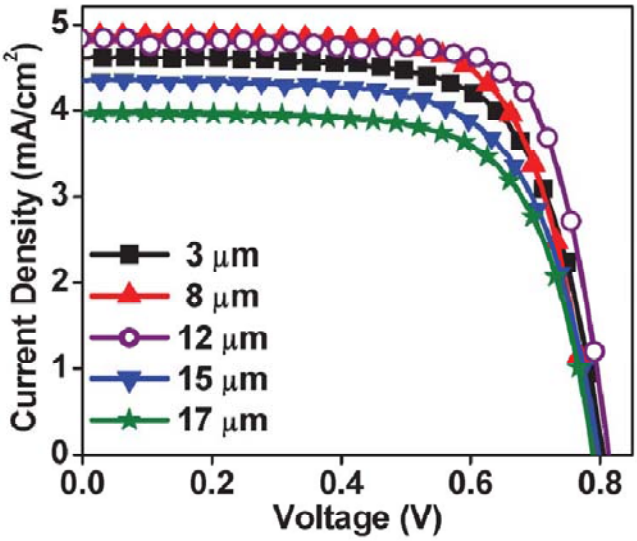

Table 2 *I–V* data with respect to film thickness

Name	V_{oc} (V)	J_{sc} (mA cm^{-2})	FF (%)	η (%)
3 µm	0.80	4.62	68.7	2.5
8 µm	0.79	4.80	70.1	2.7
12 µm	0.81	4.82	73.8	3.6
15 µm	0.79	4.30	67.3	2.3
17 µm	0.78	3.96	69.3	2.2

Figure 5. Thickness dependent I–V data and table for solar cell parameters with tBA:TiO_2 ratio 4.

6.4.3. Impedance Analysis

The results of frequency dependent impedance studies for films of different thicknesses for our best efficiency case i.e. tBA: TiO_2 ratio 4 are shown in Figure 6(B, C). The range chosen for the measurement was from 10^{-2} Hz to 10^{6} Hz with an ac-amplitude of 10 mV. The general transmission line circuit is used to fit the plots shown in Figure 6A.

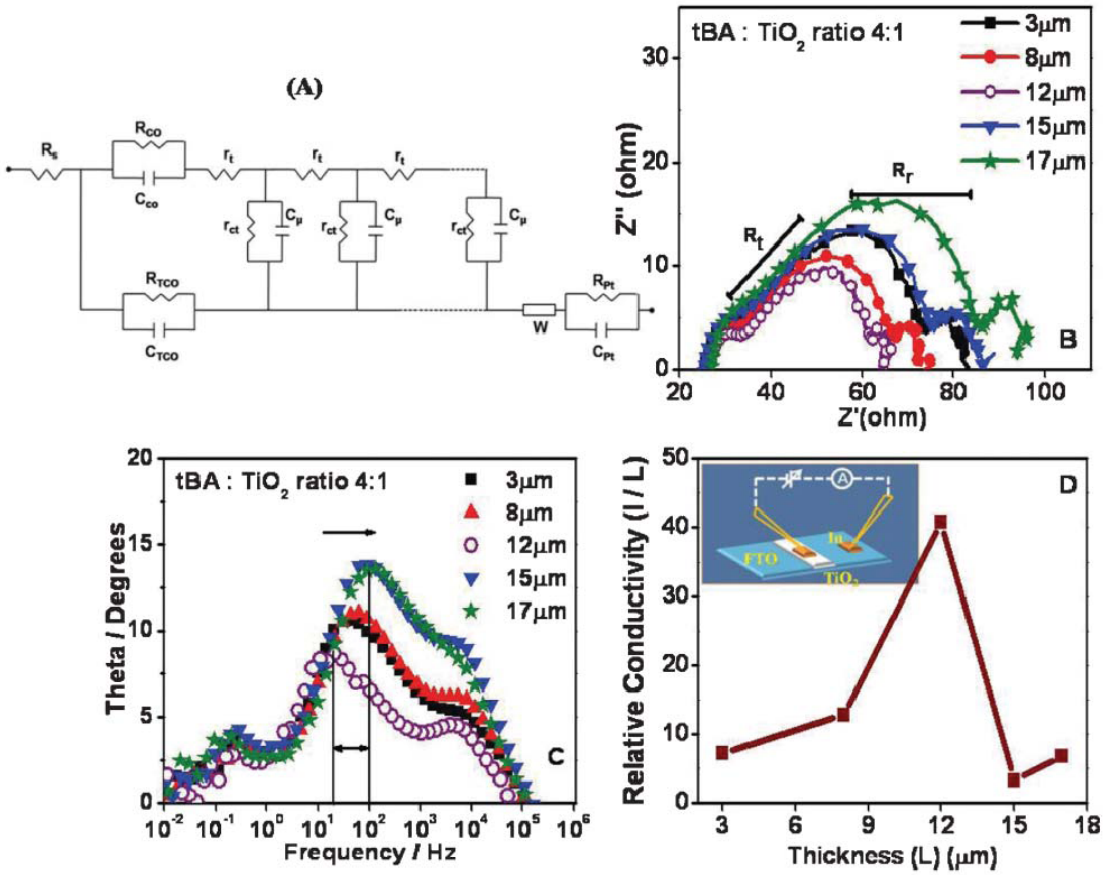

Table 3 Impedance spectroscopy data with respect to film thickness for tBA : TiO_2 ratio 4

Thickness (µm)	3	8	12	15	17
R_t (Ω)	10.8	8.49	7.2	11.4	13.8

Figure 6. (A) Equivalent circuit, (B) Nyquist plot, (C) Bode plot (D) Relative conductivity measurement and table 3 showing R_t with respect to film thickness for tBA : TiO_2 ratio 4.

Also the k_{eff} value, which is the rate of recombination of electrons, can be calculated from the peak frequency of the central arc.[47] The inverse of k_{eff} gives the lifetime (t) of electrons throughout the working electrode and has a maximum value for the 12 µm film, compared to other films. The direct current resistance of the photoanode can be obtained from current perpendicular to plane (CPP) conductivity data shown in Figure 6D. Note that the current is divided by thickness to get a measure of conductivity. It is seen that CPP, conductivity is highest (and therefore resistance is lowest) for the 12 µm film. This signifies that the process of overall grain compaction and connectivity as controlled by the fluid drying process is optimal for this thickness value. Indeed, it may be further noted from the data shown in Figure 7 that even from an optical standpoint the 12 µm film is poised for better performance. Thinner films do not absorb the full incident light and the absorption does not improve further by increasing thickness above 12 micron.

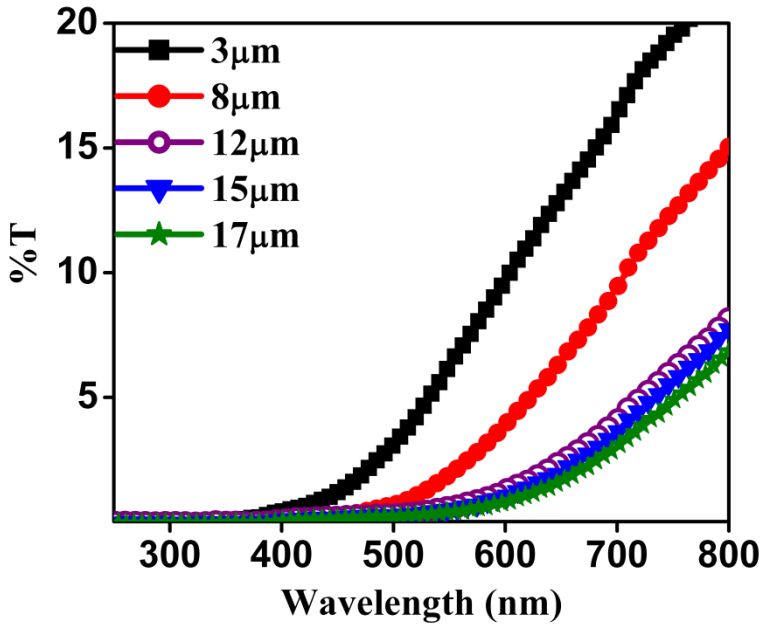

Figure 7. Percent (%) Transmittance data of thickness variation for tBA: TiO_2 ratio 4: 1

6.4.4. Effect of heat treatment on room temperature cured TiO_2 films. We explored the effect of annealing on the solar cell I–V characteristics. It is clear from the data shown in Figure 8 that annealing at 150^0C, which is also an acceptable temperature for some polymeric substrates, leads to a moderate enhancement in current density, while annealing at 450^0C leads to a significant enhancement, as expected, due to better sintering of grains and hence improvements in the solar cell quality factors.

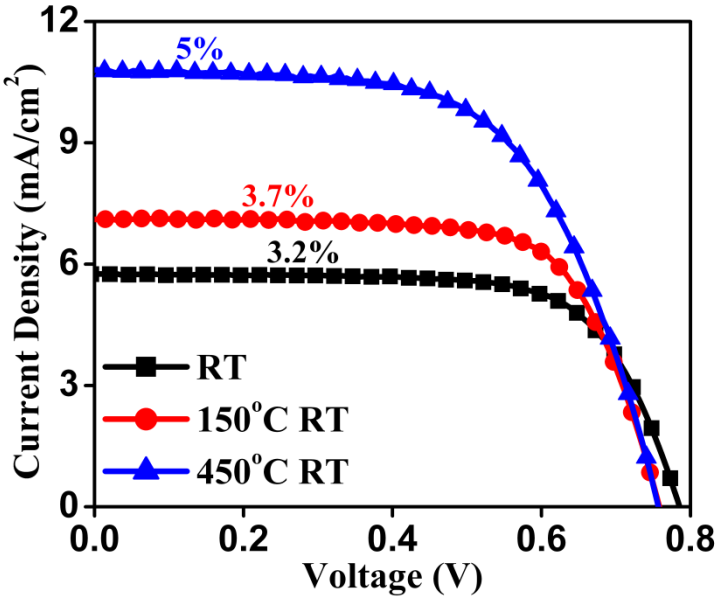

Figure 8. I–V data of cells made from solar paint at room temperature compared with those made from solar paint and annealed at 150^0C and 450^0C.

6.5. DSSCs on Flexible Substrates.

The best paste with tBA : TiO_2 ratio ~4 was tested on a flexible substrate (ITO-PET). In this case we used a third layer of TiO_2 spheres for light harvesting purposes keeping the first two layers same i.e of P25. Figure 9A shows a typical I–V curve for the same paste, which shows an efficiency of 2.4% with J_{sc} = 5 mAcm^{-2}, Voc of 0.8.V and FF of 61%. The inset shows the actual

image of the dye-loaded flexible photoanode. The use of a simple and common hand-based technique for paste application, namely a paint brush, was investigated. Figure 9B shows the I–V curve obtained using such a brush-painted photoanode, while the inset depicts the actual process of painting. A fairly high efficiency of 3% is realized, opening the way to easily paint DSSC directly on to FTO-coated smart window panes.

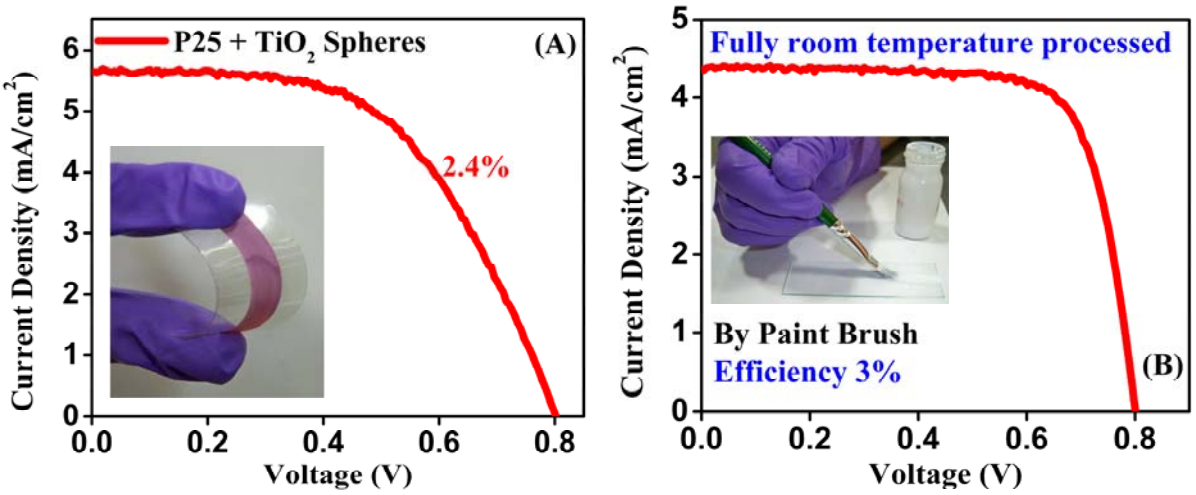

Figure 9. (A) I–V data and inset of actual images of flexible DSSC using solar paint (B) I–V data and inset of brush painted DSSC using solar paint.

6.6. Effect of silver contacts.

It may be noted that the efficiency values discussed earlier were obtained with a single point edge contact. To reduce the internal series resistance contribution (R_s) attributable to the transport resistance of the bottom and top contacts we examined U-type vapor deposited aluminum metal pads, shown in Figure 10. This is equivalent to using conducting fingers in large area solar cell geometries. Although V_{oc} decreased slightly, the current density increased

substantially as is seen in Table 4. A conversion efficiency value of 5% was achieved. This result, although promising, needs to be consolidated by further work and detailed measurements.

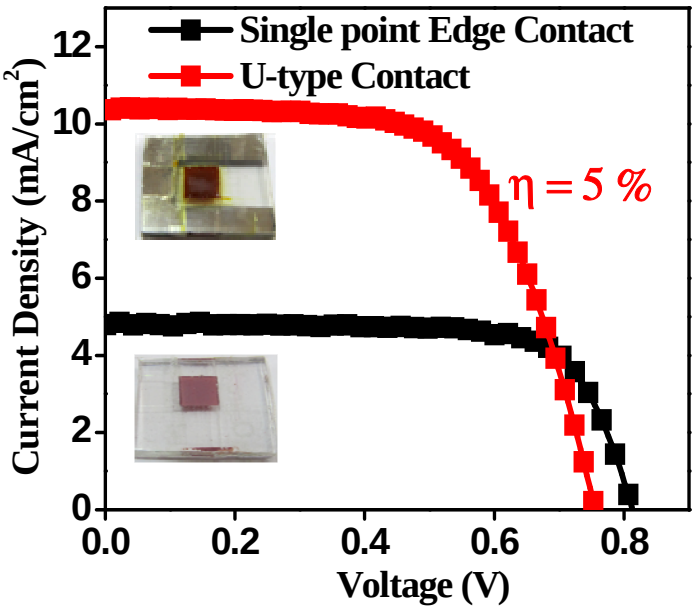

Table 4 *I–V* data for solar cells with single edge contact and U-type Al metal contacts

Name	V_{oc} (V)	J_{sc} (mA cm^{-2})	*FF* (%)	η (%)
Single point edge contact	0.81	4.8	73.7	3.6
U type contact	0.75	10.3	63.7	5.0

Figure 10. I-V data for plot for films with local and U-type Al contacts with tBA: TiO_2 ratio 4 and thickness ~12 microns.

6.7. Large area room temperature DSSCs.

We also attempted fabrication of larger area (strip type, 5 mm X 56 mm) room temperature solar cell using this optimized solar paint. We could easily achieve a conversion efficiency of 3.1%. The film configuration and the I–V data are shown in Figure 11.

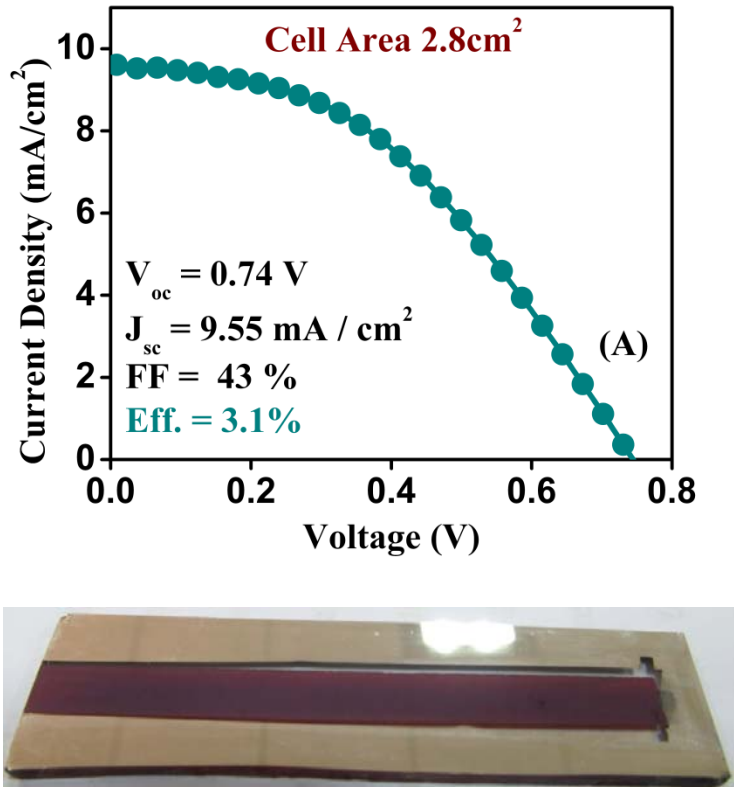

Figure 11. (A) I-V Data of large area solar paint and (B) Image of Al metal deposited large area solar cell made from solar paint.

6.8. Conclusion

In conclusion, we present a protocol for making room temperature curable titania-nanoparticle-based paint for easy application on hard as well as flexible substrates using a simple paint brush or other facile application methods (e.g. doctors blading, screen printing) to obtain fairly high conversion efficiency values. A conversion efficiency of 5% is obtained on FTO/glass substrates without any heat treatment or even an added light harvesting layer. Further optimization

including use of a light harvesting layer will push this efficiency higher. We have achieved an efficiency of 2.4% on semi-transparent flexible ITO/PET substrate amenable to roll-to-roll processing. We believe that the room temperature curable solar paint developed and demonstrated in this work can be expanded further by incorporating other functional molecules such as dyes,[48] quantum dots[49] and electrolytes as well as carbon forms such as CNT[50–52] and grapheme to create novel photo-electrodes for sensitized solar cells, hybrid cells and other energy applications.

6.9. References

1. B. O'Regan, M. Grátzel, *Nature*, **1991**, *353*, 737–740.
2. S. Muduli, O. Game, V. Dhas, A. Yengantiwar and S. B. Ogale, *Energy Environ. Sci*., **2011**, *4*, 2835–2839.
3. D. Chen, F. Huang, Y.-B. Cheng, R. A. Caruso, *Adv. Mater*., **2009**, *21*, 2206–2210.
4. D. Kim, A. Ghicov, S. P. Albu, P. Schmuki, *J. Am. Chem. Soc.*, **2008**,*130*, 16454–16455.
5. E. Ghadiri, N. Taghavinia, S. M. Zakeeruddin, M. Grátzel, J.-E.Moser, *Nano Lett.*, **2010**, *10*, 1632–1638.
6. F. Gao, Y. Wang, D. Shi, J. Zhang, M. Wang, X. Jing, R. Humphry-Baker, P.Wang, S. M. Zakeeruddin ,M. Grátzel, *J. Am. Chem. Soc.*,**2008**, *130*, 10720–10728.
7. S. Ito, S. M. Zakeeruddin, R. Humphry-Baker, P. Liska, R. Charvet, P.Comte, M. K. Nazeeruddin, P. Pe´chy, M. Takata, H. Miura, S. Uchida and M. Gra¨tzel, *Adv. Mater*., **2006**, *18*, 1202–1205.
8. R. Argazzi, N.-Y.-M. Iha, H.Zabri, F. Odobel ,C.A.Bignozzi, *Coord.Chem. Rev.*, **2004**, *248*, 1299–1316.

9. R. Y. Ogura, S. Nakane, M. Morooka, M. Orihashi, Y. Suzuki , K.Noda, *Appl. Phys. Lett.*, **2009**, *94*, 073308.
10. A. Allegrucci, N. A. Lewcenko, A. J. Mozer, L. Dennany, P. Wagner,D.L. Officer, K. Sunahara, S. Mori ,L. Spiccia, *Energy Environ. Sci.*,**2009**, *2*, 1069–1073.
11. D. Kuang, P. Walter, F. Nu¨esch, S. Kim, J. Ko, P. Comte, S. M. Zakeeruddin, M. K. Nazeeruddin , M. Gra¨tzel, *Langmuir*, **2007**, *23*,10906–10909.
12. Y. Chen, Z. Zeng, C. Li, W. Wang, X. Wang , B. Zhang, *New J.Chem.*, **2005**, *29*, 773–776.
13. M.Wu, X. Lin, T. Wang, J. Qiu ,T.Ma, *Energy Environ. Sci.*, **2011**.
14. A. Yella, H.-W. Lee, H. N. Tsao, C. Yi, A. K. Chandiran, M. K.Nazeeruddin, E. D. Wei-Guang, C.-Y. Yeh, S. M. Zakeeruddin ,M.Grátzel, *Science*, **2011**, 3344.
15. M. D. McGehee, *Science*, **2011**, *334*, 607–608.
16. T. Miyasaka, *J. Phys. Chem. Lett.*, **2011**, *2*, 262–269.
17. N.-G. Park,K.M.Kim,M.G.Kang, K. S. Ryu, S. H. Chang and Y. J.Shin, *Adv. Mater.*, **2005**, *17*, 2349–2353.
18. K.-M. Lee, S.-J.Wu, C.-Y. Chen, C.-G. Wu, M. Ikegami, K. Miyoshi, T.Miyasaka ,K.-C. Ho, *J. Mater. Chem.*, **2009**, *19*, 5009–5015.
19. Y. Kijitori, M. Ikegami, T. Miyasaka, *Chem. Lett*., **2007**, *36*, 1.
20. D. Zhang, T. Yoshida and H. Minoura, *Adv. Mater.*, **2003**, *15*, 814–817.
21. Y. Li, W. Lee, D.-K. Lee, K. Kim, N.-G. Park ,M. J. Ko, *Appl. Phys.Lett.*, **2011**, *98*, 103301.
22. L.-Y. Lin, C.-P.Lee,K.-W. Tsai,M.-H. Yeh, C.-Y.Chen, R. Vittal,C.-G.Wu , K.-C. Ho, *Prog. Photovolt: Res. Appl*, **2011**.

23. X. Fan, Z. Chu, F. Wang, C. Zhang, L. Chen, Y. Tang , D. Zou, *Adv.Mater.*, **2008**, *20*, 592–595.

24. P. Zhang,C.Wu, Y. Han, T. Jin, B. Chi, J. Pu , L. Jian, J. *Am. Ceram.Soc.*, **2011**, 1–6.

25. Y. Jiang, X. W Sun, K. W. Tan, G. Q. Lo, A. K. K. Kyaw , D. L.Kwong, *Appl. Phys. Lett.*, **2008**, *92*, 143101.

26. C-H. Lee, W-H. Chiu, K-M. Lee, W.-F. Hsieh and J.-M. Wu, *J. Mater.Chem.*, **2011**, *21*, 5114–5119.

27. T. Miyasaka, M. Ikegami and Y. Kijitori, *J. Electrochem. Soc.*, **2007**,*154*, A455–A461.

28. S. I. Cha, B. K. Koo, K. H. Hwang, S. H. Seo ,D. Y. Lee, *J. Mater.Chem.*, **2011**, *21*, 6300–6304.

29. Q. Zeng, Y. Yu, L. Wu, B. Qi , J. Zhi, *Phys. Status Solidi A*, **2010**,*207*, 2201–2206.

30. Z.Wang, H. Wang, B. Liu,W. Qiu, J. Zhang, S. Ran, H. Huang, J. Xu,H. Han, D. Chen , G. Shen, *ACS Nano*, **2011**, *5*, 8412–8419.

31. S. Uchida, M. Tomiha, H. Takizawa and M. Kawaraya, *J. Photochem.Photobiol., A*, **2004**, *164*, 93–96.

32. Z. Tebby, T. Uddin, Y. Nicolas, C. Olivier, T. Toupance, C. Labrugereand L. Hirsch, *ACS Appl. Mater. Interfaces*, **2011**, *3*, 1485–1491.

33. Z. Tebby, O. Babot, D. Michau, L. Hirsch, L. Carlos , T. Toupance, *J.Photochem. Photobiol* A., **2009**, *205*, 70–76.

34. L. Grinis, S. Dor, A. Ofir , A. Zaban, *J. Photochem. Photobiol. A*, **2008**, *198*, 52–59.

35. T. Yamaguchi, N. Tobe, D. Matsumoto, H. Arakawa, *Chem.Commun.*, **2007**, 4767–4769.

36. X. Yin, Z. Xue, L. Wang, Y. Cheng, B. Liu, *ACS Appl. Mater.Interfaces*, **2012**, *4*, 1709–1715.

37. H. Lindstrom, A. Holmberg, E. Magnusson, S.-E. Lindquist, L.Malmqvist, A. Hagfeldt, *Nano Lett.*, **2001**, *1*, 2.

38. L. Grinis, S. Kotlyar, S. Ruhle, J. Grinblat , A. Zaban, *Adv. Funct.Mater.*, **2010**, *20*, 282–288.

39. X. Liu, Y. Luo, H. Li, Y. Fan, Z. Yu, Y. Lin, L. Chen , Q. Meng, *Chem. Commun.*, **2007**, 2847–2849.

40. A. K. K. Kyaw, X. W. Sun, J. L. Zhao, J. X. D.Wang, W. Zhao, X. F.Wei, X. W. Liu, H. V. Demir , T. Wu, *J. Phys. D: Appl. Phys.*, **2011**, *44*,045102.

41. M. P. Genovese, I. V. Lightcap , P. V. Kamat, *ACS Nano*, **2012**, *6*,865–872.

42. X. Chen , S. S. Mao, *Chem. Rev.*, **2007**, *107*, 2891–2959.

43. K. Iwasak , T. Fujiyama, *J. Phys. Chem.*, **1977**, *81*, 1908–1912.

44. J. Korppi-Tommola, *Spectrochim. Acta*, **1976**, *34A*, 1077–1085.

45. J. Halme, P. Vahermaa, K.Miettunen , P. Lund, *Adv. Mater.*, **2010**, *22*,E210–E234.

46. M. Adachi,M. Sakamoto, J. Jiu, Y. Ogata, S. Isoda, *J. Phys. Chem. B.*, **2006**, *110*, 13872–13880.

47. K.-M.Lee, C.-W.Hu, H.-W.Chen, K.-C.Ho, *Sol. Energy Mater. Sol. Cells*, **2008**, *92*, 1628–1633.

48. S. A. Agarkar, R. R. Kulkarni, V. V. Dhas, A. A. Chinchansure, P. Hazra,S. Joshi , S. B. Ogale, *ACS Appl.Mater. Interfaces*, **2011**, *3*, 2440–2444.

49. W. Lee, S. K. Min, V. Dhas, S. B. Ogale , S.-H. Han, *Electrochem.Commun.*, **2009**, *11*, 103–106.

50. S.Muduli,W. Lee, V.Dhas, S.Mujawar,M. Dubey, K. Vijayamohanan,S.-H. Han , S. B. Ogale, *ACS Appl. Mater. Interfaces*, **2009**, *1*, 2030–2035.

51. A. K. K. Kyaw, H. Tantan, T. Wu, L. Ke, C. Peh, Z. H. Huang, X. T.Zeng,H. V. Demir, Q. Zhang , X. W. Sun, *Appl. Phys. Lett.*, **2011**, *99*,021107.

52. H. Zhu, H. Zeng, V. Subramanian, C. Masarapu, K.-H. Hung, B.Wei, *Nanotechnology*, **2008**, *19*, 465204.

Chapter 7

Summary and Future Scope

This chapter presents a summary of the research work reported in this thesis with concluding remarks and then lays out the scope for further work.

7.1 Summary.

Solar energy has the potential to fulfill an important part of the sustainable energy demand of future generations. With respect to the present status of PV technologies, improvements in several areas have to be made such as conversion efficiency, cost, durability, and sustainability. Semiconductor-grade silicon wafers being relatively expensive, great efforts are still being put into the development of potentially cheaper thin-film based solar cells based on earth abundant materials systems. With the emergence and rapid growth of nanotechnology, new concepts and designs of solar cell architectures harnessing the novelty rendered by the nanomaterials have emerged over the past two decades and the process of discovery and invention is continuing unabated. Towards this end the third generation excitonic solar cell design conceptualized by Grátzel based on the nature's light harvesting principle of photosynthesis and termed as the Dye Sensitized Solar Cell (DSSC) has attracted considerable scientific interest and attention. It is considered to be a promising future technology, owing to its inherent cost reduction potential, which is based on the use of inexpensive components, its relatively simple production technology and ease of its wide applicability.

In order to improve the possibility of large scale implementation of the DSSC concept we introduced and demonstrated the idea of a solar paint which can cure at room temperature, thereby reducing the time and cost for making these devices. Importantly, this also helps in fabricating these devices on flexible substrates which otherwise do not withstand high temperature processing.

In another work we applied a suitably chosen natural dye (from a flower) as a sensitizer in the DSSC application. Unfortunately, it was found that the main optical absorption of this dye is in the UV region. However, most interestingly, our work brought out that chelate formation

between TiO_2 and dye shifts the absorption of isobutrin dye significantly, from the UV to the visible region with absorption maxima at 450 nm and tail extending to 700 nm. Although the efficiency with this dye-chelate complex was not found to be very high (~2%) it showed much better thermal stability over the routinely used N719 dye. This work thus highlights that chelating can render better stability.

The research work in this thesis focused on the fabrication of high efficiency Dye Sensitized Solar Cells from the lab-synthesized TiO_2 nanoparticles. Considerable time and effort of this thesis work was devoted to the TiO_2 slurry making which is a crucial step in obtaining crack free TiO_2 photo anode which then can give high efficiency solar cells. An entire chapter of this thesis is devoted towards optimization and fabrication of DSSCs with efficiencies around 9%. It was found that for best efficiency DSSC the thickness of the photoanode must be between 12-15 microns. Also all the dye solutions, Pt counter electrode solution and electrolyte must be prepared in anhydrous solvents. Use of metal tweezers should be avoided in order to protect the devices from contamination of rust. Also the contacts used to measure the I-V or IPCE data of the devices must be rust free.

A chapter of this thesis has also dealt with some specific and key characterization techniques used to optimize the performance of DSSCs. In particular, the merits and demerits of various DSSC device configurations were analyzed using impedance measurements and specific analytical schemes were developed to elucidate individual component properties. Other important characterization techniques such as cyclic voltammetry and Tafel polarization used to characterize the counter electrodes of DSSCs were also implemented in this research.

7.2. Scope for future work.

While the research presented in this thesis was being performed, several developments have been occurring on the international front in terms of solar cells research. The silicon solar cell prices have crashed due to a major influx of cells and modules from China into the PV market which has put a significant strain on the innovation driven new solar cell technology development. In particular, cost competitiveness has acquired a center stage and hence emphasis of new technologies has been on the use of earth abundant, inexpensive and low-cost processing technologies. In the present thesis as well, the recognition of this reality was addressed through the possible use of natural dye for DSSC and developing a solar paint for room temperature solar cell making. Based on the insights gained through this effort the following points appear important for further research in this field:

- The use of Ruthenium based dyes in DSSCs is a matter of concern due to its high cost and environmental hazards as ruthenium is a heavy metal. Use of natural dyes as sensitizers can be an interesting alternative to these ruthenium complexes. But much work is clearly needed to improve the efficiency of these natural dye based sensitized solar cells. Modification of these naturally extracted dyes can be one way of improving the performance and stability of these natural dye sensitized solar cells. Thus, mixing nature's ways and laboratory based chemical manipulations may offer some interesting solutions.

- Co-sensitization by different dyes absorbing in various regions of solar spectrum is another way which can be employed to improve the performance of DSSCs. To state an example, ruthenium dyes showing absorption maxima at 550 nm can be coupled with squarine dyes which show maximum absorption at around 700 nm. This will cover the

entire visible as well as near IR region of the solar spectrum. Here the main advantage is that maximum light of the solar spectrum can be absorbed which will in turn increase the density of photo-generated carriers, thereby increasing the current and efficiency of the solar cell. This is not necessarily an easy proposition as it may seem because of the issue of competitive adsorption, conformational hindrances etc. Hence chemical tricks may have to be invoked to achieve such goal. Similarly, co-sensitization with quantum dots and suitable dyes is a possible option that may offer some specific advantages. Here again the adsorption sequences and interfaces may need adequate tailoring.

- The high temperature annealing process required for the fabrication of high efficiency DSSCs can be completely avoided using the solar paint developed in the work. This process could perhaps be improvised by additional chemical steps to enhance the electronic inter-grain connectivity even to better which would enhance the conversion efficiency. The next step would be to implement such paint based protocol on a roll-to-roll cell manufacturing. The solar paint can be used in Building Integrated Photovoltaics (BIPV) where the photoanode can be directly painted on the walls or windows of a building.
- This solar paint can also be explored in the context of the newly developed next generation solar cells, namely the $CH_3NH_3PbI_3$ based perovskite solar cells where the reported efficiencies are already above 16%. The low temperature solar paint concept can facilitate the development of such cells on flexible polymeric substrates. Also, research is needed on the effects of doping, both in the inorganic oxide skeleton as well as the hybrid perovskite to engineer the corresponding interface electronic properties. Replacement of Pb by less toxic materials is also a matter of immediate scientific interest.

Appendix

p-type $CsSnI_3$ synthesis and its use for solid state dye sensitized solar cells

This work demonstrates the synthesis of $CsSnI_3$ using two different protocols. X-ray diffraction (XRD) showed pure B-γ $CsSnI_3$ phase which is stable and has good hole mobility. This material is used in the place of routine I^-/I_3^- redox electrolyte along with an ionic liquid to realize an efficiency of 6%.

8.1. Introduction

DSSCs are considered as alternatives for energy generation as they are made of non-toxic materials and offer a low-cost processing route to device fabrication. Furthermore, they can be adapted for a variety of indoor and outdoor applications, and achieve high performance with minimal environmental impact. Despite all the benefits and high conversion efficiencies, DSSCs have liquid electrolyte which affects its long term stability as it contains volatile electrolyte. There are also problems with the counter electrode corrosion and general device assembly.[1] These issues lead to a significant decrease in the conversion efficiency, making these solar cells unsuitable for long-term use. Replacement of the corrosive, volatile liquid-state electrolyte with quasi-solid/solid-state hole conductor is one of the ways for improving the stability of DSSCs and resolving sealing issues. Here, an inorganic p-type semiconductor hole transporting material (HTM), $CsSnI_3$ is proposed as a replacement for the liquid electrolyte for its intrinsic optical and electrical properties.[2]

Solid-state dye sensitized solar cells (SSDSSCs) were first developed as an alternative to corrosive liquid electrolyte based cells which suffer from long term stability and sealing issues.[3-4] Numerous attempts have been made to replace the liquid electrolytes with a wide range of hole transporting materials (HTMs), including organic hole transporting molecules (e.g. spiro-OMeTAD), p-type conducting polymers (e.g. bis-EDOT), or p-type inorganic semiconductors (e.g. $CsSnI_3$, CuI).[4-5] The early reports on devices had the red dyes N3, N719 as sensitizers and spiro-OMeTAD as HTM. An efficiency of 2.56% was achieved in 2001 by adding TBP and $Li(CF_3SO_2)_2N$ to the HTM. Recently, significant improvements in SSDSSCs have been reported in quick succession. Solid state devices using pervoskite based inorganic HTMs have been

reported with efficiency exceeding 8%.[6] In addition, solid-state DSSCs with lead iodide pervoskite as sensitizer and spiro-OMeTAD as HTM is reported to give efficiency up to approximately 15%.[7] Although spiro-OMeTAD based devices have shown high efficiency, its low hole mobility and high fabrication cost provide motivation for further research on alternative HTMs. Work by Chung et al.[2] describes a novel inorganic solution-processable p-type semiconductor, $CsSnI_3$, that yields energy-conversion efficiencies of up to 10.2% when used as a HTM in SSDSSCs.

$CsSnI_3$ belongs to the class of pervoskite semiconductors with the chemical formula of ABX_3. It is a unique phase-change material that exhibits four polymorphs.[8-9]

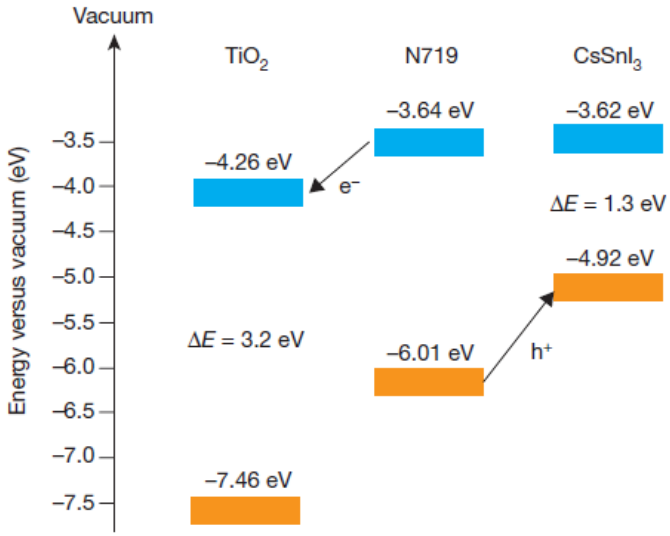

Figure 1. Energy levels of the components of the $CsSnI_3$ solid-state solar cell.[2]

Two polymorphs exist independently at room temperature,[10] one has a one-dimensional double-chain structure and is yellow in color (Y), while the other has a three-dimensional pervoskite structure and is black in color (B-γ). The B-γ $CsSnI_3$ is a direct band-gap semiconductor with an energy gap of ~1.3 eV and the yellow phase $CsSnI_3$ is an indirect band-gap semiconductor with

an energy gap of ~2.5 eV. In SSDSSCs $CsSnI_3$ has great importance due to its solution processability. It is soluble in polar solvents such as acetonitrile and DMF. A schematic diagram of the relative energy levels of $CsSnI_3$, TiO_2 and the N719 dye is shown in Figure 1. The diagram validates the excellent fit of $CsSnI_3$ for the solid-state solar cell system, giving perfect charge separation and replacement of liquid electrolytes.

8.2. Preparation of $CsSnI_3$

$CsSnI_3$ exhibits 4 different phases with respect to temperature. To obtain pure B-γ phase of $CsSnI_3$ is a challenging task. $CsSnI_3$ is synthesized mainly by two routes: solid state reaction route[2] and solution processing route.[10] The solid state reaction method is a direct approach to synthesize black-gamma $CsSnI_3$ which requires no further treatment, since the final product itself is in the B-γ phase.[2] On the other hand, when we used solution processing approach, the resultant product is in yellow phase.[10] It requires a post-heat treatment in order to obtain B-γ phase of $CsSnI_3$. The temperature profile used to obtain the yellow and B-γ phases of $CsSnI_3$ from the electrolyte prepared by solid state reaction and solution processing approach is shown in fig. 7.2.

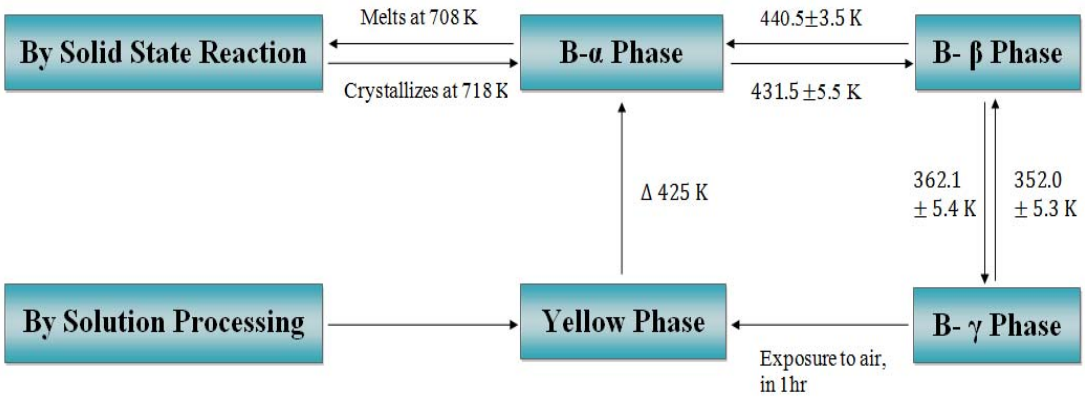

Figure 2. Temperature profile for phase conversion in $CsSnI_3$

8.2.1. Solid State Reaction/Pyrex Tube Reaction

Synthesis of $CsSnI_3$ via Pyrex tube reaction is a straightforward approach but it requires efforts and precision. First, Precursor chemicals CsI (0.2M, 0.2054 g) and SnI_2 (0.2M, 0.2946 g) were mixed and ground together in a mortar to obtain a fine, uniform mixture. This powder mixture was transferred into a Pyrex tube. The Pyrex tube was evacuated for at least 4 hours till the vacuum settled completely. The evacuated tube was heated for 1 hour at 500ºC followed by quenching to room temperature. Shiny, black colored solid mass was obtained which was further ground to obtain fine black particles of $CsSnI_3$. This powder easily dissolves in a mixture of anhydrous polar solvents namely acetonitrile (1.5 mL) and DMF (1.5 mL). The final solution was stirred for 30 minutes. For SnF_2 doping, 5 wt.% of SnF_2 powder was mixed with appropriate amount of $CsSnI_3$ powder and dissolved in 2mL mixture of polar solvents (stoichiometry 1:1) and stirred for 1 hour.

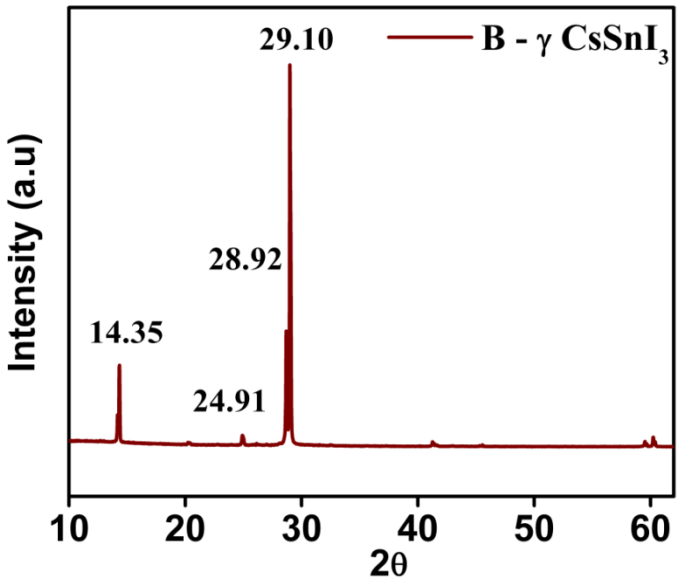

Figure 3. XRD data for CsSnI3 synthesized by solid state reaction in pyrex tube

Figure 3.shows the XRD pattern of B-γ-$CsSnI_3$ prepared by solid state reaction. The pattern for B-γ-$CsSnI_3$ shows the split peaks at 28-29º, the characteristic peaks, including peaks at 14.3º, 24.9º.[2] These together confirm pure phase B-γ-$CsSnI_3$.

8.2.2. Solution Processing

Synthesis of $CsSnI_3$ by solution processing route is a very simple approach.[10] In this method CsI (0.2M, 0.2054 g) and SnI_2 (0.2M, 0.2946 g) were dissolved in 3 mL mixture of two polar solvents. The volumetric proportion of polar solvents acetonitrile and DMF was 1:1. The final solution was stirred for 12 hours at room temperature in order to complete the reaction. A clear yellow solution was obtained. This as-prepared solution when dried gave Y- $CsSnI_3$ as shown in XRD data of Figure 4. To obtain $CsSnI_3$ nanoparticles in B-γ phase the solvent was evaporated under vacuum by heating the solution at 160ºC for an appropriate period of time.

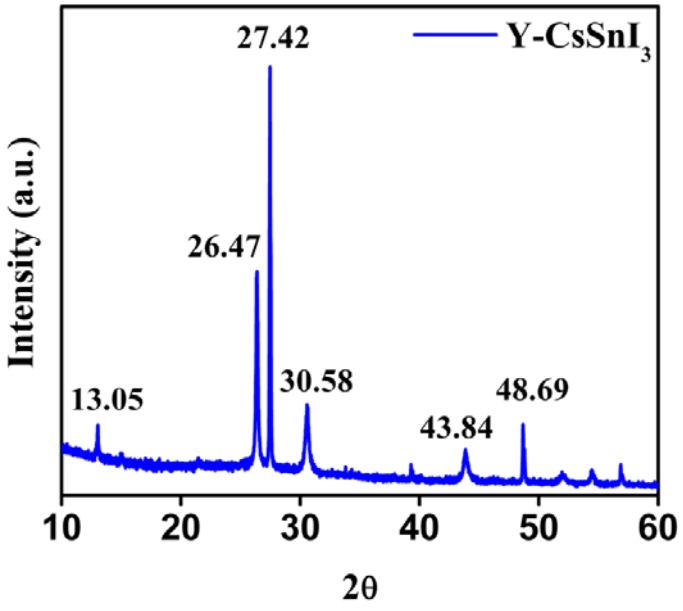

Figure 4. XRD pattern of $CsSnI_3$ formed using solution processing

Black colored particles were obtained. All the above procedures were performed in a dry-Ar glove box. The XRD pattern of the dried solution phase reaction is shown in Figure 4. The data shows Y-phase $CsSnI_3$ with characteristics peaks at 26º- 27º and peaks at 13º and 30.5º.[2]

8.3. Dye Sensitized Solar Cell Characterization

The pure phase B-γ-$CsSnI_3$ was tested as hole conductor in DSSCs. N719 dye sensitized TiO_2 was used as photoanode while Pt was used as counter electrode. The thickness of photoanode was ~10 micron. The B-γ-$CsSnI_3$ solution was injected between the two electrodes and kept for drying overnight.

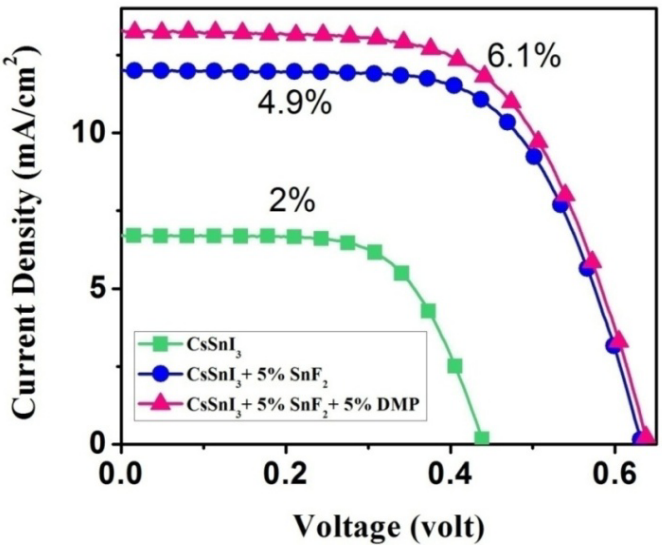

Figure 5. I-V characteristics of $CsSnI_3$, $CsSnI_3$ doped with 5% SnF_2, and $CsSnI_3$ doped with 5% SnF_2 and 5% DMPII.

Name	V_{oc} (V)	J_{sc} (mA/cm^2)	FF (%)	η (%)
$CsSnI_3$	0.43	6.65	64.65	2
$CsSnI_3$ + 5% SnF_2	0.63	12.0	64.23	4.9
$CsSnI_3$ + 5% SnF_2 + 5% DMP	0.7	13.0	67.5	6.1

Table 1. Comparison of Solar cell characteristics for DSSCs with different electrolytes

It was observed that this solution turns into a gel like substance. I-V characteristic of such cell was recorded which gave an efficiency of 2%. Same procedure was repeated but by doping 5% SnF_2 (weight percent) in the B-γ-$CsSnI_3$ solution. This cell gave an improved efficiency of 4.9% which verified the importance of SnF_2 doping. To further enhance the efficiency of this cell 5% DMPII ionic liquid (weight percent) was added to this 5% SnF_2 doped B-γ-$CsSnI_3$ solution. The efficiency of this cell increased further to 6.1%. Figure 5 shows I-V curve of all the three cases with I-V parameters in table 1.

Further work is clearly needed to analyze and improve the efficiency of these cells. This work is now in progress.

8.4. References

1. J.R. Jennings, Y. Liu, Q.Wang, *J. Phys. Chem. C*, **2011**, *115*, 15109-15120.
2. I. Chung, B. Lee, J. He, R.P.H Chang, M.G. Kanatzadis, *Nature*, **2012**, 485.
3. S. M. Zakeeruddin, M. Gratzel, *Adv Funct Mater*., **2009**, *19*, 2187-2202.
4. U. Bach, D.Lupo, P.Comte, J. E.Moser, F. Weissortel, J. Salbeck, H. Spreitzer, M. Grätzel, *Nature*, **1998**, *395*, 583-585.
5. X. Z.Liu, W. Zhang, S. Uchida, L.P. Cai, B. Liu, S. Ramakrishna, *Adv Mater*, **2010**, *22*, E150.
6. J. Burschka, N. Pellet, S.J. Moon, R.H. Baker, P. Gao, M.K. Nazeeruddin, M. Grätzel, *Nature*, **2013**, *499*, 316-319.
7. J.H.Rhee, C.C. Chung, E.W.G Diau, *Nature Photonics*, **2014**, *8*, 250-255.
8. D.E. Scaife, P.F. Weller, W.G.J. Fisher, *Solid State Chem.*, **1974,** *9*, 308−314.

9. C.Yu, Z.Chen, J.J. Wang, W. Pfenninger, N. Vockic, J.T. Kenney, K. Shum, *J.App Phy*, **2011**, *110*, 63526.
10. Y. Zhou, H.F. Garces, B.S. Senturk, A.L. Ortiz, N.P. Padture, *Mater Lett*, **2013**, *110*, 127-129.

List of Chemicals used in the research work

Chemical Name	**Supplier**	**Reference No./ CAS No.**
DMP II	Solaronix	33111
Ruthenizer 535-bis TBA	Solaronix	21612
Platisol T	Solaronix	41111
FTO TCO22-15	Solaronix	43272
TiO_2, Nanopowder, 21nm particle size	Aldrich	13463-67-7
Ethyl Cellulose (Ethoxy content 48%	Aldrich	9004-57-3
alpha-Terpineol, 97+%	Acros	98-55-5
Acetonitrile	Aldrich	75-05-8
Valeronitrile	Aldrich	110-59-8
Iodine	Aldrich	7553-56-2
4-Tert Butyl Pyridine	Aldrich	3978-81-2
PEG	Aldrich	25322-68-3
Triton X 100	Aldrich	9002-93-1

LiI	Aldrich	10377-51-2
TIP Titanium tetra Isopropoxide	Sigma Aldrich	546-68-9

List of Publications

First Author Publications

1. **Shruti A. Agarkar**, R. Kulkarni, V. V. Dhas, A. A. Chinchansure, P. Hazra, S. P. Joshi, and S. B. Ogale , Isobutrin from Butea Monosperma (Flame of Forest) as a Promising new natural sensitizer belonging to chalcone class, ACS Applied Materials and Interfaces, 2011, 3, 2440–2444.

2. **Shruti A. Agarkar**, V. V. Dhas, S. Muduli and S. B. Ogale, Dye sensitized solar cell (DSSC) by a novel fully room temperature process: a solar paint for smart windows and flexible substrates, RSC Adv., 2012, 2, 11645-11649.

Corresponding Author Publications*

3. R. A. Naphade, M. Tathavadekar, J. P. Jog, Shruti A. Agarkar* and S. B. Ogale*, Plasmonic light harvesting of dye sensitized solar cells by Au-nanoparticle loaded TiO2 nanofibers, J. Mater. Chem. A, 2014,2, 975-984.

4. A. Banerjee, K. Upadhyay, S. Bhatnagar, M. Tathavadekar, U. Bansode, **Shruti A. Agarkar*** and S. B. Ogale*, Nickel cobalt sulfide nanoneedle-array as an effective alternative to Pt as counter electrode in dye sensitized solar cell, RSC Adv., 2014, 4, 8289.

5. M. Tathavadekar, M. Biswal, **Shruti A. Agarkar***, S.B. Ogale*, Electronically and Catalytically Functional Carbon Cloth as a Permeable and Flexible Counter Electrode for Dye Sensitized Solar Cell, Electrochimica Acta.123, 248-253.

Co-Authored Publications

6. K. Sivaranjani, **Shruti A. Agarkar**, S. B. Ogale, C. S. Gopinath, Towards a Quantitative Correlation between Microstructure and DSSC Efficiency: A Case Study of TiO2xNx Nanoparticles in a Disordered Mesoporous Framework, J. Phys. Chem. C, 2012, 116, 2581–2587.

7. R. Gokhale, **Shruti A. Agarkar**, J. Debgupta, D. Shinde, B. Lefez, A. Banerjee, J. P. Jog, M. A. More, B. Hannoyer and S. B. Ogale, Laser synthesized super-hydrophobic conducting carbon with broccoli-type morphology as a counter-electrode for dye sensitized solar cells, Nanoscale, 2012, 4, 6730.

8. S. Chhatre, **Shruti Agarkar**, V. V. Dhas, S. Nagane, V. Thakare, S. B. Ogale and P. Wadgaonkar, Carboxyl-modified conjugated polymer sensitizer for dye sensitized solar cells: significant efficiency enhancement, J. Mater. Chem., 2012, 22, 23267.

9. P. P. Das, **Shruti A. Agarkar**, S. Mukhopadhyay, U. Manju, S. B. Ogale and P. Sujatha Devi, Defects in Chemically Synthesized and Thermally Processed ZnO nanorods: Implications for Active Layer Properties in Dye-Sensitized Solar Cells , Inorg. Chem, 2014, 53, 3961-3962.

10. R. Bhosale, **Shruti A. Agarkar**, I. Agrawal, R. A. Naphade and S. B. Ogale, Nanophase $CuInS_2$ nanosheets/CuS composite grown by SILAR method renders high performance as counter electrode in dye sensitized solar cells, RSC Adv., 2014, 4 , 21989 – 21996.

11. A. Jana, P. P. Das, **Shruti A. Agarkar**, P. Sujatha Devi, A Comparative Study on the Dye Sensitized Solar Cell Performance of Solution Processed ZnO, Solar Energy, 2014, 102, 143-151.

12. A. Mishra, P. Ghildiyal, **Shruti A. Agarkar**, Deepa Khushalani, Synthetic precursor to vertical TiO_2 nanowires, Materials Research Express, 2014, 1, 0025005.

13. V. V. Dhas, S. Muduli, **Shruti A. Agarkar**, A. Rana, B. Hannoyer, R. Banerjee and S. B. Ogale, Enhanced DSSC performance with high surface area thin anatase TiO_2 nanoleaves, Solar Energy, 2011, 85, 1213–1219.

14. B. Mishra, **Shruti A. Agarkar**, D. Khushalani, Novel Precursors for Anatase Nanorods and their Application in DSSCs. Materials Chemistry & Physics. In press (2014).

Patents Filed

1. Titania paint for direct room temperature fabrication of dye sensitized solar cells on window panes and flexible substrates. **Shruti Agarkar** , Vivek Dhas, Subas Muduli, Satishchandra Ogale, Application number 0798/DEL/2012, Provisional Application Filed

2. Conducting carbon cloth for sub-threshold hydrogen generation and for Dye Sensitized Solar Cell's counter electrode. Mandakini Biswal, Sarika Kelkar, Mukta Tathavedkar, **Shruti Agarkar**, Satishchandra Ogale, Provisional application filed on 7/23/2013.